NASA
Technical
Paper
2035

July 1983

Development and Evaluation of a Kalman-Filter Algorithm for Terminal Area Navigation Using Sensors of Moderate Accuracy

Gerd Kanning,
Luigi S. Cicolani,
and Stanley F. Schmidt

25th Anniversary
1958-1983

**NASA
Technical
Paper
2035**

1983

Development and Evaluation of a Kalman-Filter Algorithm for Terminal Area Navigation Using Sensors of Moderate Accuracy

Gerd Kanning and
Luigi S. Cicolani
*Ames Research Center
Moffett Field, California*

Stanley F. Schmidt
*Analytical Mechanics Associates, Inc.
Mountain View, California*

National Aeronautics
and Space Administration

**Scientific and Technical
Information Branch**

TABLE OF CONTENTS

LIST OF TABLES

LIST OF FIGURES

Page

SYMBOLS

A	square root of error state covariance matrix
Az	MODILS azimuth angle
a_i	accelerometer misalignment cone angles, i = 1,2,3, or acceleration components in level heading axes
$\underline{a},\underline{am}$	actual, measured acceleration vectors
$b, b_{tr}, b_{tb}, b_{hb}$	measurement biases: subscripts indicate data type as TACAN range and bearing or barometric altimeter
C	residual threshold factor for data rejection
d, d_{xyt}, d_{t}, etc	distance; subscripts indicate specific distances defined in context
E[ ]	expected value of contents of [ ]
$E_i(\alpha)$	transformation matrix for rotation through angle α about ith axis of any reference frame
EL, EL_m, EL_t	elevation angle with respect to MODILS elevation, MODILS Az/DME and TACAN transmitters
F	coefficient matrix of linearized stated equation
$\underline{f},\underline{fm}$	actual, measured specific force vectors, $\underline{a} - \underline{g}$
g	gravity vector
$H(w), H_{tr}$, etc	functional relation of measurement with independent variables; subscripts indicate data type
h, h_R	altitude, runway altitude
h, h_{tr}, etc	gradients of measurement function with respect to error state variables; subscripts indicate data type as TACAN range (tr), etc
h_s	measurement gradient for compressed measurement
$\{\underline{i},\underline{j},\underline{k}\}$	unit vectors along first, second, and third axis of an orthogonal reference frame; subscripts r, p, L, b indicate the reference frame as runway, path, level heading, or body
J	Jacobian matrix
K	Kalman filter gain matrix
M	number of data types or matrix as defined in context
N(m,q)	normal distribution with mean, m, and variance, q
n	number of states

n_m	number of measurements in a compressed measurement, mth data type
P,P_o	covariance, initial covariance of estimation error state, $E[\tilde{X} \tilde{X}^T]$
p	pressure
Q	covariance of state noise vector, $E[u u^T]$
q	variance
Rc	radius of curvature
$\underline{R},\underline{Rm},\underline{R}_t,\underline{R}_m,\underline{R}_e$	position vector, measured position, navaid transmitter locations
s	accelerometer scale factor error or variance of measurement residual
T	resolution of digital data
T_{ab}	transformation of vector coordinates from reference frame b to reference frame a
t	time or truncation error
U[a,b]	uniform distribution on the interval [a,b]
u	white Gaussian state variations during the filter update interval
$\underline{u}$	unit vector along TACAN-aircraft line of sight projected onto horizontal plane
$\{u_i\}$	alignment direction of ith accelerometer
$\underline{V},V$	velocity vector with respect to runway axes, speed
$\underline{Va},Va$	velocity vector with respect to air mass, airspeed
W	square root of error state covariance matrix
$\underline{W},W_x,W_y,W_z$	wind vector, runway axes coordinates of the wind vector
$X,\hat{X},\tilde{X}$	vector of state variables; actual, estimated, and estimation error, $X - \hat{X}$
(x,y,z), (x_t,y_t,z_t), etc	runway-axis position coordinates; subscripts t,m,e indicate transmitter locations for TACAN, MODILS Az/DME, and elevation
$(\dot{x},\dot{y},\dot{z})$, $(\dot{x}a,\dot{y}a,\dot{z}a)$	runway axes coordinates of $\underline{V}$, $\underline{Va}$
$(\ddot{x},\ddot{y},\ddot{z})$	runway axes coordinates of $\underline{a}$
Y,Y_{tr},Y_{tb}, etc	measurements; subscripts tr, tb, mr, ma, me, hb, r, xa, ya indicate the data type as TACAN range, bearing; MODILS range, azimuth, elevation; baro, radar altimeters; and air velocity components

y, y_s	measurement residual, residual for compressed measurement
α	angle of attack
$\{\alpha_i\}$	misalignment clock angles of accelerometers
β	sideslip angle
γ, γ_a	flightpath angles of $\underline{V}$, $\underline{Va}$
Δ	time interval in discrete time filter calculations
ΔX	estimated state estimation error from Kalman filter
$\delta\underline{R}, \delta\underline{V}$	trajectory tracking errors
η	white Gaussian state variations
θ, θ_g	pitch angle, gyroscope-indicated pitch angle
ξ	measurement errors
σ	standard deviation
τ	time constant
ϕ, ϕ_g	roll angle, gyroscope-indicated roll angle
$\psi, \psi_g, \psi_V, \psi_{Va}$	heading angles relative to the runway x-axis for $\underline{i}_b$, for $\underline{i}_b$ as measured by the directional gyroscope and for $\underline{V}$, $\underline{Va}$
ψ_R	runway heading relative to magnetic north
$(\hat{\ })$	estimate of ( )
$(\tilde{\ })$	error in estimate of ( )
$(\underline{\ })$	indicates a vector; principally position, direction, velocity, and acceleration vectors
$\langle x, y \rangle$	scalar product of vectors x,y
$(\ )_r$, etc	subscripts indicating the coordinates of the vector ( ) in the corresponding reference frame, where r, p, L, b refer to runway axes, path axes, level heading axes, and body axes
$\sim$	is distributed statistically
$\otimes$	vector cross product

Abbreviations:

CTOL	conventional takeoff and landing
DG	directional gyroscope
DME	distance measuring equipment
GPS	Global Positioning Satellite
HOT	higher order term
Hz	event occurrence rate per second, Hertz
IFR	instrument flight rules
IMU	inertial measurement unit
MLS	microwave landing system
MODILS	Modular Instrument Landing System
NALF	Navy Auxiliary Landing Field
navaid	navigational aid
rms	root mean square
rss	root sum square
SSV	Space Shuttle vehicle
std dev	standard deviation
STOL	short takeoff and landing
TACAN	tactical air navigation aid
VG	vertical gyroscope
VOR	VHF omnidirectional range navigation aid (bearing data)
VORTAC	colocated TACAN and VOR navigation aids
VTOL	vertical takeoff and landing

DEVELOPMENT AND EVALUATION OF A KALMAN-FILTER ALGORITHM FOR TERMINAL-AREA NAVIGATION USING SENSORS OF MODERATE ACCURACY

Gerd Kanning, Luigi S. Cicolani, and Stanley F. Schmidt*

Ames Research Center

SUMMARY

The optimization and accuracy of a Kalman filter estimation algorithm for an integrated terminal area navigation system for passenger operations, using sensors and components representative of those expected to be commonly available on aircraft with instrument-flight-rules (IFR) and area navigation capabilities, are discussed. These sensors are body-mounted accelerometers and vertical and directional attitude gyroscopes, along with tactical air navigation aid (TACAN) or very high frequency omnidirectional radio range and distance measuring equipment (VOR/DME), modular instrument landing system (MODILS) or microwave landing system (MLS), barometric and radar altimeters, and an airspeed sensor. This sensor set, available on several V/STOL aircraft at Ames Research Center is part of a digital flight control system called STOLAND. The principal investigative tool here is a simulation of the system, including sensors and their error processes; the discrete-time filter algorithm, together with the truncation errors and computational lags of the actual flight control system; and a simplified model of the combined aircraft and control laws together with a reference trajectory command generator. Accuracy results are given as rms errors obtained from ensembles of 10 sample approaches along a reference trajectory. The filter optimization seeks to minimize computation time with negligible loss of accuracy and considers the appropriate selection of states, partitioning of the states into independent lower-order systems, and the minimum rate for processing navaid measurements to aid the acceleration measurements. Accuracy is investigated for the terminal area and for all filter states, including the basic (input) accuracy of measuring position and acceleration; the variation of estimation (output) accuracy throughout the terminal area, with maneuvering, location, flight direction, and axis, and its sensitivity to measurement accuracy; the trajectory dispersions and control activity excited by navigation errors; and a comparison of accuracy with that required to meet various terminal area safety criteria. It is found that estimation errors for this sensor set are nonstationary and nonisotropic in the terminal area; accuracy varies with maneuvering, and by an order of magnitude for the horizontal plane translational states during an approach, and differs by an order of magnitude with direction or axis at many points in the approach. Accuracy is sufficient for safety in IFR conventional and short takeoff and landing operations based on the use of VOR/DME and MLS. In addition, in automatic reference trajectory tracking, significant tracking errors and control activity, excited by the estimation errors, affect ride quality and limit the usable control bandwidth, particularly for the horizontal plane motion.

---

*Analytical Mechanics Associates, Inc., Mountain View, California.

1. INTRODUCTION

This report considers the optimization and accuracy of a Kalman filter estimation algorithm for an integrated terminal area navigation system, using sensors and components representative of those expected to be commonly available on aircraft with instrument-flight-rules (IFR) and area navigation capabilities. The sensors assumed for this study are body-mounted accelerometers and vertical and directional attitude gyroscopes, which together form an inertial measurement unit (IMU) that measures inertial acceleration. A tactical air navigation aid (TACAN) or colocated TACAN and very-high-frequency omnidirectional radio range (VORTAC), a modular instrument landing system (MODILS), barometric and radar altimeters, and an airspeed sensor are used to aid the IMU.

This set of data types, together with a digital flight computer (Sperry 1819A) and other equipment, composes a digital flight control system (ref. 1) that is available in several vertical and short takeoff and landing (V/STOL) research aircraft operated by Ames Research Center (ARC) for flight test studies of estimation, guidance, and control algorithms. Although TACAN is a military system, it is functionally equivalent to the VOR and distance-measuring-equipment (DME) data of civil operations, and its bias statistics were set in this study to correspond to the less accurate civil data. MODILS is functionally equivalent to and represents the microwave landing system (MLS) facilities which are expected to support precision area navigation final approaches at many airports in the near future.

These sensors, together with an appropriate algorithm, provide estimates of position, velocity, wind, and Euler attitude angles for use by the flight control logic. They differ from those used in earlier applications of Kalman filtering to area navigation (refs. 2-5) in that acceleration measurements are an order of magnitude less accurate than the inertial grade IMU's of the earlier work, as a result of the fixed accelerometer errors and the maneuver-dependent dynamics of the pendulous attitude gyros. This system relies on intensive aiding of its IMU with position and airspeed data in order to obtain usable accuracy.

The principal objectives of the study reported here were (1) to develop a Kalman filter algorithm for flight studies that yields the maximum estimation accuracy inherent in the set of data types, within the constraints on computational requirements imposed by the airborne computer and flight control considerations; and (2) to evaluate the accuracy of the algorithm, particularly as it relates to the accuracy needed to support advanced, automatic, reference trajectory tracking operations.

Estimation systems are needed to support IFR and area navigation operations in the terminal area. These operations are becoming increasingly common and are advocated at various levels of complexity (two-, three-, and four-dimensional area navigation). They are considered a requirement in the integration of V/STOL operations with existing conventional-takeoff-and-landing (CTOL) operations, and are generally advocated for all commercial operations by pilots, airline operators, and the government (refs. 6-8). This broad support derives from various proved or anticipated benefits, including increased safety, economy, and operational capability, and significant reductions in fuel, noise, and pilot and controller workload.

The most demanding level of estimation and control system performance required in these operations is for automatic, four-dimensional (4-D) reference trajectory tracking and landing. The set of sensors studied here is expected to have marginal performance for 4-D operations, but has the advantage of using equipment that is much less expensive than that used in state-of-the-art inertial grade IMU's. Therefore, it is of interest to determine the maximum performance obtainable from these sensors and its suitability for 4-D operations.

For this purpose, the optimal filter (minimum estimation error variances), when only accuracy is considered, is obtained from Kalman filter theory (ref. 9), provided system dynamics and measurement errors can be modeled with sufficient accuracy in the filter. However, the optimal filter is impractical to implement within the constraints of computation storage and time limitations, because the number of variables whose uncertainties contribute to aircraft state estimation errors is unreasonably large. Thus, implementation of the Kalman filter always requires that only those variables be estimated that contribute significantly to performance in estimating the states required for the aircraft control. This entails deleting variables for which the information obtained in flight is negligible compared to the a priori information, including those variables that contribute negligibly to the estimation errors of the remaining states and those that contribute significantly to the errors but are nonetheless poorly observable to the set of data types used.

These and other approximations, such as linearization of the error state dynamics and the representation of measurement errors as Gaussian white noise, are made for tractability of the filter formulation, as well as to satisfy constraints on computational requirements. Therefore, the objective of the filter development is to minimize computation requirements with negligible loss of estimation accuracy from the optimum.

The principal investigative tool used in this study is a simulation of the system, including sensors and their error processes; the discrete-time filter algorithm, together with the truncation errors and computational lags of the actual flight control system; and a simplified model of the combined aircraft and control logic, together with a reference trajectory command generator. Accuracy results are given as rms errors obtained from ensembles of 10 sample approaches along a reference trajectory.

Various reasonable generic error models are used in the sensor simulations. For simplicity, the various types of off-nominal behavior observed in practice, other than data dropout, are neither included in the simulation nor are they within the scope of this study. These and other qualitative differences from the observed error processes exist, but the simulation suffices to determine filter performance trends with changes in the filter algorithm or in sensor accuracy and to evaluate the absolute performance of the system for nominal error behavior and statistics.

The filter algorithm uses several implementation devices developed in the earlier work to solve various problems and to minimize computational requirements. These include (1) the square root formulation of the filter (refs. 10 and 11) to eliminate computational ill-conditioning and to ensure positive definiteness of the covariance; (2) measurement compression, to reduce the number and rate of scalar measurement processings by the filter, and (3) exponentially correlated random process models for states whose deterministic dynamics are unknown. In addition, this work attempts to settle several optimization issues aimed at minimizing the computation time required with only a negligible loss of accuracy. These issues include (1) the appropriate selection of state variables, (2) the minimum rate of executing the measurement processing computations, and (3) appropriate partitioning of the states into independent, lower-order systems.

A simplified generic model of the translational degrees of freedom of the combine aircraft and control laws is derived. This model is independent of aircraft details and suffices to determine the trajectory tracking errors and control activity (measured as the corrective accelerations required for trajectory regulation) excited by navigation errors. The model yields both analytical results for these relationships and simulation results for the effects of the present system's navigation errors on trajectory tracking performance.

Sensor simulation models are described in the first section, and the filter algorithm is described in the second section. The remaining sections present a detailed analysis of the estimation accuracy achieved for all states throughout the terminal area and its sensitivity to measurement accuracy, the trajectory dispersions and control activity excited by the navigation errors, and a comparison of accuracy with that required for various terminal area operations. The available accuracy criteria generally reflect safety considerations within existing traffic separation standards and runway dimensions; they depend principally on the low frequency content of the navigation errors. Additional criteria for ride quality and control activity, which depend principally on navigation errors at or above the control bandwidth, are less developed than the safety criteria and were not considered here; however, they would significantly affect the suitability of an estimation system for use in automatic trajectory tracking.

An analysis of the basic accuracy of the sensors in measuring runway referenced position is presented in appendix A, a model of the dynamics of the attitude gyroscopes is provided in appendix B, and sensor accuracy in measuring runway referenced acceleration is discussed in appendix C. Appendix D contains an analysis of the effects of estimation errors on trajectory tracking errors.

2. SENSOR MODELS AND MEASUREMENT ACCURACY

Simulation models for all the sensors considered in this study are defined below; they are TACAN or VORTAC range and bearing; MODILS range, azimuth and elevation; barometric and radar altimeters; vertical and directional attitude gyroscopes; and three-axis, body-mounted accelerometers. Generic models are given with parameter values, transmitter locations, and other details selected to correspond to the instrumentation and flight computer available at ARC and at its terminal area STOL test facility at the Navy Auxiliary Landing Field (NALF), Crows Landing, Calif. TACAN and MODILS transmitting antennae are located, with respect to the runway, as shown in the view of the terminal area in figure 2.1. The locations of the antennae are appropriate for approach and landing operations and will permit realistic evaluation of the accuracy achievable with these sensors along STOL approach paths. The reference trajectory in this study is also shown in figure 2.1 and parameters defining this trajectory are noted in table 2.1 for later reference. The STOL runway is actually painted on a longer standard runway so that the MODILS azimuth site is farther from the landing zone than is optimum for lateral position accuracy at landing; however, this is readily accounted for in the evaluation.

Reference Frames and Transformations

The analysis makes use of several orthogonal coordinate frames; these are runway, path, body, and level heading axes. Runway axes, denoted ($\underline{i}_r$, $\underline{j}_r$, $\underline{k}_r$) (see sketch A), comprise a local vertical frame with the x-axis along the runway centerline; the navigation logic is formulated in this frame, and it is represented as an inertial

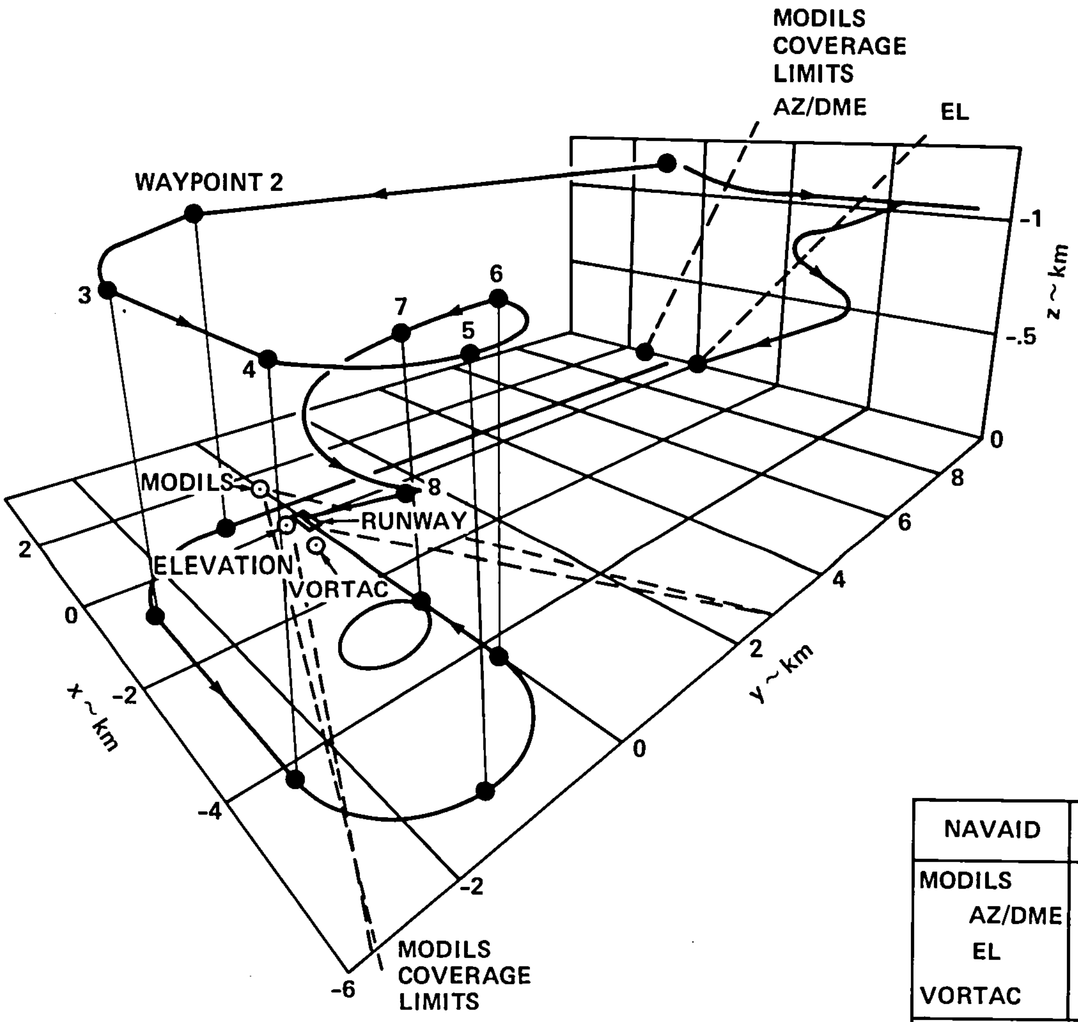

NAVAID	LOCATION ~ m x	 y	 z
MODILS			
AZ/DME	1355.9	5.2	-3.7
EL	1.8	-61.9	-1.2
VORTAC	-783.2	-308.2	0
RUNWAY:			
HEADING	-7.2°		
ALTITUDE	42.7 m		

Figure 2.1.- Terminal-area navaid sites and reference approach path.

TABLE 2.1.- TERMINAL AREA-NAVAID SITES AND REFERENCE APPROACH TRAJECTORY

Leg	Initial time, ~sec	Initial position, ~km			Initial velocity			Acceleration	
		x	y	z	V, ~knots	ψ_V, ~deg	γ, ~deg	$\dot{V}$, ~g	R_C, ~km
1. Straight	0	0.629	45.732	-1.162	140	270	0	0	-1.524
2. Helix ($\pi/2$)	647.1	0.629	-.914	-1.162	140	180	-3	0	∞
3. Straight	680.3	-.895	-2.438	-1.036	140	180	0	0.02	∞
4. Turn ($\pi/2$)	731.1	-4.298	-2.438	-1.036	120	180	0	0	-1.219
5. Turn ($\pi/2$)	762.1	-5.517	-1.219	-1.036	120	90	0	-0.035	-1.219
6. Descent	796.5	-4.298	0	-1.036	96	0	-6	-0.020	∞
7. Helix (2π)	828.7	-2.807	0	-.883	83	0	-7.5	-0.010	-.610
8. Glide slope	929.6	-2.807	0	-.381	65	0	-7.5	0	∞
9. Flare	1014.9	.024	0	-.008	65	0	-1	0	∞

frame in the motion simulation and throughout this work. The atuomatic control is formulated in path axes for independent regulation of tracking errors along and normal to the path. These axes, denoted ($\underline{i}_p$, $\underline{j}_p$, $\underline{k}_p$) in the sketch, are oriented along the aircraft velocity vector (longitudinal axis) and normal to this in the horizontal plane (lateral axis) and vertical plane (normal axis). Much of the estimation accuracy evaluation is carried out in this frame. Body axes, ($\underline{i}_b$, $\underline{j}_b$, $\underline{k}_b$), are required in the discussion of the IMU, and level heading axes, ($\underline{i}_L$, $\underline{j}_L$, $\underline{k}_L$), are also useful in some discussions under the small angle conditions of passenger operations. It is a local vertical system with $\underline{i}_L$ along the projection of $\underline{i}_b$ in the horizontal plane.

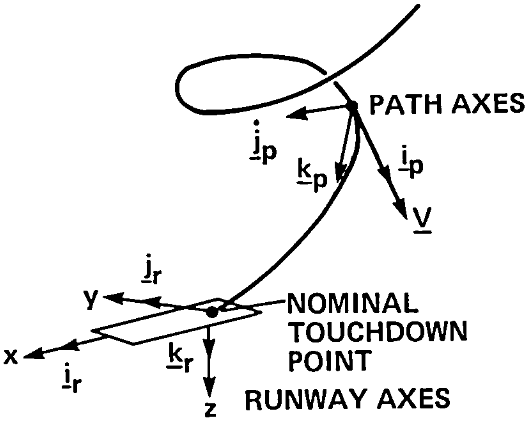

Sketch A

Several transformations among these reference frames are used in the analysis; they are listed in table 2.2. The transformation of a vector's runway axis coordinates to its body axis coordinates is given by

$$T_{br} = E_1(\phi)E_2(\theta)E_3(\psi) \tag{2.1}$$

where ϕ, θ, and ψ are the usual Euler angles. The abbreviated notation, $E_i(\sigma)$, is the transformation between orthogonal frames related by a single rotation taken about the ith axis and is defined in table 2.2. The transformation to path axes coordinates is

$$T_{pr} = E_2(\gamma)E_3(\psi_V) \tag{2.2}$$

where γ, ψ_V are the direction angles of the aircraft velocity vector (see sketch B). The transformation to path axes based on the air velocity vector is obtained using the direction angles of the air velocity vector, γ_a, ψ_{Va}.

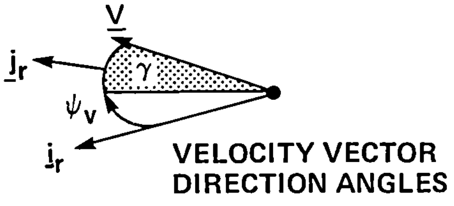

Sketch B

The transformation from air velocity path axes to body axes can be given from the above results as

$$T_{bp_a} = T_{br}T^{-1}_{p_ar} = E_1(\phi)E_2(\theta)E_3(\psi)E_3^T(\psi_{Va})E_2^T(\gamma_a) \tag{2.3}$$

Alternatively, this transformation can be given as

$$T_{bp_a} = E_2(\alpha)E_3(-\beta)E_1(\phi_V) \tag{2.4}$$

where ϕ_V is the roll angle measured about the air velocity vector, and α and β are the usual angles of attack and sideslip, respectively, which locate V_a relative to the body axes. Equations (2.3) and (2.4) can be equated to derive relations for any three angles in terms of the remaining five, as needed in the analysis.

Last, the transformation from runway to level heading coordinates is simply $E_3(\psi)$.

TABLE 2.2- TRANSFORMATION MATRICES

Single-axis rotations

$$E_1(\sigma) = \begin{bmatrix} 1 & 0 & 0 \\ 0 & \cos\sigma & \sin\sigma \\ 0 & -\sin\sigma & \cos\sigma \end{bmatrix}$$

$$E_2(\sigma) = \begin{bmatrix} \cos\sigma & 0 & -\sin\sigma \\ 0 & 1 & 0 \\ \sin\sigma & 0 & \cos\sigma \end{bmatrix}$$

$$E_3(\sigma) = \begin{bmatrix} \cos\sigma & \sin\sigma & 0 \\ -\sin\sigma & \cos\sigma & 0 \\ 0 & 0 & 1 \end{bmatrix}$$

Runway to body axes

$$T_{br} \equiv \begin{bmatrix} \cos\Theta\cos\Psi & \cos\Theta\sin\Psi & -\sin\Theta \\ \sin\Phi\sin\Theta\cos\Psi - \cos\Phi\sin\Psi & \sin\Phi\sin\Theta\sin\Psi + \cos\Phi\cos\Psi & \sin\Phi\cos\Theta \\ \cos\Phi\sin\Theta\cos\Psi + \sin\Phi\sin\Psi & \cos\Phi\sin\Theta\sin\Psi - \sin\Phi\cos\Psi & \cos\Phi\cos\Theta \end{bmatrix}$$

Runway to path axes

$$T_{pr} = \begin{bmatrix} \cos\gamma\cos\Psi_v & \cos\gamma\sin\Psi_v & -\sin\gamma \\ -\sin\Psi_v & \cos\Psi_v & 0 \\ \sin\gamma\cos\Psi_v & \sin\gamma\sin\Psi_v & \cos\gamma \end{bmatrix}$$

Air-velocity path axes to body axes

$$T_{bp_a} = \begin{bmatrix} \cos\alpha\cos\beta & -\cos\alpha\sin\beta\cos\phi_v + \sin\alpha\sin\phi_v & -\cos\alpha\sin\beta\sin\phi_v - \sin\alpha\cos\phi_v \\ \sin\beta & \cos\beta\cos\phi_v & \cos\beta\sin\phi_v \\ \sin\alpha\cos\beta & -\sin\alpha\sin\beta\cos\phi_v - \cos\alpha\sin\phi_v & \sin\alpha\sin\beta\sin\phi_v + \cos\alpha\cos\phi_v \end{bmatrix}$$

Runway to level-heading axes

$$T_{Lr} = \begin{bmatrix} \cos\Psi & \sin\Psi & 0 \\ -\sin\Psi & \cos\Psi & 0 \\ 0 & 0 & 1 \end{bmatrix}$$

Navigation Aid Measurement Models

Simulation models for the outputs of the sensors that aid the IMU are defined in table 2.3 and figure 2.2. For these sensors, a scalar measurement, Y, can be represented in general as a deterministic function of the translational states and other variables, H(w), with measurement errors, $\tilde{Y}$, superposed:

$$Y = H(w) + \tilde{Y} \tag{2.5}$$

Measurement errors arise from numerous independent sources in the equipment (sensors, receivers, transmitters, A/D devices) and from a priori calibration errors. Only the dominant error characteristics within the domain of use for a given sensor need be simulated for that sensor. Errors are represented as a sum of independent random processes with distinct statistical properties,

$$\tilde{Y} = \sum_{i=1}^{N} \xi_i + t \tag{2.6}$$

where

$$\dot{\xi}_i = (\nu_i - \xi_i)/\tau_i$$

$$\nu_i \sim N(0,\sigma_i)$$

and[1]

$$t = Y - T[\![Y/T]\!] - \text{sign}(Y)T/2$$

Here, $\{\xi_i\}$ are Gaussian error components with zero means, standard deviations $\{\sigma_i\}$, correlation times $\{\tau_i\}$ which usually differ by one or more orders of magnitude. If τ_i is much smaller than the sampling interval of the estimator (0.1 sec here) then ξ_i will be essentially independent from sample to sample. If τ_i is much larger than the terminal area flight duration, then ξ_i will appear to be a bias for the flight. In this study, the Gaussian errors are modeled simply as a sum of the bias and moderately correlated sample errors. Last, t is a truncation error resulting from the limited resolution, T, with which data are represented in the digital computer. This error is approximately a sawtooth function in time. The value of T in the present context is given by the scaling selected for each data type in the 18-bit, fixed-point STOLAND flight computer. Assuming that t is uniformly distributed on [-T/2,T/2], the variance of the combined measurement errors is

$$\sigma^2 = \sum \sigma_i^2 + \frac{T^2}{12} \tag{2.7}$$

Equation (2.6) defines the nominal error processes. In addition, there are both predictable and unpredictable situations in which a measurement is unavailable or in which its accuracy is significantly degraded from the nominal accuracy. The predictable events result from such factors as scan limits of the transmitting antenna, signal strength loss with distance and in the fringes of coverage, shadowing of the receiving antenna, and dynamic instrument lags. The estimation algorithm imposes data admissiblity conditions of the general form

---

[1] The bracket $[\![(\ )]\!]$ denotes the truncation of the magnitude of ( ) to the nearest lower integer.

TABLE 2.3- SIMULATION MODELS FOR NAVAID AND AIR-DATA MEASUREMENTS[a]

Type	Symbol	Measurement function H(w)	Error-model parameters				Measurement reception conditions, g(w)
			$\tau = 10^6$ sec, σ	$\tau = 1$ sec, σ	T	Error sum, σ	
TACAN (VORTAC)							
Range	Y_{tr}	$\lvert\underline{R} - \underline{R}_t\rvert$	61 m (305 m)	30.5 m	46 m	70 m (307 m)	$0.3 < \lvert R - R_t\rvert < 800$ km
Bearing	Y_{tb}	$\tan^{-1}\left(\frac{y_t - y}{x_t - x}\right) + \psi_R$	0.57° (2°)	0.1°	0.25°	0.58° (2°)	$0.3 < \lvert R - R_t\rvert < 800$ km $EL_t < 60°$
MODILS							
Range	Y_{mr}	$\lvert\underline{R} - \underline{R}_m\rvert$	6.1 m	12.2 m	18.5 m	15	$0.3 < \lvert\underline{R} - \underline{R}_m\rvert < 16$ km $\lvert Az\rvert < 21.2°$
Azimuth	Y_{ma}	$\tan^{-1}(y - y_m)/d_{xym}$	0.17°	0.07°	0.1°	0.19°	$EL_m < 20°$
Elevation	Y_{me}	$\tan^{-1}(-z_1/r_1)$	0.057°	0.07°	0.1°	0.095°	$0.3 < \lvert\underline{R} - \underline{R}_e\rvert < 16$ km $1.95° < EL < 16.5°$ $\lvert Az_e\rvert < 25°$ $\lvert\psi\rvert < 20°$
Altimeters							
Barometric	Y_{hb}	$h_R - z$	30.5 m	1.5 m	0.075 m	30.5 m	
Radar	Y_{hr}	$-z$	0	0.6 m	0.075 m	0.6 m	$\lvert\phi\rvert < 30°$, $\lvert\theta\rvert < 20°$, $h_r < 60$ m
Airspeed	Y_{Va}	$\lvert\underline{V} - \underline{W}\rvert$	0	0.6 mps	0.003 mps	0.6 mps	

[a] Auxiliary quantities z_1, r_1, EL_t, EL_m, d_{xym} are defined in figure 2.2.

TACAN (VORTAC)

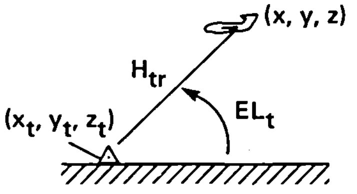

VERTICAL PLANE CONTAINING
A/C AND TACAN

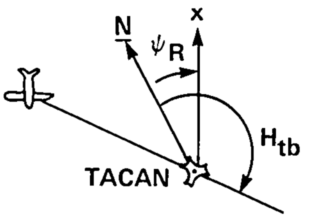

GROUND PLANE

MEASUREMENT FUNCTIONS AND AUXILIARY QUANTITIES

$R_r = (x, y, z)^T$

$R_{tr} = (x_t, y_t, z_t)^T$

$(\Delta x_t, \Delta y_t, \Delta z_t) = (x - x_t, y - y_t, z - z_t)$

$EL_t = \tan^{-1}\left(-\Delta z_t/\sqrt{\Delta x_t^2 + \Delta y_t^2}\right)$

$H_{tr} = \sqrt{\Delta x_t^2 + \Delta y_t^2 + \Delta z_t^2}$

$H_{tb} = \tan^{-1}(-\Delta y_t/-\Delta x_t) + \psi_R$

MODILS

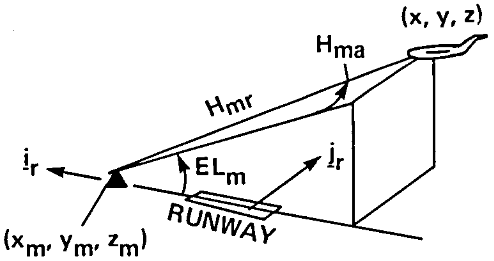

RANGE, AZIMUTH

$R_{m_r} = (x_m, y_m, z_m)^T$

$(\Delta x_m, \Delta y_m, \Delta z_m) = (x - x_m, y - y_m, z - z_m)^T$

$EL_m = \tan^{-1}(\Delta z_m/\Delta x_m)$

$d_{xym} = \sqrt{\Delta x_m^2 + \Delta z_m^2}$

$H_{mr} = \sqrt{\Delta x_m^2 + \Delta y_m^2 + \Delta z_m^2}$

$H_{ma} = \tan^{-1}\left(\frac{\Delta y_m}{d_{xzm}}\right) \quad |H_{ma}| < 90°$

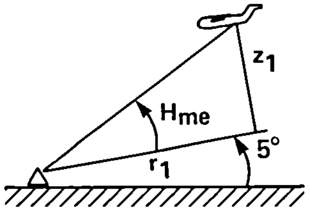

VERTICAL PLANE CONTAINING
A/C AND ELEVATION ANTENNA

$R_{e_r} = (x_e, y_e, z_e)^T$

$(\Delta x_e, \Delta y_e, \Delta z_e) = (x - x_e, y - y_e, z - z_e)^T$

$Az_e = \tan^{-1}(\Delta y_e/\Delta x_e)$

$z_1 = \Delta z_e \cos 5° - \Delta x_e \sin 5°$

$r_1 = \sqrt{\Delta x_e^2 \cos^2 5° + \Delta y_e^2 + \Delta z_e^2 \sin^2 5°}$

$H_{me} = \tan^{-1}\left(\frac{-z_1}{r_1}\right) \quad |H_{ma}| < 90°$

Figure 2.2.- Simulation models: VORTAC and MODILS measurement functions.

$$\{g_m(w) \geq 0 \quad m = 1, 2, \ldots, M\} \tag{2.8}$$

which are conservatively designed to admit data only under conditions for which the nominal error models are known to be valid, except for unpredictable signal anomalies. These conditions define the effective domain of validity, W*, for each of the present sensor error models as

$$W_m^* = \{w;\ g_m(w) \geq 0\},\ m = 1, 2, \ldots, M\} \tag{2.9}$$

Thus, it is unnecessary to model off-nominal error behavior outside W*. Within W* some measurements, such as TACAN and MODILS, are randomly subject to signal dropout and various other anomalies; signal dropout is simulated for the study of navigation accuracy during dead reckoning, but otherwise the study of these anomalies and their effects on performance is beyond the scope of the present work.

The measurement functions, error distribution parameter values, and measurement reception conditions of equations (2.5), (2.6), and (2.8) for the sensors of this study are listed in table 2.3 and figure 2.2; they are reviewed briefly below. Further discussion of navigation devices of the types used here can be found in references 12 and 13 along with additional bibliography; a summary of manufacturers' specifications for the STOLAND sensors is given in reference 14 and additional descriptive material on these devices, signal processing computations, and error analyses are presented in references 15-19.

TACAN and VORTAC both provide measurements of the magnitude and bearing from magnetic north of a vector from the aircraft to the transmitter station (fig. 2.2). Measurement errors (ref. 18) are dominated by biases and imply large position fix errors compared with those of MODILS. Range and bearing can be received well beyond the terminal area. Bearing accuracy also degrades significantly at high elevations above the station and when passing near the station, a result of dynamic receiver lags excited by high bearing rates; these conditions are avoided or limited by excluding bearing measurements at elevations above 60° and at distances from the station below 0.3 km. In addition, bearing bias can be subject to significant spatial variations, depending on the multipath characteristics of the station environs. TACAN bearing is a military navaid which is functionally equivalent to the less accurate VOR navaid available for civil flight operations. Both types of navaids are used in networks across the country in association with the National Airspace System.

Error model parameter values are listed in table 2.3 for both TACAN and VORTAC instrumentation; these differ solely in bias magnitudes. The simulation results will be based on the civil-use VORTAC navaid. Accuracies for these navaids vary widely among stations and receivers (ref. 18) but only a single grade of equipment is represented here. The TACAN model corresponds to the facility in use at Ames Research Center; it represents an average-to-good station-receiver combination and is convenient in connection with local flight studies. The VORTAC model corresponds to low accuracy VOR and DME equipment; it will provide a somewhat conservative distribution of a priori biases for evaluating the accuracy encountered by a flight control system, but a distribution for which the effects of these biases and the possibilities for their in-flight calibration are more obvious in the Monte Carlo simulation testing. In this regard, the steady state estimation accuracy will be independent of the a priori biases to the extent that in-flight calibration is possible.

Some flight recordings and analysis of the TACAN station and equipment available at Ames is reported in reference 19. The observed errors are in reasonable agreement with the present model regarding noise, biases, and behavior near the station. Signal anomalies in the samples of reference 19 and as observed in other local flight experience include isolated large error events and lengthy periods of degraded high-frequency noise standard deviation, signal hangups, and dropout. Such events are largely outside the scope of this study, but are part of the practical estimation problem.

MODILS is an experimental guidance system which provides range, azimuth, and elevation data (ref. 16). Antenna sites, coverage boundaries, and measurement geometry are indicated in figures 2.1 and 2.2 and table 2.3. Range and azimuth transmitting antennae are colocated nearly in the runway centerplane beyond the end of the runway; they provide measurements of the magnitude and angle from the centerplane of a vector from the antenna site to the aircraft (fig. 2.2). The elevation transmitting antenna is located a short distance laterally from the nominal touchdown point. It is a conical scanning antenna, tilted 5° above the ground plane and provides measurements of aircraft elevation above the ground plane. Azimuth/range and elevation coverages are limited to volumes of the terminal airspace bounded in azimuth, elevation, and distance from the antennae as noted in table 2.3. These volumes suffice to cover the final portions of an approach from negative values of x. Elevation is further restricted to a narrow band of aircraft heading angles to exclude receiver shadowing effects during turns.

Flight data (ref. 19) show gross agreement with the standard deviations of the simulation model. Sample signal error histories indicate some spatial dependence of biases, and the observed anomalies include infrequent and isolated, large elevation error events; there are also frequent episodes of linear divergence in range error (>250 m) caused by loss of receiver-transmitter synchronization. This latter type of anomaly is difficult to detect in the estimation logic. However, the poor reliability of the MODILS facility is not expected to be characteristic of future MLS's and is only of special interest here. This is confirmed by flight experience with the Phase III Basic Narrow MLS now in use at the STOL test facility (ref. 20). The present MODILS simulation model is, therefore, only representative of such systems, not a fully realistic model of the observed MODILS errors.

Altitude measurements are provided by the barometric and radar altimeters. Barometric altitude is obtained by sensing ambient free-stream pressure p_a, and converting it to altitude from a stored, standard pressure-altitude model of the atmosphere, $h^*(p_a)$ (ref. 15). On any given flight the model is calibrated to the measured pressure at the altitude of the destination runway (p_R, h_R), which is broadcast to arriving aircraft, so that barometric altitude is obtained as

$$h_b = h_R + [h^*(p_a) - h^*(p_R)]$$

The observed flight errors in this measurement are dominated by biases that vary with altitude above the point of calibration (because of departures of the actual pressure and temperature relations with altitude from the standard ones), and with speed and attitude (because of sensor calibration errors). A simplified model with fixed, 30-m rms bias is adopted for this study, but the effects of actual bias variations are noted in the evaluation where significant. Additional error types that need not be modeled in the present context are dynamic sensor lags and the large errors that can occur during flare and landing as a result of ground effects, as well as acceleration dependent errors excited by pitch up.

The radar altimeter measures altitude above the terrain based on the time required for the return of the transmitted radio signals. For commercial operations, it is used principally for final approach and landing. Here, the use of the radio altimeter is restricted to barometric altitudes under 60 m above the runway, where it can be assumed in this context that the terrain height is known. Typically, radio altimeters have very little bias error, but the random noise component increases with altitude, terrain roughness, and aircraft attitude angles; nevertheless, the measurements are much more accurate than those obtained with barometric altimeters for the restricted, low altitude range of its present use. A representative error model with null bias and fixed noise-standard-deviation of 0.6 m is adopted.

The airspeed measurement (ref. 15) is derived from measurements of differential pressure, static pressure, and stagnation temperature, using standard atmosphere temperature and density models. A simple error model with no bias and a fixed noise-standard-deviation of 0.6 m/sec is used.

Position Fix Accuracy

Aircraft position can be calculated using three simultaneous measurements of independent functions of position; for example, TACAN range and bearing, and barometric altitude or MODILS range, azimuth, and elevation. This is done, for example, in the complementary filter navigation algorithm given in reference 14 to convert the actual measurements into equivalent measurements of the aircraft coordinates before processing the data. Position fix accuracy is also of interest here as the measurement accuracy against which any position accuracy improvements obtained from the filter can be compared. This topic is discussed in appendix A; there, general formulas for position fix accuracy are derived and applied to the combinations of position navaids of interest in this study to map the accuracy available in the terminal area.

Accelerometer Measurements

A generic measurement model for the three-axis body-mounted accelerometers is given in table 2.4; the data, fm_b, measures the body axis components of specific force, f_b, corrupted by four types of accelerometer output errors and a truncation error, t_b, resulting from the selected resolution limits T_b, with which these data are represented in the flight computer. The output errors are due to scale factor error, output bias and noise, and to misalignment of the accelerometer axes and body axes. The misalignment errors can be formulated as follows: the accelerometer axes $\{\underline{u_i}\}$ are located with respect to body axes by the angles (a_i, α_i) (see sketch C) where $\{a_i\}$ are the cone angles, $\{\angle \underline{u}_1, \underline{i}_b, \angle \underline{u}_2, \underline{j}_b, \angle \underline{u}_3, \underline{k}_b\}$, and α_i is the clock angle which locates $\underline{u_i}$ on the cone. Nominal values of 0.25° are assigned to the cone angles and $\{\alpha_i\}$ are uniformly distributed on (-180°, 180°). The measured body axes components are therefore related to the actual body axes components by the misalignment matrix, M, defined in table 2.4 (for small angles, $\{a_i\}$).

An expression for the resulting measurement errors is readily derived from the measurement model:

$$\tilde{fm}_b = f_b - fm_b = -\begin{bmatrix} s_1 & a_1 \cos\alpha_1 & a_1 \sin\alpha_1 \\ a_2 \sin\alpha_2 & s_2 & a_2 \cos\alpha_2 \\ a_3 \cos\alpha_3 & a_3 \sin\alpha_3 & s_3 \end{bmatrix} \begin{bmatrix} f_{b_1} \\ f_{b_2} \\ f_{b_3} \end{bmatrix} - \xi_b - b_b - t_b \qquad (2.10)$$

TABLE 2.4.- ACCELEROMETER PACKAGE MEASUREMENT MODEL

Measured specific force

$$fm_b = \left[\diagdown\; 1 + s_i \;\diagdown\right](Mf_b + \xi_b + b_b) + t_b$$

where

$$f_b = a_b - g_b$$

$$M = \begin{bmatrix} 1 & a_1 \cos \alpha_1 & a_1 \sin \alpha_1 \\ a_2 \sin \alpha_2 & 1 & a_2 \cos \alpha_2 \\ a_3 \cos \alpha_3 & a_3 \sin \alpha_3 & 1 \end{bmatrix}$$

Error type	Distribution	Parameter values
Scale factor, s_i		$s_i = 0.01$, $i = 1, 2, 3$
Axis misalignment		
Cone angle, α_i	$\alpha_i \sim N(0,\sigma)$	$\sigma = 0.25°$
Clock angle, a_i	$a_i \sim U(-a,a)$	$a = 180°$
Bias, b_i	$b_i \sim N(0,\sigma)$	$\sigma = 0.015$ g
Noise: $\dot{\xi}_i = (\nu_i - \xi_i)/\tau$	$\nu_i \sim N(0,\sigma)$	$(\tau,\sigma) = (1 \text{ sec}, 0.003 \text{ g})$
Digital resolution, T_i		$\{T_i\} = \{0.001 \text{ g}, 0.001 \text{ g}, 0.003 \text{ g}\}$

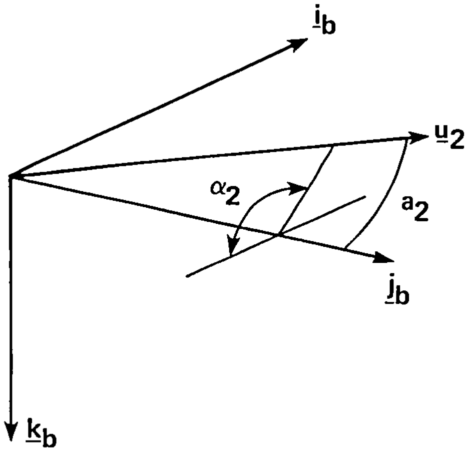

Sketch C

The corresponding error variances are

$$\sigma_1^2 = s_1^2 f_{b_1}^2 + \frac{a_1^2}{2}\left(f_{b_2}^2 + f_{b_3}^2\right) + \sigma_1^2 + \sigma_{b_1}^2 + \frac{T_1^2}{12}$$

$$\sigma_2^2 = s_2^2 f_{b_2}^2 + \frac{a_2^2}{2}\left(f_{b_1}^2 + f_{b_3}^2\right) + \sigma_2^2 + \sigma_{b_2}^2 + \frac{T_2^2}{12}$$

$$\sigma_3^2 = s_3^2 f_{b_3}^2 + \frac{a_3^2}{2}\left(f_{b_1}^2 + f_{b_2}^2\right) + \sigma_3^2 + \sigma_{b_3}^2 + \frac{T_3^2}{12}$$

Noting the parameter values listed in table 2.4 and the general restrictions on maneuver accelerations in passenger operations,

$$|f_{b_1}| < 0.15 \text{ g}, \quad |f_{b_2}| < 0.1 \text{ g}, \quad |f_{b_3}| \cong 1 \text{ g}$$

it can be calculated that the accelerometer biases dominate the measurement errors with some normal axis contribution from scale factor errors; that is,

$$\sigma_1 \cong 0.015 \text{ g}$$

$$\sigma_2 \cong 0.015 \text{ g}$$

$$\sigma_3 \cong 0.018 \text{ g}$$

The accelerometer errors are thus modeled principally as biases or as slowly varying errors of the order of 0.015 g to 0.02 g, with noise nearly an order of magnitude smaller.

Measurement Error Models of the Vertical and Directional Gyroscopes

The vertical gyroscope measures pitch and roll angle as the gimbal angles of a pendulous two-degree-of-freedom gyroscope with its fixed axis along the body longitudinal direction and its spin axis controlled to track the apparent local vertical. The directional gyroscope measures heading as a gimbal angle of a two-degree-of-freedom gyroscope with its fixed axis along the body normal axis and its spin axis controlled to track the apparent magnetic north (ref. 12). The measured angles are represented as

$$\phi_g = \phi + \tilde{\phi}_g$$

$$\theta_g = \theta + \tilde{\theta}_g$$

$$\psi_g = \psi + \tilde{\psi}_g$$

The dominant errors are dynamic tracking errors in response to aircraft maneuvering; these are deterministic functions of aircraft acceleration and attitude histories and are generated from simulation models of the dynamics of the forced gyroscope. The simulation models for STOLAND system's attitude gyroscopes were obtained from contractor's notes and are given in detail in appendix B; response to control torques, fixed and friction drifts, and rotation of the local vertical with aircraft motion and Earth's daily rotation are included.

The mathematical description of these errors is complex but their behavior in the flight conditions and maneuvers of interest is readily described. First, in an extended, unperturbed, static equilibrium flight segment, errors relax to some steady value within ±0.25°. This steady state accuracy is the best-case gyroscope performance and is limited by background torques from friction and inertial rotation of the local vertical reference frame. The maximum gimbal rates used to drive the spin axes to their reference directions are as follows:

	Maximum gimbal rates	
Vertical gyroscope, both gimbals	0.033°/sec	
Directional gyroscope, leveling gimbal	0.050°/sec	(2.11)
Directional gyroscope, heading gimbal	0.110°/sec	

These values are an order of magnitude larger than needed to balance background torques, but they also limit the rates of reducing errors induced by prior maneuvering, as is illustrated by the transient response to initial errors shown in figure 2.3(a).

Second, longitudinal accelerations affect principally the pitch measurement error. These accelerations are small and within ±0.15 g for passenger operations; they can be constant during changes of aircraft reference speed or can vary stochastically as a result of control activity to track the reference trajectory. The vertical gyroscope acts to align the spin axis with the apparent vertical, $\underline{g} - \underline{a}$, by nulling the sensed accelerations perpendicular to the spin axis. However, the control is cut off if the sensed acceleration magnitude exceeds a design value; this value is 0.05 g for the pitch gimbal and corresponds to an angle of 3° between the spin axis and apparent vertical. The cutoff is in the middle of the normal range of longitudinal acceleration activity so that various distinct types of pitch error histories can result. A step change of longitudinal acceleration from steady state static equilibrium conditions may be below or above the cutoff. If below, the pitch error rises nearly linearly to the angle between the true and apparent verticals at about the rate noted in equation (2.11). Acceleration magnitudes above the cutoff are usually developed rapidly by the aircraft before significant spin-axis misalignment from the local vertical can occur owing to control torques; after cutoff, the gyroscope is free in pitch (up to a time limit of 3 min) and subsequent misalignment develops very slowly, because of background torques. Both of these types of error histories are illustrated in figure 2.3(b). For acceleration magnitudes just above the cutoff, $\tilde{\theta}_g$ reaches -0.5° in 100 sec and subsequently continues a slow drift. For acceleration magnitudes just below the cutoff, $\tilde{\theta}_g$ is driven close to its steady state hangoff at -2.7° in 100 sec. For errors of this size, the pitch gimbal control would become locked out at a subsequent return to static equilibrium but this is countered by the cutoff time limit.

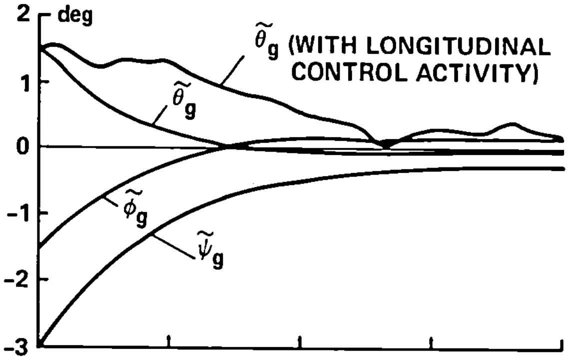

(a) BEHAVIOR IN STATIC EQUILIBRIUM

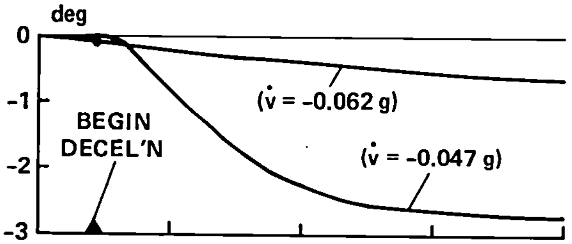

(b) PITCH ERROR FOR STEADY LONGITUDINAL DECELERATION

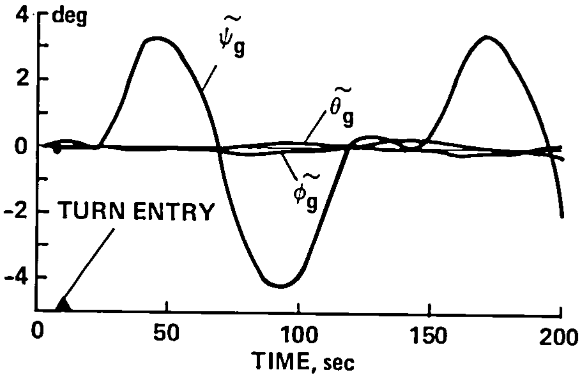

(c) BEHAVIOR IN A STEADY TURN

Figure 2.3.- Attitude-measurement errors.

Stochastic longitudinal control activity can delay the pitch error settling transient shown above; if activity is such that the sensed acceleration exceeds the cutoff for a significant percent of the time, then the settling transient is delayed and errors show some increase in steady state. An illustration of this effect was obtained by expanding the aircraft simulation to include a simple model of the control (described later); it is included in figure 2.3(b).

Third, pitchover and flare are short duration maneuvers (not shown), with very little acceleration orthogonal to the local vertical; therefore, they have almost no effect on $\tilde{\phi}_g$, $\tilde{\psi}_g$ and only a minor transient effect on $\tilde{\theta}_g$.

Fourth, steady turns result principally in large heading measurement errors, which are approximately sinusoidal and can rise to 4° or more (fig. 2.3(c)). The directional gyroscope is controlled to track a sensed magnetic north; during turning flight, a large deterministic sinusoidal error in sensing north occurs and results in a corresponding control torque history which is the principal source of the heading error history seen in figure 2.3(c). For the vertical gyroscope, the turn excites no substantial errors if the gyroscope is initially well aligned; this is illustrated by the small sinusoidal errors, $\tilde{\theta}_g$, $\tilde{\phi}_g$, of the order of 0.25°, seen in figure 2.3(c). The principal misalignment between true and apparent vertical in the turn is in roll angle, but the gyroscope's roll gimbal control is cut off if the sensed lateral acceleration exceeds 0.1 g (this corresponds to a roll misalignment of 6° between apparent vertical and the gyroscope's spin axis). For most turns, lateral acceleration is well in excess of the cutoff and is developed rapidly during turn entry, after which the vertical gyroscope is free about the roll gimbal axis, and roll gimbal errors can change only slowly with the background torques. As in the case of longitudinal accelerations, it is possible to turn at accelerations just below the roll gimbal cutoff and eventually reach errors close to 6°.

The altitude measurement errors for the last 500 sec of the test approach path of this study are shown in figure 2.4 along with time histories of the path axis components of trajectory accelerations. The attitude error behavior is consistent with that discussed above for isolated maneuvers; pitch errors are within ±1° and are associated principally with periods of acceleration below the cutoff value, 0.05 g (e.g., leg 3), and show sinusoidal behavior during turns. Roll errors rise to the order of 1° during the second and subsequent turns (legs 4, 5, and 7) as a result of

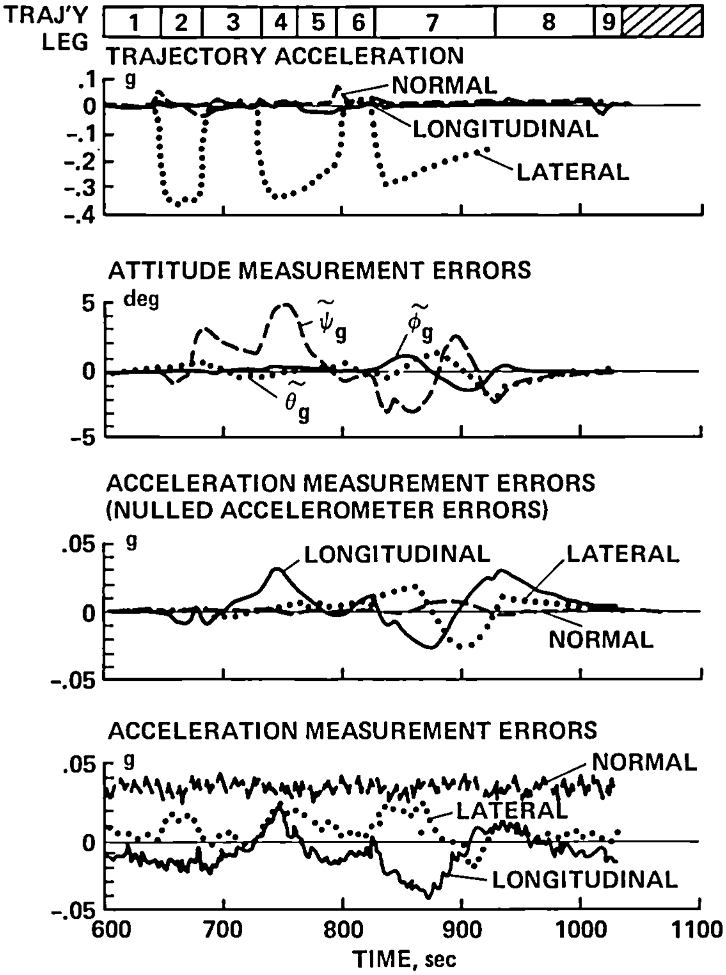

Figure 2.4.- Attitude angles and derived acceleration: sample-case measurement errors.

the initial misalignment of the vertical gyroscope at the turn entry (t = 730 sec). Heading error is within ±5°, and significant activity is confined principally to turns. All three errors show roughly continual transient activity because of aircraft maneuvering during this part of the approach, and it is only on the glide slope (t > 925 sec) that the errors settle toward their steady state values for static equilibrium flight. Flight results with STOLAND gyroscopes (ref. 21) show qualititative agreement with the present error model but show that even larger error extremes than those in figure 2.4, of the order of 2° to 3° in pitch and roll, can result from maneuvering.

Errors in Measuring Runway Axes Components of Acceleration

The estimator uses measurements of the runway axes components of acceleration, which are derived from the outputs of the accelerometer and attitude gyroscope, using

$$am_r = T_{rb}(\phi_g,\theta_g,\psi_g)fm_b + g_r \qquad (2.12)$$

Errors in the derived measurements are related to gyroscope and accelerometer measurement errors by (see appendix C):

$$\widetilde{am}_r = \begin{bmatrix} \sin\theta\, f_{r_2} + \cos\theta\sin\psi\, f_{r_3} & \cos\psi\, f_{r_3} & -f_{r_2} \\ -\sin\theta\, f_{r_1} - \cos\theta\cos\psi\, f_{r_3} & \sin\psi\, f_{r_3} & f_{r_1} \\ \cos\theta(\cos\psi\, f_{r_1} - \sin\psi\, f_{r_2}) & -\cos\psi\, f_{r_1} - \sin\psi\, f_{r_2} & 0 \end{bmatrix} \begin{bmatrix} \tilde{\phi}_g \\ \tilde{\theta}_g \\ \tilde{\psi}_g \end{bmatrix} + T_{rb}(\phi,\theta,\psi)\widetilde{fm}_b \qquad (2.13)$$

The notations am and fm indicate the measured acceleration and specific force, and $\{f_{r_i}\}$ are the runway axes specific force components.

The effects of errors in the attitude gyroscope are given by the first term in equation (2.13). It is of interest to examine the magnitude and orientation of these effects relative to the path. For this purpose, expressions for the level heading coordinates of the gyroscopic term are derived in appendix C:

$$\widetilde{am}_L^{(g)} = \begin{pmatrix}0\\ g\\ a_2\end{pmatrix}\tilde{\phi}_g - \begin{pmatrix}g\\ 0\\ a_1\end{pmatrix}\tilde{\theta}_g + \begin{pmatrix}-a_2\\ a_1\\ 0\end{pmatrix}\tilde{\psi}_g + \text{HOT's} = \begin{pmatrix}-g\tilde{\theta}_g - a_2\tilde{\psi}_g\\ g\tilde{\phi}_g + a_1\tilde{\psi}_g\\ a_2\tilde{\phi}_g - a_1\tilde{\theta}_g\end{pmatrix} + \text{HOT's} \tag{2.14}$$

where (a_1, a_2, a_3) are the level heading components of acceleration (longitudinal, lateral, and vertical) and have maximum magnitudes of about 0.15, 0.35, and 0.1 g, respectively, in passenger operations. The result assumes that θ is a small angle and that $|a_1|,|a_2| << g$. As seen in equation (2.14), roll error results in lateral acceleration error (to the order of 0.015 g) and some vertical acceleration error during turns (to the order of 0.005 g); pitch error results in longitudinal acceleration errors (to the order of 0.015 g) and in smaller vertical acceleration errors during speed changes. Heading errors cause no first-order acceleration error in static equilibrium and otherwise result principally in longitudinal errors (to the order of 0.03 g) during turns.

The gyroscopic error effects are also rearranged according to the direction of the acceleration error in equation (2.14). Longitudinal acceleration errors depend on $\tilde{\theta}_g$ and on $\tilde{\psi}_g$ during turns, and lateral errors depend on $\tilde{\phi}_g$ principally, and, to first-order, vertical errors are independent of attitude errors except for small effects, well under 0.01 g, during turns.

The effect of the accelerometer package error, $\widetilde{fm}_b$, is given by the second term in equation (2.13). This error is principally a bias vector with components of the order of 0.015 g (rms), as noted previously, and is nearly a constant vector when viewed in body axes. When mapped to runway axes, this error is also constant during straight line flight with fixed attitude; however, during turns, only the vertical component is approximately constant and the horizontal plane components vary sinusoidally with heading.

In summary, accelerometer biases and deterministic maneuver-induced gyroscopic errors dominate the horizontal plane components of $\widetilde{am}_r$, and fixed accelerometer errors dominate the vertical component. The principal errors are therefore fixed or of low frequency compared with the measurement sampling rate. Two sample histories of the path axes components of $\underline{\widetilde{am}}$ for the test approach path are included in figure 2.4. In one of these, the accelerometer errors were nulled and the resulting errors are due to errors in the attitude gyroscope; as expected, longitudinal error is proportional to $\tilde{\theta}_g$ and to $\tilde{\psi}_g$ during turns, the lateral error is proportional to $\tilde{\phi}_g$, and the vertical error is nearly independent of attitude errors. The second sample history contains randomly sampled accelerometer biases, including a large one, of the order of 0.05 g in the vertical axis; the effects of these biases are additive with the attitude error effects and are similar in magnitude. Although these errors are larger than the desired accuracy for navigation and control, they can be estimated and compensated to some degree in flight by the estimation algorithm to be described in the next section.

3. A KALMAN FILTER TRANSLATIONAL-STATE ESTIMATOR

The object of this section is to define a Kalman filter, terminal area, translation state estimation algorithm for a digital flight control system, using the set of data types previously described. Both output accuracy and computational efficiency are of acute importance in view of (1) the marginal accuracy of the IMU and VORTAC compared with that thought necessary for good IFR and automatic control, and (2) the large execution time of the Kalman filter computations in a multifunction flight computer compared to the fraction of each 0.05-sec computer cycle available for estimation computations. Therefore, the design objective is to minimize computation time while maintaining performance near the maximum that can be realized from the given sensors.

Overview

Estimates of a number of variables and parameters are required by the aircraft control; of these, the ones considered in this study are

$$\{R_r, V_r, W_r, a_r, \phi, \theta, \psi\} \tag{3.1}$$

The basic approach to their estimation uses measurements of attitude angles and body axes acceleration components to determine the runway axes acceleration; the trajectory states are then obtained by integrating the equations of motion:[2]

$$\left.\begin{aligned} am_r &= T_{rb}(\phi,\theta,\psi)fm_b + g_r \\ \dot{V}_r &= am_r \\ \dot{R}_r &= V_r \end{aligned}\right\} \tag{3.2}$$

The wind is estimated by combining airspeed and attitude measurements with the velocity estimate. Since errors are present in these measurements, as outlined in the previous section, estimation errors using equation (3.2) will grow with time. However, these errors can be estimated and corrected, using the other data types which are available and functionally related to aircraft position and velocity. Kalman filter theory (ref. 9) provides a formal basis for deriving an algorithm for this purpose. Measurements are made at discrete times, and corrections to the estimated variables are computed in proportion to the difference between the measurements and their values predicted from the current state estimate (measurement residuals); this provides an optimum (minimum variance) correction of the estimate in accordance with the relative accuracy of the measured and predicted values. Further, since the filter works on errors from the current estimate, the linear filtering theory can be applied using equations linearized about the current estimated state.

Special devices used in the application include the square root formulation of the filter equations, exponentially correlated stochastic process models for some error states, and data compression. The square root formulation provides increased precision in finite word length computations and reduces computational errors owing to ill-conditioning to insignificant levels in the present application. It also enforces positive definiteness of the error covariance matrix. Error states whose deterministic dynamics are unknown (winds, measurement biases) are modeled as exponentially correlated random processes, with the results that the filter's covariance for these states degrades toward realistic values (to the a priori accuracy) during

---

[2] Runway axes are approximated as inertial in this study of terminal area navigation since the errors involved are negligible compared with the measurements errors.

periods when no measurements are processed, and that realistic filter gains are computed when new measurements are subsequently processed. Data compression reduces the computation time required for measurement processing by summing multiple measurements of the same data type taken over a short time interval into a single nearly equivalent scalar measurement which can be processed in place of the individual measurements.

State Estimation Equations

The state X is an n-vector of the variables to be estimated and is assumed to satisfy the differential equation

$$\dot{X} = \underline{f}(t) \tag{3.3}$$

from which the estimated state is computed as

$$\hat{X}(t) = \begin{cases} \hat{X}(t_k) + \int_{t_k}^{t} \hat{\dot{X}}(\tau)d\tau & t_k \leq t < t_{k+1} \\ \hat{X}(t_{k+1}^-) + \Delta X(t_{k+1}) & t = t_{k+1} \end{cases} \tag{3.4}$$

Here, the times (t_k, $k = 1, 2, \ldots$) are those discrete times at which a correction, ΔX, is provided by the Kalman filter algorithm; at these times, $\hat{X}$ is changed discretely, and between these times $\hat{X}$ is obtained from measured or assumed values of $\hat{\dot{X}}$ or its integral. Equations for the variables of interest are given in table 3.1. These include measurement biases $\underline{b}$, used in the filter algorithm in addition to the variables noted in equation (3.1).

Estimation Error State

Between filter corrections, the estimation error state $\tilde{X}$ is assumed to be governed by linear perturbation equations forced by a Gaussian white noise vector process, $\eta(t)$:

$$\tilde{X}(t) \equiv X(t) - \hat{X}(t) \tag{3.5}$$

$$\dot{\tilde{X}} = F\tilde{X} + \eta \tag{3.6}$$

$$\eta_i \sim N(0,q_i) \qquad i = 1, 2, \ldots, n$$

The general solution for $\tilde{X}(t)$ is given from the transition matrix, $\phi(t,t_k)$, which can be satisfactorily approximated by a truncated Taylor series for the short intervals that occur in this work:

$$\tilde{X}(t) = \phi(t,t_k)\tilde{X}(t_k) + u(t) \tag{3.7}$$

where

$$\phi(t_k + \delta,t_k) = e^{-F\delta} = I - F\delta + F^2\delta^2/2 + \ldots$$

TABLE 3.1.- STATE ESTIMATE AND ERROR STATE VARIABLES

State	Estimate between corrections, $t_k \le t < t_{k+1}$ $X(t) = X(t_k) + \int_{t_k}^{t} X(\tau)d\tau$	Estimate at a correction $\hat{X}(t_{k+1}) = \hat{X}(t_{k+1}^{-}) + \Delta X(t_{k+1})$
R_r	$\hat{R}_r(t) = \hat{R}_r(t_k) + \int_{t_k}^{t} \hat{V}_r(\tau)d\tau$	$\hat{R}_r(t_{k+1}^{-}) + \Delta R_r(t_{k+1})$
V_r	$\hat{V}_r(t) = \hat{V}_r(t_k) + \int_{t_k}^{t} \hat{a}_r(\tau)d\tau$	$\hat{V}_r(t_{k+1}^{-}) + \Delta V_r(t_{k+1})$
a_r	$\hat{a}_r(t) = am_r(t) + \Delta am_r(t_k)$	$am_r(t_{k+1}) + \Delta am_r(t_{k+1})$
$\begin{pmatrix}\phi\\ \theta\\ \psi\end{pmatrix}$	$\begin{pmatrix}\hat{\phi}\\ \hat{\theta}\\ \hat{\psi}\end{pmatrix}_t = \begin{pmatrix}\phi_g\\ \theta_g\\ \psi_g\end{pmatrix}_t + \begin{pmatrix}\Delta\phi\\ \Delta\theta\\ \Delta\psi\end{pmatrix}_{t_k}$	$\begin{pmatrix}\phi_g\\ \theta_g\\ \psi_g\end{pmatrix}_{t_{k+1}} + \begin{pmatrix}\Delta\phi\\ \Delta\theta\\ \Delta\psi\end{pmatrix}_{t_{k+1}}$
W_r	$\hat{W}_r(t) = \hat{W}_r(t_k)$	$\hat{W}_r(t_k) + \Delta W_r(t_{k+1})$
$\underline{b}$	$\underline{\hat{b}}(t) = \underline{\hat{b}}(t_k)$	$\underline{\hat{b}}(t_k) + \Delta b(t_{k+1})$

Error state variables

$\tilde{R}_r$	position estimation error
$\tilde{V}_r$	velocity estimation error
$\widetilde{am}_r$	acceleration measurement bias, runway axes components
$\widetilde{am}_L$	acceleration measurement bias, level heading components
$\tilde{\ddot{z}}$	vertical acceleration measurement bias
$\tilde{\phi},\tilde{\theta},\tilde{\psi}$	attitude gyroscope biases
$\tilde{W}_x,\tilde{W}_y$	wind error, runway x,y-axes components
$\tilde{b}_{tr},\tilde{b}_{tb},\tilde{b}_{hb}$	VORTAC range and bearing, and baroaltimeter calibration errors

$$u(t_k + \delta) = \int_{t_k}^{t_{k+\delta}} \phi(\tau, t_k)\eta(\tau)d\tau$$

The selection of the filter's error state variables affects both estimation accuracy and the time required for executing the filter equations. For maximum accuracy, the state should include not only errors for the variables required by the control but also errors for all variables and parameters of the measurement functions for which values must be given in order to define the relation between measurements and the control variables. However, the filter execution time rises with the cube of the number of state variables to be estimated (ref. 5); as a result, it is essential to omit variables that do not significantly affect the accuracy of the control variables or that if included do not substantially improve the estimates of the control variables. These are variables for which the amount of on-line information is small compared with the amount of a priori information (they are poorly observable to the measurements). The effect of their a priori estimation errors on the accuracy of the remaining variables can range from negligible to significant.

The process of choosing appropriate error state variables is specific to each application and ultimately rests on simulation testing. The variables considered in the present study are listed in table 3.1. The horizontal plane components of the wind are included but the vertical component is omitted, because the on-line information on it is negligible and its error has little effect on estimation accuracy for the inertial vertical axis motion. Measurement biases are included for VORTAC and baroaltimeter, since their corresponding position errors are statistically large a priori compared with the desired position accuracy; moreover, they can be estimated on-line by the more accurate MODILS and, to a limited degree, by other data types. MODILS biases are nontrivial, but they are omitted for lack of independent calibrating measurements of sufficient accuracy among the navaids. Transmitter location and runway parameter errors have negligible effects and need not be considered. In addition, this study considers three candidate formulations of the acceleration measurement errors in an effort to maximize the filter's capacity to detect and compensate the significant low-frequency errors encountered during maneuvering. The first formulation represents these errors simply as biases of the measured runway axis components of acceleration and results in a filter with 14 states; the second uses attitude and vertical acceleration measurement biases (15 states), with the object of detecting the gyroscopic error transients more accurately and possibly improving the attitude accuracy; and the third is formulated as biases of the measured level-heading-axes components of acceleration (14 states), with the object of avoiding the sinusoidal inertial acceleration measurement errors that occur during turns for the runway axes formulation owing to the accelerometer package bias vector.

State equations for the variables of these three filter cases are given in table 3.2, from which the matrices F, ϕ of equations (3.6) and (3.7) can be given by inspection. The wind and measurement error state variables are all modeled in an ad hoc manner by first-order differential equations forced by white noise; that is, they are represented as exponentially correlated random processes. The variance and time-constant (σ^2, τ) for each variable are selected to correspond to the time scale at which significant changes occur and the steady-state accuracy reached in the absence of new navaid measurements. The forced term u is a random variable whose variance $\sigma^2[1 - \exp(-2\delta/\tau)]$ is such that the desired steady-state variance is obtained $(E[\tilde{z}^2] \to \sigma^2)$.

TABLE 3.2- ESTIMATION ERROR STATE EQUATIONS

States	State equation	Error propagation equation	Parameter values	
$\tilde{X}$	$\dot{\tilde{X}} = F\tilde{X} + \eta$	$\tilde{X}(t_k + \delta) = \phi(t_k + \delta, t_k)\tilde{X}(t_k) + u(\delta)$	σ	τ, sec
14-State filter				
$\tilde{R}_r$	$\dot{\tilde{R}}_r = \tilde{V}_r$	$\tilde{R}_r(t_k + \delta) = \tilde{R}_r(t_k) + \tilde{V}_r(t_k) + \tilde{am}_r\ \delta^2/2$	0	
$\tilde{V}_r$	$\dot{\tilde{V}}_r = \tilde{am}_r$	$\tilde{V}_r(t_k + \delta) = \tilde{V}_r(t_k) + \tilde{am}_r\ \delta$	0	
	General form	General form		
$\tilde{am}_r$	$\dot{\tilde{z}} = -\frac{1}{\tau}\tilde{z} + \eta$	$\tilde{z}(t_k + \delta) = e^{-(2\delta/\tau)}\ \tilde{z}(t_k) + u(\delta)$	.03g,.03g,.03g	25, 25, 10^3
$\tilde{W}_x$	↓	$u(\delta) \sim N(0,\delta^2(1 - e^{-(2\delta/\tau)})$	6.1 mps	20
$\tilde{W}_y$	↓	↓	6.1 mps	20
$\tilde{b}_{tr}$	↓	↓	305 m	10^4
$\tilde{b}_{tb}$	↓	↓	2°	10^4
$\tilde{b}_{hb}$	↓	↓	30.5 m	10^4
15-State filter				
$\tilde{R}_r^{\,a}$	$\dot{\tilde{R}} = \tilde{V}_r$	$\tilde{R}_r(t_k + \delta) = \tilde{R}_r(t_k) + \tilde{V}_r(t_k) + M(\tilde{\phi},\tilde{\theta},\tilde{\psi},\ddot{\tilde{z}})^T\ \frac{\delta^2}{2}$	0	
$\tilde{V}_r^{\,a}$	$\dot{\tilde{V}}_r = M\begin{pmatrix}\tilde{\phi}\\ \tilde{\theta}\\ \tilde{\psi}\\ \ddot{\tilde{z}}\end{pmatrix}$	$\tilde{V}_r(t_k + \delta) = \tilde{V}_r(t_k) + M(\tilde{\phi},\tilde{\theta},\tilde{\psi},\ddot{\tilde{z}})^T\ \delta$	0	
$\tilde{\phi}$			1°	25
$\tilde{\theta}$	$\dot{\tilde{z}} = \frac{1}{\tau}\tilde{z} + \eta$	$\tilde{z}(t_k + \delta) = e^{-(2\delta/\tau)}\ \tilde{z}(t_k) + u(\delta)$	1°	25
$\tilde{\psi}$	↓	$u(\delta) \sim N(0,\sigma^2(1 - e^{-(2\delta/\tau)})$	1°	25
$\ddot{\tilde{z}}$	↓	↓	0.03g	10^3
$\tilde{W}_x$	↓	↓	6.1 mps	20
$\tilde{W}_y$	↓	↓	6.1 mps	20
$\tilde{b}_{tr}$	↓	↓	305 m	10^4
$\tilde{b}_{tb}$	↓	↓	2°	10^4
$\tilde{b}_{hb}$	↓	↓	30.5 m	10^4
14 States, level heading acceleration measurement bias components				
$\tilde{R}_r$	$\dot{\tilde{R}}_r = \tilde{V}_r$	$\tilde{R}_r(t_k + \delta) = \tilde{R}_r(t_k) + \tilde{V}_r(t_k) + E_3(\psi)\tilde{am}_L\ \frac{\delta^2}{2}$	0	
$\tilde{V}_r$	$\dot{\tilde{V}}_r = E_3(\psi)\tilde{am}_L$	$\tilde{V}_r(t_k + \delta) = \tilde{V}_r(t_k) + E_3(\psi)\tilde{am}_L\ \delta$	0	
$\tilde{am}_L$			0.03g	25, 25, 10^3
$\tilde{W}_x$	$\dot{\tilde{z}} = -\frac{1}{\tau}\tilde{z} + \eta$	$\tilde{z}(t_k + \delta) = e^{-(2\delta/\tau)}\ \tilde{z}(t_k) + u(\delta)$	6.1 mps	20
$\tilde{W}_y$	↓	$u(\delta) \sim N[0,\sigma^2(1 - e^{-(2\delta/\tau)})]$	6.1 mps	20
$\tilde{b}_{tr}$	↓	↓	305 m	10^4
$\tilde{b}_{tb}$	↓	↓	2°	10^4
$\tilde{b}_{hb}$	↓	↓	30.5 m	10^4

Footnote *a*:

$$M = \begin{bmatrix} \sin\theta\ f_{r2} + \cos\theta\ \sin\psi\ f_{r3} & \cos\psi\ f_{r3} & -f_{r2} & 0 \\ -\sin\theta\ f_{r1} - \cos\theta\ \cos\psi\ f_{r3} & \sin\psi\ f_{r3} & f_{r1} & 0 \\ \cos\theta(\cos\psi\ f_{r2} - \sin\psi\ f_{r1}) & -\cos\psi\ f_{r1} - \sin\psi\ f_{r2} & 0 & 1 \end{bmatrix}$$

Error State Covariance

Measurement processing in the filter is referenced to discrete times (t_k) at which the error state covariance, $P(t_k)$, defined by

$$P(t_k) \equiv E[\tilde{X}(t_k)\tilde{X}^T(t_k)] \tag{3.8}$$

is required. Its propagation between these times follows from equations (3.7) and (3.8) as

$$P(t_{k+1}^-) = \phi(t_{k+1},t_k)P(t_k)\phi^T(t_{k+1},t_k) + Q \tag{3.9}$$

where

$$Q \equiv E[u(\Delta)u^T(\Delta)] \cong \text{diag}[\sigma_i^2(1 - 2\Delta/\tau_i)]$$

$$\Delta \equiv t_{k+1} - t_k$$

In forming Q, noise components for the kinematic states and correlations between the components of u have been neglected. The resulting matrix is diagonal, with elements and parameter values as given in table 3.2. Equation (3.9) describes the theoretical behavior of accuracy with time, Δ, in the absence of new navaid measurements. Both terms vary with Δ, and, in view of table 3.2, they combine such that the variance of each error state (diagonal terms of $P(t_{k+1}^-)$) either increases indefinitely with Δ (e.g., $\tilde{R}_r$, $\tilde{V}_r$) or increases to the steady state value, σ_i^2, which reflects the appropriate sensor accuracy (e.g., $\tilde{am}_r$, $\tilde{\phi}$) or the a priori accuracy (e.g., $\tilde{b}_{tr}$, $\tilde{W}_x$).

The square root covariance will be used in the filter formulation. This is an n × n matrix, W, such that $P = WW^T$. An n × 2n square root of the propagated covariance is readily given by separating equation (3.9) into the form

$$P(t_{k+1}^-) = AA^T \tag{3.10}$$

where

$$A = [\phi(t_{k+1},t_k)W(t_k) \,\vdots\, \sqrt{Q}]$$

and then the matrix A^T can be reduced to an n × n upper triangular, square root matrix, $W(t_{k+1}^-)$, using Householder's algorithm, $\mathscr{H}$ (ref. 10), since the product, AA^T, is invariant for these operations:

$$W^T(t_{k+1}^-) = \mathscr{H}(A^T)$$

that is, equation (3.10), together with Householder's algorithm, is used to advance the square-root covariance in time.

Measurement Models

The filter computes corrections, ΔX, by processing samples of the available data types, which it assumes can be modeled by a deterministic function, H, with a superposed Gaussian white noise process, $\tilde{Y}$:

$$Y_m = H_m(X,p_o) + \tilde{Y}_m \qquad m = 1, 2, . . ., M$$

$$\tilde{Y}_m \sim N(0,q_m) \tag{3.11}$$

Here, M is the number of data types and p refers to those parameters on which the measurement depends, in addition to X, but for which a priori values p_o are assigned and estimation errors $\tilde{p}$ are neglected. The Gaussian white errors only approximately represent the errors between $H_m(X,p_o)$ and the actual measurements; these can include, for example, truncation errors, moderately correlated sample errors, and nontrivial biases. The noise variance q_m is, therefore, adjusted empirically from simulation tests or recorded flight data to obtain the best fit.

The measurement models and parameter values for this study are listed in table 3.3. A comparison with the simulation models (table 2.3) indicates the differerences in error model details. In addition, note that the MODILS elevation measurement has been modified to a derived altitude measurement and that the airspeed

TABLE 3.3- MEASUREMENT MODELS

$$Y = H(X,p) + \tilde{Y}$$

$$\tilde{Y} \sim N(0,q)$$

Measurement	Symbol	Measurement function, H(X,p)	$\sqrt{q}$
TACAN (VORTAC) Range	Y_{tr}	$[(x - x_t)^2 + (y - y_t)^2 + (z - z_t)^2]^{1/2} + b_{tr}$	91.4 m
Bearing	Y_{tb}	$\tan^{-1}\left(\dfrac{y_t - y}{x_t - x}\right) + \psi_R + b_{tb}$	1°
MODILS DME	Y_{mr}	$[(x - x_m)^2 + (y - y_m)^2 + (z - z_m)^2]^{1/2}$	45.7 m
Azimuth	Y_{ma}	$\tan^{-1}(y - y_m)/[(x - x_m)^2 + (y - y_m)^2 + (z - z_m)^2]^{1/2}$	0.3°
Elevation	Y'_{me}	$-z$	0.005 $\hat{r}_1$ m (see note)
Baro altimeter	Y_{hb}	$-z + h_R + b_{hb}$	1.5 m
Radar altimeter	Y_{hr}	$-z$	1.8 m
Air velocity	$Y_{\dot{x}a}$	$\dot{x} - W_x$	1.8 m/sec
	$Y_{\dot{y}a}$	$\dot{y} - W_y$	1.8 m/sec

Note: $\hat{r}_1 \equiv [(\Delta\hat{x}_e \cos 5° + \Delta\hat{z}_e \sin 5°)^2 + \Delta y_e^2]^{1/2}$; $\Delta x_e = (x - x_e)$, etc.

measurement has been combined with heading to yield derived measurements of the horizontal plane coordinates of the air velocity vector. The derived altitude measurement Y'_{me} is introduced to facilitate division of the state variables and measurements into separate filters for the horizontal plane and vertical axis motions. This measurement is derived from the elevation measurement and current position estimate, using an expression derived from the simulation model.

$$Y'_{me} = z_e + \Delta\hat{x}_e \tan 5^\circ - r_1 \tan Y_{me}/\cos 5^\circ \tag{3.12}$$

This is modeled in the filter as

$$Y'_{me} = -z + \tilde{Y}'_{me}$$

Using the simulation model, the error $\tilde{Y}'_{me}$ can be related to the elevation measurement and position estimation errors. After neglecting second-order effects, this yields the standard deviation of $\tilde{Y}'_{me}$ as

$$\sigma'_{me} = \hat{r}_1 \sigma_{me}$$

which increases with distance from the elevation antenna.

The derived air velocity components are calculated from airspeed and heading measurements, using

$$\begin{pmatrix} Y_{\dot{x}a} \\ Y_{\dot{y}a} \end{pmatrix} = Y_{Va} \begin{pmatrix} \cos\psi_g \\ \sin\psi_g \end{pmatrix} \tag{3.13}$$

Its measurement model is

$$\begin{pmatrix} Y_{\dot{x}a} \\ Y_{\dot{y}a} \end{pmatrix} = \begin{pmatrix} \dot{x} \\ \dot{y} \end{pmatrix} - \begin{pmatrix} W_x \\ W_y \end{pmatrix} + \begin{pmatrix} \tilde{Y}_{\dot{x}a} \\ \tilde{Y}_{\dot{y}a} \end{pmatrix}$$

The measurement error can be derived by expressing the air velocity components in terms of airspeed and heading, using

$$Va_r = T^T_{pr} Va_p \tag{3.14}$$

where

$$Va_r = (\dot{x}_a, \dot{y}_a, \dot{z}_a)^T$$

$$Va_p = (V_a, 0, 0)^T$$

The transformation T_{pr} can be rewritten as $T_{pb}T_{br}$ and evaluated using table 2.2, after which the horizontal plane coordinates can be obtained as

$$\begin{pmatrix} \dot{x}_a \\ \dot{y}_a \end{pmatrix} = Va \begin{pmatrix} \cos(\psi + \Delta\psi) \\ \sin(\psi + \Delta\psi) \end{pmatrix} \tag{3.15}$$

where

$$\Delta\psi = \beta \cos \phi - \alpha \sin \phi + \text{HOT's}$$

This result assumes that α, β, and θ are small angles. The measurement errors for the derived air velocity components can now be given as:

$$\begin{pmatrix} \tilde{Y}_{\dot{x}a} \\ \tilde{Y}_{\dot{y}a} \end{pmatrix} = \begin{pmatrix} Y_{\dot{x}a} \\ Y_{\dot{y}a} \end{pmatrix} - \begin{pmatrix} \dot{x}_a \\ \dot{y}_a \end{pmatrix} = \tilde{Y}_{Va} \begin{pmatrix} \cos \psi \\ \sin \psi \end{pmatrix} + Va(\tilde{\psi}_g - \Delta\psi) \begin{pmatrix} -\sin \psi \\ \cos \psi \end{pmatrix} + \text{HOT's} \tag{3.16}$$

where the error sources ($\tilde{Y}_{Va}$, $\tilde{\psi}_g$, and $\Delta\psi$) are the airspeed measurement error, the directional gyroscope error, and the unmodeled effects of (α,β). The two error vectors in equation (3.16) are mutually orthogonal and in the horizontal plane along the direction of the aircraft heading and lateral to that heading. Thus, for the derived measurements, the error in measuring the longitudinal air velocity component is given by the airspeed sensor error, $\tilde{Y}_{Va}$, as expected, and the error in the lateral direction is proportional to both the error in the directional gyroscope and to unmodeled angle effects; the error in the lateral direction can be of the same magnitude as the air velocity component in this direction. The complex errors of the derived measurements in equation (3.16) are represented only approximately in the filter; measurement error correlation for the two components is neglected, and standard deviations of 1.8 m/sec were assumed for these errors.

Measurement Preprocessing

Navaid measurements are received and processed at discrete times as outlined in sketch D. Measurements are received and accumulated at a rapid rate (10 Hz) and these are processed by the filter to compute a correction to the state estimate, ΔX, at a slower rate (rates of 0.1 to 2 Hz are studied). For convenience, the preprocessing logic refers all measurements taken during (t_k,t_{k+1}) to a reference time, t_k. Further, all admissible measurements of a single type are accumulated as a single nearly equivalent measurement for the interval. The state estimate correction is then computed by sequential processing of a single scalar measurement of each type.

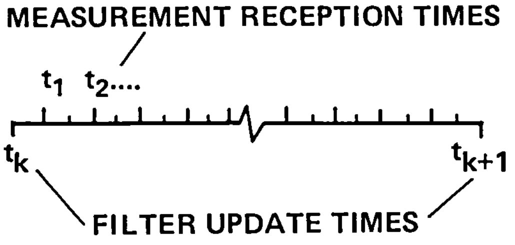

Sketch D

The processing uses measurement residuals; that is, the difference between the measurement and its predicted value from the current state estimate:

$$y_m(t) \equiv Y_m(t) - H_m(\hat{X}(t),p) \qquad m = 1, 2, \ldots, M \tag{3.17}$$

Its relation with the estimation error at the reference time is obtained by linearizing equation (3.11) about $\hat{X}(t)$ and using equation (3.7):

$$y_m(t) = h_m(t)\phi(t,t_k)\tilde{X}(t_k) + \tilde{Y}_m \qquad m = 1, 2, \ldots, M \tag{3.18}$$

where

$$h_m(t) = [\nabla_x H(X,p_o)]_{\hat{x}}$$

$$\tilde{Y}_m \quad N(0,q_m)$$

The forced solution, u, in equation (3.7) can be neglected here, provided the filter update interval is small relative to the correlation times of the estimation error variables.

The measurement gradients (h_m) for the present application are listed in table 3.4. In this table, the state variables are separated into two sets associated with the horizontal plane and vertical axis motions, respectively, to facilitate the analysis of separate filters for these two sets of variables in a later section. The filter algorithm is implemented with this same ordering of the variables to facilitate simulation study of the separate filters.

Degraded navaid data can occur randomly; this refers to data which may have no relation to the state or contain errors generated by processes significantly larger than postulated in the filter design. In the present context, this can occur in isolated samples or for periods of any duration, and can occur as signal dropouts, signal hangups or divergence, or increased noise variance. We seek to exclude such data which, if processed, can result variously in large amplitude excitation of the filter's impulse response, or divergence of the estimation error for a period of time or excessively noisy estimates. Much of the degraded data is excluded by receiver validity checks and conservatively computed coverage boundaries for admitting data (given in table 2.3). However, this does not suffice to exclude all degraded data, so the filter rejects residuals which are large compared to its standard deviation computed from the filter's covariance; that is,

$$\text{If:} \quad \frac{y_m^2}{h_m P h_m^T + q_m} > c^2 \qquad \text{then: delete } y_m \tag{3.19}$$

Values of 2 to 4 have proved satisfactory for c in empirical tests with real data. This device succeeds in excluding dropouts of any duration and isolated large residual samples which would otherwise excite the filter's impulse response. Note that large residuals also result from sufficiently poor prior estimates as well as degraded data so that normal measurements would be locked out if errors in the predicted measurement exceeded the threshhold. For example, if VORTAC or baroaltimeter biases fortuitously exceeded the threshhold then the swith to one or more MODILS measurement can become impossible or require reinitialization. However, this is a low probability event and was never observed with real data or in simulation tests with the normal system model.

No attempt is made here to treat signal hangups or divergence and increased noise levels; schemes for signal hangups are unknown and various schemes to detect and treat changes in noise model parameters are available (e.g., some schemes and applications are discussed in refs. 22 and 23) but are elaborate and probably ineffective in the present application.

TABLE 3.4.- MEASUREMENT GRADIENTS AND RESIDUALS: 14-STATE FILTER

$$
\begin{bmatrix} y_{tr} \\ y_{tb} \\ y_{mr} \\ y_{ma} \\ y_{\dot{x}a} \\ y_{\dot{y}a} \\ \hline y_{me} \\ y_{hb} \\ y_{hr} \end{bmatrix}
=
\left[\begin{array}{cccccccccc|cccc}
\cos\psi_t \cos EL_t & \sin\psi_t \cos EL_t & 0 & 0 & 0 & 0 & 1 & 0 & 0 & 0 & -\sin EL_t & 0 & 0 & 0 \\
\frac{\sin\psi_t}{d_{xyt}} & \frac{-\cos\psi_t}{d_{xyt}} & 0 & 0 & 0 & 0 & 0 & 1 & 0 & 0 & 0 & 0 & 0 & 0 \\
\cos Az \cos EL_m & \cos Az & 0 & 0 & 0 & 0 & 0 & 0 & 0 & 0 & \cos Az \sin EL_m & 0 & 0 & 0 \\
\frac{\cos Az \cos EL_m}{d_m} & -\frac{\cos EL_m}{d_m} & 0 & 0 & 0 & 0 & 0 & 0 & 0 & 0 & \frac{\sin Az \sin EL_m}{d_m} & 0 & 0 & 0 \\
0 & 0 & 1 & 0 & 0 & 0 & 0 & 0 & -1 & 0 & 0 & 0 & 0 & 0 \\
0 & 0 & 0 & 1 & 0 & 0 & 0 & 0 & 0 & -1 & 0 & 0 & 0 & 0 \\
\hline
0 & 0 & 0 & 0 & 0 & 0 & 0 & 0 & 0 & 0 & -1 & 0 & 0 & 0 \\
0 & 0 & 0 & 0 & 0 & 0 & 0 & 0 & 0 & 0 & -1 & 0 & 0 & 1 \\
0 & 0 & 0 & 0 & 0 & 0 & 0 & 0 & 0 & 0 & -1 & 0 & 0 & 0
\end{array}\right]
\begin{bmatrix} \tilde{x} \\ \tilde{y} \\ \tilde{\dot{x}} \\ \tilde{\dot{y}} \\ \tilde{\ddot{x}} \\ \tilde{\ddot{y}} \\ \tilde{b}_{tr} \\ \tilde{b}_{tb} \\ \tilde{w}_x \\ \tilde{w}_y \\ \hline \tilde{z} \\ \tilde{\dot{z}} \\ \tilde{\ddot{z}} \\ \tilde{b}_{hb} \end{bmatrix}
+ \nu
$$

Notes: In the 15-state filter $\frac{\partial H}{\partial \phi} = \frac{\partial H}{\partial \theta} = \frac{\partial H}{\partial \psi} = 0$ for all measurements.

ψ_t, EL_t, EL_m, d_{xyt}, d_m are defined in appendix A, table A1.

Multiple measurements of a single data type received during the interval (t_k,t_{k+1}) can be compressed to a single scalar measurement that is nearly equivalent to the set of measurements by summing residuals, gradients, and variances:

$$\left.\begin{aligned} y_{sm} &= \sum_{i=1}^{n_m} y_m(t_i) \\ h_{sm} &= \sum_{i=1}^{n_m} h_m(t_i)\phi(t_i,t_k) \\ q_{sm} &= q_m n_m^{1.4} \end{aligned}\right\} \quad m = 1, 2, \ldots, M \tag{3.20}$$

where n_m is the number of admitted measurements for the mth data type. In general, two sets of measurements, $\{(h_i,q_i),\ i = 1, 2, \ldots, n\}$ and $\{(h_i',q_i'),\ i = 1, 2, \ldots, n\}$ are equivalent, that is, yield identical accuracy P after processing, provided they have the same information, that is, provided

$$\sum_{i=1}^{n} \frac{h_i^T h_i}{q_i} = \sum_{i=1}^{n'} \frac{h_i'^T h_i'}{q_i'} \tag{3.21}$$

In the simple case in which all measurements are identical and denoted (h,q), the information can be written variously as

$$\sum_{i=1}^{n} \frac{h_i^T h_i}{q_i} = n\,\frac{h^T h}{q} = \frac{h_s^T h_s}{nq}$$

where h_s is the summed gradient, nh. Thus, $\{(h_i,q_i)\}$ is equivalent to the single summed measurement (h_s,nq) which can be processed in place of $\{(h_i,q_i)\}$ at a considerable savings in computation time and with no loss of accuracy. More generally, any collection of measurements $\{(h_i,q_i)\}$ can be compressed to a minimum equivalent set, $\{(h_i',q_i')\}$ in which $\{h_i'\}$ is a basis of the space spanned by $\{h_i\}$ (ref. 24). In the present application, the measurements of a single data type taken during (t_k,t_{k+1}) are nearly identical and can be equivalenced to the single summed measurement of equation (3.20) with negligible error. In addition, the actual measurement errors can be moderately correlated at the 10-Hz sampling rate used here. Therefore, the summed measurement is weighted conservatively in equation (3.20) by increasing its error variance by the factor $n^{0.4}$ over its value in the case of independent errors, nq. This adjustment was selected empirically using recorded flight data.

Measurement Processing Equations

Each summed measurement is processed using the following square root, Kalman filter algorithm (Potter's algorithm, refs. 10 and 11). The variance of the residual s_m, optimal (minimum variance) gain K, error state correction Δx, and posterior square root covariance W, are given by

$$\left.\begin{aligned} \rho &= W^T h_{sm} \\ s_m &= \rho\rho^T + q_{sm} \\ K &= W\rho/sm \\ \Delta X &= \Delta X + K(y_{sm} - h_{sm}\,\Delta X) \\ W^T &= W^T - \rho K^T/[1 + (q_{sm}/s_m)^{1/2}] \end{aligned}\right\} m = 1, 2, \ldots, M \qquad (3.22)$$

Here, the equal sign indicates replacement in the computational sense and all quantities are associated with the reference time, t_k. Note that in computing ΔX, the summed residual, y_{sm}, is modified to account for the error correction already accumulated but not used to calculate the residuals, y_{sm}.

Filter Initialization

Starting values of the state estimate and estimation error covariance are required. In general, the initialization can be formulated as in equation (3.23). An initial set of measurements, or assigned a priori values, designated $\underline{Y}_o$, suffice to define uniquely the state variables; that is, $\underline{Y}_o$ and X are n-vectors and $\underline{H}(X,p_o)$ has a nonsingular Jacobian with respect to X. Then, the initial state estimate is given from the inverse function, $\underline{H}^{-1}(\underline{Y}_o,p_o)$, and the initial state estimation error, $\tilde{X}_o$, and its square-root covariance, W, are given from the Jacobian of the inverse function, J, and from the measurement errors, $\tilde{Y}$, and their variances, $\{q_i\}$. The measurement errors can be assumed independent so that D is diagonal:

$$\left.\begin{aligned} \underline{Y}_o &= \underline{H}(X,p_o) + \tilde{\underline{Y}}_o \\ \hat{X}_o &= \underline{H}^{-1}(Y_o,p_o) \\ J &\equiv [\nabla_{\underline{Y}} H^{-1}]_{\underline{Y}_o} \\ \tilde{X}_o &= -J\tilde{\underline{Y}}_o \\ D &\equiv E[\tilde{\underline{Y}}_o\tilde{\underline{Y}}_o^T] = \mathrm{diag}\{q_i\} \\ P_o &= J\,DJ^T \\ W_o^T &= \sqrt{D}\,J^T \end{aligned}\right\} \qquad (3.23)$$

In the present application, the following simple initialization can be used at arrival in the terminal area. The winds, measurement biases, and vertical velocity are all assigned their a priori mean values (zero) and then the kinematic states are calculated from TACAN or VORTAC, baroaltimeter, airspeed, attitude, and accelerometer measurements. The corresponding initial estimate, expressions for the initial state estimation errors, and standard deviations for the initial measurement errors are given in table 3.5. Last, the rows of W_o^T are listed in table 3.6 for the 14-state filter; the ith row is associated with the ith measurement,

TABLE 3.5- INITIAL STATE ESTIMATE

Initial estimate, $\hat{x}_o$	Initial estimation error, $\tilde{x}_o$	Error sources and standard deviations	
		Error	σ
$\hat{x} = x_t - [Y_{tr}^2 - (Y_{hb} - h_R + z_t)^2]^{1/2}\cos(Y_{tb} - \psi_R)$	$\tilde{x} = (b_{tr} + \tilde{Y}_{tr})\cos(Y_{tb} - \psi_R) - (y_t - \hat{y})(b_{tb} + \tilde{Y}_{tb})$	b_{tr}	30.5 m
$\hat{y} = y_t - [Y_{tr}^2 - (Y_{hb} - h_R + z_t)^2]^{1/2}\sin(Y_{tb} - \psi_R)$	$\tilde{y} = (b_{tr} + \tilde{Y}_{tr})\sin(Y_{tb} - \psi_R) + (x_t - \hat{x})(b_{tb} + \tilde{Y}_{tb})$	$\tilde{Y}_{tr}$	91.4 m
$\hat{z} = -Y_{hb} + h_R$	$\tilde{z} = b_{hb} + \tilde{Y}_{hb}$	b_{tb}	2°
$\hat{\dot{x}} = Y_{\dot{x}a}$	$\tilde{\dot{x}} = W_x + \tilde{Y}_{\dot{x}a}$	$\tilde{Y}_{tb}$	0.0174 rad
$\hat{\dot{y}} = Y_{\dot{y}a}$	$\tilde{\dot{y}} = W_y + Y_{\dot{y}a}$	b_{hb}	61 m
$\hat{\dot{z}} = 0$	$\tilde{\dot{z}} = \dot{z}$	$\tilde{Y}_{hb}$	1.5 m
$\hat{a}_r = am_r$	$\tilde{a}_r = \widetilde{am}_r$ or $\tilde{a}_L = \widetilde{am}_L$	$\tilde{\phi}$	1°
$\hat{\phi} = \phi_g$	$\tilde{\phi} = \tilde{\phi}_g$	$\tilde{\theta}$	1°
$\hat{\theta} = \theta_g$	$\tilde{\theta} = \tilde{\theta}_g$	$\tilde{\psi}$	1°
$\hat{\psi} = \psi_g$	$\tilde{\psi} = \tilde{\psi}_g$	$\tilde{Y}_{\dot{x}a}$	0.61 m/sec
$\hat{W}_x = 0$	$\tilde{W}_x = W_x$	$\tilde{Y}_{\dot{y}a}$	0.61 m/sec
$\hat{W}_y = 0$	$\tilde{W}_y = W_y$	$\dot{z}$	3.1 m/sec
$b_{tr} = 0$	$\tilde{b}_{tr} = b_{tr}$	W_x	6.1 m/sec
$b_{tb} = 0$	$\tilde{b}_{tb} = b_{tb}$	W_y	6.1 m/sec
$b_{hb} = 0$	$\tilde{b}_{hb} = b_{hb}$	$\widetilde{am}_r, \widetilde{am}_L$	0.305 m/sec^2 (all)

TABLE 3.6.- INITIAL SQUARE-ROOT COVARIANCE: 14-STATE FILTER

Error source	$W_o^T = \left(\sigma_{Y_i} \frac{\partial x^{(j)}}{\partial Y_i} (\underline{Y}_o), \quad i,j = 1, 2, . . ., n\right)$													
	$\tilde{x}$	$\tilde{y}$	$\tilde{\dot{x}}$	$\tilde{\dot{y}}$	$\tilde{\ddot{x}}$	$\tilde{\ddot{y}}$	$\tilde{W}_x$	$\tilde{W}_y$	$\tilde{b}_{tr}$	$\tilde{b}_{tb}$	$\tilde{z}$	$\tilde{\dot{z}}$	$\tilde{\ddot{z}}$	$\tilde{b}_{hb}$
b_{tr}	$\sigma_{b_{tr}} \cos \psi_g$	$\sigma_{b_{tr}} \sin \psi_g$							$\sigma_{b_{tr}}$					
Y_{tr}	$\sigma_{Y_{tr}} \cos \psi_g$	$\sigma_{Y_{tr}} \sin \psi_g$												
b_{tb}	$\sigma_{b_{tb}} \Delta y_t$	$-\sigma_{b_{tb}} \Delta x_t$								$\sigma_{b_{tb}}$				
Y_{tb}	$\sigma_{Y_{tb}} \Delta y_t$	$-\sigma_{Y_{tb}} \Delta x_t$												
$\dot{x}_a$			$\sigma_{Y_{xa}}$											
$\dot{y}_a$				$\sigma_{Y_{ya}}$										
W_x			σ_{W_x}				σ_{W_x}							
W_Y				σ_{W_y}				σ_{W_y}						
$\tilde{\ddot{x}}$					$\sigma_{\ddot{x}}$									
$\tilde{\ddot{y}}$						$\sigma_{\ddot{y}}$								
b_{hb}											$\sigma_{b_{hb}}$			$\sigma_{b_{hb}}$
Y_{hb}											$\sigma_{y_{hb}}$			
$\dot{z}$												$\sigma_{\dot{z}}$		
$\tilde{\ddot{z}}$													$\sigma_{\ddot{z}}$	

$$r_i = \left[\frac{\partial \underline{H}^{-1}}{\partial Y_i}\right]_{\underline{Y}_o} \sqrt{q_i} = \left[\frac{\partial \hat{X}_o}{\partial Y_i}\right]_{\underline{Y}_o} \sigma_i \qquad i = 1, 2, \ldots, n$$

and W_o^T can be formed with its rows taken from table 3.6 in any order.

The initial estimate defined above can be in substantial error; for example, the initial measurement bias errors equal the a priori calibration errors, the initial horizontal plane velocity and wind errors both equal the actual wind, and the initial vertical velocity error equals the actual vertical velocity. After initialization, the filter converges to some "steady-state" covariance; this convergence is rapid and the covariance (theoretical accuracy) becomes independent of the initial covariance for those states for which new measurements provide information that rapidly outweighs the initial information in P_o^{-1}. For other states, information is acquired very slowly or is unavailable until later in the approach and their accuracy is dominated by the a priori accuracy.

In general, the estimation error can diverge following initialization for sufficiently large initial errors as a result of dynamic and measurement nonlinearities neglected in the filter. In some applications, convergence is sensitive to these nonlinearities and special devices are useful (e.g., ref. 25). In the present work the boundaries of convergence were not studied systematically, but we note that no divergence was ever encountered in simulation tests with 2σ and 3σ biases and winds and initialization at various distances from the runway. Thus, initial convergence of the estimate in the terminal area navigation problems appears insensitive to initial errors for the present initialization scheme and measurement error statistics.

A Kalman Filter Algorithm

A computational flow diagram and equation summary of the Kalman filter algorithm for this study are given in figure 3.1 and table 3.7.

The computational flow is structured to permit reduction of the required computation time in the flight computer with negligible loss of accuracy. For this purpose, computations are separated into parts corresponding to (1) integration of the equations of motion, (2) data reception and preprocessing, and (3) measurement processing with the Kalman filter to obtain a new estimate of the error state. This permits execution of these parts at different rates which can be separately optimized.

Integration of the equations of motion requires little time and is executed at the maximum possible rate allowed by the computer's cycle time (20 Hz) for maximum accuracy. Execution time for the measurement reception and preprocessing equations is moderate and is done at 10 Hz. More frequent samples have increasingly correlated errors and would not significantly increase the actual rate of accumulating information; less frequent sampling saves little computation time and loses significant information for some data types. In addition, the preprocessing deletes some data types whose contribution to estimation accuracy becomes negligible when more accurate and functionally equivalent data types are available; for example, VORTAC is deleted when MODILS is available.

Execution time for the algorithm is dominated by the Kalman-filter measurement processing equations (ref. 5); therefore, the required computation time, as a percent of real time, depends principally on the rate of processing scalar measurements.

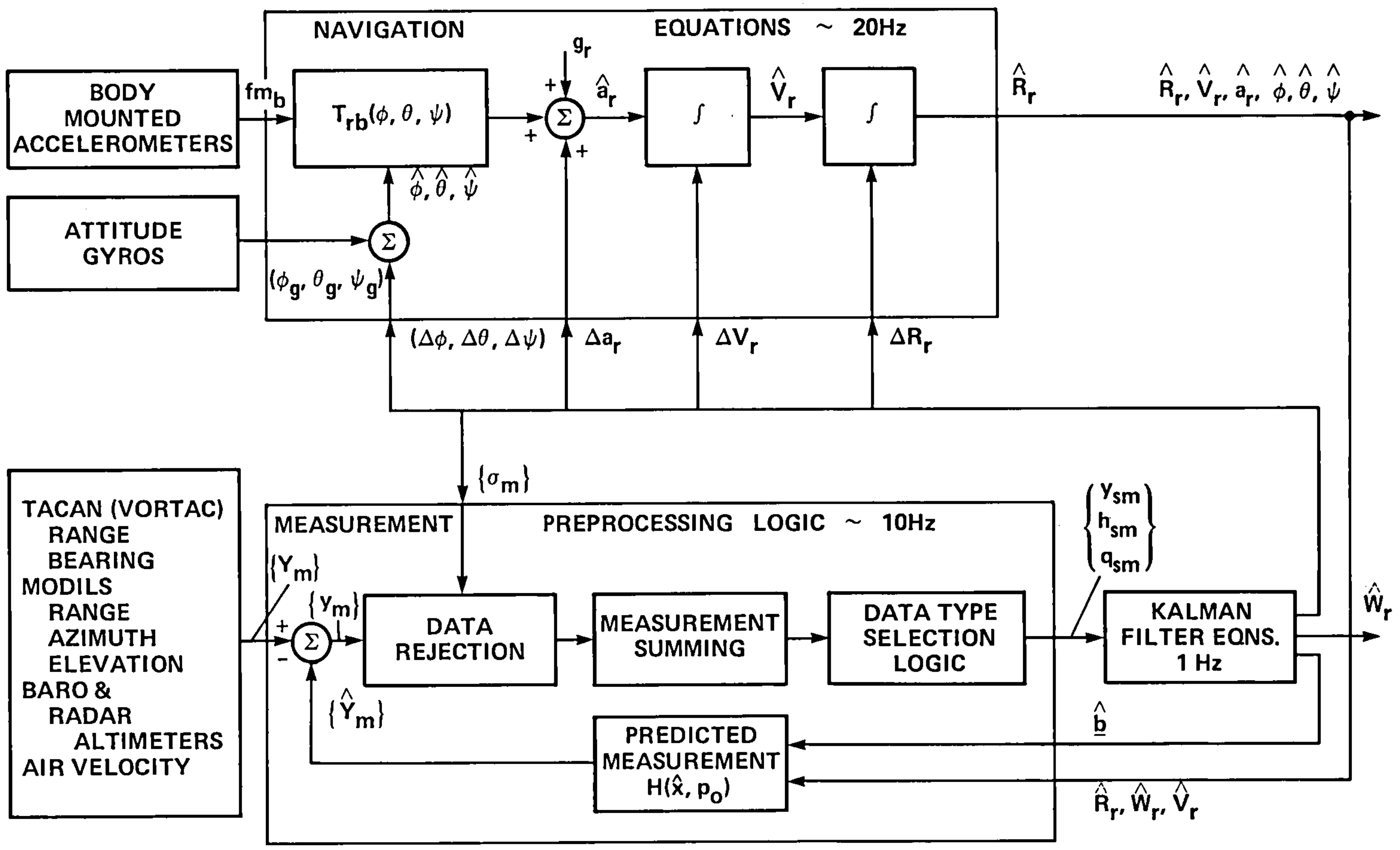

(1) NOTE: FOR 14 AND 15 STATE FORMULATIONS, THE FILTER OUTPUT IS RESTRICTED AS FOLLOWS:

$\Delta\phi = \Delta\theta = \Delta\psi \equiv 0$	14 STATE FILTER
$\Delta a_r \equiv (0, 0, \Delta\dot{z})$	15 STATE FILTER

Figure 3.1.- Kalman-filter estimation algorithm: logical flow diagram.

TABLE 3.7.- KALMAN-FILTER ESTIMATION ALGORITHM: EQUATION SUMMARY

Rate	Equation	Comments
10 Hz	Preprocessing logic: accumulate measurements for each data type, m = 1, 2, . . ., 9	
	If measurement is valid, continue	Validity test
	$y_m = Y_m - H_m(\hat{x})$	Residual
	If $\lvert y_m \rvert < c\sigma_m$, continue	Data rejection test
	$y_{s_m} = y_{s_m} + y_m$	Residual sum
	$h_m = [\nabla H_m(\hat{x})]\phi(t,t_k)$	Measurement gradient with $\tilde{x}(t_k)$
	$h_{s_m} = h_{s_m} + h_m$	Gradient sum
	$n_m = n_m + 1$	Number of accumulated measurements
	$q_{s_m} = q_m(n_m)^{1.4}$	Error variance of summed measurement
1 Hz	Process summed measurement for each data type selected and update estimated state	
	If data type selected, continue	Selection test
	$\rho = W^T h_{sm}^T$	
	$s_m = \rho\rho^T + q_{sm}$	Variance of summed residual
	$K = W\rho/s_m$	Kalman gain
	$\Delta X = \Delta X + K(y_{sm} - h_{sm}\,\Delta X)$ $\Big\}$ m = 1, . . ., 9	Posterior error state estimate
	$W^T = W^T - \rho K^T/[1 + (q_{sm}/s_m)^{1/2}]$	Posterior square-root covariance
	$\sigma_m = (s_m/n_m)^{1/2}$	Standard deviation, single measurement residual
	$(h_{sm}, q_{sm}, y_{sm}) = (0,0,0)$	Reset measurement sums
	$\hat{X} = \hat{X} + \phi(t_{k+1},t_k)\Delta X$	Posterior state estimate at current time, t_{k+1}
	$\Delta X = 0$	Reset state correction
	$A^T = \begin{bmatrix} W^T\phi \\ \sqrt{Q} \end{bmatrix}$	Propagate square-root covariance to t_{k+1}
	$W^T = \mathcal{H}(A^T)$	Upper triangular nxn$\sqrt{P}$, (Householder algorithm)

Maximum accuracy is achieved by processing all available data as soon as received, but this can be traded for computation time by reducing the processing rate. Factors in optimizing this rate are (1) the IMU accuracy, which governs the rate of accuracy loss for the kinematic states between filter updates; and (2) the measurement summing logic, which compresses measurements taken during the filter update interval into one measurement per data type with minimal loss of information. The net rate of processing scalar measurements is then Mf, where M is the number of data types and f is the filter update frequency. The possibilities for minimizing M are limited, and a value of 1 Hz was found satisfactory for f in the simulation tests described next.

The influence of filter update interval on accuracy was of considerable interest in the prospective flight application. Between updates, the filter is an unaided inertial navigator with error divergence behavior which reflects its acceleration estimation accuracy. This accuracy is sufficiently low in the present system during maneuvering that performance losses become significant for update intervals in the range of 1 to 10 sec. The nature of these effects is illustrated by the comparison of sample case histories in figure 3.2 for intervals of 0.5 and 10 sec. Position and velocity error histories are sawtooth-like functions which drift during the update interval relative to the error histories corresponding to continuous or high-rate measurement processing; they drift according to the equations

$$\tilde{R}(t_o + \Delta) = \tilde{R}_o + \tilde{V}_o\Delta + \iint_{t_o}^{t_o+\Delta} \tilde{a}\, dt^2$$

$$\tilde{V}(t_o + \Delta) = \tilde{V}_o + \int_{t_o}^{t_o+\Delta} \tilde{a}\, dt \qquad t_o < t < t_o + \Delta$$

and are approximately returned to the continuous processing error history discretely at a filter update. The amount of drift depends on the update interval, Δ, the velocity error just after the previous update, $\tilde{V}_o$, and the acceleration error, $\tilde{a}$. In figure 3.2(a) the lateral axis results show significant position and velocity error drifts for the 10-sec interval; drifts for the normal axis are much smaller (after the initial transient) as a result of much better acceleration accuracy. In addition, the lag and loss of information at larger intervals results in poorer transient response, as is evident in the degraded initial transients for all states and the significant loss of lateral acceleration accuracy during the turn (legs 4 and 5), where maneuver-induced gyroscopic error transients occur. The performance effects of practical interest are those on trajectory tracking errors and control activity. A generic, automatic, trajectory tracking system was included in the simulation, and its response to the sample case estimation errors is shown in figure 3.2(b). Several effects are visible, particularly for the lateral axis. First, estimation error jumps at each update result in corresponding control command histories (calculated as a corrective acceleration command) that are increasingly characterized by rate and authority limit saturation as the interval increases, and, second, tracking errors show increased excursion extremes and lags. Thus, both tracking accuracy and control activity degrade significantly with increasing interval over the range of intervals tested here.

Finally, Monte Carlo simulation results for some effects of filter update interval are shown in figure 3.3. These data are taken from a turning segment of the STOL

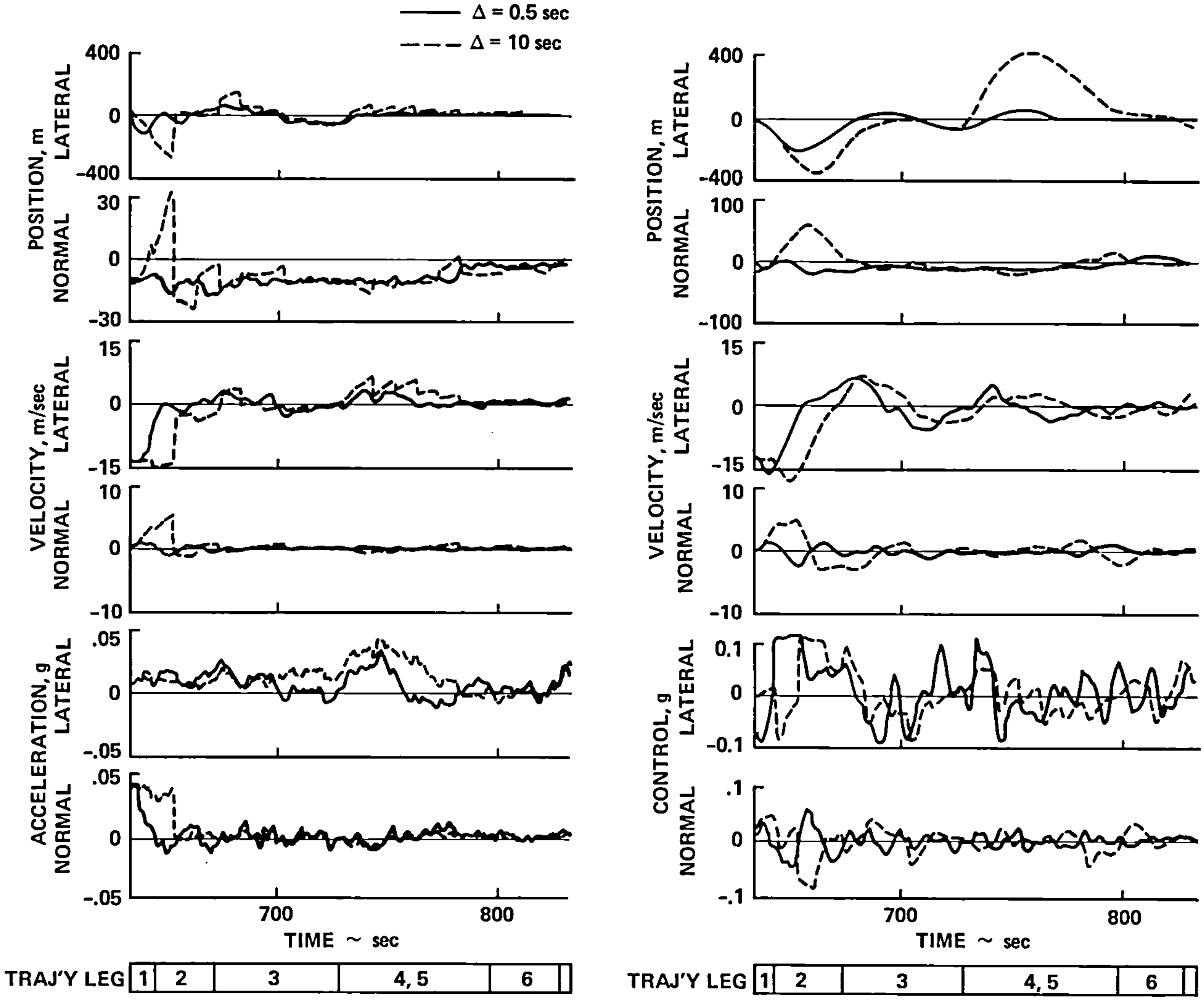

(a) ESTIMATION ERRORS

(b) TRAJECTORY TRACKING ERRORS AND CONTROL ACTIVITY

Figure 3.2.- Effects of update interval on estimation and control performance: sample case, STOL approach trajectory.

approach where acceleration estimation accuracy is poorest. Root-mean-square jumps in the estimate at the update increase nearly linearly with update interval, and the corresponding effects on tracking accuracy and control activity (not shown) are also proportional to the interval. Root-mean-square estimation errors at the end of the interval indicate the poorest accuracy that occurs during a filter cycle; these errors are seen to be insensitive to the interval size below intervals of 2 to 3 sec. This occurs because some error drifts can be temporarily in the direction of smaller magnitudes, but this effect is lost as interval size increases. Thus, these data indicate that intervals of 1 sec can be selected with no significant increase in the estimate jumps or loss of estimation accuracy compared with measurement processing at higher rates, and this choice has been found satisfactory generally. Larger intervals may also be satisfactory, but further increases in interval size are decreasingly effective in reducing the required computation time.

The algorithm outlined above was simulated on a CDC 7600 digital computer, and an equation summary for this simulation is provided in table 3.7. These equations

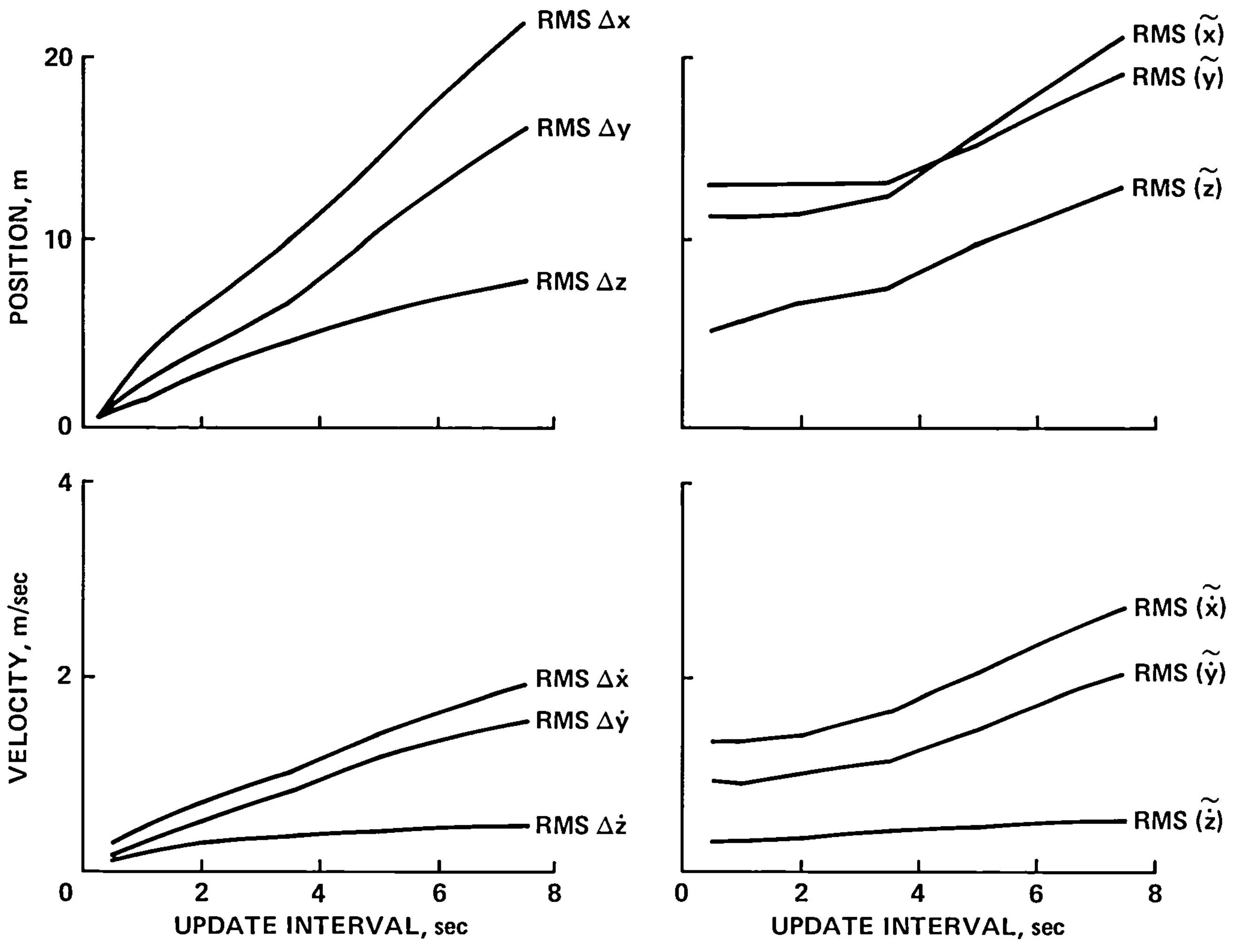

(a) ESTIMATE JUMP SIZE AT UPDATE (b) ACCURACY AT END OF UPDATE INTERVAL

Figure 3.3.- Effect of filter update interval on estimation accuracy: STOL approach, turn segment.

repeat those previously given in this section and require little additional comment. We note that ϕ, $\{\nabla H_m\}$, Q are sparse matrices and that only their nonnegligible elements are stored in the implemented algorithm along with arrays of indices which permit the elimination of trivial multiples. The simulation includes the computation lags associated with real time operation (0.4 sec for the filter equations). Further details on these lags and on coordination of the multirate computations in real time are given in reference 26. We also note that other square-root covariance algorithms have been proposed in the literature since Potter's algorithm was selected for this work and routine developed. Some of these offer potential reductions in computation time and their evaluation for real-time, fixed or floating computations would be of interest. However, navigation accuracy would not be affected since it is insensitive to measurement reception and processing rates at the rates used in the present algorithm.

Summary

The existing theory and applications devices have been applied to obtain a Kalman filter algorithm appropriate to the context of this study. The principal design issue is to realize the maximum available estimation accuracy from the set of sensors that is used while minimizing the required computation time in a real time flight computer implementation. The required computation time depends principally on the rate of processing scalar measurements with the Kalman filter; this rate is minimized with negligible loss of information by accumulating measurements over an interval and compressing them to a single, nearly equivalent, scalar measurement for each data type which can then be processed by the filter once per interval. For this purpose it was found empirically that measurements could be sampled and accumulated at 10 Hz with negligible loss of information and processed at 1-sec intervals without significant loss of estimation accuracy. Measurement sample error correlation times and the IMU accuracy are important factors in establishing these values. This device provides an order of magnitude reduction in the rate of processing scalar measurements from that which would be required without measurement compression.

Additional design factors affecting computation time and estimation accuracy remain to be studied in simulation tests described in the following sections. These include (1) evaluation of several candidate separations of the system and filter into independent lower-order systems and filters to obtain significant reductions in the time required to process a scalar measurement, and (2) appropriate choice of acceleration measurement error states from the three candidate formulations noted in this section in order to improve accuracy. The selection of state variables is otherwise largely dictated by control requirements and by a brief review of the parameters of the measurement functions, their a priori accuracy, and the availability of significant information from the sensors compared with the a priori information.

4. ATTITUDE AND ACCELERATION ESTIMATION ACCURACY

The object of this section is to determine the best of several candidate formulations of the acceleration-measurement error states, the acceleration and attitude accuracies achieved by the filter, and the sensitivity of the acceleration and attitude accuracies to sensor accuracy.

Three formulations of the acceleration measurement errors will be studied; these are given in terms of (1) runway axes measurement biases (14-state filter), (2) attitude measurement biases and a vertical acceleration measurement bias (15-state filter), and (3) level heading axes measurement biases (modified 14-state filter).

These formulations are approximate models of the low frequency error processes that result in acceleration measurement errors; the principal error sources are the fixed accelerometer errors (biases, misalignments, and scale factor errors) and maneuver-induced error transients in the attitude gyroscopes. The 15-state filter models the gyroscope error sources directly and is of interest for possible accuracy increases in attitude, as well as acceleration estimation. The modified 14-state filter uses an axis frame in which the acceleration measurement errors due to the fixed accelerometer errors are nearly constant, thus removing one source of the time variations found in the runway axis error states.

Reference Trajectory and Ensemble of Approaches

Accuracy results are given as rms estimation error histories for a 10-sample ensemble of approaches along a reference trajectory. The reference trajectory is defined in figure 2.1 and table 2.1 from terminal area entry to landing. It contains the range of maneuvers, accelerations, speeds, and flightpath angles expected in STOL approach operations, including a speed range from 140 to 65 knots at landing, and a decelerating, helical descent and glide slope at -7.5°. The path is coarsely defined as a sequence of straight-line and circular-arc legs for which kinematic data are listed in table 2.1. The coarsely defined trajectory is discontinuous in velocity and acceleration at the leg junctions, but the trajectory generating algorithm (given in ref. 27) smooths this to a continuous trajectory which satisfies appropriate operational and aircraft limits on velocity excursions, acceleration, and jerk.

Measurement biases, noise, and other error types for the ensemble of 10 approaches are sampled randomly or generated in accordance with the statistical and deterministic models previously defined. The wind environment is constructed by superposition of mean and turbulent wind components generated by models commonly used in aircraft simulations for the low-altitude winds. The direction and magnitude of the mean wind are selected randomly for each approach such that its 3σ values match those recommended by the FAA for the landing zone as a function of direction (25-knot headwind, 15-knot crosswind, 10-knot tailwind). The mean wind is assumed constant for periods much longer than the approach flight duration and increases with altitude by a factor of 2 in the atmospheric boundary layer (up to 300 m) and is constant above that. The wind turbulence history is that encountered by an aircraft flying through a space-frozen turbulence field and is generated as a three-dimensional Gaussian random process (Dryden model) with zero means and variances that depend on aircraft axis, attitude, and airspeed, and that are proportional to the field intensity (field intensity is measured as the landing zone horizontal gust variance and is a random variable with a mean value of 0.7 m/sec). Documentation of this wind model is omitted here, but an extensive literature on this subject exists, including theory, observations, and recently recommended models for terminal area aircraft simulations (e.g., refs. 28 and 29). The aircraft motion simulation omits aircraft attitude dynamics and turbulence response so that their effects on actual aircraft accelerations and some higher frequency sideslip and attitude angle variations are absent; their effects on navigational accuracy are noted where significant.

The randomly selected constants for each of the 10 sample approaches are listed in table 4.1; these sample values are used in all ensemble results of the report unless otherwise stated. In this section, interest focuses on performance during the maneuvering segments of the trajectory. Empirical results are, therefore, given beginning near waypoint 2 (t = 647) where maneuvering starts.

Attitude Estimation

Attitude estimation accuracy for the 15-state filter is compared with the accuracy of the gyroscope, $\tilde{\phi}_g$, $\tilde{\theta}_g$, $\tilde{\psi}_g$, in figure 4.1. A legend indicates the trajectory leg number and navaids in use. These results show no success in improving attitude accuracy. Roll and pitch estimation accuracies are considerably poorer than the errors in the vertical gyroscope, and the heading error is nearly identical to the error in the directional gyroscope; that is generally,

$$\mathrm{rms}(\tilde{\phi}) > \mathrm{rms}(\tilde{\phi}_g)$$

$$\mathrm{rms}(\tilde{\theta}) > \mathrm{rms}(\tilde{\theta}_g)$$

$$\mathrm{rms}(\tilde{\psi}) \cong \mathrm{rms}(\tilde{\psi}_g)$$

This occurs in part because accelerometer errors are significant and must be interpreted by the 15-state filter as equivalent attitude measurement biases. Both equation (2.14) and the empirical results for sample cases show that longitudinal and lateral accelerometer biases are interpreted, respectively, as pitch and roll measurement biases. In addition, equation (2.14) shows that the principal deterministic effect of $\tilde{\psi}_g$ on $\underline{\tilde{am}}$ is longitudinal, nonzero only in turns, and indistinguishable from the effects of $\tilde{\theta}_g$, which have a much larger gradient throughout the present test trajectory. The result is that the filter interprets the effect of $\tilde{\psi}_g$ almost entirely as an equivalent pitch bias; this is evidenced in figure 4.1, both by the

TABLE 4.1- RANDOMLY SELECTED CONSTANTS FOR ENSEMBLE OF APPROACH FLIGHTS

Sample	Wind parameters			Measurement biases								
	Mean wind, m/sec		Turbulence intensity, m/sec	VORTAC		Baro-altimeter, m	MODILS			Body-mounted accelerometers, g		
	$W_x(0)$	$W_y(0)$		Range, m	Bearing, deg		Range, m	Azimuth, deg	Elevation, deg	Longi-tudinal	Lateral	Normal
1	-1.2	-7.6	1.0	252	0	-11	-3.7	0.02	-0.046	0.012	-0.004	-0.042
2	4.0	6.6	.8	-121	-1.0	17	10.5	.15	.016	.017	.010	-.010
3	.9	-7.1	1.7	282	-2.5	41	-9.9	-.15	.015	.014	-.031	-.018
4	9.2	7.3	1.0	-134	-2.9	-15	4.4	-.11	-.027	.018	.001	.007
5	9.8	1.8	.7	61	-1.3	4	1.5	.11	-.008	.011	.032	.003
6	13.0	-2.1	.8	-93	-.4	24	-3.0	.17	-.031	-.003	-.004	.010
7	2.7	5.9	.5	-348	-.6	67	-12.8	0	.016	-.016	-.006	.004
8	.5	3.6	1.3	-386	-2.4	-14	-2.0	.14	.041	-.011	-.025	-.004
9	5.5	.4	1.0	2	-.3	-27	4.1	.12	.055	-.007	-.021	.004
10	14.6	-3.7	1.4	233	2.6	6	1.9	.23	.051	-.004	-.002	-.010
Mean	5.9	0.5	1.0	-76	-0.9	9	-0.9	0.07	0.008	0.003	-0.005	-0.006
RMS	7.9	5.2	1.1	226	1.7	32	6.6	0.15	0.035	0.0125	0.018	0.016

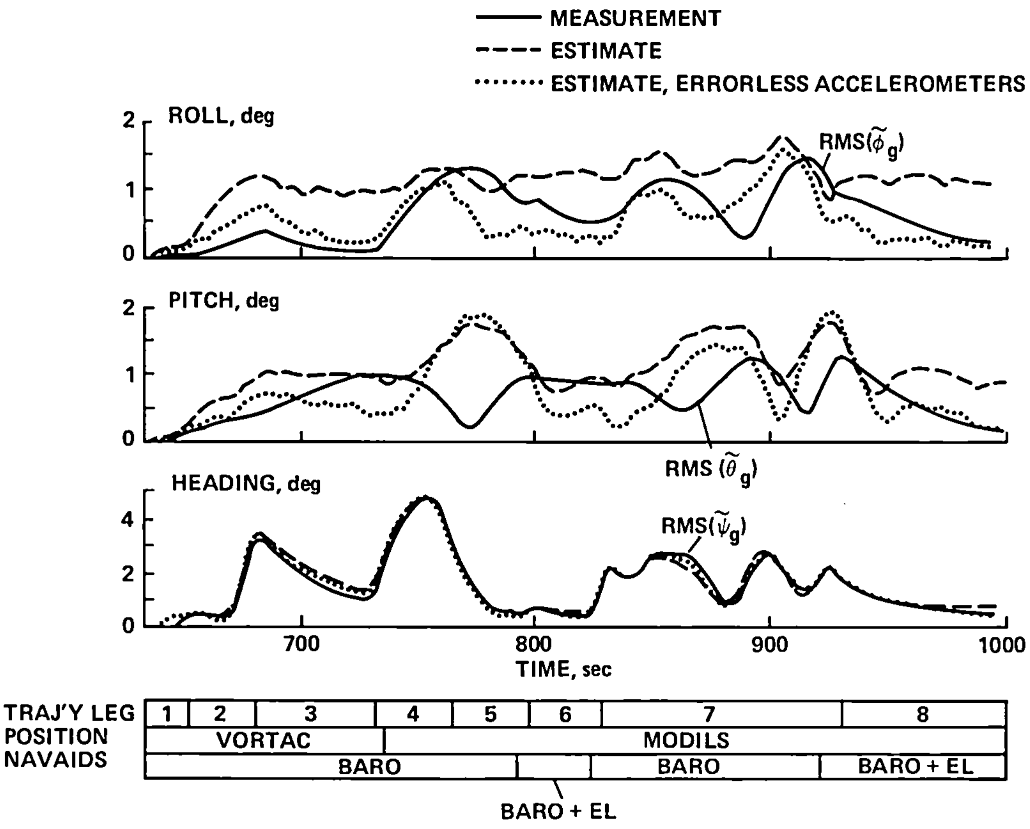

Figure 4.1.- Attitude estimation accuracy of 15-state filter (rms errors).

behavior of $\tilde{\psi}$ and the (delayed) correspondence of some variations in $\tilde{\theta}$ with variations in $\tilde{\psi}_g$.

Additional results with errorless accelerometers were obtained to determine if improvements in this sensor would permit the filter to estimate gyroscopic errors to a useful degree. The results (fig. 4.1) show no success; roll angle is unambiguously detectable in this case but is improved only to about the accuracy of the gyroscopic roll angle, and the pitch error excursions, which are well above $\tilde{\theta}_g$, owing to misinterpretation of the effects of $\tilde{\psi}_g$, remain present, and $\tilde{\psi}_g$ is virtually unchanged.

The filter's information on attitude errors is derived from position measurements; figure 4.1 shows similar performance using either VORTAC or MODILS and suggests that performance is insensitive to position measurement accuracy in the accuracy range of these navaids. This is confirmed by results using errorless position measurements (not shown); in this case, roll estimation accuracy is significantly improved, with peak excursions to 0.7°, but pitch and heading remain subject to the error effects noted above and are unimproved.

These results show that the present sensors, in combination with an appropriate formulation of the filter states, cannot improve the accuracy of the measurements of the attitude gyroscope.

Acceleration Estimation

The estimation accuracy for the path axes coordinates of acceleration is shown in figure 4.2, where it is compared with the accuracy of the measured acceleration derived from instantaneous sensor outputs. As seen, the two filters perform similarly. Both succeed in reducing measurement errors significantly as a result of their ability to estimate and remove some effects of the fixed and low frequency accelerometer and gyroscopic errors; both give good, nearly invariant normal axis accuracy in excess of 0.01 g after the initial transient; and both give similar lateral axis accuracy. For the longitudinal axis, the error reduction is modest and the performance of the 15-state filter is poorer, with several excursions in excess of the measurement error that can be traced to excursions in $\tilde{\theta}_g, \tilde{\psi}_g$.

Accuracy for the vertical axis and horizontal plane components of acceleration differ significantly because (1) the first-order effects of gyroscopic error transients are confined to the horizontal plane (eq. (2.14)) and (2) the fixed accelerometer errors are nearly constant along the vertical axis because of the low roll and pitch angles used in passenger operations; however, the latter are time-varying relative to the horizontal plane runway axes during turns. Thus, the vertical acceleration measurement error is nearly constant and the filter succeeds quite well in estimating this from position measurements. In contrast, the horizontal plane components are both larger and time varying during maneuvering flight and this continually excites the filter's transient response. It is the variation rate of the measurement errors rather than their magnitude that limits the accuracy obtained here.

In view of the results seen in figures 4.1 and 4.2, the 15-state filter can be dropped from the discussion; the increased number of states adds a poorly observable state, $\tilde{\psi}$, to the computations, without increasing the accuracy of the estimated acceleration.

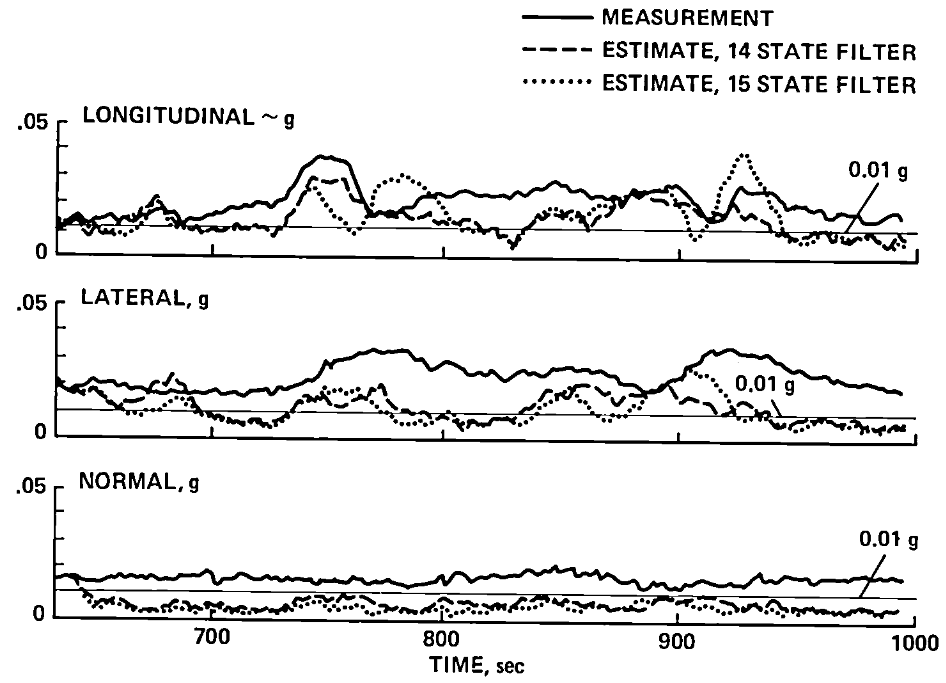

Figure 4.2.- Acceleration estimation accuracy: 14- and 15-state filters.

The separate influence of the attitude gyroscope and accelerometer errors is examined in figure 4.3, in which the existing acceleration estimation accuracy is compared with that achieved with (1) errorless gyroscopes and (2) errorless accelerometers. In each case, the magnitude of the estimation error indicates the contribution of the normal sensor type to the total error, as well as the maximum performance available from sensor improvements. For the longitudinal and lateral components, estimation errors owing to accelerometer errors are close to the total error over most of the trajectory, and those owing to gyroscopic errors are usually somewhat smaller; performance for both components is poorer than for the normal axis and shows excursions above 0.01 g over some or most of the trajectory. Thus, accelerometer errors dominate the estimation error for this filter.

The same comparison is made in figure 4.3(b) for the modified 14-state filter which uses level heading axes acceleration measurement bias states. As seen, acceleration estimation errors for the longitudinal and lateral axes appear to be almost entirely the result of gyroscopic errors (except initially); the variations in estimation errors follow the gyroscopic error histories of figure 4.1 in accordance with equation (2.14). This result is quite different from that obtained in figure 4.3(a) and indicates much poorer performance for the modified 14-state filter in detecting the effects of gyroscopic errors. The cause of this difference in performance is not clear. On the other hand, the modified 14-state filter shows excellent performance in estimating accelerometer biases when the gyroscopes are errorless (accuracy is invariant and exceeds 0.01 g on all axes), as was anticipated.

Comparing the two 14-state filters, the net result is that each filter performs better with one type of sensor error but does poorly with the other. The accuracy achieved by the modified 14-state filter is nearly identical to that of the 15-state filter, which also has the potentially favorable property that the fixed accelerometer errors map into nearly constant state errors (in this case, $\tilde{\phi}$, $\tilde{\theta}$, $\tilde{z}$). Thus, a comparison of the two filters would give the same result as that shown in figure 4.2, and we select the runway-axis formulation of the acceleration bias states for the filter as a result of its somewhat better accuracy, which is due to its greater (but limited) ability to detect the error effects of the attitude gyroscopes.

The effect of position measurement accuracy on acceleration estimation accuracy was also examined. In figure 4.2 both VORTAC and MODILS data result in the same range of minimum to maximum errors during maneuvering so that performance appears insensitive to position measurement accuracy over the range obtained from these navaids. Further tests were made comparing performance for errorless and normal position measurements. First, results were obtained for a straight line static equilibrium path, using VORTAC data and large accelerometer biases (0.05 g); the ensemble averages showed that VORTAC gave good steady state, acceleration estimation performance (below 0.01 g) — equivalent to that for the normal axis in figure 4.2. Thus, under the restricted circumstances of inertially constant acceleration measurement biases, even fairly poor position measurements suffice to calibrate the present IMU to better than 0.01 g. The errorless position data, therefore, yielded little improvement in steady state accuracy, but significantly reduced the filter's settling time in estimating a_r. Secondly, the same comparison was made for the STOL approach path to determine if the faster response time would maintain the acceleration estimation accuracy closer to the steady state performance during maneuvering. The results (fig. 4.4) show moderate improvements throughout the approach in longitudinal and lateral acceleration, with rms errors of 0.02 g or better, but accuracy remains time-varying in turns.

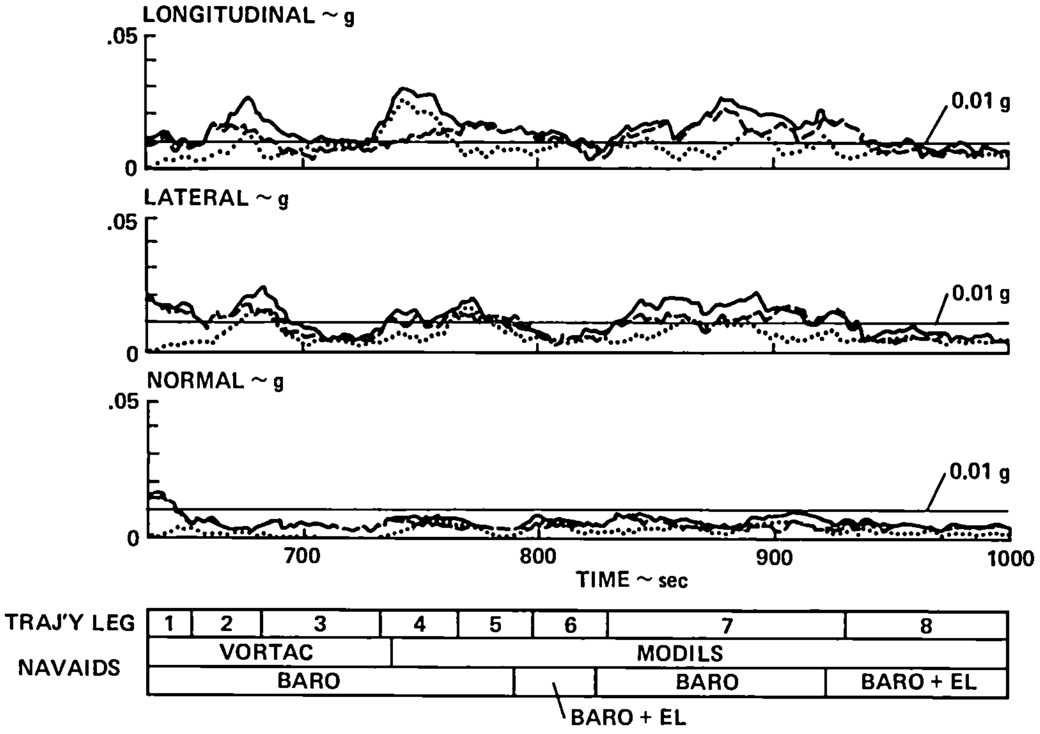

(a) 14-state filter.

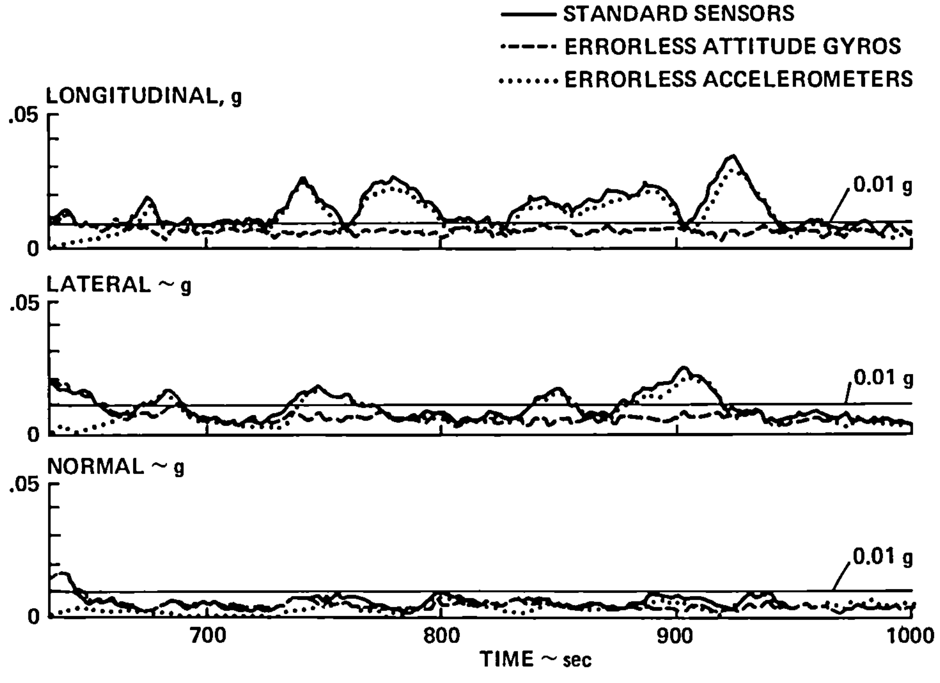

(b) 14-state filter with level-heading axes acceleration bias states.

Figure 4.3.- Acceleration estimation accuracy: effects of acceleration error model and sensor accuracy.

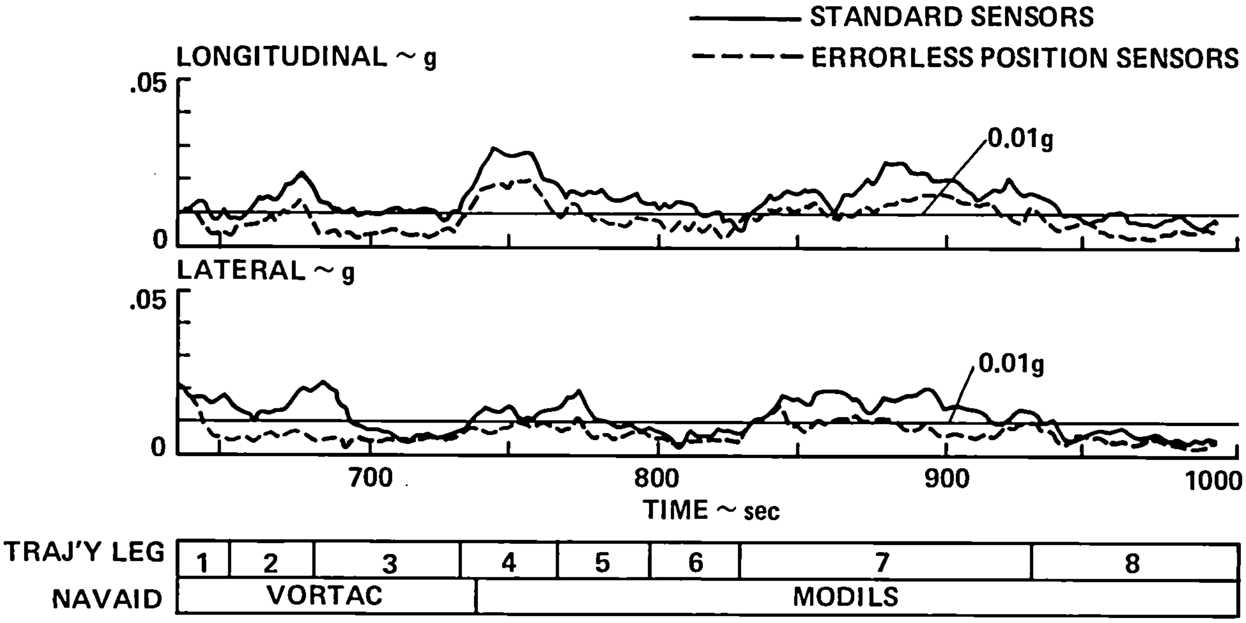

Figure 4.4- Acceleration accuracy: effect of position-sensor accuracy.

Other simulation tests (not shown) indicated that acceleration estimation performance of the three filters was insensitive to the airspeed sensor accuracy and to the values of the correlation time-constants used in the filter's state equations for acceleration-measurement errors (table 3.2). These models are tractable but fictional, and their parameters are "tuned" to achieve the best performance with the simulated sensor error models. Although it is best to tune a flight system with recorded flight data or with well-verified simulation models, the observed insensitivity to these time constants implies a related insensitivity of the in-flight accuracy to simulation model inaccuracies.

Summary

The simulation tests discussed in this section lead to six major conclusions regarding attitude and acceleration estimation.

1. Three formulations of the acceleration measurement error states were tested and the formulation as runway axis bias errors was selected, based on its somewhat better acceleration estimation accuracy on a maneuvering STOL approach.

2. Attitude estimates can be given only to the accuracy of the attitude gyroscopes. Efforts to improve on this by formulating the filter states as gyroscope errors resulted in even poorer accuracy because (1) the fixed accelerometer errors are interpreted as equivalent gyroscope errors, and (2) $\tilde{\theta}_g$ and $\tilde{\psi}_g$ are indistinguishable as causes of position residuals. Further, tests with errorless accelerometer and position data showed that any success deriving from these sensor improvements was limited to roll angle.

3. The dynamics of the attitude gyroscope were continually excited by maneuvering on the final part of the STOL approach path until the glide slope segment; this resulted in rms pitch and roll errors between 0.5° and 1.5° and rms heading errors between 1.5° and 5° during most of the time.

4. The filter succeeds in estimating acceleration more accurately than acceleration can be measured by using position data to detect the fixed and low frequency acceleration measurement errors. Accuracy for the vertical axis is good, with nearly stationary estimation errors below 0.01 g rms throughout the approach; this is a result of the easily detected, near-constant acceleration measurement bias for this axis. Accuracy for the horizontal plane components is significantly poorer, with time-varying estimation errors resulting from the dynamics of the attitude gyroscopes and the time-varying runway axis components of the fixed accelerometer package errors during maneuvering. The accuracy range on the test approach path was as follows:

Component	Estimation error, rms
Longitudinal	0.01 to 0.03 g
Lateral	0.005 to 0.025 g
Normal	<0.01 g

5. Tests showed that the fixed accelerometer package errors were the principal source of the horizontal plane acceleration estimation errors. An alternative formulation of the acceleration bias error states in level heading axes succeeded in detecting the fixed accelerometer errors to better than 0.01 g but was unsuccessful in improving accuracy because of reduced performance in detecting gyroscope errors.

6. Significant improvements over the acceleration and attitude accuracies achieved here do not appear possible by further development of the filter formulation nor from improved accelerometer or position sensors; such improvements can be obtained, however, from a more accurate IMU, such as an inertial platform or Schuler-tuned strapdown system (ref. 30) or, perhaps, by adding rate gyroscopes to the present set of sensors.

5. POSITION, VELOCITY, AND WIND ESTIMATION ON A STRAIGHT LINE PATH

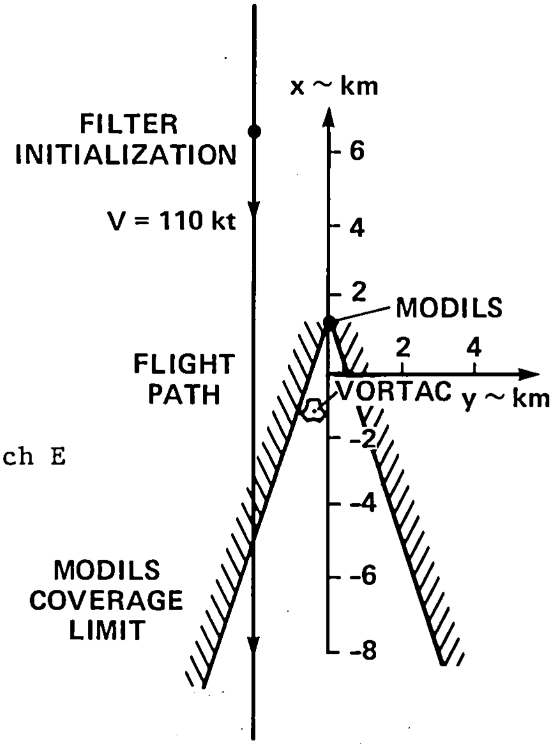

Sketch E

Performance details are studied next, using results from a level, straight flightpath near the runway. In these tests, maneuver-induced acceleration measurement error transients are absent and acceleration accuracy exceeds 0.01 g on all axes. This simplifies somewhat the analysis of the dependence of estimation accuracy on sensor accuracy and flightpath. The flightpath (see sketch E) is parallel to the runway at 2,200 m and is flown at 110 knots; the filter is initialized outside MODILS coverage and acquires MODILS after 200 sec.

The objectives of this section are to determine estimation accuracy, to determine its principal transients on unaccelerated paths, to determine its sensitivity to sensor accuracy, and to settle empirically several filter design issues. Performance details are reviewed separately for each type of state and for states associated with the horizontal plane and vertical axis motions. Ensemble rms errors for all states of interest here are given in figure 5.1. Note that scales are changed at the switch to MODILS data for some states in order to improve resolution.

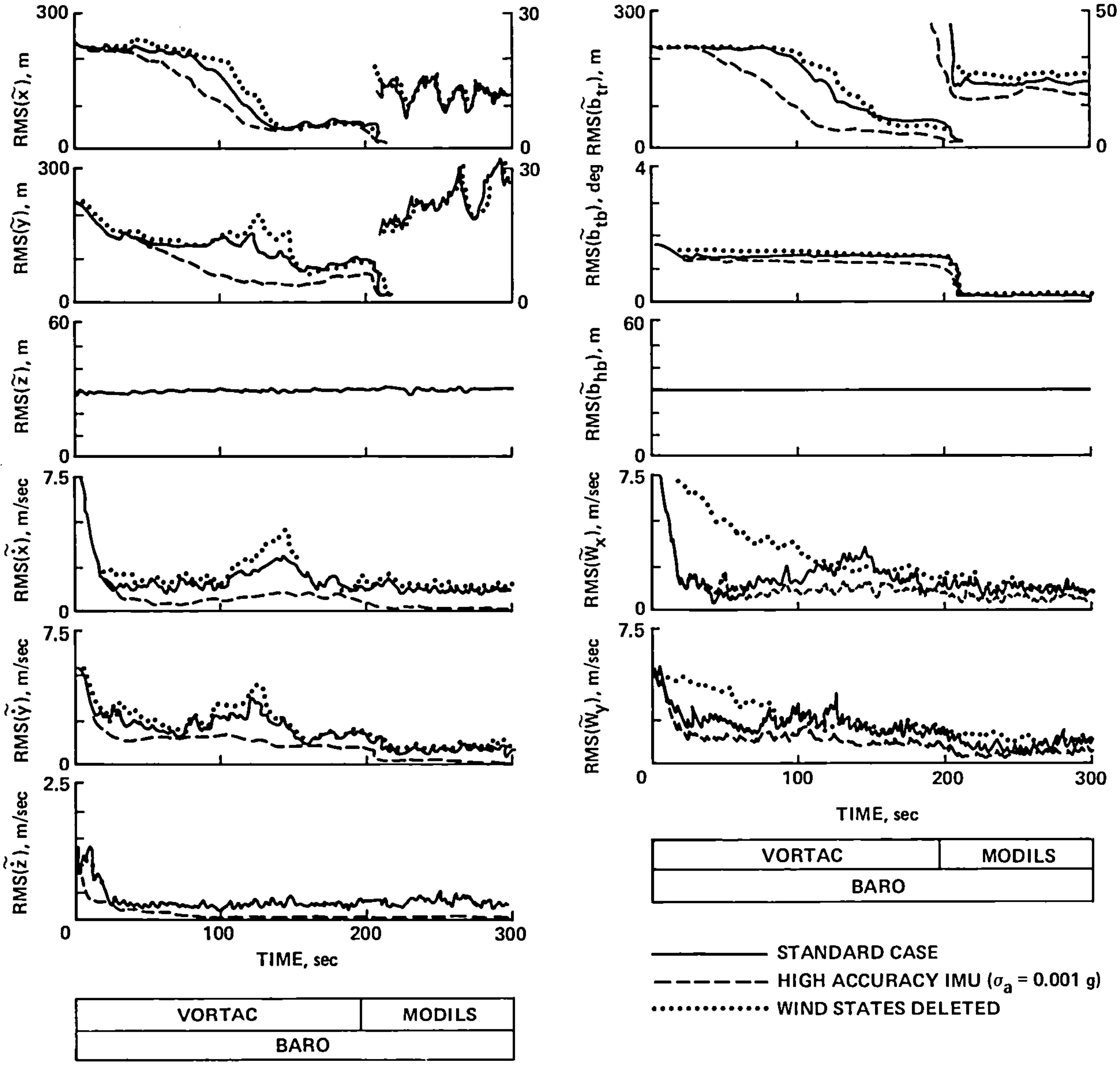

Figure 5.1.- Performance comparisons for (1) standard case, (2) high-accuracy IMU, (3) filter without wind states.

VORTAC Biases

The VORTAC bias states are estimated as zero at filter initialization so that their initial sample and ensemble rms errors equal the sample case and average biases, respectively. Subsequently, information on these biases is negligible on the straight line path compared with the a priori information, until (1) passage close to the VORTAC site (during 100 sec < t < 150 sec in fig. 5.1) permits calibration of the range bias to an accuracy of 60 m from acceleration measurements; and (2) entry to MODILS coverage (at $t = 200$ sec) permits calibration of both VORTAC biases to the accuracy of the MODILS measurements (15 m, 0.25°). After these events, the VORTAC remains calibrated to the accuracy of MODILS regardless of later switches between MODILS and VORTAC so that no significant maneuvering to an offset trajectory is excited by the estimator at such switches.

Before receiving MODILS data, information on the bias states can be obtained theoretically from (1) acceleration measurements, and (2) mutual calibration of the range and bearing to, at best, the accuracy of the better distance measurement. These possibilities are explained next, but the empirical results show only limited success from these sources.

First, suppose that position is calculated from biased VORTAC measurements. The acceleration required to follow this calculated position differs from the acceleration that is measured along the actual path and the difference provides nonnegligible information on the VORTAC biases, provided the acceleration measurements are sufficiently accurate. More explicitly, the error in computing position from noiseless VORTAC measurements with unknown biases, $\tilde{b}_{tr}, \tilde{b}_{tb}$ is

$$\underline{\tilde{R}}^{(b)} = \tilde{b}_{tr}\underline{u} + r_t\tilde{b}_{tb}\underline{p} \tag{5.1}$$

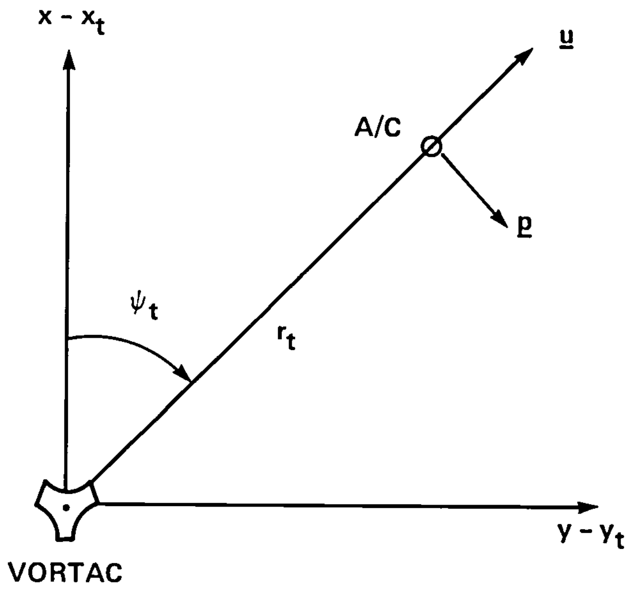

Sketch F

where $(\underline{u},\underline{p})$ are the unit radial vectors from the VORTAC and its perpendicular (see sketch F). If, now, velocity and acceleration are calculated as derivatives of the computed position, the errors that are due to the unknown bias are given by derivatives of equation (5.1):

$$\underline{\tilde{V}}^{(b)} = \tilde{b}_{tr}\dot{\psi}_t\underline{p} + \tilde{b}_{tb}\underline{k}_r \otimes \underline{V} \tag{5.2}$$

$$\underline{\tilde{a}}^{(b)} = \tilde{b}_{tr}(\ddot{\psi}_t\underline{p} - \dot{\psi}_t^2\underline{u}) + \tilde{b}_{tb}\underline{k}_r \otimes \underline{a} \tag{5.3}$$

where ψ_t is the bearing angle. Bearing bias error results in (1) an apparent velocity that is lateral to the actual aircraft velocity and (2) an apparent acceleration error that is lateral to the actual aircraft acceleration. The apparent acceleration $\tilde{b}_{tb}a$ is zero for the present unaccelerated straight flightpath so that bearing bias error is unobservable to the acceleration measurements here. The estimator, however, will settle on parameter values such that the VORTAC measurement residuals have zero mean; this can be any combination of errors such that

$$E[\underline{\tilde{V}} + \underline{\tilde{V}}^{(b)}] = 0 \tag{5.4}$$

Using equation (5.2), the result for the lateral axis is

$$E[\underline{\tilde{V}} \cdot \underline{j}_p + \tilde{b}_{tb}V + \tilde{b}_{tr}\dot{\psi}_t\underline{p} \cdot \underline{j}_p] = 0 \tag{5.5}$$

In most situations, the term in $\tilde{b}_{tr}$ is negligible, so that the bearing-bias error results in a corresponding lateral velocity estimation error bias that satisfies

$$E[\underline{\tilde{V}} \cdot \underline{j}_p] = -V\ E[\tilde{b}_{tb}] \tag{5.6}$$

The initial errors ($\underline{\tilde{V}}(0)$, $\tilde{b}_{tb}(0)$) are independent and do not satisfy equation (5.6) in general, but their steady state mean values are driven to this line. This can result in noticeable sample case transient changes in the bearing bias estimate, even though the ensemble average for $\tilde{b}_{tb}$ changes very little in figure 5.1. This is demonstrated in figure 5.2(a), which shows the trajectories of $\{(\underline{\tilde{V}} \cdot \underline{j}_p, \tilde{b}_{tb}), t \geq 0\}$ from selected initial errors. In each case, the figure gives the mean trajectory for an ensemble of samples having the restricted initial errors. As seen, the combined bearing bias and lateral velocity estimation errors are driven to the line defined by equation (5.6).

On the other hand, if we consider accelerating flightpaths, then the apparent acceleration $|\tilde{b}_{tb} a|$ is largest during turns when it is oriented along the level longitudinal axis ($\underline{k}_r \otimes \underline{a} = g \tan \phi\ \underline{i}_L$), but is, at most, only 0.006 g per degree of bearing bias in passenger operations ($\phi \leq 20°$). This provides only crude bearing calibration accuracy of the same size as its a priori accuracy (2°) from an IMU with an accuracy of 0.013 g, but a substantially better calibration can be achieved by an inertial grade IMU. Figure 5.2(b) shows results for both the standard and high accuracy IMU during a turn at a distance of about 23 n. mi. from the VORTAC station. As seen, the standard IMU achieves some improvement in spite of poor acceleration

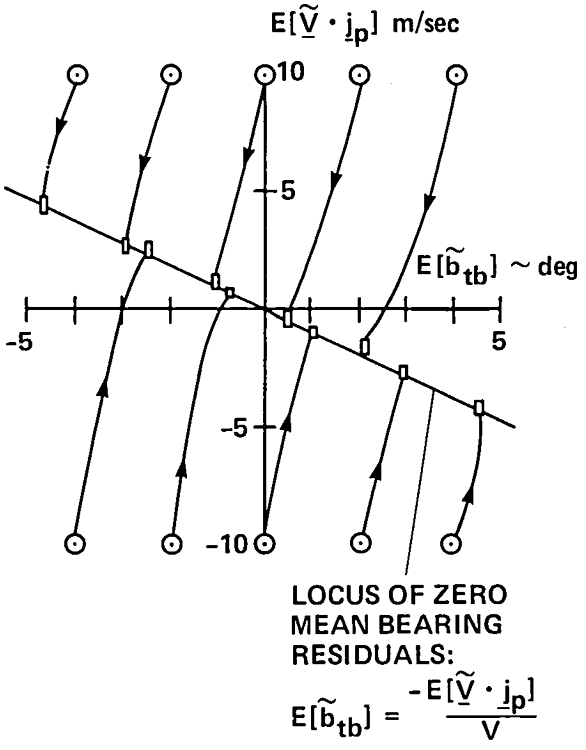

(a) Behavior of bearing bias and lateral velocity estimation errors.

Figure 5.2.- VORTAC bearing-bias estimation outside MODILS coverage.

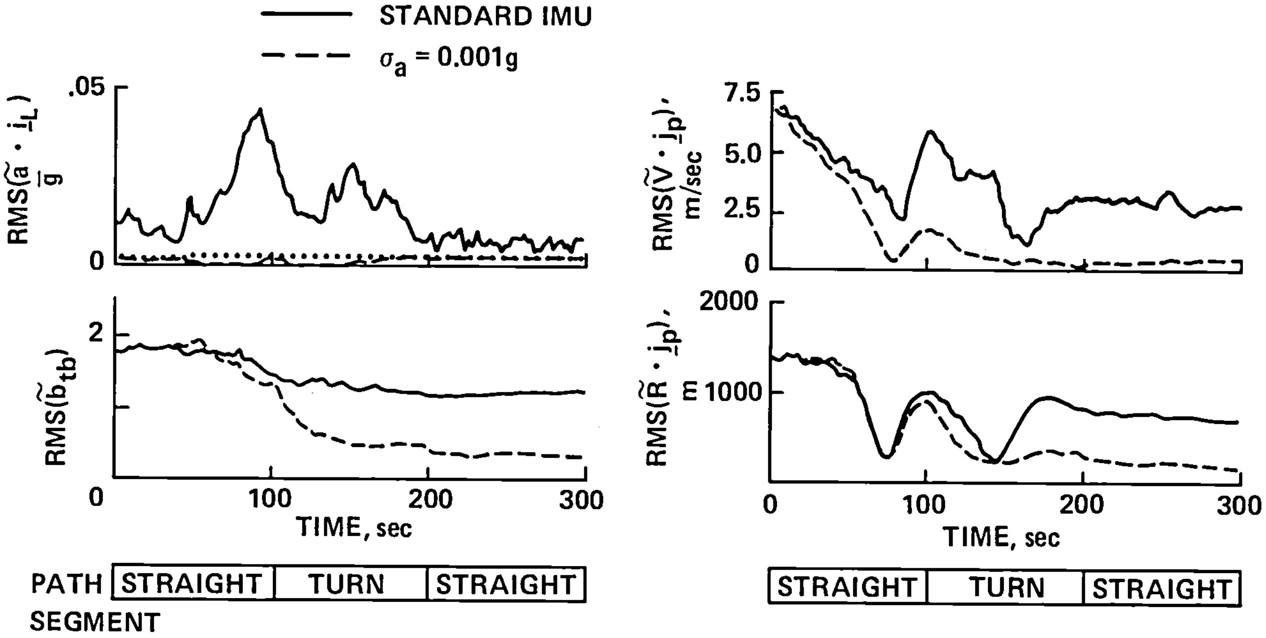

(b) Bearing calibration by IMU during a turn (V = 150 knots, R_c = 1675 m).

Figure 5.2.- Concluded.

estimation accuracy, and the inertial grade IMU detects the bearing bias to an accuracy better than 0.5°; this results in useful reductions of position errors and of the lateral velocity bias error due to bearing bias error. Results with the inertial grade IMU on a straight line path at the same distance are included in the figure and demonstrate that the turn is required, as well as the inertial grade IMU, to obtain these performance benefits. Note that the required turn can be executed early in the approach, since the available calibration accuracy is independent of distance to the VORTAC. However, the capacity to calibrate angle measurements with this IMU is limited and does not suffice to similarly improve the a priori accuracy of the MODILS azimuth calibration.

The apparent acceleration due to range bias error is negligible in equation (5.3), except during periods of nonzero bearing rate, $\dot{\psi}_t$; for rates of 1.75°/sec, which occur when passing close to the VORTAC station in the present example, the rms acceleration error resulting from range bias is 0.03 g along the VORTAC radial. This permits calibration to 100 m, with 0.01-g acceleration estimation accuracy and accounts for the improved range calibration accuracy seen in figure 5.1 before entering MODILS coverage. More generally, higher bearing rates result in greater calibration accuracy, but this effective opportunity to calibrate the range measurement occurs only when passing close by the VORTAC station.

The range and bearing bias errors can be functionally related by taking VORTAC measurements at different times along any path that is not a VORTAC radial. If one of the measurement types provides a sufficiently more accurate distance measurement than the other, the estimated bias of the poorer measurement can be improved. For example, near the VORTAC station, bearing provides a distance measurement 3 or 4 times more accurate than the a priori range bias estimate, but at a distance of 20 n. mi. the converse is true. However, this source gave only negligible information on the bias errors compared with the a priori or IMU information and we omit an analysis.

The initial estimate is computed from VORTAC data so that initial errors are dictated by VORTAC measurement errors and depend on the location where filter initialization occurs. In the present test, initialization occurs close to the VORTAC site and rms errors are of the order of 250 m in both directions. At other locations, initial errors would be unchanged in the direction of the VORTAC radial, but would increase with range for the direction lateral to this and are much larger (0.75 n. mi.) at entry to the terminal area. After initialization (fig. 5.1), accuracy changes very little until passage close to the VORTAC permits calibration of the range bias to 60 m and a corresponding reduction in rms position error below 100 m in both coordinates; this is followed by a rapid reduction by an order of magnitude at entry to MODILS coverage. Before these events, the position estimation error is biased by the VORTAC calibration error vector (eq. (5.1)) and sample case position errors are larger or smaller, depending on the sample case VORTAC biases.

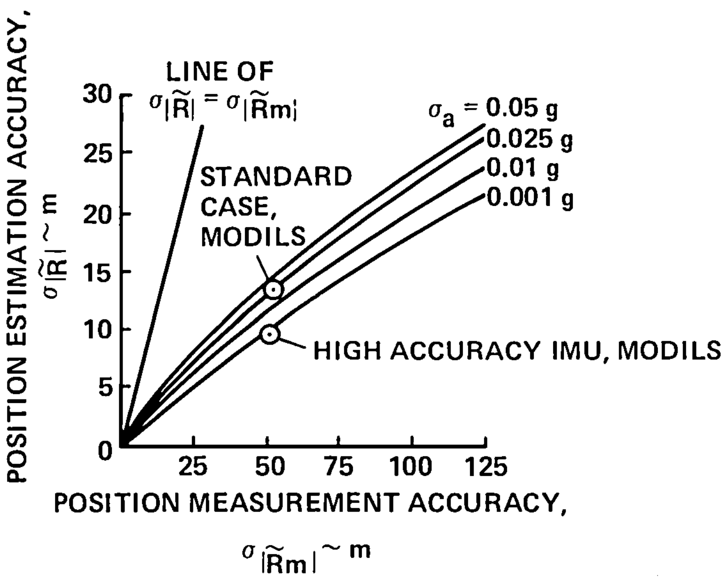

(a) POSITION ESTIMATION ACCURACY

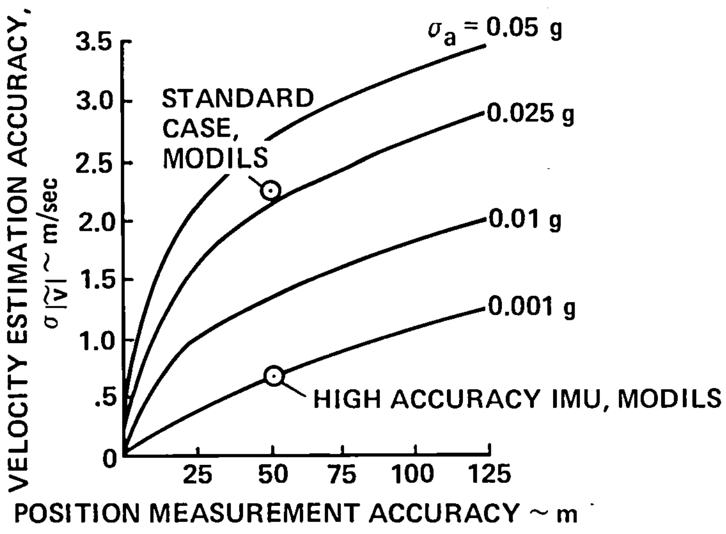

(b) VELOCITY ESTIMATION ACCURACY

Figure 5.3.- Effect of position and acceleration measurement accuracy on performance.

Sensitivity to acceleration measurement accuracy is shown in figure 5.1 by the comparison with results for a high accuracy IMU (σ_a = 0.001 g). Improvements for the position states are limited to an improved capacity to detect range bias when passing close to the VORTAC and related local improvements in position accuracy.

The dependence of position estimation accuracy on the combined accuracy of both position and acceleration measurements is examined further in figure 5.3(a). These results were obtained in a series of simulation tests; the estimation accuracy was obtained from the covariance matrix as

$$\sigma^2_{|R|} = E[(\tilde{x}^2 + \tilde{y}^2)] = \sigma^2_x + \sigma^2_y$$

and measurement accuracy was varied over the range of interest, using unbiased MODILS measurements with error and flightpath parameter values selected to give equal accuracy in all horizontal directions in the expression

$$\sigma^2_{|\tilde{R}m|} = E[(\tilde{Y}_{mr}\underline{u} + d_{xym}\tilde{Y}_{ma}\underline{p})^2]$$

$$= \sigma^2_{mr} + d^2_{xym}\sigma^2_{ma}$$

The results indicate several conclusions. First, estimation accuracy is substantially better than the position measurement accuracy in all conditions — a result of the filter's smoothing of measurement noise. Second, improvements in either acceleration or position sensing accuracy yield some reduction in estimation errors, but greater reduction is achieved by reducing position sensing errors than by reducing acceleration sensing errors by the same factor. Two points, labeled "standard" case and "high-accuracy IMU," indicate that only a moderate improvement in position estimation accuracy would be realized by replacing the present accelerometer attitude-gyroscope system with an inertial grade IMU. Thus, figures 5.1 and 5.3(a) both indicate that position estimation accuracy depends principally on the position measurement accuracy, and significant improvements in position accuracy over the present performance requires improved position sensors.

Horizontal Plane Velocity Coordinates

The velocity estimate is initialized at the measured air velocity vector, $(Y_{\dot{x}a}, Y_{\dot{y}a}, 0)$, and its initial error is dominated by the actual wind with a theoretical standard deviation of 6.1 m/sec in each coordinate. Subsequently (fig. 5.1), the velocity accuracy settles in about 25 sec to about 2 m/sec, shows a modest transient when passing close to the VORTAC, and settles to 1 to 1.5 m/sec after acquiring MODILS data. For comparison, the airspeed sensor accuracy is 0.6 m/sec, and this sensor has been used in restricted control modes (e.g., automatic airspeed capture and hold modes and airspeed-referenced trajectory tracking). Accuracy for the horizontal plane inertial velocity coordinates with the present sensors and estimator is significantly poorer than this, except under conditions of maximum position and acceleration measurement accuracy.

More generally, the transient and steady state behaviors of the velocity accuracy show several features. First, the initial settling time depends somewhat on position accuracy and direction; it is faster using MODILS data, slower at large distances for the direction lateral to the VORTAC radial, and is faster for the longitudinal axis than for the lateral axis because of aiding by airspeed measurements.

Second, the steady state lateral velocity error, using VORTAC data, is moderately biased by the bearing bias error. Bearing bias is very poorly observable before entering MODILS coverage, but its presence is interpreted as a lateral velocity in the amount $\tilde{b}_{tb}V$ in accordance with equation (5.2). This effect is illustrated in figure 5.4(a), which shows the ensemble means for velocity in the restricted case in which the bearing is 4° in all samples; as seen, the lateral velocity error, $\dot{\tilde{y}}$, has a steady state bias (4 m/sec) while the longitudinal velocity error, $\dot{\tilde{x}}$, is unbiased. The steady state velocity accuracy is otherwise independent of the remaining, randomly sampled constants of each flight (mean winds and measurement biases).

Third, significant error transients when passing close to the VORTAC site can occur in some samples. Equation (5.2) indicates that estimation errors in VORTAC range bias, velocity lateral to the VORTAC radial, and acceleration along the radial are all possible causes of range measurement residuals. If one of these errors is significantly larger than its standard deviation in the filter's covariance matrix, then the filter temporarily misinterprets the residuals when near the VORTAC and produces error excursions in all of these states. This is illustrated in figure 5.4(b) by the ensemble means in the case in which range bias is restricted to its 2σ value (610 m) in all samples; as seen, velocity accuracy shows a significant transient. The remaining source of significant velocity accuracy transients is the IMU errors, and they are discussed in a later section.

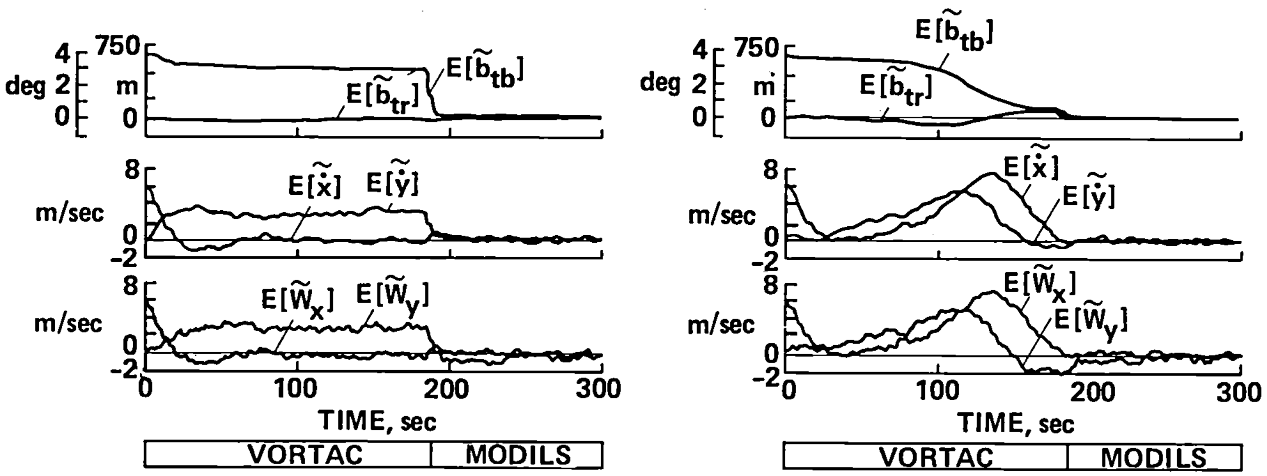

(a) $(b_{tr}, b_{tb}) = (0, 4°)$ (b) $(b_{tr}, b_{tb}) = (610\text{ m}, 0)$

Figure 5.4.- Velocity and wind estimation: effects of large VORTAC calibration errors.

The dependence of velocity accuracy on position and acceleration measurement accuracies is shown in figure 5.3(b). Velocity estimation accuracy is obtained from the filter's covariance, using

$$\sigma^2_{|\tilde{v}|} = \sigma^2_{\dot{x}} + \sigma^2_{\dot{y}}$$

and the results correspond to white Gaussian sensor errors. These results show significant dependence on the accuracy of both types of measurements. Two points, labeled "standard" and "high accuracy IMU" are noted in the figure. They indicate that a substantial improvement, to 0.6 m/sec, would be achieved with MODILS data by using an inertial grade IMU. More generally, to achieve a velocity estimation accuracy of 1 m/sec throughout the terminal area requires improvements in both the position and acceleration measurement accuracy of the present system. Improved position sensing is needed to remove the transient and steady state effects of the VORTAC biases discussed above, and a high accuracy IMU is needed to eliminate the effects of acceleration measurement error excursions excited during maneuvering segments of the approach. A high accuracy IMU by itself cannot achieve this performance for lack of the ability to estimate the VORTAC biases accurately (as shown in fig. 5.1), and an improved position sensor by itself lacks the ability to estimate acceleration measurement errors on maneuvering paths (as shown in the previous section).

Wind States, Airspeed Measurements, and Sideslip Effects

Because the wind is initially estimated as null, initial errors equal the actual winds and have a standard deviation of 6.1 m/sec. Subsequently, accuracy (fig. 5.1) is nearly identical to that of the velocity coordinates. This gross behavior can be understood from the approximate wind estimate, $\underline{\hat{W}}'$, obtained from the current velocity estimate and derived air velocity measurement,

$$\begin{pmatrix} \hat{W}'_x \\ \hat{W}'_y \end{pmatrix} \equiv \begin{pmatrix} \hat{\dot{x}} \\ \hat{\dot{y}} \end{pmatrix} - \begin{pmatrix} Y_{\dot{x}_a} \\ Y_{\dot{y}_a} \end{pmatrix}$$

with estimation errors that have zero mean and variances

$$\left.\begin{aligned} \sigma^{2\prime}_{W_x} &= \sigma^2_{\dot{x}} + \sigma^2_{\dot{x}_a} \\ \sigma^{2\prime}_{W_y} &= \sigma^2_{\dot{y}} + \sigma^2_{\dot{y}_a} \end{aligned}\right\} \qquad (5.7)$$

In most of the present test, these errors are dominated by the inertial velocity terms, which range from 6.1 m/sec initially to 1.5 m/sec in steady state on MODILS data; this compares with the theoretical air velocity measurement accuracy of 1.8 m/sec. Thus, wind estimation accuracy and its transient and steady state response to initial errors and VORTAC biases, and its sensitivity to position and acceleration measurement accuracy are largely the same as for the velocity coordinates previously discussed. In cases in which the velocity estimate is much more accurate than the air velocity measurement, as in the high accuracy IMU case with MODILS data shown in figure 5.1, the air velocity measurement accuracy limits the steady state wind estimation accuracy.

The treatment of wind estimation was an issue in the filter design. The inclusion of wind states in the filter permits processing air velocity measurements, which improves output accuracy both normally and during dead reckoning in the event of position navaid dropout. Alternatively, a substantial saving in computation time can be obtained by removing the wind states and air velocity measurements to a separate filter, as shown in sketch G. This can be done without affecting the observability of the remaining states. The effect on accuracy is examined in figure 5.1, which includes results for both the normal and separated filters; their comparison shows significant accuracy losses in all states associated with the horizontal plane motion, principally during VORTAC use. Thus, the separated filter discards substantial information on these states; because it does, we retain the wind states in an integrated filter.

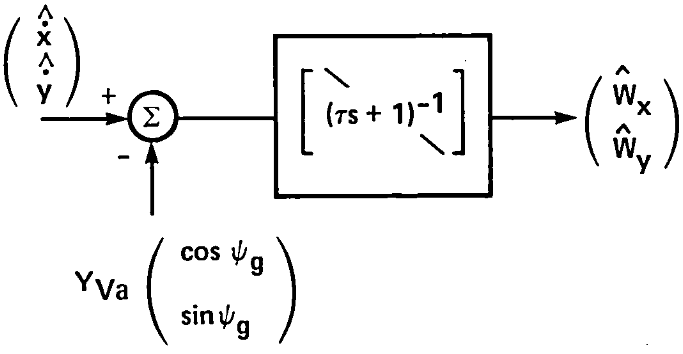

Sketch G

Crosswind is indistinguishable from sideslip angle and heading error for the present sensors. The air velocity measurement is the only measurement with functional dependence on the wind. Recalling equations (3.13) and (3.16) (which are repeated here), the air velocity measurement is derived from airspeed and heading measurements as

$$\begin{pmatrix} \dot{Y}_{\dot{x}a} \\ \dot{Y}_{\dot{y}a} \end{pmatrix} \equiv Y_{Va} \begin{pmatrix} \cos \psi_g \\ \sin \psi_g \end{pmatrix} \qquad (3.13)$$

and represented in the filter as

$$\begin{pmatrix} Y_{\dot{x}a} \\ Y_{\dot{y}a} \end{pmatrix} = \begin{pmatrix} \dot{x} \\ \dot{y} \end{pmatrix} - \begin{pmatrix} W_x \\ W_y \end{pmatrix} + \begin{pmatrix} \tilde{Y}_{\dot{x}a} \\ \tilde{Y}_{\dot{y}a} \end{pmatrix}$$

with Gaussian white errors. However, the actual errors are

$$\begin{pmatrix} \tilde{Y}_{\dot{x}a} \\ \tilde{Y}_{\dot{y}a} \end{pmatrix} = \tilde{Y}_{Va}\begin{pmatrix} \cos\psi \\ \sin\psi \end{pmatrix} + Va(\tilde{\psi}_g - \beta\cos\phi + \alpha\sin\phi)\begin{pmatrix} -\sin\psi \\ \cos\psi \end{pmatrix} + \text{HOT's} \qquad (3.16)$$

The second term is lateral to the flightpath and consists of low-frequency transients when the DG or aircraft sideslip dynamics are excited; it is a bias in the case that a steady sideslip is imposed by the pilot. The filter interprets these errors as an equivalent crosswind in the amount

$$\underline{\tilde{W}} \cdot \underline{j}_L = Va(\tilde{\psi}_g - \beta\cos\phi + \alpha\sin\phi) \qquad (5.8)$$

Sideslip dynamics are omitted from the aircraft motion simulation so that the crosswind accuracy in figure 5.1, rms($\tilde{W}_y$), is somewhat optimistic. However, figure 5.5 illustrates the effect of sideslip; the actual winds are null and sideslip is a 10° square wave. As seen, the ensemble mean crosswind estimate, E[$\hat{W}_y$], rises to the value of $Va\beta$ predicted from equation (5.8) (9.6 m/sec), and the longitudinal wind estimate is unaffected. Additional effects include transients in lateral velocity and acceleration, $\dot{\tilde{y}}$, $\ddot{\tilde{y}}$, excited by the brief, impulse-like excursions in $\dot{\beta}$ which the filter misinterprets as nonzero crosswind shear.

Thus, the air velocity measurements detect a combination of crosswind and β, but they are individually unobservable. The addition of an air velocity vector sensor (e.g., refs. 31 and 32) or β-vane is necessary for their observability and the control of β or lateral air velocity. Aircraft have natural weather vane stability so that control of β is not necessary for attitude stabilization. However, if an estimate of $\hat{\beta}$ is calculated from the filter output and fed back for attitude control, then the combined estimator and control system is neutrally stable in β. Such an estimate can be derived, using the theoretical relation

$$\sin\beta = \langle \underline{j}_b, \underline{i}_{Pa} \rangle \qquad (5.9)$$

where $\underline{j}_b$ is the lateral body axis ($(\underline{j}_b)_r$ is the second row of T_{br} in table 2.2) and $\underline{i}_{Pa}$ is the air-velocity direction (along $\underline{V} - \underline{W}$). Since zero sideslip was assumed in the filter, the estimate of β from equation (5.9) and the filter output must also give zero, approximately; that is,

$$\sin\hat{\beta} = \langle \hat{\underline{j}}_b, \hat{\underline{i}}_{Pa} \rangle \cong 0$$

and, therefore,

$$\tilde{\beta} \cong \beta$$

The transient response of the filter to sample wind histories is examined in figure 5.6. Figure 5.6(a) shows response to a mean wind sample with short periods of high shear (1 m/sec^2); response time for the average estimates, E[$\hat{W}_x$],E[$\hat{W}_y$] is similar, using either VORTAC or MODILS data and on either axis. Excursions in rms errors associated with the shear events appear in the velocity and accelerometer bias states. These effects result from over-weighting acceleration bias and prior velocity estimation error as the causes of the higher-than-expected airspeed residuals which occur during periods of higher-than-expected wind rates. As seen in figure 5.6(a), the effect on the longitudinal component of $\underline{\tilde{a}}$, [rms($\tilde{\ddot{x}}$)], is pronounced whereas the lateral component shows little sensitivity. These effects are also present during periods of higher wind rates in a turbulence sample. This observed influence of wind variation on estimation errors for the inertial states, V_r, a_r, is suppressed if an inertial grade IMU is used, since the weighting of acceleration and prior inertial velocity estimation error as the causes of airspeed residuals is much smaller relative to the prior wind-estimation error.

Figure 5.6(b) shows response to a single turbulence sample with higher-than-average intensity. Here, wind shear is nonzero almost everywhere. Root-mean-square wind estimation errors resemble those of figure 5.6(a), with excursions superposed in association with wind shear. These errors are about the same size as those of the turbulence sample itself. Although rms velocity and acceleration errors are excited by wind variations, they are seen to be much smoother than the rms wind errors and are not significantly degraded from the results in figure 5.6(a); that is, accuracy for these states is only moderately affected by the turbulent wind variations.

The filter models the wind with linear, first-order state equations forced by white noise and the parameters (τ_w, σ_w) whose values are to be selected. This only approximates the actual wind, which is simulated as a superposition of independent constant and turbulence components. The filter's parameters (τ_w, σ_w) have been selected at 20 sec, corresponding to the more rapid average rate of the turbulence, and at 6 m/sec, corresponding to the larger standard deviation of the mean wind. This choice results in the insensitivity of the velocity and acceleration bias estimate to the turbulent wind variations noted above and the relatively good agreement of the mean estimated wind with the total wind.

Dead Reckoning

In practice, position data are occasionally lost for periods of varying length, during which time position estimation errors diverge. For unaided dead reckoning, error growth is given by

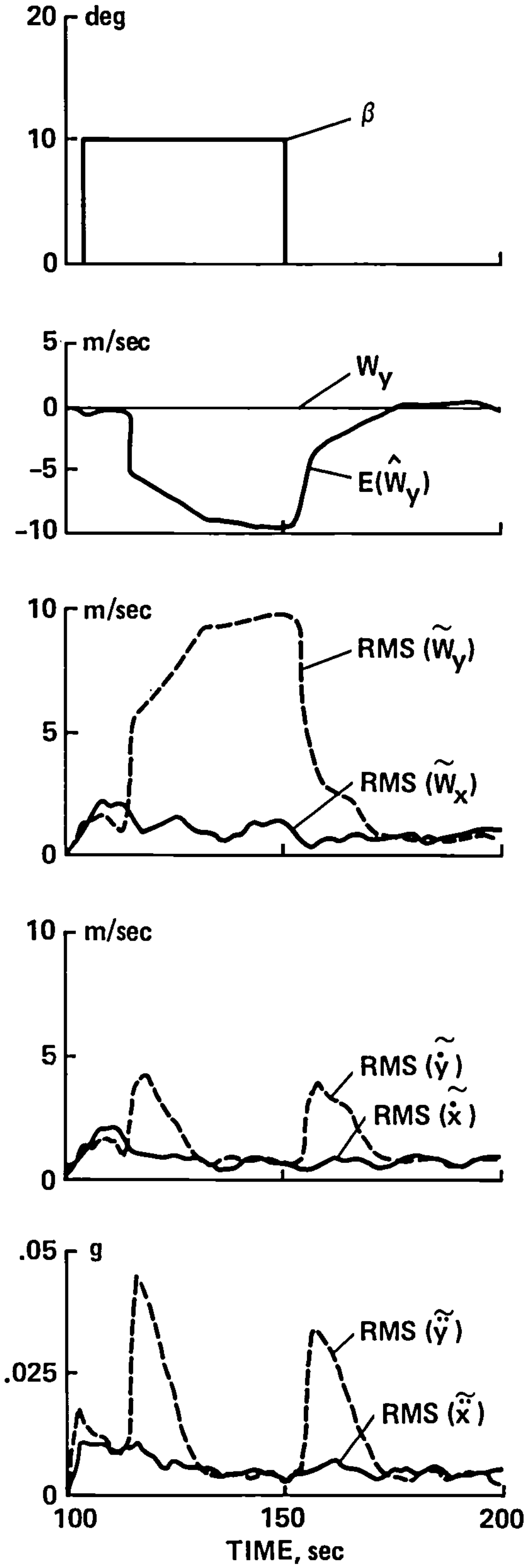

Figure 5.5.- Effect of steady sideslip on wind estimation.

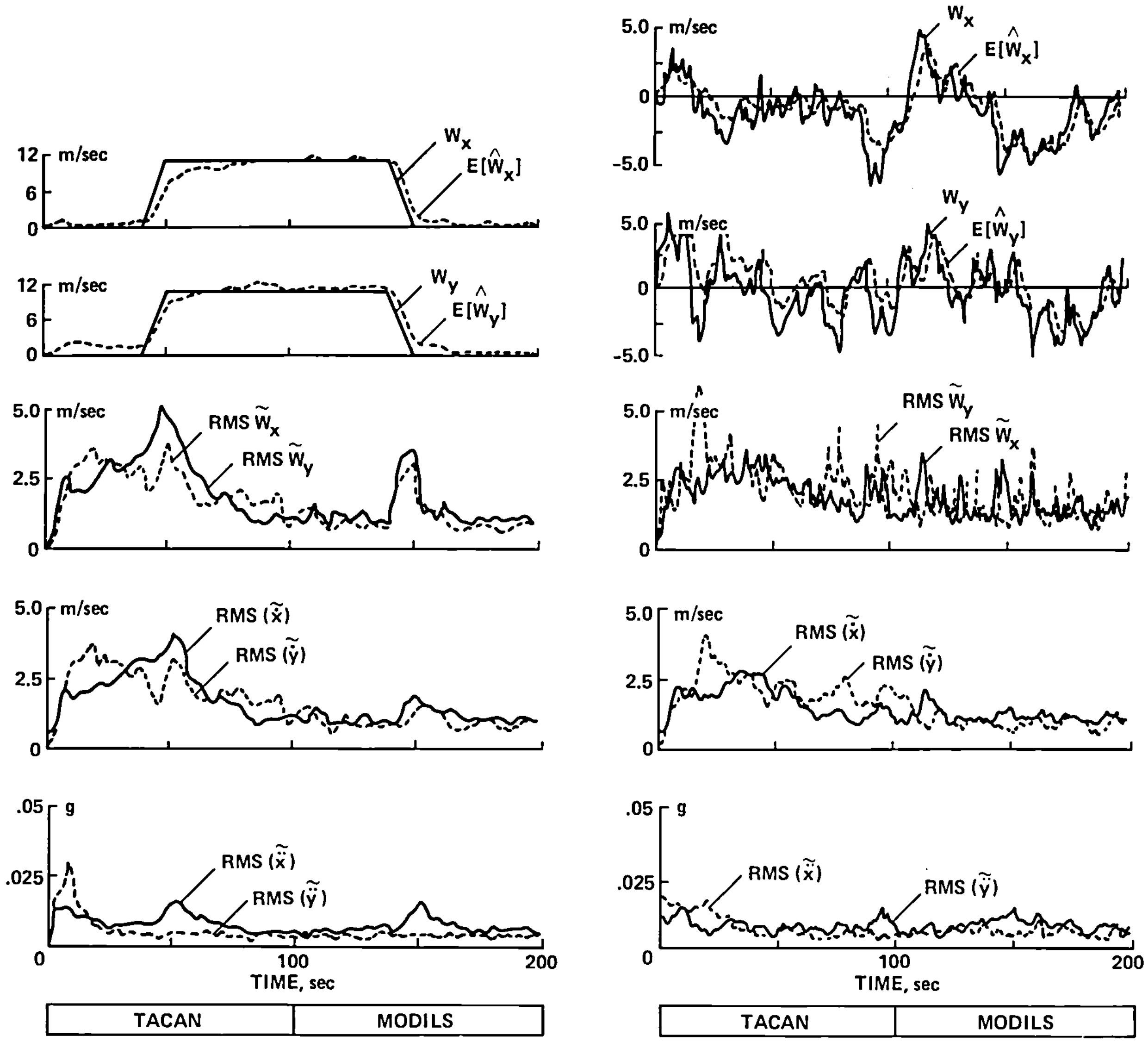

(a) RESPONSE TO MEAN WIND VARIATION

(b) RESPONSE TO TURBULENCE

Figure 5.6.- Wind estimation error response.

$$\tilde{V}_r = \tilde{V}_r(t_o) + \int_{t_o}^{t} \widetilde{am}_r(\tau)d\tau$$

$$\tilde{R}_r = \tilde{R}_r(t_o) + \tilde{V}_r(t_o)(t - t_o) + \iint_{t_o}^{t} \widetilde{am}_r(\tau)d\tau \, d\tau$$

In the case in which $\widetilde{am}(t)$ is constant, velocity and position errors diverge linearly and quadratically with time, respectively. The amount of divergence for a given data dropout interval depends on the initial errors and on the IMU accuracy. The addition of airspeed aiding stabilizes the velocity error, and position error diverges only linearly.

The potential magnitude of these effects during 100 sec of dead reckoning in a maneuvering segment of the STOL approach outside MODILS coverage is shown in figure 5.7. These are unfavorable conditions for initial errors and IMU accuracy, but ones that nonetheless occur in practice. Without airspeed aiding, velocity errors diverge to 15 to 25 m/sec and position errors reach 1,000 m. With airspeed aiding, accuracy is clearly improved; velocity errors are stabilized, but position errors diverge by 500 to 600 m after 100 sec, and significant maneuvering to return to the reference trajectory is still required when the reception of position data is resumed. Naturally, a high accuracy IMU diverges much more slowly, as shown in figure 5.7, and provides for much longer periods of dead reckoning before errors become large. Here, the divergence is negligible after 100 sec.

Vertical Axis Filter States

An important design issue in this study was the trade-off between computation time and accuracy associated with the subdivision of the 14-state system into an independent 4-state subsystem associated with vertical motion, $(\tilde{b}_{hb}, \tilde{z}, \dot{\tilde{z}}, \ddot{\tilde{z}})$, and the remaining 10 states associated with motion in the horizontal plane. The computation time for multiplying system matrices rises with the cube of system order; the proposed partitioning would, therefore, reduce this time by 60% and result in a corresponding major reduction in the time required to execute the filter.

The dynamics of the two subsystems (table 3.2) are mutually independent. In addition, the navaids can be similarly separated approximately. After partitioning the state into lower-order vectors associated with the two subsystems, denoted by

$$\tilde{X} = \begin{pmatrix} \tilde{X}_H \\ - - - \\ \tilde{X}_V \end{pmatrix}$$

then the dependence of the measurement residuals on these states can also be partitioned,

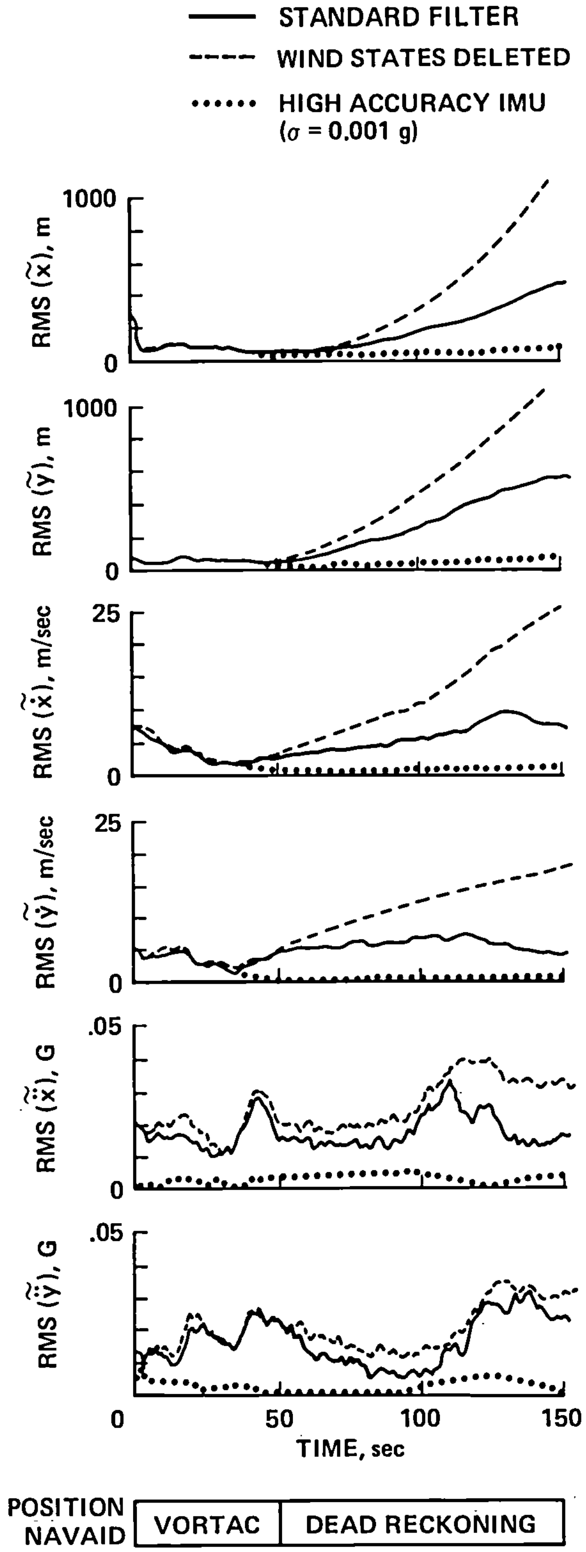

Figure 5.7.- Performance during dead reckoning.

$$y = h_H \tilde{X}_H + h_V \tilde{X}_V + \tilde{Y}$$

and the separation of the navaids can be made, provided the residuals for every navaid depend statistically almost entirely on the error state of one or the other subsystem; that is, if the residuals satisfy

$$E[(h_V \tilde{X}_V)^2] << E[(h_H \tilde{X}_H)^2]$$

or

$$E[(h_V X_V)^2] >> E[(h_H \tilde{X}_H)^2]$$

The gradient vectors for the navaids have been partitioned in this manner in table 3.4, and a review of that table shows that they divide into two sets: residuals for the derived MODILS altitude and altimeters are independent of $\tilde{X}_H$ and residuals for VORTAC, MODILS azimuth and range, and air velocity have only second-order or smaller gradients with respect to the vertical-axis states, compared to their sensitivities to $\tilde{X}_H$. This assumes that the elevation angles, EL_m, EL_t are small: EL_m is always small because of its coverage restrictions (table 2.3) and EL_t can reach high values temporarily on some trajectories. However, the dependence of VORTAC residuals on the vertical position error remains statistically negligible since $\sigma_z << \sigma_x, \sigma_y$.

This separation of navaids degrades the accuracy of both subsystems by neglecting some information on one subsystem while erroneously assigning the entire residual to the error states of the other. The actual accuracy loss was evaluated in simulation tests, using the reference STOL approach trajectory, and was found to be negligible for all states; therefore, the independent filter formulation is adopted in this study.

Accuracy for the states of the vertical axis filter on the straight line test path (fig. 5.1) shows several features. First, baroaltimeter bias accuracy is invariant. This occurs because this bias is unobservable in the absence of altitude measurements from an independent source and will therefore be fixed on any approach until MODILS elevation data are acquired. Second, vertical position error is dominated by the baroaltimeter bias, and the accuracy is the same as for the bias; on sample cases with null bias, position accuracy is the same size as the altimeter noise (1.5 m). Third, vertical velocity accuracy settles rapidly to 0.3 m/sec and does so independently of the random constants of each flight. This is considerably better accuracy than for the horizontal-plane velocity coordinates and results from the following factors: (1) the altitude-measurement bias error is constant and nearly uncorrelated with $\tilde{\dot{z}}$; (2) the position measurement noise is much smaller for the altimeter than for VORTAC; and (3) the vertical acceleration measurement bias is nearly constant and can be accurately estimated from altimeter measurements. Note also that accuracy for all vertical axis states is independent of the position navaid used by the horizontal plane filter. Further, accuracy is insensitive to vertical-axis maneuvering (flares and pitchovers) because of (1) accurate calibration of the vertical acceleration measurement and (2) the low values of $|\ddot{z}|$, below 0.10 g, used in passenger operations. These favorable factors are present on all flightpaths appropriate for passenger operations, and the good, invariant accuracy seen here will be achieved throughout the terminal area. The vertical wind, W_z, is not a filter state; it is unobservable but consists of turbulence only and does not affect accuracy for the vertical-axis inertial motion.

Flightpath Angle and Angle-of-Attack Estimation

Inertial flightpath angle and angle of attack are variables of interest in automatic control systems and can be derived from the estimator's output with an accuracy that depends largely on the performance of the vertical axis filter. Formulas for estimating these angles are

$$\left.\begin{aligned} \hat{\gamma} &= \sin^{-1}(-\hat{\dot{z}}/\hat{V}) \\ \hat{\alpha} &= \sin^{-1}(\langle \hat{\underline{k}}_b, \hat{\underline{i}}_{Pa} \rangle / \cos \hat{\beta}) \end{aligned}\right\} \tag{5.10}$$

and expressions for estimation errors, derived from equation (5.10) are

$$\begin{aligned} \tilde{\gamma} &= \langle \underline{k}_r, \tilde{\underline{V}} \rangle / V + \text{HOT's} \\ \tilde{\alpha} &= \langle \underline{k}_b, \tilde{\underline{i}}_{Pa} \rangle + \langle \tilde{\underline{k}}_b, \underline{i}_{Pa} \rangle \end{aligned}$$

where

$$\left.\begin{aligned} \tilde{\underline{i}}_{Pa} &= -\underline{k}_{Pa}\tilde{\gamma}_a + \underline{i}_{Pa}\tilde{\psi}_{Va} \\ \tilde{\gamma}_a &= -\langle \underline{k}_{Pa}, \tilde{\underline{V}} - \tilde{\underline{W}} \rangle / Va \\ \tilde{\psi}_{Va} &= \langle \underline{j}_{Pa}, \tilde{\underline{V}} - \tilde{\underline{W}} \rangle / Va \\ (\tilde{\underline{k}}_b)_r &= -(\underline{j}_b)_r \tilde{\phi}_g + (\underline{i}_b)_r \cos \phi \tilde{\theta}_g + \begin{pmatrix} \sin \phi \cos \psi - \cos \phi \sin \theta \sin \psi \\ \sin \phi \sin \psi - \cos \phi \sin \theta \cos \psi \\ 0 \end{pmatrix} \tilde{\psi}_g \end{aligned}\right\} \tag{5.11}$$

Expressions for the runway axes components of the vectors $\underline{i}_b, \underline{j}_b, \underline{k}_b, \underline{i}_{Pa}, \underline{j}_{Pa}, \underline{k}_{Pa}$, required to evaluate the inner products above are given by the rows of $T_{br}, T_{P_a r}$ (table 2.2) and can be computed from $\phi, \theta, \psi, V_r, W_r$. The errors $\tilde{\gamma}, \tilde{\alpha}$ depend on $\tilde{V}_r, \tilde{W}_r, \tilde{\phi}_g, \tilde{\theta}_g, \tilde{\psi}_g$; variational expressions derived from equation (5.11), assuming that $\gamma, \theta, \psi_{Va} - \psi$ are small angles, are

$$\left.\begin{aligned} \tilde{\gamma} &= -\frac{\tilde{\dot{z}}}{V} + \text{HOT's} \\ \tilde{\alpha} &= \cos \phi [\tilde{\theta}_g + (\tilde{\dot{z}} - W_z)/Va] + \text{HOT's} \end{aligned}\right\} \tag{5.12}$$

As seen, $\tilde{\gamma}$ depends on $\tilde{\dot{z}}$ and inversely on inertial speed; $\tilde{\alpha}$ has several significant error sources ($\tilde{\theta}_g, \tilde{\dot{z}}, W_z$) and varies inversely with airspeed.

Ensemble averages for $\tilde{\gamma}$ and $\tilde{\alpha}$ on a straight line path are shown in figure 5.8; speed is varied over the approach speed range (60 to 140 knots) during the test, as plotted in the figure. Root-mean-square ($\tilde{\dot{z}}$) is invariant at 0.3 m/sec and rms($\tilde{\gamma}$) varies inversely with speed, as expected, from 0.25° to 0.6°. Results for rms($\tilde{\alpha}$) show the expected dependencies on $\tilde{\theta}_g, W_z, \tilde{\dot{z}}$, and Va; accuracy is much poorer than for γ and varies from 0.7° in favorable conditions (higher speed, no pitch error) to 3° in unfavorable conditions (low speed, large pitch error). The dominant error sources are the unknown turbulence, W_z, with a time average of 0.7 m/sec here, and the VG pitch error. These results imply significant corresponding errors in estimating or

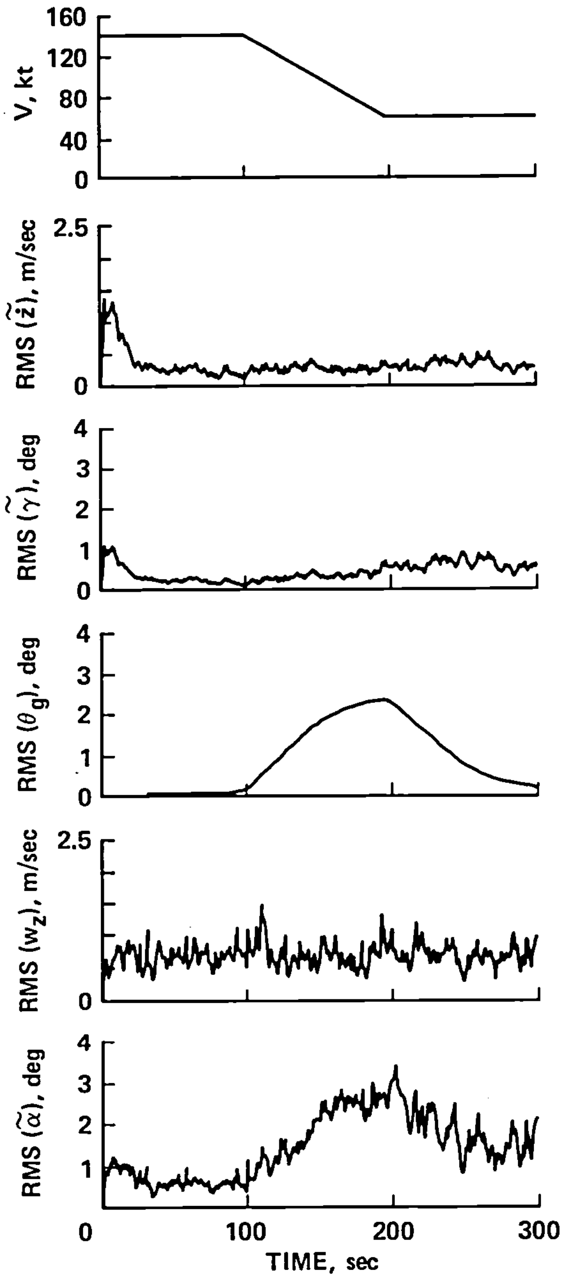

Figure 5.8.- Accuracy of inertial flightpath angle and angle of attack.

controlling lift force directly; for conventional aircraft (1/W)(dL/dα) = C_{L_α}/C_L, and this varied from 0.04 to 0.2 g/deg over the approach speed range for an example aircraft.

Vertical Axis Filter Parameter Values

The performance effects of varying the selected values of the filter's state process noise correlation time can be examined readily for the vertical axis filter. These parameters, $\tau_{\ddot{z}}, \tau_{b_{hb}}$, represent the time scale at which acceleration measurement and altimeter biases are varying. They control the rate at which the accuracies of the estimated biases are assumed by the filter to degrade in the absence of new measurements and the weighting given to information from new measurements relative to the prior information. In the present simulation, the two measurement biases are constant, or nearly so, and the filter is easily matched to the simulation model by selecting the same correlation times as in table 3.2 ($\tau_{\ddot{z}}, \tau_{hb} = 10^3, 10^4$ sec). The effect of various mismatches of the filter's values from those values are shown in figure 5.9; results for four cases with the following parameter values are given:

Case	$\tau_{\ddot{z}}$	τ_{hb}
1	10^3	10^4
2	20	10^4
3	10^3	50
4	20	50

The figure includes a sample case history along with the theoretical standard deviation from the filter's covariance and the ensemble average. The existing design values (case 1) result in good agreement between theoretical and actual accuracy in both $\tilde{\dot{z}}$ and $\tilde{\ddot{z}}$ and show the best transient and steady state performance of the four cases. If $\tau_{\ddot{z}}$ is reduced (case 2), excess weight is placed on acceleration biases as the cause of measurement residuals, and the results show the poorest performance among the four cases with degraded theoretical and actual steady state performance, particularly in acceleration. A reduction of τ_{hb} (case 3) reduces the capacity of the altimeter measurements to calibrate the acceleration bias and the results show degraded theoretical transient response but retain good actual steady state accuracy. Finally, case 4 has reduced values for both correlation times; the filter predicts poor accuracy for both $\tilde{\dot{z}}$ and $\tilde{\ddot{z}}$, with little capacity to calibrate the acceleration measurement or improve the initial accuracy (if the selected correlation times were accurate it would be pointless to process the measurements in this case). However, the actual accuracy

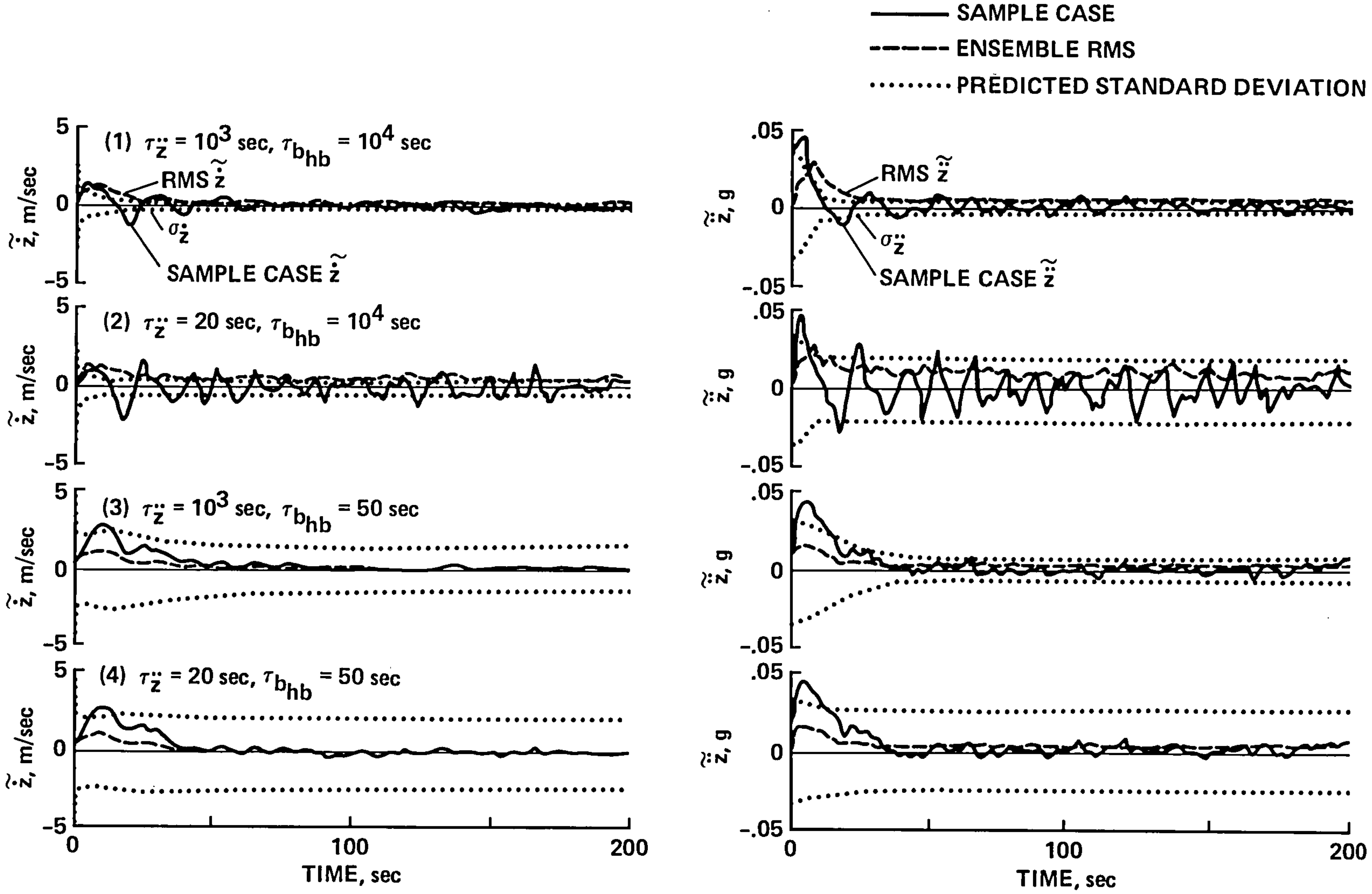

Figure 5.9.- Performance variations with error state noise correlation times: vertical-axis filter.

is similar to that of case 3; transient response is slower than case 1 but the acceleration bias is successfully estimated and steady state accuracy is good.

These data illustrate some significant performance changes with the order of magnitude of errors in the selected values of $\tau_{\ddot{z}}, \tau_{b_{hb}}$. Inaccuracies affect performance in one or more states and can result in reduced transient response and steady state accuracy and in increased disagreement between predicted and actual accuracies. Therefore, if the actual measurement bias processes differ significantly from the simulated ones, parameter adjustments based on recorded flight data would be useful in optimizing filter accuracy.

Summary

Performance details have been studied using simulation results from a straight path near the runway, and other data. Several general conclusions on filter design issues and estimation accuracy trends are indicated.

1. The 14 states can be separated into independent lower-order systems associated with vertical axis motion (4 states) and motion in the horizontal plane (10 states) with negligible loss of estimation accuracy for any state and a large reduction in the required computation time to process a scalar measurement.

2. The wind states and air velocity measurements cannot be separated from the horizontal plane filter into an independent wind filter without a significant loss of accuracy in position, velocity, and wind estimates during VORTAC use and dead reckoning.

3. Selection of parameter values for the state noise and measurement error models is based on simulation tests with realistic models or recorded flight data and is generally aimed at a reasonable fit of the observed state and measurement error variations, at reasonable agreement between Monte Carlo rms errors and the filter's covariance for those states sensitive to the parameter values, and at minimizing the resulting ensemble averages for these states.

4. Horizontal plane position estimation accuracy depends principally on position measurement accuracy; IMU accuracy improvements yield only limited position-accuracy improvements. Before entering MODILS coverage, position accuracy is dominated by VORTAC calibration accuracy. Although information on the VORTAC biases is theoretically available from the IMU and by cross-calibration, it was found that this information was negligible until close to the runway, when passing near the VORTAC station permits range bias calibration to about 60 m by the IMU, and entry to MODILS coverage permits calibration of the VORTAC biases to the accuracy of the MODILS measurements (~15 m). An inertial grade IMU would increase range calibration accuracy when passing close to the VORTAC station and would provide a capacity to calibrate bearing to better than 0.5°, if a turn were executed for this purpose.

5. The accuracy of horizontal plane velocity estimation is sensitive to both position measurement and IMU accuracy; improvements in both types of sensors are required over the present sensors to achieve 1 m/sec accuracy throughout the terminal area. During VORTAC use, lateral velocity is biased proportionally to bearing bias, and noticeable velocity and wind-error transients occur when passing near the VORTAC in samples with larger-than-expected range bias.

6. The accuracy of horizontal plane wind estimation is dominated by inertial velocity estimation accuracy throughout VORTAC use, and rms wind estimation errors are about the same size as the turbulent component of the wind. In addition, crosswind is indistinguishable from sideslip and directional gyroscope error so that crosswind and β are unobservable and β is uncontrollable. Vertical wind and α are also unobservable, and additional sensors are necessary for the observability of α and β, and of the direction of the air velocity vector.

7. Vertical axis inertial motion $(\tilde{z},\tilde{\dot{z}},\tilde{\ddot{z}})$ is generally estimated to much greater accuracy than the horizontal plane motion (30 m, 0.3 m/sec, less than 0.01 g). This accuracy or better is achieved throughout the terminal area.

8. In dead reckoning, airspeed measurements stabilize the velocity estimation error, but rms position error rates of 5 m/sec can occur on maneuvering flightpath segments, and significant maneuvering to return to the reference path is required after 100 sec of dead reckoning. An inertial grade IMU would provide at least an order of magnitude improvement.

6. ESTIMATION ACCURACY ON A V/STOL APPROACH

Accuracy during the reference STOL approach trajectory (fig. 2.1) is evaluated in this section. The filter is initialized at approximately the terminal area entry distance (25 n. mi.). Results are shown for the initial 200 sec, to illustrate initial transients, and for the last 500 sec, to illustrate accuracy near the runway and during maneuvering. The results obtained are typical of most approach paths. Accuracy is shown graphically (fig. 6.1) and as a table of values for various points along the approach (table 6.1), and its general behavior for all states of interest in the control is summarized in table 6.2. In addition, a sample case and the ensemble extremes are reviewed to indicate the range of error histories encountered in an approach (fig. 6.2). Scales are changed in these figures where useful for greater resolution. Accuracy is given for the path axis components of the kinematic states; these are useful working axes for an automatic control system, which is assumed decoupled in these axes so that system exitation owing to estimation errors is similarly decoupled.

Measurement Biases and Navaid Selection

Results for the VORTAC biases confirm the conclusions of the previous section: these biases are poorly observable until passing close to the VORTAC station ($500 \text{ sec} < t < 550 \text{ sec}$) at high bearing rates (3°/sec), and favorable IMU accuracy (0.01 g) results in range bias calibration to 30 m by the IMU. Bearing bias is very poorly observable until entry to MODILS coverage (at $t = 740$ sec) permits VORTAC calibration to about 20 m and 0.2°. During MODILS coverage, the VORTAC is well calibrated, but its equivalent position fix accuracy remains much poorer than that of MODILS because of signal noise; therefore, VORTAC data processing can be dropped with negligible loss of accuracy. VORTAC processing resumes in the event of a failure of MODILS reception or of exit from MODILS coverage in a missed approach. At these events, both of which occur in practice, the VORTAC calibration is renewed and its good accuracy avoids the maneuvering to a biased position estimate that would arise from large calibration errors.

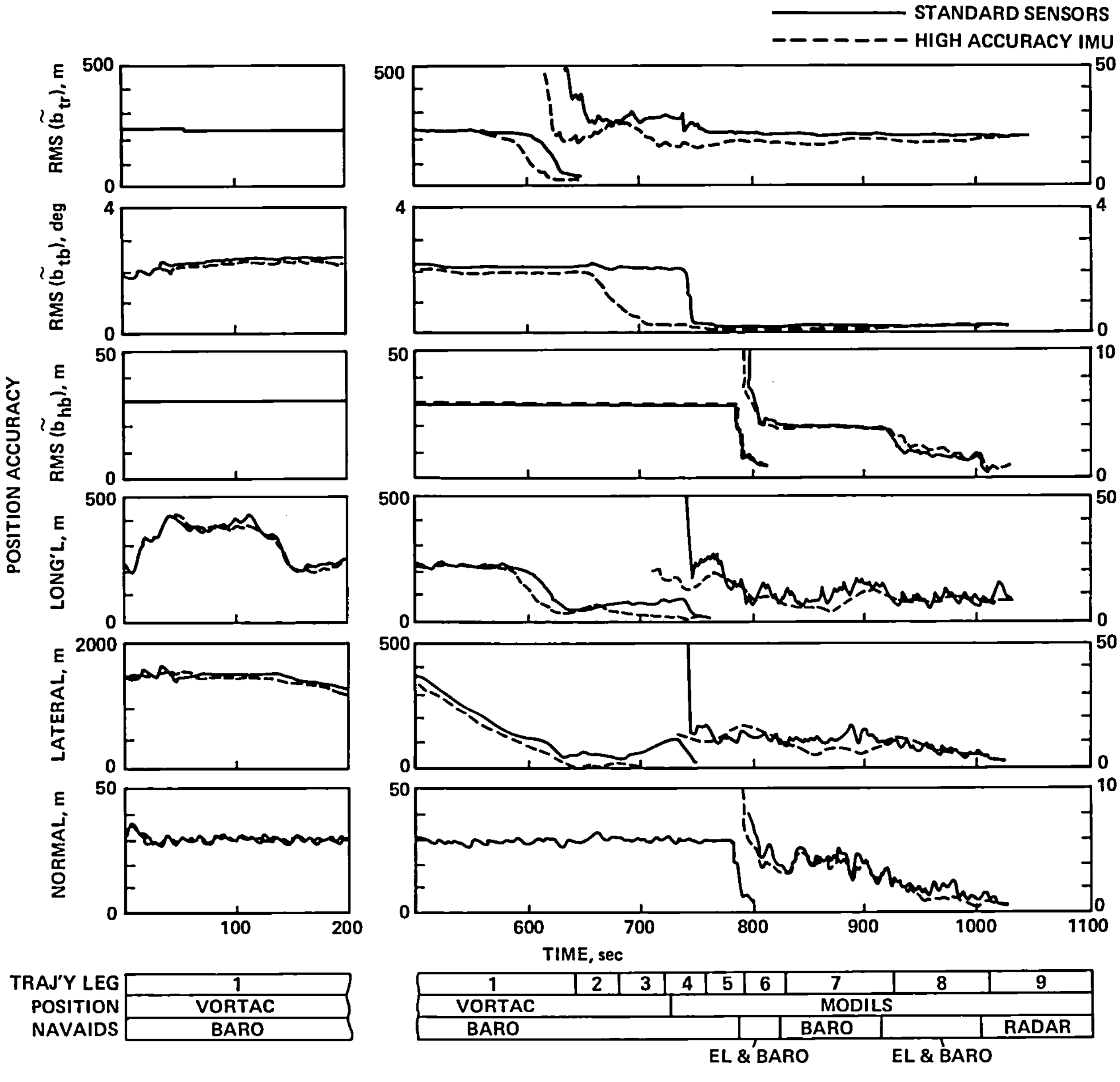

(a) Measurement biases and position.

Figure 6.1.- Estimation accuracy on a STOL approach trajectory.

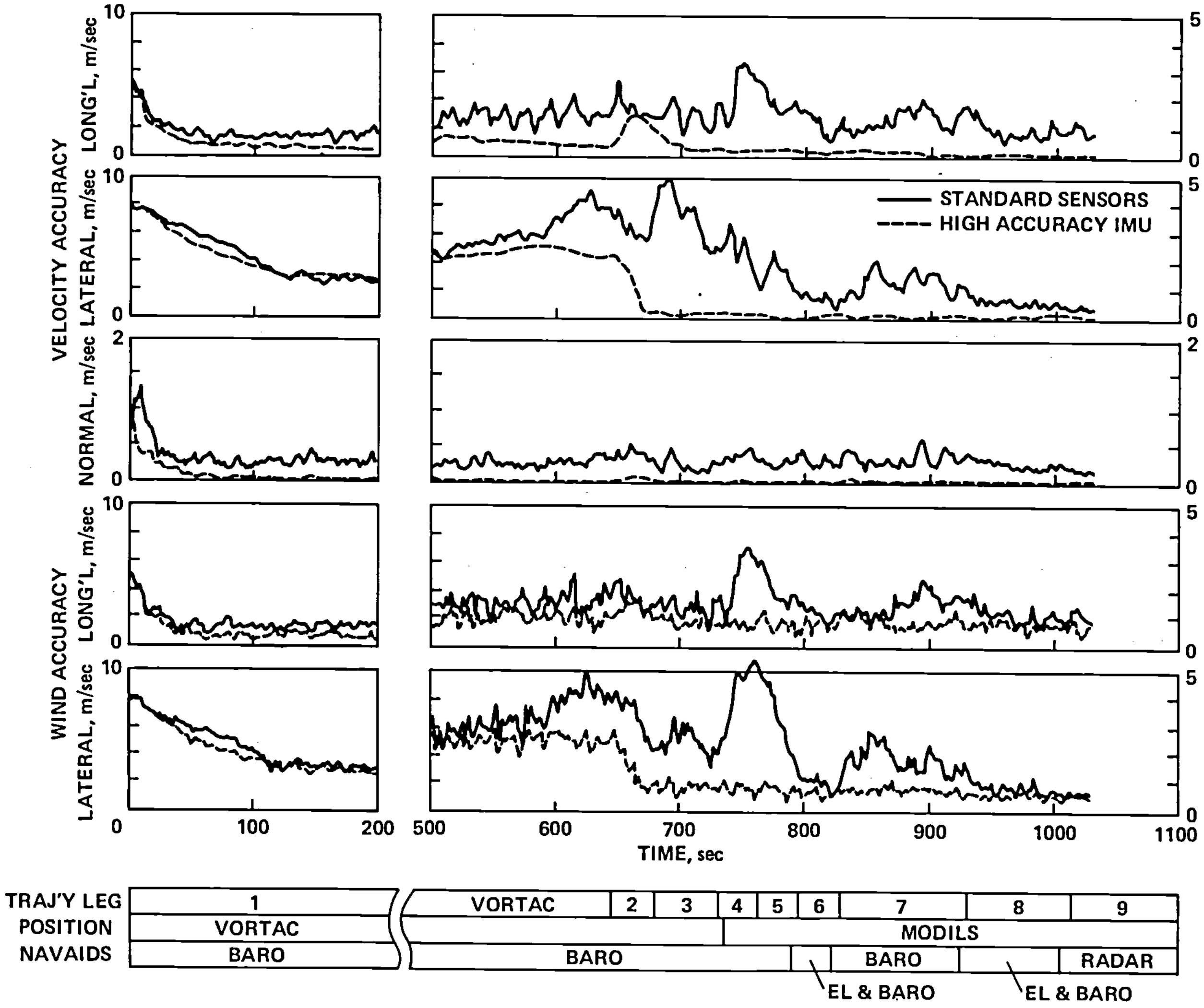

(b) Velocity and winds.

Figure 6.1.- Continued.

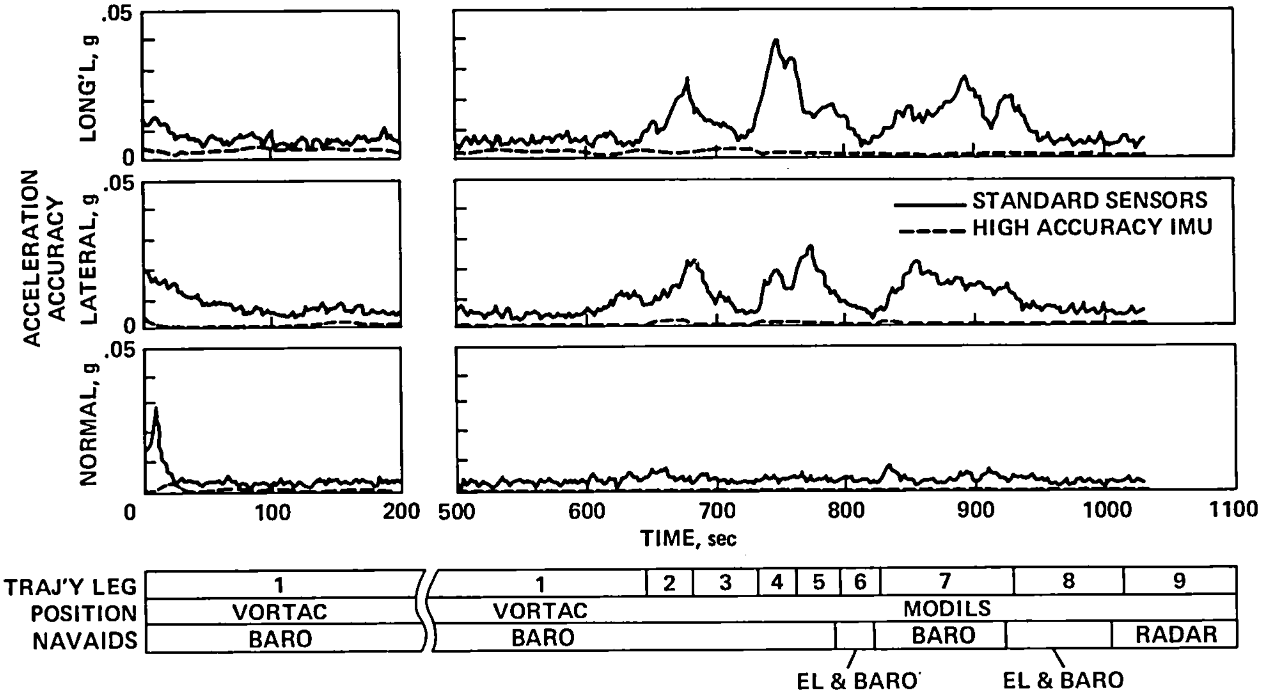

(c) Accelerations.

Figure 6.1.- Concluded.

TABLE 6.1- PERFORMANCE SUMMARY — ENSEMBLE RMS TRANSLATIONAL-STATE ESTIMATION ERRORS ON A STOL APPROACH

	Location on reference trajectory, m			Navaid[a]	Position errors, rms, m			Velocity errors, rms, m/sec			Acceleration errors, rms, g		
	x	y	z		Longi-tudinal	Lateral	Normal	Longi-tudinal	Lateral	Normal	Longi-tudinal	Lateral	Normal
Initialization	629	45730	-1161	V,B	245	1475	27	5.3	7.8	0	0.012	0.021	0.015
First segment	629	31300	-1161	V,B	256	1260	29	1.5	2.6	0.3	.007	.007	.007
First turn entry	629	-915	-1161	V,B	47	55	29	1.8	3.5	.3	.01	.007	.007
First turn exit	-895	-2438	-1036	V,B	75	30	30	1.4	4.0	.3	.019	.022	.006
Second turn entry	-4298	-2438	-1036	V,B	64	115	30	1.4	2.0	.3	.019	.012	.006
Second turn exti	-4298	0	-1036	M,B,E	10	14	5	1.2	1.2	.3	.013	.006	.005
Midhelix	-2807	-2440	-627	M,B	14	12	4	2.0	1.2	.5	.025	.025	.005
Glide slope capture	-2807	0	-318	M,B,E	11	12	3	1.8	1.0	.3	.020	.012	.005
Glide slope	-1500	0	-207	M,B,E	11	8	2.5	1.2	.6	.3	.010	.007	.005
Glide slope	-750	0	-109	M,B,E	10	6	2.5	1.2	.6	.3	.010	.007	.005
Flare start	-236	0	36	M,R	14	4.5	2.5	1.0	.6	.3	.010	.007	.005
Landing zone	≥-100	0	<10	M,R	10	3	1	1.0	.6	.3	.010	.007	.005

[a] V = VORTAC, M = Modils Az and DME, B = Baroaltimeter, E = Modils elevation, R = Radar altimeter.

TABLE 6.2.- SUMMARY OF ESTIMATION ERROR CHARACTERISTICS FOR A TERMINAL-AREA APPROACH TRAJECTORY

State	Error behavior	Significant error sources	Range of rms errors
Position			
Longitudinal	Heading, location dependent; typically piecewise stationary	VORTAC range MODILS range	10-250 m
Lateral	Heading, location dependent; rms typically linear in range	VORTAC bearing, MODILS azimuth	6-1500 m
Normal	Invariant or linear rms	Altimeters, elevation	1-30 m
Velocity			
Longitudinal	Maneuver dependent; stationary in equilibrium flight	Heading, pitch, accelerometers	1.5 to 5 m/sec
Lateral	Maneuver dependent; biased by VORTAC bearing bias	Roll angle, VORTAC biases	0.6 to 5 m/sec
Normal	Stationary		0.3 m/sec
Acceleration			
Longitudinal	Maneuver dependent	Heading, pitch, accelerometers	0.01-0.04 g
Lateral	Maneuver dependent	Roll, accelerometers	0.01-0.03 g
Normal	Stationary		0.005 g
Attitude			
Pitch, roll	Maneuver dependent	VG	to 2°
Heading	Maneuver dependent	DG	to 6°
Wind			
Longitudinal	Contains $\tilde{V}$	$\tilde{V}$	1-4 m/sec
Lateral	Contains $\tilde{V}$, indistinguishable from $\tilde{\beta}$, ψ_g. Slow transient response.	$\tilde{V}, \beta$,DG	1-6 m/sec
Vertical	Not estimated	Unobservable	
System in dead reckoning	Linear position divergence	IMU	Drift to 5 m/sec

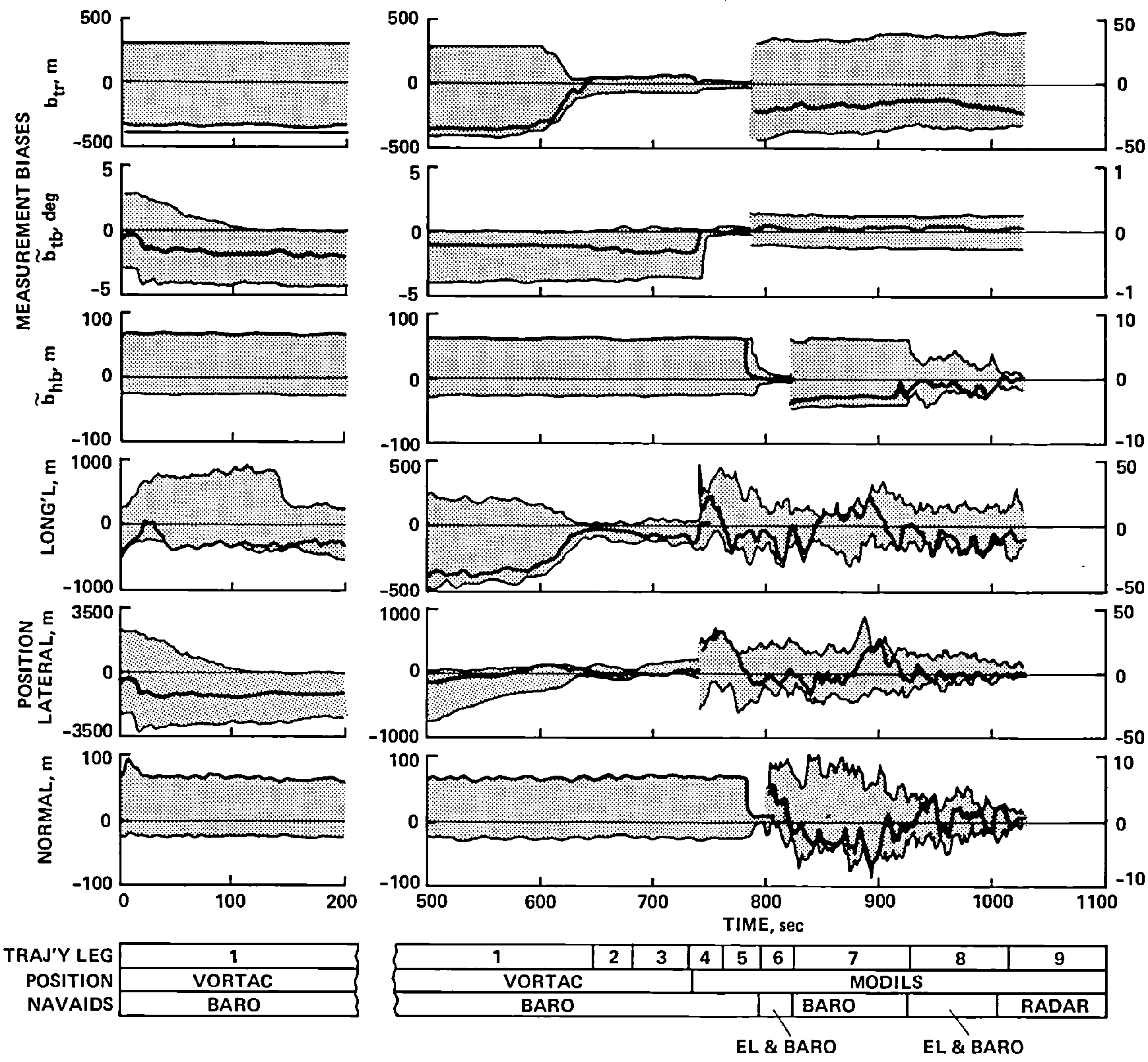

(a) Measurement biases and positions.

Figure 6.2.- Sample case and extreme estimation errors.

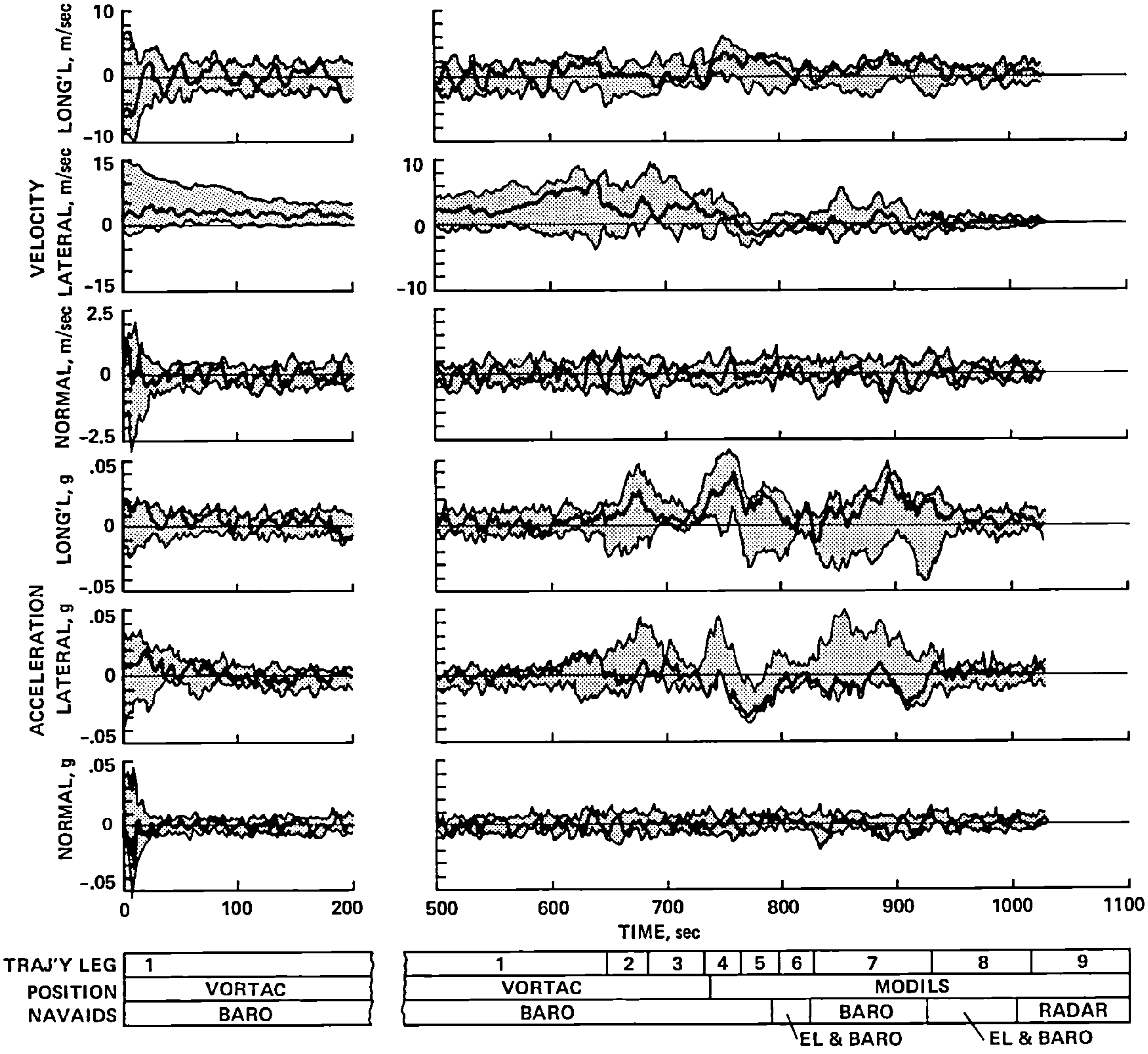

(b) Velocity and acceleration.

Figure 6.2.- Concluded.

The baroaltimeter bias is unobservable in the absence of an independent altitude measurement, so that the bias error is stationary at 30-m accuracy until the nearly unbiased elevation data become available in midturn (at $t = 785$ sec) and improves calibration accuracy an order of magnitude to 3 m. Subsequently, elevation data drops out temporarily in the helix (825 sec < t < 925 sec) because of heading limits on signal reception, but reception resumes near the start of the glide slope, after which the derived altitude measurement accuracy of the elevation data and the corresponding baroaltimeter calibration improves and reaches 1 m at landing.

Baroaltimeter data are processed throughout the approach up to the landing zone, whether or not elevation data are available because the baroaltimeter measurement has lower noise standard deviation ($\sigma_V = 1.5$ m) than the derived elevation altitude (6.5 m at entry to elevation coverage on the present test path) and yields a more accurate vertical velocity estimate than do elevation data alone. This is readily demonstrated in simulation tests (not shown). Conversely, elevation data are nearly unbiased and yield a more accurate altitude estimate throughout the coverage of altitude than does the baroaltimeter; results for the remaining states of the vertical axis filter show that this is the principal benefit of processing elevation data.

The baroaltimeter bias is constant in the present simulation model so that no loss of calibration accuracy occurs in figure 6.1, once the calibrating signal is lost. However, this result is optimistic; flight data show a significant variation in baroaltimeter bias with altitude over the altitude range of this test so that the altimeter calibration cannot be maintained in practice, following the loss of the calibrating signal. Additional effects are that (1) altitude estimation accuracy will degrade more rapidly toward its a priori value in the absence of new calibrating data, (2) vertical velocity will degrade slightly on nonlevel paths because the fictitious vertical velocity, $\dot{h}(db_{hb}/dh)$, implied by altimeter bias variations or because of calibration lags on the glide slope, and (3) the appropriate time constant for the filter's baroaltimeter bias process noise model is smaller than that selected here. Some possibilities for improving this situation are (1) redesign of the receiving system to remove the heading restriction on elevation signal reception, and (2) a study of actual baroaltimeter bias errors to determine if a more accurate model would permit on-line determination of their altitude dependence to a useful degree.

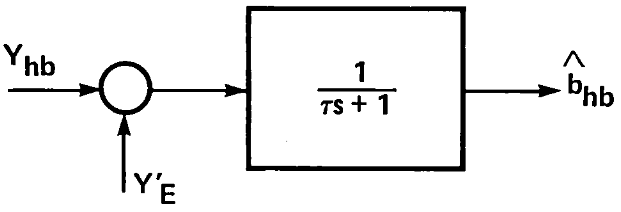

Sketch H

Finally, we note that it is possible to simplify the vertical filter by removing the baroaltimeter bias state to a separate filter where it is calibrated by the elevation data (see sketch H) of an independent baroaltimeter calibration filter. However, this trades a small reduction in the computation time of the complete filter algorithm (about 3%) for some loss in altitude accuracy during elevation coverage. Similar separate filters to calibrate VORTAC biases from MODILS data are also possible, but they result in significant accuracy losses outside MODILS coverage. These devices could, however, be useful in applications in which lower accuracy is acceptable and as a means of adding the capability for on-line calibration to the conventional complementary filter estimator.

Position

Longitudinal accuracy is dominated by range-measurement accuracy for most of the approach, which is nearly along a VORTAC radial until close to the runway, and along a MODILS radial during most of the final segments. This approximate relation is expected to be typical of approach paths for the present antenna sitings. Thus, accuracy (fig. 6.1 and table 6.1) settles to a nearly constant value at 225 m until near the VORTAC station, reaches 30 m at closest approach to the station ($t = 640$ sec), and further improves to 10 m after entry to MODILS coverage; it then remains there until landing. This accuracy sequence reflects the VORTAC range calibration accuracy history and the invariant MODILS range measurement accuracy. Briefly, longitudinal errors are approximately piecewise stationary and change by more than an order of magnitude during the approach.

Lateral position accuracy depends primarily on the VORTAC bearing and MODILS azimuth accuracies, which results in range dependent lateral position accuracy. Initial accuracy is poor at 1,500 m and drops linearly with range to the MODILS station during the glide slope segment, reaching 3 m at landing. Lateral position accuracy changes by three orders of magnitude during an approach, with periods of approximately linear, step, or invariant behavior.

Normal position accuracy follows the baroaltimeter accuracy closely; it is 30 m until elevation data are available, after which it improves rapidly to 5 m and then declines on the glide slope, reaching 1 m at landing. The accuracy change exceeds one order of magnitude for the approach, with periods of invariant, step, or linear behavior. Finally, it is apparent in figure 6.1 that position accuracy varies widely between the three control axes (errors are nonisotropic), with order-of-magnitude differences in some segments, particularly at entry to the terminal area.

Velocity, Wind, and Acceleration

Initially, longitudinal velocity accuracy settles to a steady state value (1.5 m/sec) in about 30 sec; this repeats the initial accuracy behavior previously seen in the straight-test-path results, because the relevant measurements (range, acceleration, airspeed) and their accuracies are identical. Subsequently, accuracy shows modest excursions to 2 to 4 m/sec in the half turn (legs 4 and 5) and helix (leg 7) and settles to 1 m/sec for the glide slope and landing zone. The excursions can be traced to excursions in $\tilde{\psi}_g$ and corresponding longitudinal acceleration measurement error transients that recur in most samples.

Initially, lateral velocity accuracy settles to 3 m/sec; the settling transient is much slower and the steady state accuracy poorer than for the longitudinal axis as a result of (1) the larger position measurement noise and lack of lateral air velocity information, and (2) the presence of a bias error proportional to the bearing calibration error. During MODILS coverage accuracy improves gradually to 1 m/sec and then shows excursions, because of maneuvering, followed by progressive improvement on the glide slope with improving position and acceleration measurement accuracies, reaching 0.6 m/sec at landing.

Normal axis velocity accuracy settles rapidly to 0.25 to 0.5 m/sec, and this is obtained uniformly throughout the approach independent of location or the availability of elevation data.

Longitudinal wind accuracy is dominated by the inertial velocity error and settles rapidly to 1 to 2 m/sec for most of the approach, with excursions during legs 4, 5, and 7 paralleling those of the inertial velocity. Crosswind accuracy follows the lateral inertial velocity accuracy closely, with excursions resulting from ψ_g excursions superposed (legs 4 and 5, particularly). Thus, the DG error transients during turns appear in both the longitudinal and lateral wind estimates via different routes. Further, the crosswind results are modestly optimistic, since sideslip also appears in its errors, and sideslip dynamics are omitted from the motion simulation.

The acceleration accuracy history is consistent with the conclusions of the previous sections: accuracy exceeds 0.01 g on the unaccelerated segments (throughout the initial straight leg and the glide slope) and for the normal axis over the entire approach, but degrades in maneuvering segments to 0.025 g to 0.04 g for the longitudinal and lateral axes.

Accuracy Summary

The estimation accuracy encountered in this example STOL approach is expected to be typical of most terminal area approach trajectories with similar navaid sitings, both in magnitude and behavior. The empirical results for various points along the approach and the observed trends in error behavior and the principal error sources for all states used in the control are recapitulated in tables 6.1 and 6.2. Table 6.2 indicates that the system of this study is characterized by complex navigation errors along a terminal area approach. Accuracy is best for the normal axis motion, with simple behavior for position and invariant velocity and acceleration accuracy independent of location, maneuvering, and navaid. For the horizontal plane motion, position accuracy tends to be piecewise linear or stationary, with order of magnitude changes along the approach and differences among control axes, and velocity and acceleration accuracy excursions occur during speed changes and turns.

Results with an Inertial Grade IMU

Figure 6.1 includes a comparison of results for the present system with accuracies achieved using an inertial grade IMU (0.001 g, 0.01° accuracy for acceleration and attitude measurements, respectively) in order to show the performance improvements and its limitations from this sensor improvement. The results show a somewhat earlier and more accurate calibration of the VORTAC range when passing near the VORTAC station and exhibits the capacity of a sufficiently accurate IMU to calibrate bearing (to 0.2°) during the quarter turn (leg 2). The position accuracy shows no important gains, but we note from earlier analyses that (1) a turn executed early in the approach would provide a significant improvement in lateral accuracy throughout VORTAC use from the IMU's calibration of bearing, and (2) position accuracy in dead reckoning would improve to an important degree.

The velocity components show major improvements in accuracy. The velocity error excursions during maneuvering owing to the pendulous attitude gyrodynamics of the standard IMU have been eliminated, and accuracy is well below 1 m/sec for the longitudinal axis over nearly the entire approach and for the lateral axis during MODILS coverage. On the lateral axis, the slow initial settling time cannot be reduced significantly by the improved IMU, nor is the bias caused by bearing calibration error significantly reduced (although it can be by executing a turn early in the approach). On the longitudinal axis, the modest excursion in accuracy during the quarter turn is due to mapping of the remaining lateral velocity bias onto the longitudinal axis as the path axes rotate. Longitudinal wind accuracy is improved to the accuracy of the airspeed measurement nearly everywhere. Crosswind accuracy is also improved by the absence of DG error transients and throughout MODILS coverage; the effect of lateral velocity bias during VORTAC use is unchanged here (but can be nearly eliminated), but the lack of observability of crosswind, sideslip, and vertical wind is unaffected by IMU accuracy.

Sample Case and Ensemble Extreme Errors

Error histories for a sample approach, together with an envelope of extreme errors for the ensemble of 10 approaches, are shown in figure 6.2. Estimation errors are not ergodic; that is, sample case time averages can differ considerably from the ensemble averages. Figure 6.2 provides a view of typical error histories experienced by the control system during an approach and the range of these errors. The ensemble extreme magnitudes are generally twice the rms values for all states at all times; that is, 2σ errors are experienced within 10 approaches in which all random variables are randomly sampled.

The VORTAC range bias error sample follows the behavior of the ensemble average closely; that is, the error is nearly unobservable and constant until passing near the VORTAC station results in an error reduction to 30 m and until a further reduction to 15 m occurs at entry to MODILS coverage. Other samples with significant range bias show the same calibration error behavior. The VORTAC bearing bias error sample shows an initial loss of accuracy by 1° as the filter settles the combined initial lateral velocity error and bearing bias error to a combination that satisfies equation (5.6); subsequently, the error remains constant until MODILS calibrates bearing to 0.1°. The same settling to a combination that satisfies equation (5.6) occurs on all samples after initialization, but the steady state error can be fortuitously reduced as well as increased; one sample showed a reduction from 2° bias error to nearly perfect calibration. The ensemble of 10 bearing bias samples (table 4.1) is significantly skewed from the statistical distribution of b_{tb} and contains only one sample with $b_{tb} > 0$; this sample is the one mentioned immediately above, which settles to zero steady state error, and which defines the unexpected ensemble maximum and nonzero mean extreme seen in figure 6.2(a). Nevertheless, bearing bias is nearly unobservable in this segment of the approach, and a larger ensemble would give the expected invariant extremes and zero ensemble mean value. Corresponding effects appear in the extremes of the lateral position and velocity errors discussed below, and similar effects appear in the baroaltimeter bias and normal position error extremes as a result of skewing of the b_{hb} ensemble. The baroaltimeter bias error is unobservable and constant in the absence of elevation data, as seen in both the sample case and extremes. Otherwise, the extreme magnitude is reduced to 6 m after entry to elevation coverage; this improves to 2.5 m on the glide slope and to 1.5 m at landing, where the radar altimeter is used.

The longitudinal position error sample is biased by the VORTAC range bias initially with smaller variations superposed because of VORTAC noise (these errors are of the order of 50 to 75 m in samples with no range bias). On the glide slope, the sample shows a mean negative value, which results from an unusually large sample value of the MODILS range bias (-12.8 m). Lateral position error sample is initially biased by the VORTAC bearing bias errors; it degrades initially with $\tilde{b}_{tb}$ and then improves linearly with reducing range to the VORTAC. On the glide slope, it is unbiased because of the small sample case MODILS azimuth bias. However, bias is statistically the dominant azimuth error, and in many other samples lateral position error is dominated by a range-dependent bias in proportion to the azimuth signal bias. The normal position error sample is initially dominated by the baroaltimeter bias, with small variations superposed (±5 m) because of altimeter noise. After entering elevation coverage, this error is within ±10 m, a result equally of the altimeter noise and of the remaining bias error, and then improves to ±5 m on the glide slope, where the bias error is much smaller. During the final approach, the ensemble extremes have properties similar to the ensemble averages; that is, they are relatively constant for longitudinal position (±20 m), decrease with distance to the runway for lateral position (±20 m declining to ±5 m), and are ±5 m for normal position, improving to ±1.5 m at landing.

The longitudinal velocity error sample is unbiased and within ±2.5 m/sec on the unaccelerated segments; during maneuvering segments, error excursions are induced by acceleration measurement error excursions, and the extreme magnitude expands to 5 m/sec at several times. The lateral velocity sample is biased by the bearing bias error sample during VORTAC coverage but is unbiased on the glide slope, with extremes declining to ±1 m/sec at landing. The extreme magnitude is about 5 m/sec for most of the approach before the glide slope as a result of the effects of both VORTAC bearing bias errors and maneuver-induced lateral acceleration transients. The normal axis velocity error is stationary and unbiased and remains within 1 m/sec for the entire approach in this and all samples.

As previously noted, acceleration errors are stationary and unbiased for the initial straight segment, on the glide slope, and for the normal axis over the entire approach; in these cases, the sample errors are typical of all samples, and the extreme errors are nearly constant at ±0.01 to ±0.015 g for all axes. During the maneuvering segments, the sample case longitudinal and lateral errors show increased low-frequency excursions, which are reflected in similar excursions or expansions of the ensemble extremes and an increase in the magnitude of the maximum error to 0.05 g at several times.

7. DISCUSSION

This discussion focuses on an evaluation of the adequacy of the present estimation system's accuracy in applications to automatic and IFR operation of an aircraft in the terminal area along an area navigation route to a final approach and landing. One approach to the evaluation is a simulation demonstration that the estimation and control system satisfies the performance criteria on tracking errors and control activity that suffice for system acceptability. However, performance criteria for the flight operations of interest are incompletely known. Some safety criteria are given in FAA publications and other sources; they concern principally position tracking accuracy, which is shown to depend mostly on low-frequency estimation errors. Criteria for ride quality and control activity, which depend principally on higher frequency estimation errors, are undefined. A complete evaluation is, therefore, beyond the scope of this work. Nevertheless, a generic automatic trajectory tracking system (4D) can be introduced into the simulation to determine the trajectory errors and control activity excited by the translational state estimation errors of the present system; moreover, the estimation accuracy required to satisfy the known operational criteria and the filter's ability to meet these can be determined.

Effect of Estimation Errors on the Trajectory Tracking Performance of an Automatic Control System

A simplified generic model of the combined automatic control logic and aircraft is derived in appendix D. This model does not require representation of any details of the aircraft force, moment, and thrust generation processes and suffices to determine the effects of translational state estimation errors on control of the translational degrees of freedom. Additional but independent effects arise from errors in the estimates of other states not considered here but required by the control system, such as those required to control attitude, engine, configuration, and actuator dynamics. Appendix D also contains analytical and simulation results, including transfer functions, frequency response amplitude ratios, and Monte Carlo evaluation of the output statistics along the STOL approach.

Estimates of the translational states are used by the control to estimate the current trajectory tracking errors for feedback to the control laws, as outlined in appendix D. Estimation errors enter the control system through this feedback as differences between the true and estimated tracking errors; those differences excite erroneous control activity and corresponding tracking errors. The estimated path axes tracking errors can be written as

$$\delta\hat{z}_p = T_{pr}(\hat{\psi}_{Va},\hat{\gamma}_a)(zc_r - \hat{z}_r) \tag{7.1}$$

where $\underline{z}$ refers to any of the vectors $\underline{R}$, $\underline{V}$, and $\underline{a}$, and where $\underline{zc}(t)$ is its current commanded value. The feedback control law is decoupled in path axes, and this results in the same decoupling of system response to estimation errors. The error in estimating the feedback quantities is

$$\delta\tilde{z}_p = -T_{pr}\tilde{z}_r + \text{HOT's} \tag{7.2}$$

Here, transformation angle errors introduce only second-order effects. Thus, the effects of estimation errors are defined by the control law acting directly on these errors and the rms estimation errors shown in figure 6.1 are also the rms input disturbances to the control.

The analysis of frequency response amplitude ratios (appendix D) indicates several trends for the steady state response to sinusoidal estimation errors. Position dispersions respond principally to the low-frequency content of $\tilde{R}$, $\tilde{V}$, and $\tilde{a}$, that is, to frequencies below the control bandwidth (given as the natural frequency of the translational transient response dynamics imposed by the feedback control law). Biases in $\tilde{V}$ or $\tilde{a}$ do not appear in the velocity or acceleration dispersions but, instead, are converted by the control into position hang offs which are superposed with any bias in $\tilde{R}$. Velocity dispersions have peak sensitivity to the content of $\tilde{R}$, $\tilde{V}$, and $\tilde{a}$ at the control bandwidth; that is, the control maps velocity estimation errors at this frequency into velocity dispersions of the same amplitude. Control activity can be calculated as the corrective acceleration required to impose the desired transient response on the translational states. For CTOL aircraft this acceleration maps into corresponding engine power, roll angle, and pitch angle activity. It responds to $\tilde{R}$, $\tilde{V}$, and $\tilde{a}$ principally at frequencies at and above the control bandwidth. The system response to estimation errors therefore depends on errors in all three states, $\tilde{R}$, $\tilde{V}$, and $\tilde{a}$ and their distributions on the frequency spectrum relative to the control bandwidth, and on their mutual correlations.

Simulation results for sample case and ensemble rms behavior with the present estimator (appendix D) indicate that position dispersions are predominantly at low frequencies and that rms(δR) and rms($\tilde{R}$) are the same size during most of the approach; however, there are significant excursions of rms(δR) in excess of rms($\tilde{R}$) occurring during turns and in response to large changes in rms($\tilde{R}$), such as the step changes seen at entry to MODILS and elevation coverage. Velocity dispersions are dominated by low-frequency transient variations caused by continual control effort to regulate position tracking errors, combined with the system response to $\tilde{V}$ at frequencies near the control bandwidth. The result is that rms(δV) exceeds rms($\tilde{V}$) by a factor of 1.5 to 2 in most circumstances.

Control activity is principally at frequencies near and above the control bandwidth. Control authority for regulating tracking errors is typically 0.1 g in passenger operations, and it is desirable to limit the control activity owing to estimation errors in order to retain sufficient margin for regulating the effects of turbulence. For a given estimation-error environment, control activity increases with control bandwidth; the bandwidth can be selected for acceptable activity levels. The results, using suitable bandwidths, show rms activity that is roughly uniform over the approach for each axis; bandwidth and rms activity were 0.3 rps and 0.02 g, respectively, for the normal axis and 0.125 rps and 0.04 g for the longitudinal axis. In flight, turbulence maps principally into normal axis acceleration disturbances so that greater estimation accuracy is needed for this axis to achieve sufficient control margin reserve and bandwidth. For the longitudinal and lateral axes it is likely that the estimation errors of the present system are the dominant disturbances. For a given control bandwidth, control activity depends on sensor accuracies; a comparison of activity for VORTAC and MODILS and for IMU's of different accuracies indicates that control activity is dominated by position sensor accuracy when IMU accuracy is good, and is dominated by IMU accuracy when position accuracy is good. Thus, activity depends on both position sensor and IMU accuracies. It was found that an inertial grade IMU, combined with position accuracy equivalent to that of MODILS, was needed to obtain negligible control activity (0.01 g) because of estimation errors at the control bandwidths studied.

Estimation Accuracy Requirements for Terminal Area Operations

Some tracking accuracy criteria for various operations is available from FAA publications and other sources. Corresponding estimation accuracy requirements can be derived from these and compared with the accuracy achieved by the present estimation system. These tracking accuracy criteria generally reflect the position accuracy needed for a sufficiently low risk of collision or unsuccessful landing within the existing or prospective traffic separation standards and runway dimensions. In turn, these separation standards reflect the generally available or expected navigation aid accuracies relevant to the National Airspace System and its users (that is, accuracies corresponding to VOR/DME, ILS localizer or MLS, altimetry, and air data systems).

Table 7.1 summarizes the maximum allowed standard deviations of the system dispersions. Automatic landing requirements for CTOL indicate allowed dispersions of the touchdown point under Category II visibility conditions (ref. 33); those for the Space Shuttle Vehicle (SSV) are for dispersions at the nominal touchdown time on a 45 × 3,050-m runway (ref. 34), and those for STOL operations are estimated assuming a 46 × 610-m runway. The requirements for CTOL Category II automatic approaches were derived from data in reference 35. In addition, criteria for IFR area navigation operations are defined in reference 36. These are compatible with use of existing VOR/DME equipment and conventional altimetry so that it can be assumed that the present system satisfies these operational criteria.

TABLE 7.1- SOME COMPARISONS OF ESTIMATION ACCURACY WITH OPERATIONAL REQUIREMENTS

State	Trajectory-tracking requirements, 1σ					Navigation accuracy requirements, 1σ						Kalmal-filter estimation accuracy, 1σ			MLS	RAINPAL
	Automatic landing			CTOL, Cat. II		Automatic landing				CTOL, Cat. II		Landing zone	CTOL, Cat. II		Cat. IV specification	Landing zone
	CTOL	SSV	STOL	Decision height	At 5 n. mi.	CTOL	SSV	STOL	VTOL	Decision height	At 5 n. mi.		Decision height	At 5 n. mi.		
Position, m																
Longitudinal	229	73	31	*	*	132	42	19	3.8	*	*	10	10	10	6.1	0.9
Lateral	4.1	2.6	12.5	10	5.3	2.4	1.5	1.4	3.8	5.8	31	3	4	25	1.4	1.2
Vertical	*	4.6	*	1.8	13.4	*	2.7	.6	.6	1.1	7.7	0.6	0.6	6	.2	.9
Velocity, m/sec																
Longitudinal	*	3.1	*	1.3	1.3	*	1.8	*	.5	.75	.75	1.0	1.0	1.2		.15
Lateral	*	1.5	*	1.15	*	*	.9	*	.5	.65	*	.6	.6	1.2		.30
Vertical	*	.15	*	*	*	*	.09	.09	.06	*	*	.25	.25	.3		.15

Note: Asterisks indicate that no values were found.

The actual dispersions are usually rationalized as a sum of independent random errors with zero means, and this sum is required to satisfy the above constraints; for example, the position dispersion is of the form

$$\delta R = \sum_i \delta R_i$$

and its standard deviation must not exceed the dispersion criteria, $\sigma^*_{\delta R}$, given in table 7.1:

$$\sigma_{\delta R} = \left(\sum_i \sigma_i^2\right)^{1/2} < \sigma^*_{\delta R} \tag{7.3}$$

A traditional working model for position dispersion (e.g., ref. 36) is that it is the superposition of (1) sensor errors (ground and airborne equipment), (2) navigation and guidance equipment errors (e.g., input data truncation, computation lags, and errors in computing reference trajectory and flight director or control commands), and (3) flight technical errors (e.g., differences between indicated and reference position owing to pilot or control response lags, aircraft dynamics, and external disturbances). A similar and commonly used rationale views the dispersions as the sum of independent errors arising from guidance, navigation, and control subsystems:

$$\delta R = \delta R_G + \tilde{R} + \delta R_C$$

which are allowed to make nearly equal contributions to total dispersion. The navigation error must therefore satisfy

$$\sigma_{\tilde{R}} \leq \sigma^*_{\delta a}/(3)^{1/2} \tag{7.4}$$

and, similarly

$$\sigma_{\tilde{V}} \leq \sigma^*_{\delta V}/(3)^{1/2}$$

Equation (7.4) is used to calculate the required navigation accuracies, which are included in table 7.1, except that values for VTOL landings are taken from reference 37 and assume a 50-m square landing pad.

The estimation accuracy of the present system is also summarized in table 7.1 for comparison with the required estimation accuracy. In the landing zone, the system meets requirements for longitudinal position (except for VTOL landings) and vertical position, but is deficient in lateral position. Lateral velocity requirements for the cases given are very nearly satisfied, but those for vertical velocity are not, and longitudinal velocity accuracy is midway between the VTOL and SSV requirements. The deficient lateral position accuracy is readily improved by relocating the MODILS transmitter or by replacing the MODILS navaid with the more accurate prospective Category III MLS system. Accuracy specifications at the runway threshold for the MLS are listed in table 7.1 (refs. 38 and 39) and are seen to provide sufficient lateral position measurement accuracy for all automatic landing operations noted in table 7.1. The landing zone accuracy is also compared in table 7.1 with the performance achieved in flight tests by the "RAINPAL" Kalman filter estimation system (ref. 3), which used acceleration and position sensors with significantly higher accuracy than the present sensors (an LTN51 inertial grade IMU and three appropriately sited Cubic range transponders). This system yields significantly greater accuracy than the present one for the longitudinal and lateral coordinates and satisfies all automatic landing requirements for these axes. Finally, estimation accuracy on a 3° glide slope is compared with requirements for Category II automatic approaches in table 7.1. The known position and lateral velocity requirements are readily met. The longitudinal velocity requirement applies to airspeed rather than ground velocity and is met by the airspeed sensor, which has an accuracy of 0.6 m/sec.

Criteria for automatically controlled area navigation operations are incompletely known. Position tracking accuracy criteria for area navigation are available; they are designed to accommodate VOR/DME and conventional altimetry and are satisfied by the present estimation system. However, several problems arise from the off-nominal and higher-frequency nominal errors of VOR/DME or TACAN which limit the usefulness of these navaids in support of automatic flight operations. Local experience with these navaids indicates that various types of error abnormalities are likely to occur on an approach, such as (1) extended periods of signal dropout and (2) periods of signal hangup or with noise standard deviation much larger than nominal. Signal dropouts result in dead reckoning, with linear divergence in position estimation and tracking errors at a rate that depends on the duration of dropout and on the IMU accuracy. For example, 90 sec of dropout and 500 m of drift have been experienced in the vicinity of the runway with the present sensor hardware. The possible costs of dropout include a reduction in safety and the maneuvering required to return to the reference path when navaid data are regained. Solutions for this difficulty include sensor changes to an inertial grade IMU or to position navaids with acceptable signal-dropout-duration statistics. Signal hangups pass through the present data rejection logic and result in potentially significant filter output transients at the end of the hangup, with corresponding control activity and tracking error transients. Abnormally noisy data are overweighted by the filter and result in higher-frequency, higher-amplitude velocity estimation errors and related control activity and velocity tracking errors. These errors have their principal effects on ride quality and control activity during automatically controlled flight rather than on position tracking errors. In addition, the results in appendix D indicate that the nominal VOR/DME and TACAN accuracies result in significant longitudinal (in 4D guidance) and lateral control activity because of estimation errors at moderate values of control bandwidth, but that accuracies corresponding to MODILS would reduce this activity to negligible levels when combined with sufficient IMU accuracy.

The satellite-based NAVSTAR Global Positioning System (GPS), which is under development, offers a potential alternative to TACAN and VOR/DME (refs. 40-42). Projected receiver cost is comparable to VOR/DME receivers and the system accommodates both military and civilian users. The accuracy specification for civilian use results in the position fix accuracy (coarse acquisition data) given in the table below.

Error	Standard deviation, m
Bias	15.6
Random	15.9
Total (RSS)	21.9

This accuracy applies to all three axes, is independent of location and heading, and is equivalent to MODILS and MLS accuracy at their coverage boundaries. For the longitudinal and lateral axes this accuracy would significantly increase bandwidth capability and tracking accuracy; it would also reduce control activity, compared to that obtained here with VORTAC, and would provide excellent position data for automatic control globally as well as in terminal area operations.

8. CONCLUSIONS

This report considers the optimization and accuracy of a Kalman filter estimation algorithm for an integrated terminal area navigation system, using sensors and components representative of those expected to be commonly available on aircraft with IFR and RNAV capability.

The goal of the optimization was to minimize computation time requirements while maintaining accuracy near the maximum that could be realized from the given sensors. A feasible Kalman filter algorithm that satisfied this goal was obtained using various effective applications devices, including (1) the square root filter formulation to maintain computational accuracy; (2) exponentially correlated random process models for error states with unknown dynamics to maintain realistic measurement weighting; (3) partitioning the computations for measurement compression and multirate execution to minimize the rate of processing scalar measurements; and (4) the elimination of poorly observable state variables and partitioning the states and measurements for independent filtering to minimize the computation time for processing scalar measurements. For the measurement compression it was found that measurements could be accumulated at 10 Hz, compressed to a single measurement for each data type, and processed at 1 Hz, with only negligible loss of estimation accuracy and an order of magnitude reduction from the required processing rate without measurement compression. The time required to process scalar measurements rises with the cube of the system order. Elimination of poorly observable states minimizes this order, with only negligible loss of accuracy for the retained states; it resulted in a 14-state system. Partitioning exploits the lower execution time of independent, lower-order filters; it resulted in two filters associated with the horizontal-plane motion (10 states) and vertical motion (4 states), with a 60% reduction in execution time and only a negligible loss of accuracy.

The system's accuracy throughout the terminal area, its dependence on sensor accuracy, its effects on automatic trajectory tracking accuracy, and its suitability for terminal area operations were the subjects of extensive simulation study. Results of the study indicate the following conclusions.

Estimation accuracy exhibits complex behavior in the terminal area, including (1) order-of-magnitude differences in position accuracy with control axis at any point on an approach and with location along an approach because of the range-angle nature of the position data; (2) significant accuracy variations in the horizontal plane motion states during maneuvering because of gyroscopic error transients; and (3) indistinguishable crosswind, sideslip, and heading measurement errors. Accuracy is best for the vertical axis motion, which shows simple near-stationary errors, and during the favorable conditions when on the glide slope and in the landing zone.

The filter adds various useful capabilities to those of the sensors alone, including (1) estimation of velocity and wind, (2) improved position and acceleration accuracy through noise smoothing and calibration of measurement biases, and (3) velocity error stabilization in dead reckoning. Significant further improvements do not appear available from further development of the filter formulation but can be obtained from better sensors. In this regard, position accuracy is sensitive principally to position sensor accuracy, velocity to both position and IMU accuracy, acceleration and attitude to gyroscope accuracy, and wind to velocity estimation and heading measurement accuracy and to lateral air velocity or sideslip sensing.

The operational suitability of the estimator depends on the trajectory tracking errors and control activity excited by the estimation errors. Analysis indicates that in an automatic control system these effects depend primarily on the frequency of the errors relative to the control bandwidth: (1) position tracking errors depend on translational state estimation errors at frequencies below the control bandwidth, (2) velocity tracking depends on estimation errors at frequencies around the control bandwidth, and (3) control activity depends on the estimation error spectrum at and above the control bandwidth. Simulation results show (1) that position tracking errors exceed position estimation errors significantly during large changes in position estimation accuracy at navaid switches and during maneuvering but are otherwise the same size as position estimation accuracy; (2) that velocity tracking errors usually exceed velocity estimation errors, except that the control converts velocity estimation biases to position hangoffs; and (3) that control activity tends to be stationary on all axes throughout the approach, is largest for the horizontal plane control, and is sensitive to both position navaid and IMU accuracies.

The estimation system accuracy is satisfactory or marginal relative to safety criteria for various autoland operations (CTOL, STOL, SSV), Category II CTOL approaches, and for CTOL RNAV based on the existing VOR/DME facilities, but is expected to be inadequate for future VTOL operations. Additional criteria for its use in fully automatic control are not available, but this report indicates the available estimation accuracy and its effects on the performance of an automatic (4D) control system for use in future evaluations. These results also indicate that comprehensive and usable improvements in translational state estimation and automatic control for the full terminal area passenger operational envelope are potentially available by replacing VORTAC, accelerometers, and gyroscopes with GPS and a Schuler tuned IMU of sufficient accuracy, and adding air velocity vector sensing.

Ames Research Center
National Aeronautics and Space Administration
Moffett Field, California 94035, October 15, 1982.

APPENDIX A

POSITION FIX ACCURACY

Aircraft position can be calculated from three simultaneous measurements of independent functions of position. These can be represented in this discussion as

$$Y_i = H_i(R_r) + \tilde{Y}_i \qquad i = 1,2,3$$

or, more briefly, as the measurement vector

$$\underline{Y} = \underline{H}(R_r) + \underline{\tilde{Y}} \tag{A1}$$

where the errors, $(\tilde{Y}_i)$, can be assumed independent random variables with zero means.

An estimate or position fix, $\hat{R}_r$, is obtained as the solution of equation (A1), neglecting the noise; that is, $\hat{R}_r$ satisfies

$$\underline{Y} = \underline{H}(\hat{R}_r) \tag{A2}$$

The position fix error is defined by

$$\tilde{R}_r \equiv \hat{R}_r - R_r \tag{A3}$$

The relation between measurement errors and position fix errors is obtained by substituting equation (A3) into (A1), expanding in a Taylor series in $\tilde{R}_r$ to first order, and subtracting equation (A2). This yields

$$\underline{\tilde{Y}} = J(\hat{R}_r)\tilde{R}_r \tag{A4}$$

where

$$J \equiv [\nabla_R \underline{H}]$$

Here, J is the Jacobian matrix of $\underline{H}$ in which the ith row is the position gradient of the ith measurement type, and J is nonsingular, since it was assumed that a solution of equation (A2) existed. In that case, the deterministic relation between position-fix and measurement errors is

$$\tilde{R}_r = J^{-1}\underline{\tilde{Y}} \tag{A5}$$

and the relationship between their statistics can be obtained by applying the expectation operation,

$$E[\tilde{R}_r\tilde{R}_r^T] = J^{-1}E[\underline{\tilde{Y}}\ \underline{\tilde{Y}}^T]J^{-T}$$

Or, more briefly,

$$P_r = J^{-1}QJ^{-T} \tag{A6}$$

where Q is diagonal, since the measurement errors ($\tilde{Y}_i$) are independent,

$$Q = \mathrm{diag}(\sigma_i)$$

and P_r is the covariance matrix of position estimation errors and contains the variances and correlations among $\tilde{x},\tilde{y},\tilde{z}$ which are denoted

$$P_r = \begin{bmatrix} \sigma_x^2 & q_{xy} & q_{xz} \\ q_{xy} & \sigma_y^2 & q_{yz} \\ q_{xz} & q_{yz} & \sigma_z^2 \end{bmatrix}$$

From equation (A6), the diagonal terms of P_r can be given in terms of the elements $\{a_{ij}\}$ of J^{-1}:

$$\left.\begin{aligned} \sigma_x^2 &= a_{11}^2\sigma_1^2 + a_{12}^2\sigma_2^2 + a_{13}^2\sigma_3^2 \\ \sigma_y^2 &= a_{21}^2\sigma_1^2 + a_{22}^2\sigma_2^2 + a_{23}^2\sigma_3^2 \\ \sigma_z^2 &= a_{31}^2\sigma_1^2 + a_{32}^2\sigma_2^2 + a_{33}^2\sigma_3^2 \end{aligned}\right\} \tag{A7}$$

Thus, the matrix $J^{-1}(\hat{R}_r)$ maps measurement errors $\underline{\tilde{Y}}$ into position errors $\tilde{R}_r$. In general this mapping is position-dependent so that position fix accuracy varies with location in the terminal area.

Analogous formulas for the path axes position coordinates can be obtained by recalling that

$$\tilde{R}_p = T_{pr}(\gamma,\psi_V)\tilde{R}_r$$

Equation (A4) then becomes

$$\underline{\tilde{Y}} = J(\hat{R}_r)T_{pr}^T(\gamma,\psi_V)\tilde{R}_p$$

Thus, the Jacobian matrix for these coordinates is defined by

$$J_p \equiv J(\hat{R}_r)T_{pr}^T(\gamma,\psi_v) \tag{A8}$$

This matrix and the resulting position coordinate errors $\tilde{R}_p$ are functions of both location and velocity vector direction, but since T_{pr} is orthogonal, the total position error is unchanged ($|\tilde{R}_p| = |\tilde{R}_r|$). The covariance matrix for $\tilde{R}_p$ is

$$P_p = J_p^{-1}QJ_p^{-T} \tag{A9}$$

The matrices P_r,P_p define the position fix accuracy obtained. In the following analysis, equations (A4), (A6), (A8), and (A9) are used to evaluate the accuracy obtained, using several combinations of measurement types of interest in the terminal area.

POSITION FIX ACCURACY WITH TACAN AND BAROALTIMETER

This set of measurements is relied on for position information everywhere in the terminal area except in the region of MODILS coverage. Their position gradients were derived from the measurement functions listed in table 2.3 and figure 2.2 and results are given in table A1. The Jacobian matrix for these data types is readily assembled from the expressions in table A1, and its inverse is then used in equation (A5) to obtain the following relation between position and measurement errors:

$$\tilde{R}_r = \begin{pmatrix} \cos\psi_t \\ \sin\psi_t \\ 0 \end{pmatrix} \frac{\tilde{Y}_{tr}}{\cos EL_t} + \begin{pmatrix} -\sin\psi_t \\ \cos\psi_t \\ 0 \end{pmatrix} d_{xyt}\tilde{Y}_{tb} + \begin{pmatrix} -\cos\psi_t \tan EL_t \\ -\sin\psi_t \tan EL_t \\ -1 \end{pmatrix} \tilde{Y}_{hb} \qquad \text{(A10)}$$

where ψ_t and EL_t are the heading and elevation of the line of sight to the TACAN station. The contributions of range, bearing, and altimeter errors to position errors have been separated in equation (A10). As seen, the range error contribution lies along the line of sight projected in the ground plane, and it increases with elevation above the TACAN station; the bearing error effect is orthogonal to this in the ground plane and increases with distance from the TACAN; and the altimeter error defines $\tilde{z}$ and contributes some error in the same direction as the range error, which increases with elevation above the TACAN station.

Formulas for estimation error variances are obtained using equations (A7) and (A10):

$$\begin{aligned} \sigma_x^2 &= \cos^2\psi_t\left[\frac{\sigma_{tr}^2}{\cos^2 EL_t} + \tan^2 EL_t\sigma_{hb}^2\right] + (\sin\psi_t\, d_{xyt}\sigma_{tb})^2 \\ \alpha_y^2 &= \sin^2\psi_t\left[\frac{\sigma_{tr}^2}{\cos^2 EL_t} + \tan^2 EL_t\sigma_{hb}^2\right] + (\cos\psi_t\, d_{xyt}\sigma_{tb})^2 \qquad \text{(A11)} \\ \sigma_z &= \sigma_{hb} \end{aligned}$$

and, further, the variance of the total ground plane position error is

$$\sigma_d^2 = \sigma_x^2 + \sigma_y^2 = \left(\frac{\sigma_{tr}}{\cos EL_t}\right)^2 + (d_{xyt}\sigma_{tb})^2 + (\tan EL_t\sigma_{hb})^2$$

The gross horizontal plane accuracy is indicated by σ_d, whose variation with distance is shown in figure A1(a) for a fixed altitude (600 m). Position accuracy improves from 500 m at a distance of 50 km to 75 m at a distance of 2 km. These errors are dominated by biases which may be greater or smaller on any given approach and which result in correspondingly better or poorer measurement accuracy. Results in figure A1 for the cases that (1) all biases are small compared to the remaining errors and (2) all have 3σ values indicate the large range of accuracies possible, depending on the bias sample values. Accuracy for VORTAC varies from 330 m to 1,800 m over the terminal area and is much poorer than that for TACAN.

TABLE A1.- POSITION GRADIENTS FOR TACAN, BAROALTIMETER, AND MODILS MEASUREMENT FUNCTIONS

Measurement	Position gradients				Definitions of auxiliary quantities
	Symbol	$\partial H/\partial x$	$\partial H/\partial y$	$\partial H/\partial z$	
TACAN					$(\Delta x_t, \Delta y_t, \Delta z_t) = (x - x_t,\ y - y_t,\ z - z_t)$
Range	h_{tr}	$\frac{\Delta x_t}{d_t}$ or: $-\cos \psi_t \cos EL_t$	$\frac{\Delta y_t}{d_t}$ $-\sin \psi_t \cos EL_t$	$\frac{\Delta z_t}{d_t}$ $-\sin EL_t$	$d_t = (\Delta x_t^2 + \Delta y_t^2 + \Delta z_t^2)^{1/2}$ $d_{xy_t} = (\Delta x_t^2 + \Delta y_t^2)^{1/2}$
Bearing	h_{tb}	$\frac{\Delta y_t}{d_{xyt}^2}$ or: $\sin \psi_t / d_{xyt}$	$-\frac{\Delta x_t}{d_{xyt}^2}$ $-\cos \psi_t / d_{xyt}$	0 0	$\sin \psi_t = -\Delta y_t / d_{xyt}$ $\cos \psi_t = -\Delta x_t / d_{xyt}$ $\tan EL_t = -\Delta z_t / d_{xyt}$
Baroaltimeter	h_{hb}	0	0	-1	
MODILS					$(\Delta x_m, \Delta y_m, \Delta z_m) = (x - x_m,\ y - y_m,\ z - z_m)$
Range	h_{mr}	$\frac{\Delta x_m}{dm}$ or: $\cos Az \cos EL_m$	$\frac{\Delta y_m}{dm}$ $\cos Az$	$\frac{\Delta z_m}{dm}$ $-\cos Az \sin EL_m$	$d_m = (\Delta x_m^2 + \Delta y_m^2 + \Delta z_m^2)^{1/2}$ $d_{xzm} = (\Delta x_m^2 + \Delta z_m^2)^{1/2}$
Azimuth	h_{ma}	$\frac{\Delta y_m \ \Delta x_m}{d_m^2 \ d_{xzm}}$ or: $\cos Az \cos EL_m / d_m$	$-\frac{d_{xzm}}{d_m^2}$ $-\cos EL_m / d_m$	$\frac{\Delta y_m \ \Delta z_m}{d_m^2 \ d_{xzm}}$ $\sin Az \sin EL_m / d_m$	$\tan Az = -\Delta y_m / d_{xzm}$ $\sin EL_m = -\Delta z_m / d_{xzm}$ $\cos EL_m = -\Delta x_m / d_{xzm}$
Elevation	h_{me}	$\left(\frac{d_{x_1 y}}{d_e} \sin 5° + \frac{z_1 x_1}{d_e d_{x_1 y}}\right) \frac{1}{d_e}$	$\frac{z_1 \ \Delta y_e}{d_e^2 \ d_{x_1 y}}$	$\left[-\frac{d_{x_1 y}}{d_e} \cos 5° + \frac{z_1 x_1}{d_e d_{x_1 y}} \sin 5°\right] \frac{1}{d_e}$	$(\Delta x_e, \Delta y_e, \Delta z_e) = (x - x_e,\ y - y_e,\ z - z_e)$ $x_1 = \Delta x_e \cos 5° + \Delta z_e \sin 5°$ $z_1 = \Delta x_e \sin 5° + \Delta z_e \cos 5°$ $d_e = (\Delta x_e^2 + \Delta y_e^2 + \Delta z_e^2)^{1/2}$ $d_{x_1 y} = (x_1^2 + \Delta y_e^2)^{1/2}$

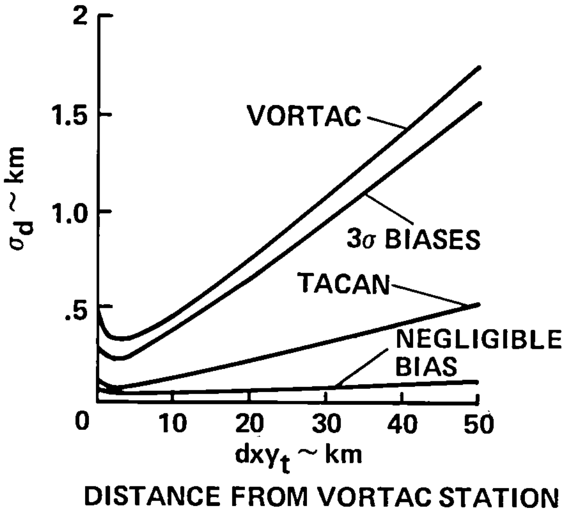

(a) Ground plane position accuracy.

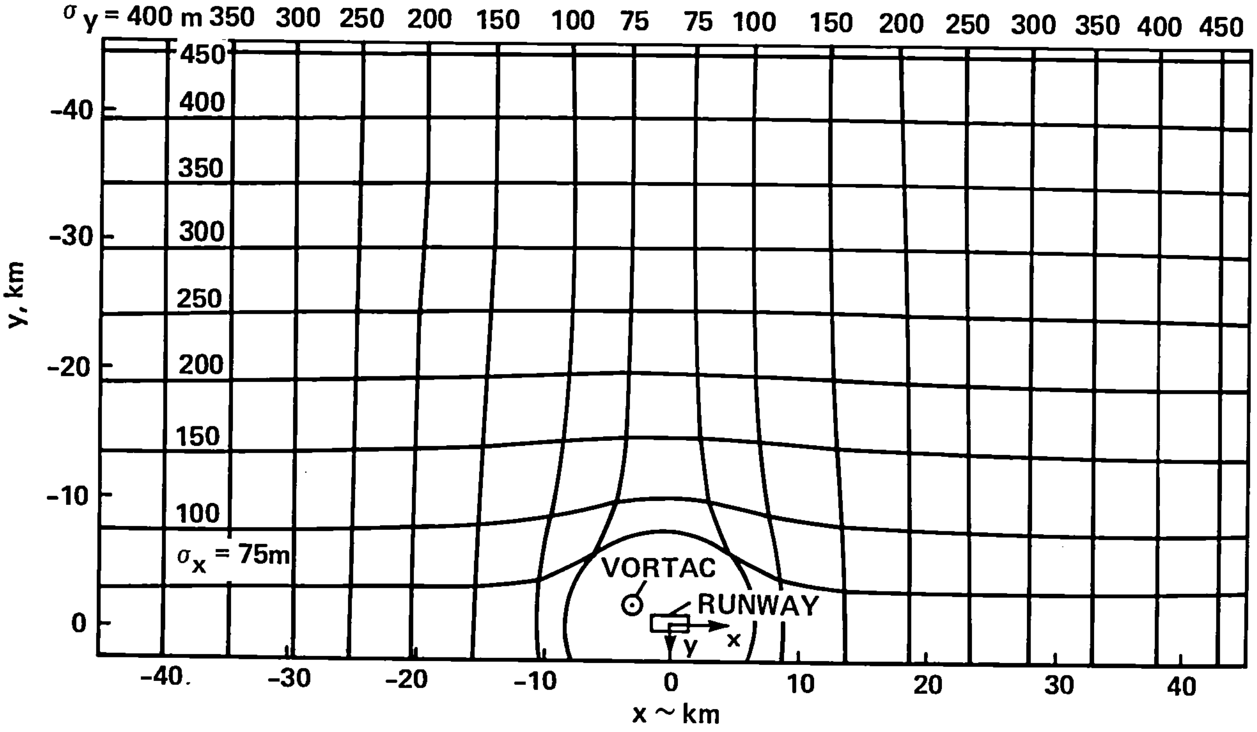

(b) σ_x, σ_y contours in terminal area.

Figure A1.- Position accuracy using TACAN and baroaltimeter measurements (σ_{tr} = 70 m, σ_{tb} = 0.58°, σ_{hb} = 30.5 m, z = -600 m).

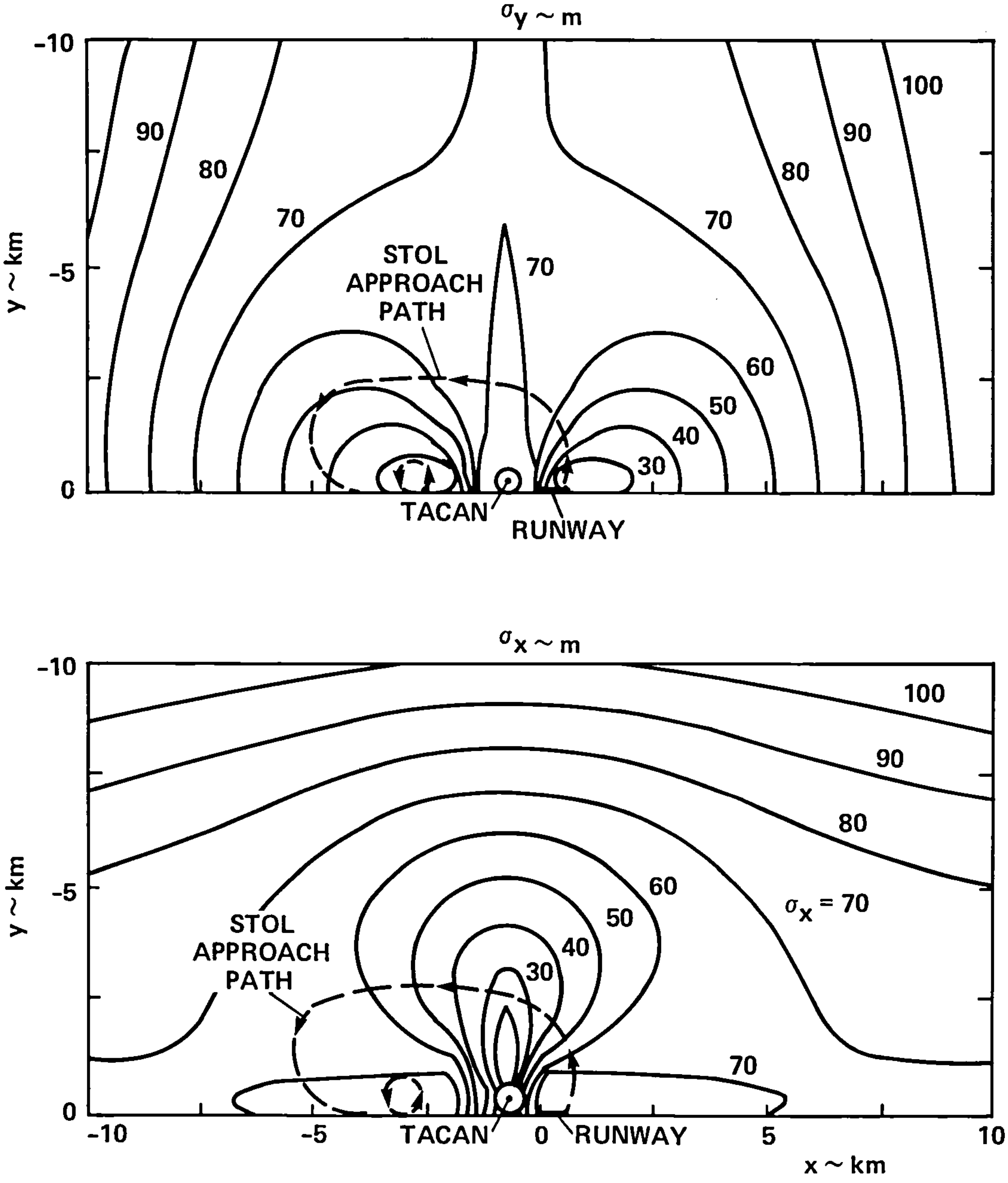

(c) σ_x,σ_y contours near the TACAN site and runway.

Figure A1.- Continued.

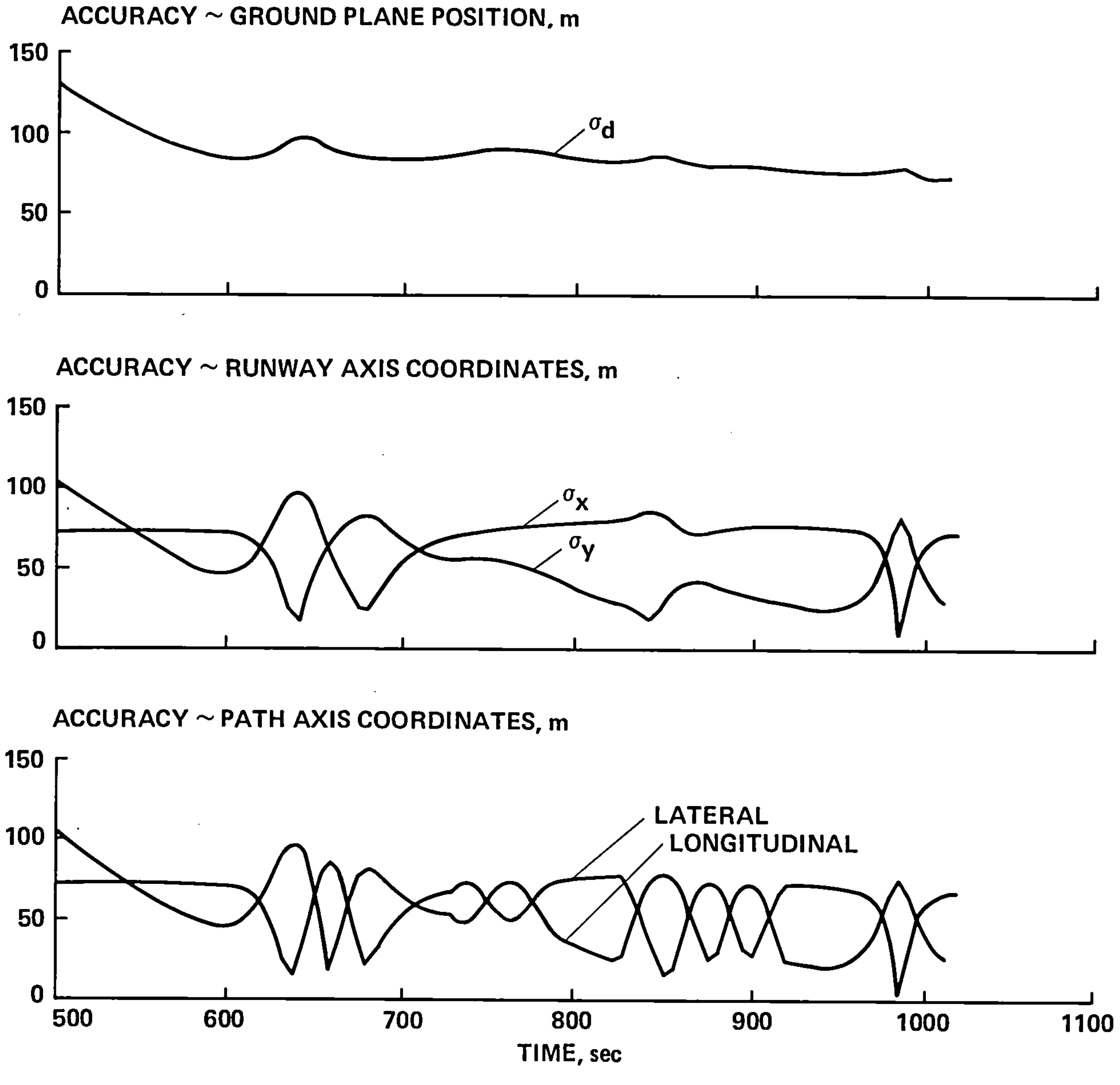

(d) Accuracy along a STOL approach.

Figure A1.- Concluded.

A terminal area map of accuracy for the x,y coordinates (fig. A1(b)) shows the asymptotic behavior at large distances from the station. The contour patterns for both coordinates are symmetric about axes through the TACAN station parallel to the runway x and y axes, and these two patterns are related by a 90° rotation. As seen, σ_x (σ_y) is approximately constant along lines parallel to the x-axis (y-axis) and reaches a minimum of σ_{tr} (70 m) on the TACAN x-axis (y-axis). Contours for σ_x, σ_y in the region close to the runway (fig. A1(c)) show more complex patterns but have the same symmetry and rotation properties noted above. The contours for $\sigma_x, \sigma_y = \sigma_{tr}$ enclose a large region around the runway within which accuracy for both x and y exceeds σ_{tr}. This region contains the final portion of the reference STOL approach shown in the figure. Position accuracy varies with location in the terminal area and differs for the x,y coordinates at a given location so that an approach path flown through these patterns can encounter large variations in the accuracy of the measured coordinates. For example, accuracy time histories for the STOL approach (fig. A1(d)) show nearly constant ground plane position accuracy, σ_d, but the x,y coordinate accuracies show large variations associated with crossings of the TACAN y-axis (these excite the estimator's transient responses), and even greater variability for the path axes coordinates as a result of turns (these excite the control system's transient response).

POSITION ACCURACY WITH MODILS AND BAROALTIMETERS

In this application, four measurements are used to calculate $\hat{R}_r$; $\hat{x}, \hat{y}$ are calculated from barometric altitude and MODILS range and azimuth, and then $\hat{z}$ is computed from $\hat{x}, \hat{y}$, and MODILS elevation. This solution method follows that of reference 14 and allows computation of $\hat{x}, \hat{y}$ independent of the elevation measurement, whose volume of coverage is interior to that of the range azimuth measurements.

The accuracy obtained from this solution method can be computed from the position gradients listed in table A1. First, the Jacobian matrix for the measurements used to compute $\hat{x}, \hat{y}$ is

$$J = \begin{bmatrix} h_{mr} \\ h_{ma} \\ h_{hb} \end{bmatrix} \tag{A12}$$

The relation of $\tilde{x}, \tilde{y}$ to measurement errors is given from the inverse of equation (A12) as

$$\begin{pmatrix} \tilde{x} \\ \tilde{y} \end{pmatrix} = \begin{pmatrix} -\cos Az/\cos EL_m \\ -\sin Az \end{pmatrix} \tilde{Y}_{mr} + \begin{pmatrix} \tan Az/\cos EL_m \\ -1 \end{pmatrix} d_{xzm} \tilde{Y}_{ma} + \begin{pmatrix} \tan EL_m \\ 0 \end{pmatrix} \tilde{Y}_{hb} \tag{A13}$$

where Az and EL_m (aircraft elevation above the azimuth antenna) and d_{xzm} are defined in table A1. At the small azimuth angles for which the MODILS system is in use, the range error contributes principally to $\tilde{x}$, and this increases with elevation; azimuth error contributes principally to $\tilde{y}$, and this grows with distance from the antenna; and the altimeter error appears solely in $\tilde{x}$ and is elevation-dependent. At the low elevations of normal approach paths, the altimeter error has only negligible effect on the accuracy of the ground plane coordinates. The corresponding position error variances are obtained using equations (A7) and (A13):

$$\left.\begin{aligned}
\sigma_x^2 &= \left(\frac{\cos Az}{\cos EL_m}\sigma_{mr}\right)^2 + \left(\frac{\tan Az}{\cos EL_m} d_{xzm}\sigma_{ma}\right)^2 + (\tan EL_m \sigma_{hb})^2 \\
\sigma_y^2 &= (\sin Az \sigma_{mr})^2 + (d_{xzm}\sigma_{ma})^2 \\
q_{xy} &= E[\tilde{x}\tilde{y}] = (\cos^2 Az \sigma_{mr}^2 - d_{xzm}^2\sigma_{ma}^2)\tan Az/\cos EL_m
\end{aligned}\right\} \qquad (A14)$$

The error correlation q_{xy} is included for use below in the analysis of $\tilde{z}$.

Second, $\tilde{z}$ for the solution method defined above is obtained using the MODILS elevation gradient in the expression

$$\tilde{Y}_{me} = \langle h_{me}, \tilde{R}_r \rangle = \alpha_x \tilde{x} + \alpha_y \tilde{y} + \alpha_z \tilde{z}$$

where α_x, α_y, and α_z refer to the elevation-gradient components in table A1. Solving for $\tilde{z}$ yields

$$\tilde{z} = \frac{\tilde{Y}_{me}}{\alpha_z} - \left(\frac{\alpha_x}{\alpha_z}\right)\tilde{x} - \left(\frac{\alpha_y}{\alpha_z}\right)\tilde{y} \qquad (A15)$$

Expressions for $\tilde{x},\tilde{y}$, given by equation (A13), can be substituted into equation (A15) to give $\tilde{z}$ in terms of the independent measurement errors. A simpler computation is provided by forming $E[\tilde{z}^2]$ from equation (A15) to obtain

$$\sigma_z = \left(\frac{d_e\sigma_{me}}{d_e\alpha_z}\right)^2 + \left(\frac{\alpha_x}{\alpha_z}\sigma_x\right)^2 + 2\left(\frac{\alpha_x\alpha_y}{\alpha_z^2}\right)q_{xy} + \left(\frac{\alpha_y}{\alpha_z}\sigma_y\right)^2 \qquad (A16)$$

The distance from the elevation antenna d_e is introduced to analyze the relative magnitudes of the terms in equation (A16); since elevation coverage is restricted to small elevation angles, $d_e\alpha_z$ is of the order of 1, and $(\alpha_x/\alpha_z),(\alpha_y/\alpha_z) << 1$ in this expression. The accuracy therefore depends principally on elevation accuracy and decreases with distance from the antenna site.

Position accuracy was computed from equations (A14), (A16), and (2.7), using the parameter values and MODILS coverage limits given in table 2.3. Accuracy for the x coordinate is nearly constant over the region of coverage and is given by the range error:

$$\sigma_x \cong \sigma_{mr} = 15 \text{ m}$$

The x-coordinate accuracy using TACAN is also nearly constant in this region and is given by the TACAN range error, but is much larger (70 m) so that a large jump in σ_x occurs on entering the MODILS range-azimuth coverage. Maps of σ_y and σ_z over the ground plane are given in figure A2; values outside the MODILS coverage correspond to TACAN-baroaltimeter use. Within the MODILS region, σ_y decreases an order of

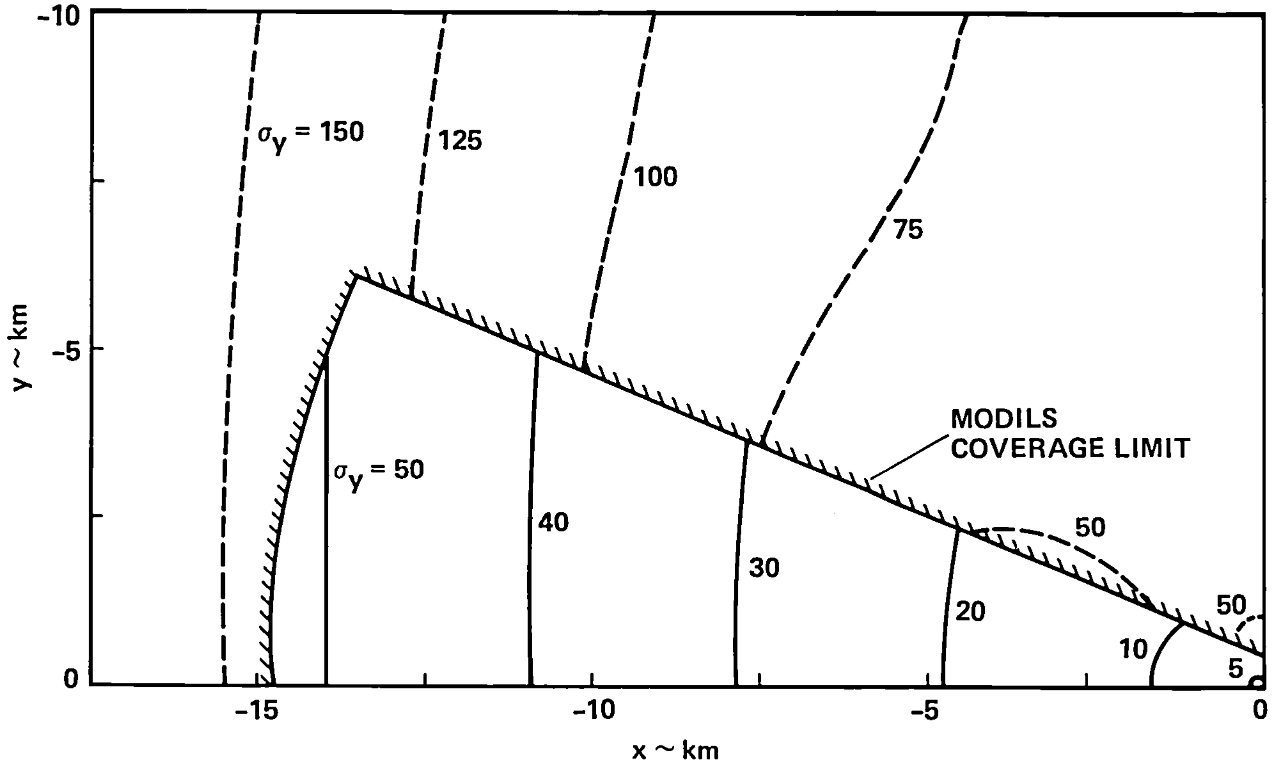

(a) σ_y, m.

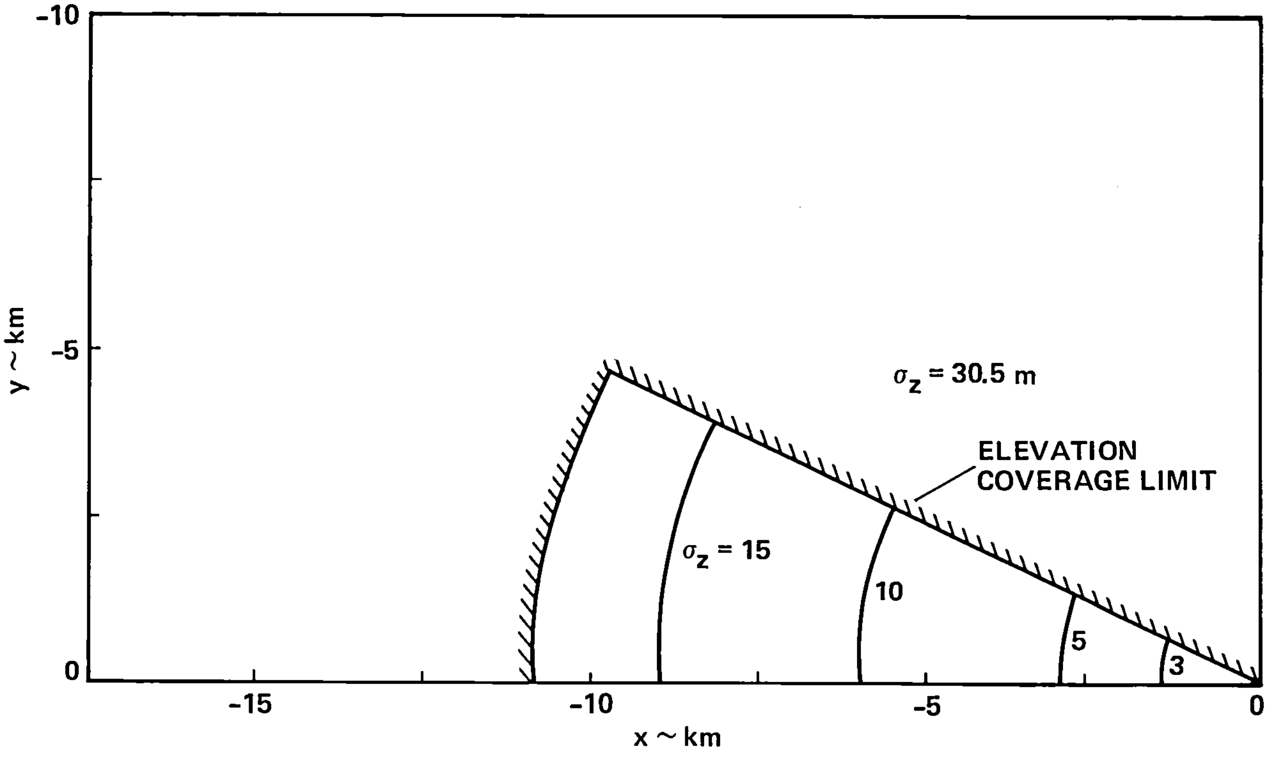

(b) σ_z, m.

Figure A2.- Position-fix accuracy in MODILS coverage region and vicinity: ground-plane map.

magnitude, from 50 m at maximum distance, to 5 m in the landing zone, and this is everywhere better than can be achieved with TACAN. Similar behavior occurs for σ_z in the region of elevation coverage where σ_z decreases from 15 m to 2 m at the runway.

The effects of altitude on accuracy are shown in figure A3 in which the runway centerplane is mapped. σ_z is insensitive to altitude, and σ_y shows some loss of accuracy with altitude or glide slope angle. Outside MODILS coverage, accuracy corresponds to TACAN use; for σ_y, the accuracy contours in this region are complex and include a vertical plane cut of the cone of confusion.

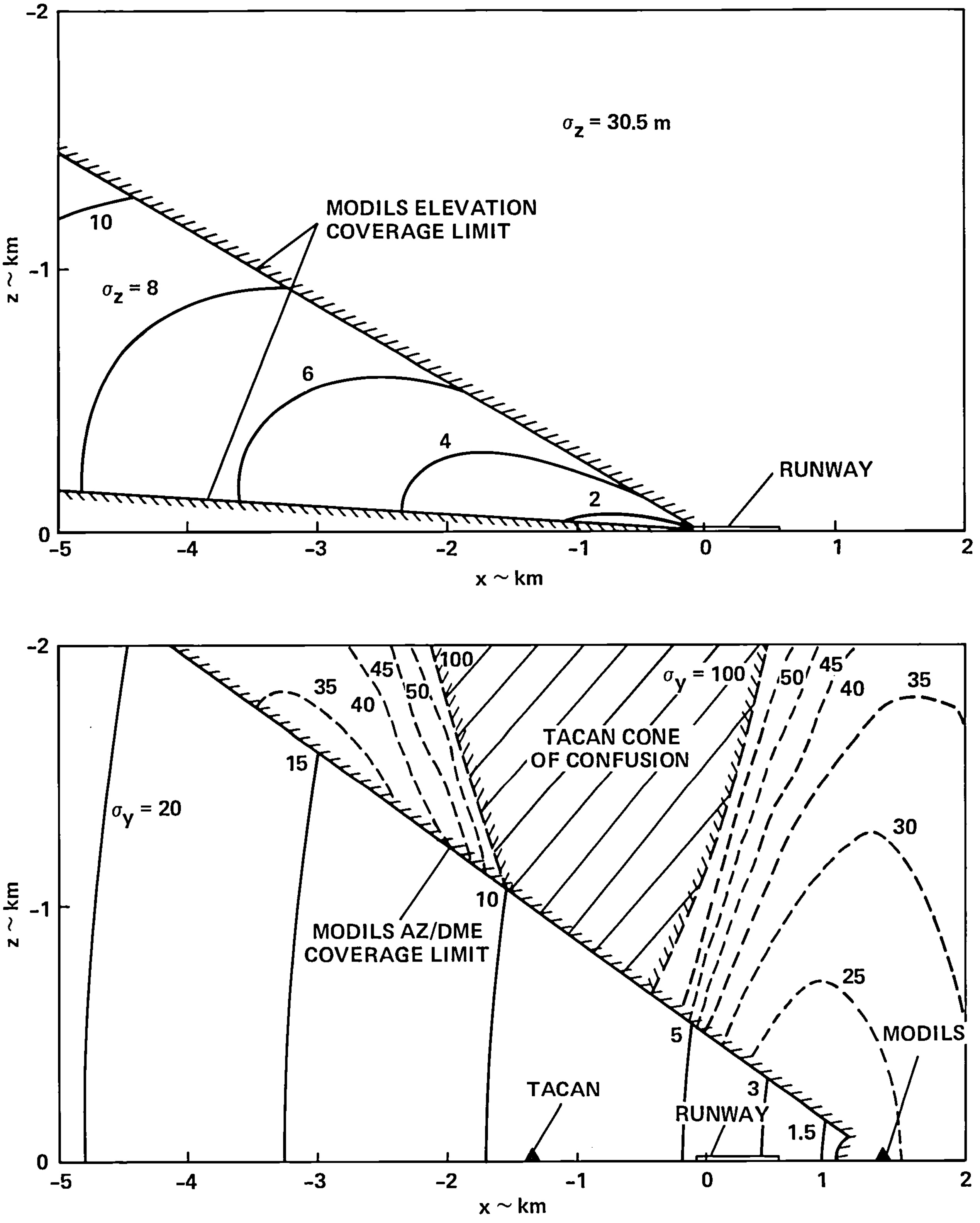

Figure A3.- Position-fix accuracy in MODILS coverage region and vicinity: runway center-plane map.

APPENDIX B

SIMULATION MODELS FOR VERTICAL AND DIRECTIONAL GYROSCOPES

This appendix provides details of the simulation models of the vertical and directional gyroscopes; the models were used to generate attitude measurement errors in this study. The vertical gyroscope has two degrees of freedom, with its outer gimbal axis fixed in the aircraft parallel to the body longitudinal axis and its spin axis controlled to align with the local vertical. Aircraft pitch and roll angles are measured directly as the inner and outer gimbal angles, respectively, and contain errors determined by the misalignment of the spin axis from the local vertical. The misalignment is governed by a dynamic equation and depends on aircraft acceleration and attitude histories. The directional gyroscope has two degrees of freedom, with its outer gimbal axis parallel to the body-normal axis; its spin axis is controlled to align with magnetic north. Heading is measured as the outer gimbal angle and contains errors determined by the aircraft attitude and misalignment of the spin axis from magnetic north. These errors are also deterministic functions of the aircraft motion.

VERTICAL GYROSCOPE

Axis Frames, Orientation Angles, and Transformations

Earth, local vertical, and body-axes systems are the usual orthogonal reference frames; they are illustrated in figures B1 and B2. These frames are denoted F_e, F_v, and F_b and are defined by the unit vectors

$$F_e\colon \{\underline{I},\underline{J},\underline{K}\}$$

$$F_v\colon \{\underline{N},\underline{E},\underline{D}\}$$

$$F_b\colon \{\underline{i}_b,\underline{j}_b,\underline{k}_b\}$$

The transformation from local vertical to body axes coordinates is given by

$$T_{br} \equiv \begin{bmatrix} \cos\theta\cos\psi & \cos\theta\sin\psi & -\sin\theta \\ \sin\phi\sin\theta\cos\psi-\cos\phi\sin\psi & \sin\phi\sin\theta\sin\psi+\cos\phi\cos\psi & \sin\phi\cos\theta \\ \cos\phi\sin\theta\cos\psi+\sin\phi\sin\psi & \cos\phi\sin\theta\sin\psi-\sin\phi\cos\psi & \cos\phi\cos\theta \end{bmatrix} \tag{B1}$$

The vertical gyroscope is mounted in the aircraft with its outer gimbal axis along the body longitudinal axis, $\underline{i}_b$. A gyroscope axis frame is illustrated in figure B3 and is defined as

$$F_g = \{\underline{g}_x,\underline{g}_i,\underline{g}_s\}$$

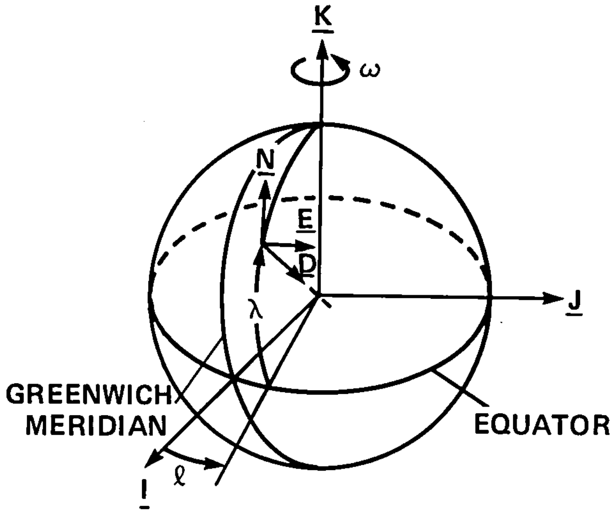

$F_e = \{\underline{I},\underline{J},\underline{K}\}$	Earth axes; Earth centered and rotating with Earth, referenced to equatorial plane and Greenwich meridian
$F_v = \{\underline{N},\underline{E},\underline{D}\}$	local vertical axes; north, east, down, with origin at the gyroscope location given by spherical coordinates (R,ℓ,λ)
R	Earth radius
ℓ	longitude angle
λ	latitude angle
ω	Earth's angular velocity

Figure B1.- Earth and local vertical reference axes.

where $\underline{g}_i$ and $\underline{g}_s$ are the inner gimbal axis and the rotor spin axis of the gyroscope, and $\underline{g}_x$ is orthogonal to the two vectors. This frame is obtained from F_b by successive rotations through the outer gimbal angle, G_o, counterclockwise about $\underline{i}_b$, and through the inner gimbal angle, G_i, counterclockwise about $\underline{g}_i$. The transformation from F_b to F_g is, therefore,

$$T_{gb} = E_2(-G_i)E_1(-G_o) = \begin{bmatrix} \cos G_i & \sin G_i \sin G_o & \sin G_i \cos G_o \\ 0 & \cos G_o & -\sin G_o \\ -\sin G_i & \cos G_i \sin G_o & \cos G_i \cos G_o \end{bmatrix} \qquad \text{(B2)}$$

The spin axis is located in the local vertical frame by angles E and F, shown in figure B3. These angles measure the misalignment of the spin axis from the local vertical. It is useful to construct the misalignment axis frame, F_m, as

$$F_m = \{\underline{i}_m,\underline{j}_m,\underline{g}_s\}$$

which is oriented relative to F_v by angles E and F; from the geometry shown in figure B3, the transformation from F_v to F_m is given by

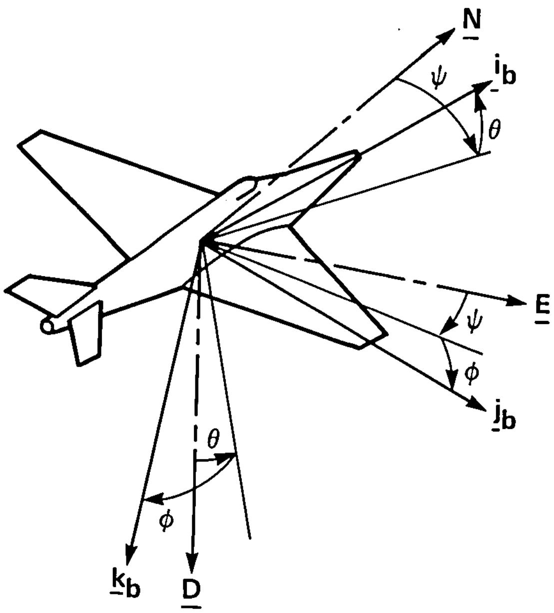

$F_b = \{i_b, j_b, k_b\}$	axis system fixed to the aircraft
ψ	heading; angle from north in the horizontal plane
θ	pitch; angle between $\underline{i}_b$ and the horizontal plane
ϕ	roll; angle of rotation about $\underline{i}_b$ from the horizontal plane to $\underline{j}_b$

Figure B2.- Aircraft body axes and Euler angles.

$$T_{mv} = E_2(F)E_1(E) = \begin{bmatrix} \cos F & \sin F \sin E & -\sin F \cos E \\ 0 & \cos E & \sin E \\ \sin F & -\sin E \cos F & \cos E \cos F \end{bmatrix} \tag{B3}$$

Finally, the gyroscope frame, F_g, can be obtained by a rotation about the spin axis. The required angle is denoted G_s; then,

$$T_{gm} = E_3(G_s) = \begin{bmatrix} \cos G_s & \sin G_s & 0 \\ -\sin G_s & \cos G_s & 0 \\ 0 & 0 & 1 \end{bmatrix} \tag{B4}$$

It is noted here for later use in vector operations that the elements of a transformation between orthogonal reference frames, say from $\{\underline{a}_1, \underline{a}_2, \underline{a}_3\}$ to $\{\underline{b}_1, \underline{b}_2, \underline{b}_3\}$, are the inner products of the unit vectors

$$T_{ab} = \left(\langle \underline{a}_i, \underline{b}_j \rangle\right) \tag{B5}$$

and that the ith row of the T_{ab} expresses the vector $\underline{a_i}$ as a linear combination of the axis vectors of F_b

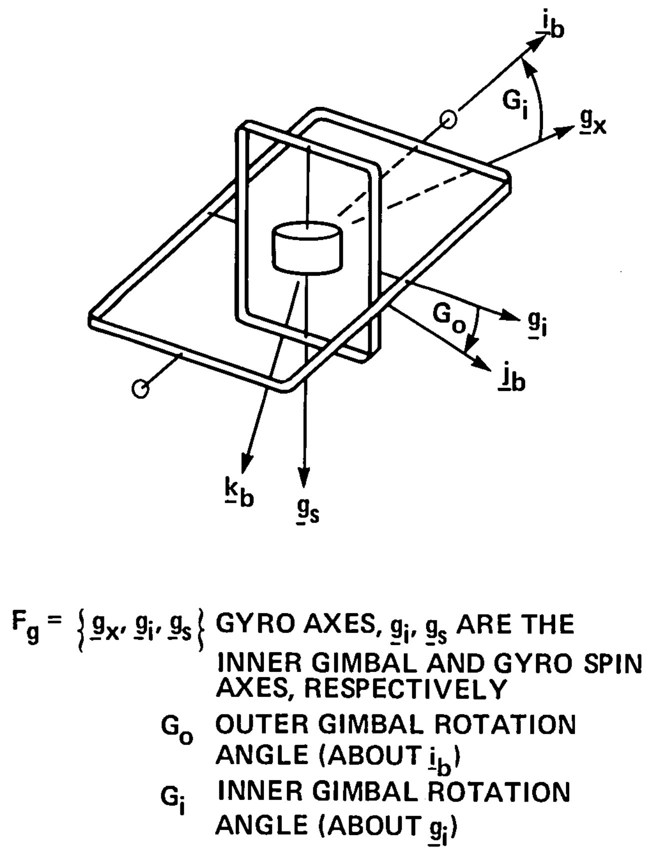

(a) Orientation in aircraft body axes.

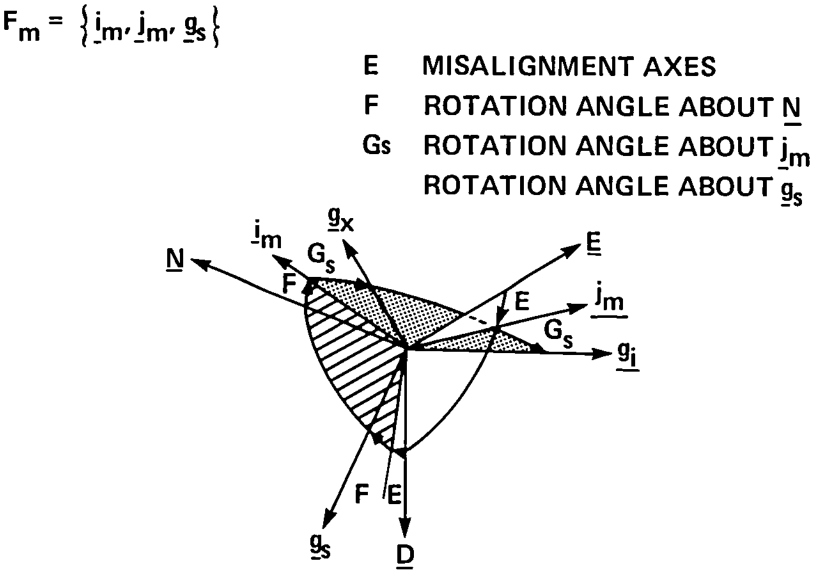

(b) Orientation in local vertical reference frame.

Figure B3.- Vertical gyroscope: axes and orientation angles.

$$\underline{a}_i = \langle \underline{a}_i, \underline{b}_1 \rangle \underline{b}_1 + \langle \underline{a}_i, \underline{b}_2 \rangle \underline{b}_2 + \langle \underline{a}_i, \underline{b}_3 \rangle \underline{b}_3 \tag{B6}$$

Similarly, the jth column of T_{ab} gives $\underline{b}_j$ as a linear combination of $\{\underline{a}_1, \underline{a}_2, \underline{a}_3\}$.

Gimbal Angles

The angles G_o, G_i, and G_s can be expressed in terms of the aircraft attitude angles and spin axis misalignment angles as follows. The transformation T_{gv} can be formed from alternative sets of angles,

$$T_{gv} = T_{gm}(G_s) T_{mv}(E,F) = T_{gb}(G_i, G_o) T_{bv}(\phi, \theta, \psi) \tag{B7}$$

and this can be rearranged as

$$T_{gb}^T(G_i, G_o) T_{gm}(G_s) = T_{bv}(\phi, \theta, \psi) T_{mv}^T(E,F)$$

or

$$E_1(G_o) E_2(G_i) E_3(G_s) = E_1(\phi) E_2(\theta) E_3(\psi) E_1(-E) E_2(-F) \tag{B8}$$

From equation (B8), $\{G_o, G_i, G_s\}$ are identical to $\{\phi, \theta, \psi\}$, respectively, if the spin axis is aligned with the local vertical ($E = F = 0$), and conversely. Solutions are readily obtained after expanding the left-hand side of equation (B8) and using elements of the right-hand side as needed; in an abbreviated form these are

$$\begin{aligned} \tan G_s &= \langle \underline{i}_b, \underline{j}_m \rangle / \langle \underline{i}_b, \underline{i}_m \rangle \\ \sin G_i &= -\langle \underline{i}_b, \underline{g}_s \rangle \\ \tan G_o &= \langle \underline{j}_b, \underline{g}_s \rangle / \langle \underline{k}_b, \underline{g}_s \rangle \end{aligned} \tag{B9}$$

The inner products are readily expanded in terms of ϕ, θ, ψ, E, and F, using the rows of T_{bv}, T_{mv} (eqs. (B1) and (B3)) and equations (B5) and (B6). The results are listed in the simulation equation summary (see table B1).

Misalignment Equation

Equations governing the spin axis misalignment angles can be obtained from the equations governing the forced gyroscope dynamics. These satisfy

$$\underline{p} = \underline{\omega}_{g/I} \otimes \underline{g}_s \tag{B10}$$

where

$\omega_{g/I}$ = angular velocity of F_g relative to inertial space

$\underline{p}$ = torques applied to the gyroscope

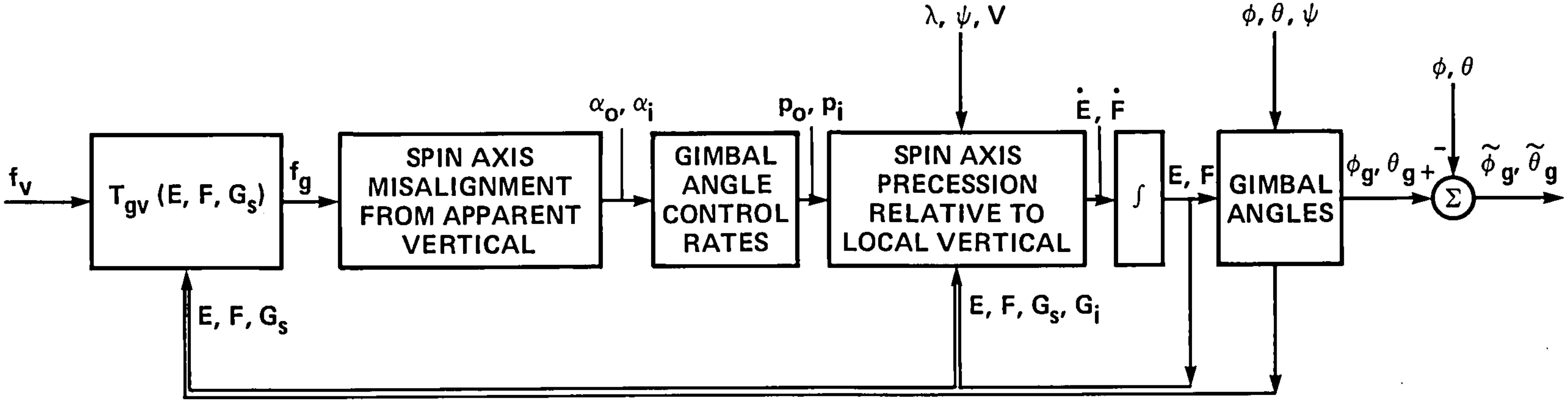

Figure B4.- Simulation of vertical gyroscope: computational flow diagram.

TABLE B1.- SIMULATION OF VERTICAL GYROSCOPE: EQUATION SUMMARY

Total acceleration and spin-axis misalignment from apparent vertical

$$f_v = a_v - g_v$$

$$f_g = \begin{bmatrix} fg_1 \\ fg_2 \\ fg_3 \end{bmatrix} = \begin{bmatrix} \cos G_s \cos F & \sin G_s \cos E + \cos G_s \sin F \sin E & \sin G_s \sin E - \cos G_s \sin F \cos E \\ -\sin G_s \cos F & \cos G_s \cos E - \sin G_s \sin F \sin E & \cos G_s \sin E + \sin G_s \sin F \cos E \\ \sin F & -\cos F \sin E & \cos F \cos E \end{bmatrix} f_v$$

$$\alpha_o = fg_1/|fg_3|$$

$$\alpha_i = fg_2/|fg_3|$$

Gimbal angle control rates, rad/sec

$$P_i = P_E(\alpha_i) + 1.92\times10^{-5}$$

$$P_o = P_E(\alpha_o) + 3.84\times10^{-5}$$

$$P_E = \begin{cases} -5.7596\times10^{-4}\alpha & |\alpha| < 0.017453 \\ 5.7596\times10^{-4} \text{ sign}(\alpha) & |\alpha| \in [0.017453,\ c],\ (c = 0.1047 \text{ for } P_i,\ c = 0.0436 \text{ for } P_o) \\ 0 & |\alpha| > c \end{cases}$$

Spin-axis precession relative to local vertical

$$\begin{bmatrix} \dot{E} \\ \dot{F} \end{bmatrix} = \begin{bmatrix} -\cos G_s/\cos F & -\sin G_s \cos G_i/\cos F \\ -\sin G_s & \cos G_s \cos G_i \end{bmatrix} \begin{bmatrix} P_i \\ P_o \end{bmatrix} + \omega \begin{bmatrix} -(\cos \lambda + \sin \lambda \cos E \tan F) \\ \sin \lambda \sin E \end{bmatrix}$$
$$+ \frac{V}{R} \begin{bmatrix} -\sin \psi(1 + \tan \lambda \cos E \tan F) + \cos \psi \sin E \tan F \\ \sin \psi \tan \lambda \sin E + \cos \psi \cos E \end{bmatrix}$$

Gimbal angles and gyroscope pitch and roll outputs

$$\sin G_i = \cos F \sin E \sin \psi \cos \theta + \cos F \cos E \sin \theta - \sin F \cos \psi \cos \theta \qquad G_i \in \pm \frac{\pi}{2}$$

$$\tan G_o = \frac{\cos E \cos \theta \sin \phi - \sin E(\sin \psi \sin \theta \sin \phi + \cos \psi \cos \phi) + \tan F(\cos \psi \sin \theta \sin \phi - \sin \psi \cos \phi)}{\cos E \cos \theta \cos \phi - \sin E(\sin \psi \sin \theta \cos \phi - \cos \psi \sin \phi) + \tan F(\cos \psi \sin \theta \cos \phi + \sin \psi \sin \phi)} \qquad G_o \in \pm \frac{\pi}{2}$$

$$\phi_g = G_o$$

$$\theta_g = G_i$$

$$\tilde{\phi} = \phi_g - \phi$$

$$\tilde{\theta} = \theta_g - \theta$$

$$\tan G_s = \frac{\cos E \sin \psi \cos \theta + \sin E \sin \theta}{\cos F \cos \psi \cos \theta + \sin F(\sin E \sin \psi \cos \theta + \cos E \sin \theta)}$$

Initialization

$$G_i = \theta + \tilde{\theta}_o$$

$$G_o = \phi + \tilde{\phi}_o$$

$$\sin F = -(\sin G_i \cos \theta - \cos \tilde{\phi}_o \cos G_i \sin \theta)\cos \psi - \sin \tilde{\phi}_o \cos G_i \sin \psi \qquad F \in \pm \frac{\pi}{2}$$

$$\sin E = \frac{(\sin G_i \cos \theta - \cos \tilde{\phi}_o \cos G_i \sin \theta)\sin \psi - \sin \tilde{\phi}_o \cos G_i \cos \psi}{\cos F} \qquad E \in \pm \frac{\pi}{2}$$

$$\tan G_s = \frac{\cos \tilde{\phi}_o \sin \psi + \sin \tilde{\phi}_o \sin \theta \cos \psi}{(\cos G_i \cos \theta + \cos \tilde{\phi}_o \sin G_i \sin \theta)\cos \psi - \sin \tilde{\phi}_o \sin G_i \sin \psi}$$

The torque is expressed as an angular rate (torque per unit angular momentum) in equation (B10) and throughout this appendix. From the geometry of figures B1-B3, the angular velocity can be given as the sum of independent rotational rates,

$$\underline{\omega}_{g/I} = (\omega + \dot{\ell})\underline{K} - \dot{\lambda}\underline{E} + \dot{E}\underline{N} + \dot{F}\underline{j}_m \tag{B11}$$

where $\dot{\ell}, \dot{\lambda}$ are given from the aircraft velocity as

$$\dot{\ell} = V \sin \psi / R \cos \lambda$$

$$\dot{\lambda} = V \cos \psi / R$$

All unit vectors in equation (B11) can be given in terms of the unit vectors defining F_m, using T_{mv} (eqs. (B3) and (B6)) as needed,

$$\underline{N} = \cos F \, \underline{i}_m + \sin F \, \underline{g}_s$$

$$\underline{E} = \sin F \sin E \, \underline{i}_m + \cos E \, \underline{j}_m - \sin E \cos F \, \underline{g}_s$$

$$\begin{aligned} \underline{K} &= \cos \lambda \, \underline{N} - \sin \lambda \, \underline{D} \\ &= (\cos \lambda \cos F + \sin \lambda \sin F \cos E)\underline{i}_m - \sin \lambda \sin F \, \underline{j}_m \\ &\quad + (\cos \lambda \sin F - \sin \lambda \cos E \cos F)\underline{g}_s \end{aligned}$$

and then the cross-products required in equation (B10) are

$$\left.\begin{aligned} \underline{N} \otimes \underline{g}_s &= -\cos F \, \underline{j}_m \\ \underline{E} \otimes \underline{g}_s &= \cos E \, \underline{i}_m - \sin F \sin E \, \underline{j}_m \\ \underline{K} \otimes \underline{g}_s &= -\sin \lambda \sin E \, \underline{i}_m - (\cos \lambda \cos F + \sin \lambda \sin F \cos E)\underline{j}_m \end{aligned}\right\} \tag{B12}$$

Finally, substituting equations (B11) and (B12) into (B10) and taking inner products with the orthogonal vectors $\underline{i}_m, \underline{j}_m$ yields the following equations for the misalignment angles:

$$\left.\begin{aligned} \dot{E} &= -\frac{\langle \underline{p}, \underline{j}_m \rangle}{\cos F} - \omega[\cos \lambda + \sin \lambda \tan F \cos E] \\ &\quad + \frac{V}{R}[-\sin \psi(1 + \tan \lambda \tan F \cos E) + \cos \psi \tan F \sin E] \\ \dot{F} &= \langle \underline{p}, \underline{i}_m \rangle + \omega \sin \lambda \sin E + \frac{V}{R}(\sin \psi \tan \lambda \sin E + \cos \psi \cos E) \end{aligned}\right\} \tag{B13}$$

These equations are integrated in the simulation to obtain E and F, once the control torque $\underline{p}$ is given.

Gyroscope Control Torques

Torque is applied along the inner and outer gimbal axes, and can be written as

$$\underline{p} = p_i \underline{g}_i + p_o \underline{i}_b \tag{B14}$$

Noting that $\underline{i}_b$ can be represented as

$$\underline{i}_b = \cos G_i \underline{g}_x - \sin G_i \underline{g}_s$$

then the inner products required in equation (B11) can be written as

$$\left.\begin{aligned} \langle \underline{p}, \underline{i}_m \rangle &= -p_i \sin G_s + p_o \cos G_i \cos G_s \\ \langle \underline{p}, \underline{j}_m \rangle &= p_i \cos G_s + p_o \cos G_i \sin G_s \end{aligned}\right\} \tag{B15}$$

For both gimbal axes, the applied torque is due to control torques and fixed drifts associated with mass unbalance. These are denoted as

$$\left.\begin{aligned} p_i &= p_{iC} + p_{iD} \\ p_o &= p_{oC} + p_{oD} \end{aligned}\right\} \tag{B16}$$

and suitable drift values are

$$\left.\begin{aligned} p_{iD} &= 0.0011°/\text{sec} \\ p_{oD} &= 0.00225°/\text{sec} \end{aligned}\right\} \tag{B17}$$

The control torques are functions of the misalignment of the spin axis of the gyroscope from the apparent vertical; the misalignment angles are sensed by orthogonally located bubble levels on the rotor case and are given by

$$\left.\begin{aligned} \alpha_o &= \langle \underline{f}, \underline{g}_x \rangle / \langle \underline{f}, \underline{g}_s \rangle \\ \alpha_i &= \langle \underline{f}, \underline{g}_i \rangle / \langle \underline{f}, \underline{g}_s \rangle \end{aligned}\right\} \tag{B18}$$

where $\underline{f}$ is the specific force acting on the gyroscope,

$$\underline{f} = \underline{a} - \underline{g}$$

and its direction is the apparent vertical. The gyroscope axes coordinates of $\underline{f}$ needed to evaluate equation (B18) can be computed from its local vertical axes components, which are available from the aircraft motion simulation, using equations (B3) and (B4):

$$f_g = E_3(G_s) E_2(F) E_1(E) f_v \tag{B19}$$

The misalignment α_o is controlled by precessing the inner gimbal using torque along the outer gimbal axis in accordance with equation (B10). Similarly, α_i is controlled

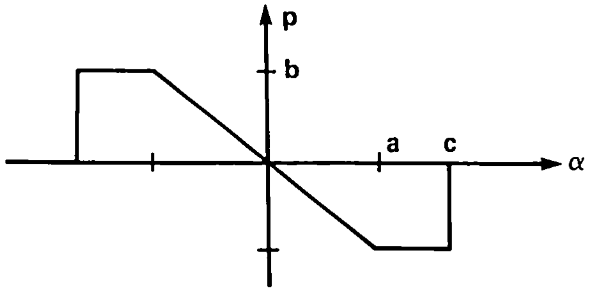

GIMBAL CONTROL LAW

Sketch I

by precessing the outer gimbal, using torque along $\underline{g}_i$. The gimbal control law for both gimbal axes is modeled approximately by the functional form shown in sketch I.

$$p_c(\alpha) = \begin{cases} -(b/a)\alpha & |\alpha| < a \\ -b \ \mathrm{sign}(\alpha) & |\alpha| \in [a,c] \\ 0 & |\alpha| > c \end{cases} \qquad \text{(B20)}$$

where the parameter values are

$a_i = a_o = 1°$

$b_i = b_o = 0.033°/\mathrm{sec}$ = maximum gimbal rates

$c_o = 2.5°$

$c_i = 6°$

The control is linear, with saturation at a maximum gimbal rate of 0.033°/sec and with disengagement at large misalignments from the apparent vertical. In static equilibrium flight, the apparent and local vertical are aligned and the misalignments α_o and α_i remain small and within their cutoff values. During aircraft maneuvering, substantial angles between the two verticals develop, but they develop at a much higher rate (by one to two orders of magnitude) than the maximum gimbal control rates. Thus, for accelerations sufficiently large to exceed the cutoff misalignment (0.05 g longitudinally and 0.1 g laterally) the gyroscope control is disengaged before significant misalignments from the local vertical, E and F, can be developed by the control torques. After disengagement, the gyroscope is uncontrolled about the disengaged axis, but the rate of precession is sufficiently small that very little error develops during typical maneuver durations.

Simulation Summary

The vertical gyroscope can be simulated using equations (B9), (B13), (B16), and (B20), with aircraft accelerations, Euler attitude angles, and latitude as inputs. A computational flow chart is presented in figure B4 and an equation summary for the simulation is given in table B1. The gyroscope can be initialized at nonzero errors, $\tilde{\phi},\tilde{\theta}$, by calculating appropriate initial values for the gimbal and misalignment angles. Formulas for these values were derived from equation (B8) and are included in the equation summary.

DIRECTIONAL GYROSCOPE

Axes and Transformations

The directional gyroscope is mounted in the aircraft with the outer gimbal axis fixed along the body normal axis, $\underline{k}_b$. A gyroscopic axis frame is illustrated in figure B5 and is defined as

$$F_g = \{\underline{g}_s, \underline{g}_i, \underline{g}_z\}$$

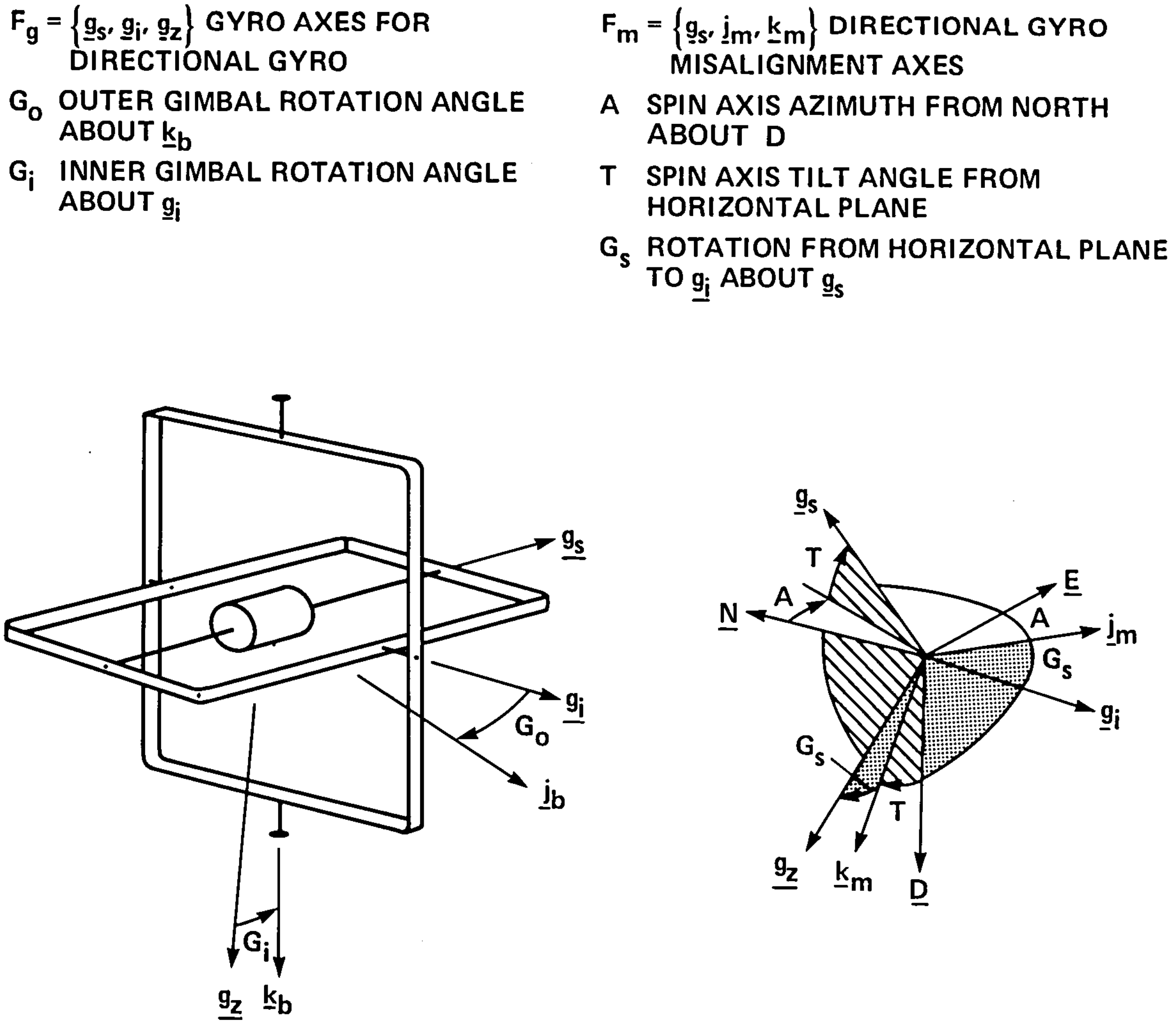

(a) Orientation in body axes.

(b) Orientation in local vertical reference frame.

Figure B5.- Directional gyroscope: axes and orientation angles.

where g_s and g_i are the rotor spin and inner gimbal axes and g_z is orthogonal to these two vectors. This frame is obtained from the body-axes frame, F_b, by successive counterclockwise rotations through G_o about k_b and G_i about g_i (see fig. B5); hence

$$T_{gb} = E_2(-G_i)E_3(-G_o) = \begin{bmatrix} \sin G_i \cos G_o & -\cos G_i \sin G_o & \sin G_i \\ \sin G_o & \cos G_o & 0 \\ -\sin G_i \cos G_o & \sin G_i \sin G_o & \cos G_i \end{bmatrix} \qquad \text{(B21)}$$

The spin axis is located in the local vertical frame by the azimuth (A) and tilt (T) angles shown in figure B5. These angles measure the misalignment of the spin axis from local magnetic north. A misalignment axis frame is defined as

$$F_m = \{\underline{g}_s, \underline{j}_m, \underline{k}_m\}$$

and is oriented relative to F_v by the successive rotations A about $\underline{D}$ and T about $\underline{j}_m$; hence

$$T_{mv} = E_2(T)E_3(A) = \begin{bmatrix} \cos T \cos A & \cos T \sin A & -\sin T \\ -\sin A & \cos A & 0 \\ \sin T \cos A & \sin T \sin A & \cos T \end{bmatrix} \tag{B22}$$

Finally, the gyroscopic frame, F_g, can be obtained from F_m by a rotation G_s about the spin axis which locates $\underline{g}_i$ in the misalignment frame:

$$T_{gm} = E_1(G_s) = \begin{bmatrix} 1 & 0 & 0 \\ 0 & \cos G_s & \sin G_s \\ 0 & -\sin G_s & \cos G_s \end{bmatrix} \tag{B23}$$

Gimbal Angles

Expressions for G_o, G_i, and G_s in terms of aircraft attitudes and spin axis misalignment angles are obtained from the transformation identity

$$T_{gv} = T_{gm}(G_s)T_{mv}(A,T) = T_{gb}(G_i,G_o)T_{bv}(\phi,\theta,\psi)$$

which can be rearranged as

$$E_3(G_o)E_2(G_i)E_1(G_s) = E_1(\phi)E_2(\theta)E_3(\psi)E_3(-A)E_2(-T) \tag{B24}$$

Solutions for G_o, G_i, and G_s are given in the equation summary, table B2. In abbreviated form, these are

$$\begin{aligned} \tan G_o &= -\langle \underline{j}_b, \underline{g}_s \rangle / \langle \underline{i}_b, \underline{g}_s \rangle \\ \sin G_i &= \langle \underline{k}_b, \underline{g}_s \rangle \\ \tan G_s &= -\langle \underline{k}_b, \underline{j}_m \rangle / \langle \underline{k}_b, \underline{k}_m \rangle \end{aligned} \tag{B25}$$

The inner products can be expanded using equations (B1) and (B20). For G_o this gives

$$\tan G_o = \frac{\cos \phi \sin(\psi - A) - \sin \phi \sin \theta \cos(\psi - A) - \tan T \sin \phi \cos \theta}{\cos \theta \cos(\psi - A) + \tan T \sin \theta} \tag{B26}$$

In the case in which ϕ and θ are zero, the measurement error depends only on the azimuth misalignment $G_o = \psi - A$ and is zero if A is nulled. For flight with $\phi = 0$,

TABLE B2.- SIMULATION OF DIRECTIONAL GYROSCOPE: EQUATION SUMMARY

Heading and heading misalignment angles

$$f_g = \begin{bmatrix} f_{g_1} \\ f_{g_2} \\ f_{g_3} \end{bmatrix} = \begin{bmatrix} \cos T \cos A & \cos T \sin A & -\sin T \\ \sin G_s \sin T \cos A - \cos G_s \sin A & \sin G_s \sin T \sin A + \cos G_s \cos A & \sin G_s \cos T \\ \cos G_s \sin T \cos A + \sin G_s \sin A & \cos G_s \sin T \sin A - \sin G_s \cos A & \cos G_s \cos T \end{bmatrix} f_v$$

$$\alpha_o = f_{g_1}/|f_{g_3}|$$

$$\tan \tilde{\psi}_c = \frac{\cos \psi[\sin \psi(\cos \phi - 1) - \tan \gamma_D \sin \phi]}{1 + \sin \psi[\sin \psi(\cos \phi - 1) - \tan \gamma_D \sin \phi]}$$

$$\varepsilon_\psi = \psi + \tilde{\psi}_c - G_o$$

Gimbal angle control rates, rad/sec

$$p_i = p_c(\varepsilon_\psi) + 3.491\times10^{-5}$$

$$p_o = p_c(\alpha_o) + 4.887\times10^{-5} + p_{o_{D_f}}$$

$$p_c(\alpha) = \begin{cases} (b/a)\alpha & |\alpha| \le a \\ b \operatorname{sign}(\alpha) & |\alpha| \ge a \end{cases}$$

$$(a,b) = \begin{cases} (8.73\times10^{-2}, & -1.92\times10^{-3} \text{ rad/sec}) \quad \text{for} \quad p_i \\ (1.745\times10^{-2}, & 8.73\times10^{-4} \text{ rad/sec}) \quad \text{for} \quad p_o \end{cases}$$

$$p_{o_{D_f}} = \begin{cases} 0 & |\dot{G}_o| < 1.745\times10^{-5} \text{ rad/sec} \\ 3.49\times10^{-4} \operatorname{sign}(\dot{G}_o) & |\dot{G}_o| > 1.745\times10^{-5} \text{ rad/sec} \end{cases}$$

Spin axis precession relative to magnetic north

$$\begin{bmatrix} \dot{A} \\ \dot{T} \end{bmatrix} = \begin{bmatrix} \cos G_s/\cos T & -\cos G_i \sin G_s/\cos T \\ -\sin G_s & -\cos G_i \cos G_s \end{bmatrix} \begin{bmatrix} p_i \\ p_o \end{bmatrix} + \omega \begin{bmatrix} \sin \lambda - \cos \lambda \tan T \cos A \\ \cos \lambda \sin A \end{bmatrix}$$

$$+ \frac{V}{R} \begin{bmatrix} \sin \psi(\tan \lambda - \tan T \cos A) + \cos \psi \tan T \sin A \\ \sin \psi \sin A + \cos \psi \cos A \end{bmatrix}$$

Gimbal angles and heading measurement

$$\tan G_o = \frac{\cos \phi \sin(\psi - A) - \sin \phi \sin \theta \cos(\psi - A) - \tan T \sin \phi \cos \theta}{\cos \theta \cos(\psi - A) + \tan T \sin \theta}$$

$$\sin G_i = \cos T \cos A(\cos \phi \sin \theta \cos \psi + \sin \phi \sin \psi) + \cos T \sin A(\cos \phi \sin \theta \sin \psi - \sin \phi \cos \psi) - \sin T \cos \phi \cos \theta$$

$$\tan G_s = \frac{-[-\sin A(\cos \phi \sin \theta \cos \psi + \sin \phi \sin \psi) + \cos A(\cos \phi \sin \theta \sin \psi - \sin \phi \cos \psi)]}{\sin T \cos A(\cos \phi \sin \theta \cos \psi + \sin \phi \sin \psi) + \sin T \sin A(\cos \phi \sin \theta \sin \psi - \sin \phi \cos \psi) + \cos T \cos \phi \cos \theta}$$

$$\psi_g = G_o$$

$$\tilde{\psi}_g = \psi_g - \psi$$

Initialization with error $\tilde{\psi}_o$ and gimbal angle G_i

$$G_o = \psi + \tilde{\psi}_o$$

$$\tan(A - \psi) = \frac{-\cos G_i \sin G_o \cos \phi - \sin G_i \sin \phi}{\cos G_i(\cos G_o \cos \theta - \sin G_o \sin \theta \sin \phi) + \sin G_i \cos \phi \sin \theta}$$

$$\sin T = \cos G_i(\cos G_o \sin \theta + \sin G_o \cos \theta \sin \phi) - \sin G_i \cos \phi \cos \theta \qquad T \in \pm \frac{\pi}{2}$$

$$\tan G_s = \frac{-\sin G_o \sin \theta + \cos G_o \cos \theta \sin \phi}{\sin G_i(\cos G_o \sin \theta + \sin G_o \cos \theta \sin \phi) + \cos G_i \cos \phi \cos \theta}$$

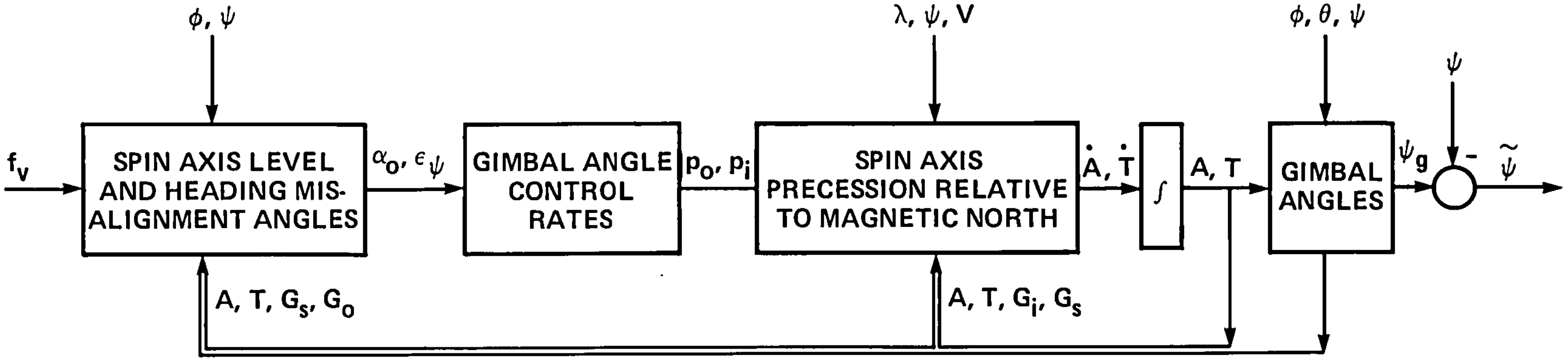

Figure B6.- Simulation of directional gyroscope: computational flow diagram.

$$\tan G_o = \left[\frac{\sin(\psi - A)}{\cos(\psi - A) + \tan T \tan \theta}\right] \frac{1}{\cos \theta}$$

Perfect azimuth alignment does not null the measurement error in this case, but the error is small and insensitive to small values of both θ and T. For nonzero ϕ, errors are dynamic and dominated by inaccurate control as discussed later.

Misalignment Equations

Equations governing the spin axis misalignment angles are again obtained from the dynamics of the forced gyroscope. These satisfy

$$\underline{P} = \omega_{g/I} \otimes \underline{g}_s \tag{B10}$$

where, for the directional gyroscope,

$$\underline{\omega}_{g/I} = (\omega + \dot{\ell})\underline{K} - \dot{\lambda}\underline{E} + \dot{A}\underline{D} + \dot{T}\underline{j}_m \tag{B27}$$

Express all unit vectors in equation (B27) in terms of F_m using equation (B22),

$$\underline{N} = \cos T \cos A \, \underline{g}_s - \sin A \, \underline{j}_m + \sin T \cos A \, \underline{k}_m$$

$$\underline{E} = \cos T \sin A \, \underline{g}_s + \cos A \, \underline{j}_m + \sin T \sin A \, \underline{k}_m$$

$$\underline{D} = -\sin T \, \underline{g}_s + \cos T \, \underline{k}_m$$

$$\begin{aligned} \underline{K} = \cos \lambda \, \underline{N} - \sin \lambda \, \underline{D} &= (\cos \lambda \cos T \cos A + \sin \lambda \sin T)\underline{g}_s \\ &- \cos \lambda \sin A \, \underline{j}_m + \cos \lambda(\sin T \sin A - \sin \lambda \cos T)\underline{k}_m \end{aligned}$$

and then the cross-products required in equation (B10) are

$$\left.\begin{aligned} \underline{N} \otimes \underline{g}_s &= \sin T \cos A \, \underline{j}_m + \sin A \, \underline{k}_m \\ \underline{E} \otimes \underline{g}_s &= \sin T \sin A \, \underline{j}_m + \cos A \, \underline{k}_m \\ \underline{D} \otimes \underline{g}_s &= \cos T \, \underline{j}_m \\ \underline{K} \otimes \underline{g}_s &= (\cos \lambda \sin T \cos A - \sin \lambda \cos T)\underline{j}_m + \cos \lambda \sin A \, \underline{k}_m \end{aligned}\right\} \tag{B28}$$

Substitution of equations (B27) and (B28) into (B10), and formation of inner products with $\underline{j}_m$ and $\underline{k}_m$, yields the following equations for the misalignment angles:

$$\left.\begin{aligned} \dot{A} &= \frac{\langle \underline{p}, \underline{j}_m \rangle}{\cos T} + \omega(\sin \lambda - \cos \lambda \tan T \cos A) \\ &\quad + \frac{V}{R}\left[\sin \psi(\tan \lambda - \tan T \cos A) + \cos \psi \tan T \sin A\right] \\ \dot{T} &= -\langle \underline{p}, \underline{k}_m \rangle + \omega \cos \lambda \sin A - \frac{V}{R}\left[\sin \psi \sin A + \cos \psi \cos A\right] \end{aligned}\right\} \qquad \text{(B29)}$$

Gyroscope Control Torques

Torques can be applied along the inner and outer gimbal axes,

$$\underline{p} = p_i \underline{g}_i + p_o \underline{k}_b$$

Noting that

$$\underline{k}_b = -\sin G_i \underline{g}_s + \cos G_i \underline{g}_z$$

then the inner products required in equation (B29) can be written, using equation (B23), as

$$\left.\begin{aligned} \langle \underline{p}, \underline{j}_m \rangle &= p_i \cos G_s - p_o \cos G_i \sin G_s \\ \langle \underline{p}, \underline{k}_m \rangle &= p_i \sin G_s + p_o \cos G_i \cos G_s \end{aligned}\right\} \qquad \text{(B30)}$$

The applied torques along both axes are due to control torques and drifts and are denoted as

$$\left.\begin{aligned} p_i &= p_{iC} + p_{iD} \\ p_o &= p_{oC} + p_{oD} \end{aligned}\right\} \qquad \text{(B16)}$$

where suitable drift values are

$$\left.\begin{aligned} p_{iD} &= 0.002°/\text{sec} \\ p_{oD} &= 0.0028 + \begin{cases} 0 & |\dot{G}_o| < 0.001°/\text{sec} \\ 0.02 \,\text{sign}(\dot{G}_o) & |\dot{G}_o| > 0.001°/\text{sec} \end{cases} \end{aligned}\right\} \qquad \text{(B31)}$$

The outer gimbal drift contains a fixed drift owing to mass unbalance and a friction drift owing to gimbal rate which is fixed in magnitude for rates above a threshold rate. The rate $\dot{G}_o$ can be approximated as the aircraft yaw angular velocity in the simulation.

The outer gimbal control (see sketch J) acts to maintain the spin axis in the apparent horizontal plane by precessing the inner gimbal to null the misalignment angle,

$$\alpha_o \equiv \langle \underline{f}, \underline{g}_s \rangle / |\langle \underline{f}, g_z \rangle| \qquad \text{(B32)}$$

using the control

$$p_{oC} = \begin{cases} b/a\ \alpha_o & |\alpha_o| < a \\ b\ \text{sign}(\alpha_o) & |\alpha_o| > a \end{cases}$$

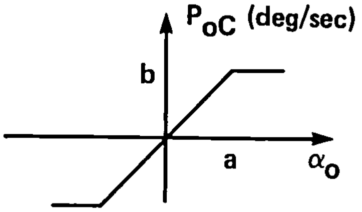

Sketch J

Suitable values for the saturation angle and maximum gimbal precession are

$$a = 1°$$

$$b = 0.05°/\text{sec}$$

The inner gimbal control torque acts to null the error between the outer gimbal angle and the apparent heading, ψ_C, sensed by a pendulous magnetic sensor and is modeled by

$$p_{iC} = \begin{cases} -0.022\ \varepsilon_\psi & |\varepsilon_\psi| < 5° \\ -0.11\ \text{sign}(\varepsilon_\psi) & |\varepsilon_\psi| > 5° \end{cases} \qquad \text{(B33)}$$

where

$$\varepsilon_\psi \equiv \psi_C - G_o$$

The principal error in the apparent heading

$$\psi_C = \psi + \tilde{\psi}_C$$

occurs in turning flight and results from detection of the direction of the magnetic field in the apparent horizontal plane rather than the true horizontal plane. To model this error, let $\underline{h}$ be the direction of Earth's magnetic field. Neglecting field anomalies, then

$$\underline{h} = \cos \gamma_D\ \underline{N} + \sin \gamma_D\ \underline{D}$$

where γ_D is the dip angle and varies with geographic location. At Ames Research Center, the dip angle is 61.8°. Assume that both the sensor pendulum axis and body-normal axis $\underline{k}_b$ align with the apparent vertical and that θ is zero. Then the sensed direction of north is located in the plane of $(\underline{h}, \underline{k}_b)$ and is perpendicular to $\underline{k}_b$, that is, along

$$\underline{n} = \underline{h} - (\underline{h} \cdot \underline{k}_b) \underline{k}_b$$

The apparent heading angle is given from

$$\cos \psi_C = \langle \underline{i}_b, \underline{n} \rangle / |\underline{n}| = \langle \underline{i}_b, \underline{h} \rangle / |\underline{n}| = \cos \gamma_D \cos \psi / |\underline{n}|$$

$$\sin \psi_C = -\langle \underline{j}_b, \underline{n} \rangle / |\underline{n}| = -\langle j_b, \underline{h} \rangle / |\underline{n}| = (\sin \psi \cos \phi \cos \gamma_D - \sin \phi \sin \gamma_D) / |n|$$

The error angle is obtained by forming $\sin(\psi_C - \psi)$, $\cos(\psi_C - \psi)$ and then

$$\tan \tilde{\psi}_C = \frac{\sin(\psi_C - \psi)}{\cos(\psi_C - \psi)} = \frac{\cos \psi[\sin \psi(\cos \phi - 1) - \tan \gamma_D \sin \phi]}{1 + \sin \psi[\sin \psi(\cos \phi - 1) - \tan \gamma_D \sin \phi]} \tag{B34}$$

This error is illustrated in figure B7; it is zero at zero roll angle and otherwise varies sinusoidally with heading during a turn and has large amplitude, even at modest roll angles (10°). During turns, this error dominates the heading error ε_ψ used for the inner-gimbal control (eq. (B33)), but the control saturation limit (0.11°/sec), along with the sinusoidal nature of ε_ψ, limits the resulting measurement error amplitudes during typical turns at about 5° (see fig. 2.2(c) of the text).

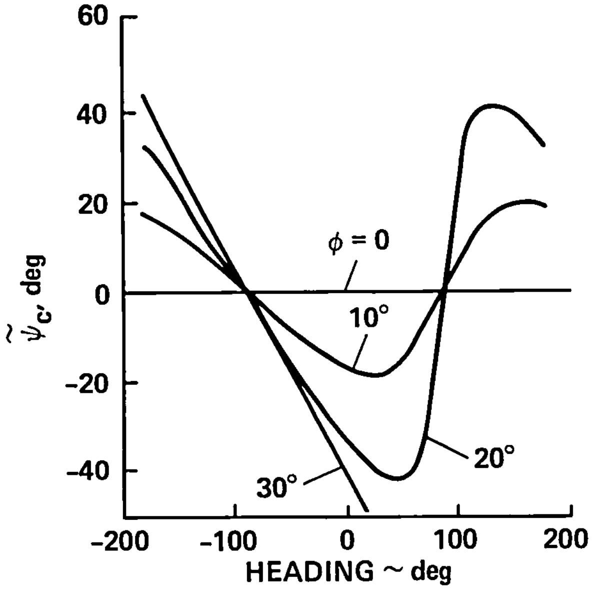

Figure B7.- Directional gyroscope: error in sensing north during turns (γ_D = 61.8°).

Simulation Summary

The directional gyroscope can be simulated using equations (B25) and (B29) through (B34), with aircraft accelerations and speeds, Euler attitudes, and latitude as inputs. A computational flow chart and equation summary for the simulation is given in figure B6 and table B2.

APPENDIX C

ERRORS IN MEASURING RUNWAY-REFERENCED ACCELERATIONS

The measured runway axis components of acceleration are derived from specific force and attitude measurements provided by body mounted accelerometers and attitude gyroscopes:

$$am_r = T_{rb}(\phi_g, \theta_g, \psi_g) fm_b + g_r \tag{C1}$$

This differs from the actual acceleration by the measurement error

$$am_r = a_r + \tilde{a}_r \tag{C2}$$

where $\tilde{a}_r$ can be expressed in terms of the sensor errors by the variational equation,

$$\widetilde{am}_r = \left[\frac{\partial am_r}{\partial \phi}, \frac{\partial am_r}{\partial \theta}, \frac{\partial am_r}{\partial \psi} \right] \begin{bmatrix} \tilde{\phi}_g \\ \tilde{\theta}_g \\ \tilde{\psi}_g \end{bmatrix} + T_{rb} \widetilde{fm}_b \tag{C3}$$

and

$$\left. \begin{aligned} \frac{\partial am_r}{\partial \phi} &= \frac{\partial T_{rb}}{\partial \phi} fm_b = \frac{\partial T_{rb}}{\partial \phi} T_{br} fm_r \\ \frac{\partial am_r}{\partial \theta} &= \frac{\partial T_{rb}}{\partial \theta} T_{br} fm_r \\ \frac{\partial am_r}{\partial \psi} &= \frac{\partial T_{rb}}{\partial \psi} T_{br} fm_r \end{aligned} \right\} \tag{C4}$$

Recalling the transformation T_{br} (table 2.2),

$$T_{br} = E_1(\phi)E_2(\theta)E_3(\phi) = \begin{bmatrix} 1 & 0 & 0 \\ 0 & \cos\phi & \sin\phi \\ 0 & -\sin\phi & \cos\phi \end{bmatrix} \begin{bmatrix} \cos\theta & 0 & -\sin\theta \\ 0 & 1 & 0 \\ \sin\theta & 0 & \cos\theta \end{bmatrix} \begin{bmatrix} \cos\psi & \sin\psi & 0 \\ -\sin\psi & \cos\psi & 0 \\ 0 & 0 & 1 \end{bmatrix} \tag{C5}$$

then the required derivatives in equation (C4) are found to be

$$\frac{\partial am_r}{\partial\phi} = E_3^T(\psi)E_2^T(\theta)\,\frac{\partial E_1(\phi)}{\partial\phi}\,E_1(\phi)E_2(\theta)E_3(\psi)fm_r$$

$$= \begin{pmatrix} \sin\theta\ fm_{r_2} + \sin\psi\cos\theta\ fm_{r_3} \\ -\sin\theta\ fm_{r_1} - \cos\psi\cos\theta\ fm_{r_3} \\ \cos\theta(-\sin\psi\ fm_{r_1} + \cos\psi\ fm_{r_2}) \end{pmatrix}$$

$$\frac{\partial am_r}{\partial\theta} = E_3^T(\psi)\,\frac{\partial E_r^T(\theta)}{\partial\theta}\,E_2(\theta)E_3(\psi)fm_r = \begin{pmatrix} \cos\psi\ fm_{r_3} \\ \sin\psi\ fm_{r_3} \\ -\cos\psi\ fm_{r_1} - \sin\psi\ fm_{r_2} \end{pmatrix}$$

$$\frac{\partial am_r}{\partial\psi} = \frac{\partial E_3^T(\psi)}{\partial\psi}\,E_3(\psi)fm_r = \begin{pmatrix} -fm_{r_2} \\ fm_{r_1} \\ 0 \end{pmatrix}$$

and the complete expression for the measurement error in equation (C3) is

$$\tilde{am}_r = \begin{bmatrix} \sin\theta\ fm_{r_2} + \sin\psi\cos\theta\ fm_{r_3} & \cos\psi\ fm_{r_3} & -fm_{r_2} \\ -\sin\theta\ fm_{r_1} - \cos\psi\cos\theta\ fm_{r_3} & \sin\psi\ fm_{r_3} & fm_{r_1} \\ \cos\theta(-\sin\psi\ fm_{r_1} + \cos\psi\ fm_{r_2}) & -\cos\psi\ fm_{r_1} - \sin\psi\ fm_{r_2} & 0 \end{bmatrix} \begin{bmatrix} \tilde{\phi}_g \\ \tilde{\theta}_g \\ \tilde{\psi}_g \end{bmatrix} + T_{rb}\tilde{fm}_b \tag{C6}$$

The first term in this expression provides the model of the dependence of acceleration errors on the errors of the attitude gyroscope that is used in the 15-state filter.

It is also of interest to express the error term of the attitude gyroscopes in equation (C6) in level heading axes and to introduce aircraft accelerations. One way to do this is to express $\underline{f}$ as

$$\underline{f} = \underline{a} - \underline{g} = a_1\underline{i}_L + a_2\underline{j}_L + (a_3 - g)\underline{k}_L \tag{C7}$$

where $\{a_i\}$ are the level heading coordinates of acceleration, and to note the vector relations between the level heading axes and runway axes:

$$\left.\begin{aligned} \underline{i}_L &= \cos\psi\ \underline{i}_r + \sin\psi\ \underline{j}_r \\ \underline{j}_L &= -\sin\psi\ \underline{i}_r + \cos\psi\ \underline{j}_r \\ \underline{k}_L &= \underline{k}_r \end{aligned}\right\} \tag{C8}$$

Using (C7) and (C8), we have

$$\begin{pmatrix} f_{r_1} \\ f_{r_2} \\ f_{r_3} \end{pmatrix} = \begin{pmatrix} \langle \underline{f}, \underline{i}_r \rangle \\ \langle \underline{f}, \underline{j}_r \rangle \\ \langle \underline{f}, \underline{k}_r \rangle \end{pmatrix} = \begin{pmatrix} a_1 \cos\psi - a_2 \sin\psi \\ a_1 \sin\psi + a_2 \cos\psi \\ a_3 - g \end{pmatrix} \tag{C9}$$

The columns of the attitude error coefficient matrix in equation (C6) can now be given in terms of $\{\underline{i}_L, \underline{j}_L, \underline{k}_r\}$, using equations (C7) to (C9). For example, the third column gives the effect of $\tilde{\psi}_g$, and it can be rewritten as

$$\begin{aligned} \underline{\widetilde{am}}^{(\tilde{\psi}g)} &= (-f_{r_2}\underline{i}_r + f_{r_1}\underline{j}_r)\tilde{\psi}_g \\ &= [a_1(-\sin\psi\ \underline{i}_r + \cos\psi\ \underline{j}_r) + a_2(-\cos\psi\ \underline{i}_r - \sin\psi\ \underline{j}_r)]\tilde{\psi}_g \\ &= (a_1\underline{j}_L - a_2\underline{i}_L)\tilde{\psi}_g \end{aligned}$$

Proceed similarly for the remaining columns, except to assume θ is a small angle, $|a_1|, |a_3| << g$, and retain only the leading terms. The resulting expression for the gyroscopic error term is then

$$\underline{\widetilde{am}}^{(\mathrm{gyro})} = (g\underline{i}_L + a_2\underline{k}_r)\tilde{\phi}_g - (g\underline{i}_L + a_1\underline{k}_r)\tilde{\theta}_g + (a_1\underline{j}_L - a_2\underline{i}_L)\tilde{\psi}_g \tag{C10}$$

APPENDIX D

EFFECT OF ESTIMATION ERRORS ON TRANSLATIONAL CONTROL

The effect of estimation errors on control of the aircraft translational motion is examined in this appendix. For this purpose a simplified generic model of the closed loop, automatic control system is derived and used to relate trajectory tracking errors and control activity to estimation errors and to generate both analytical results (transfer functions and frequency responses) and simulation results for these relationships. The simplified model represents solely the effects of translational state estimation errors on translational control and does not require representation of any details of the aircraft force and moment generation processes. The effects of estimation errors in other states required by the complete system (e.g., those required to control attitude, engine, configuration, and actuator dynamics) are independent.

A SIMPLIFIED MODEL OF AUTOMATIC TRANSLATIONAL CONTROL

A model of the complete reference trajectory tracking system is shown in figure D1(a). Only the translational control will be considered and, in general, this can be formulated as an inverse of the aircraft translational motion. Referring to figure D1(a), the aircraft translational motion model begins with the control u which generates the accelerations F(z,u), whose integrals give the states R_r, V_r. The control u includes those independent variables of the acceleration generation process which the control laws have at their disposal (e.g., for CTOL aircraft these are flap, engine rpm, roll angle, angle of attack, and sideslip angle) and z refers to the remaining variables affecting acceleration (e.g., dynamic pressure, atmospheric parameters, and aircraft weight). The control inverts this logical flow. It begins with a reference trajectory command, $[RC_r(t), VC_r(t), ac_r(t), t_o < t < t_f]$, which is assumed to satisfy Newtonian mechanics, aircraft acceleration generation limits, and operational constraints. In the absence of disturbances, this can be executed using a partial inverse of the acceleration generation process, $\hat{G}(z,a)$, to calculate those control settings, uc(t), that generate $ac_r(t)$, at the estimated current flight conditions, $\hat{z}(t)$.

Trajectory tracking errors develop from various external and internal disturbances (wind turbulence, estimation errors, control errors) and their estimates, $\hat{\delta R}_r, \hat{\delta V}_r$ are fed back to obtain stable tracking. The regulator output is a corrective acceleration command, Δa_r, which is executed by summing with ac_r and passing the total, act_r, through the plant inverse, and which imposes transient response dynamics on the translational tracking errors, as specified in the feedback control law. An appropriate control law is given in figure D1(b); the selected dynamics (1) are decoupled in path axes; (2) are second order in the linear domain, with damping and natural frequency determined by the gains in accordance with the relations given in figure D1(b); and (3) have saturation limits on the control authority Δa_{LIM} and on the velocity excursions that can be used to null large position errors, δV_{LIM}. Path axes decoupling is used in view of the nearly decoupled control over accelerations along these axes provided by the conventional controls governing engine rpm, roll

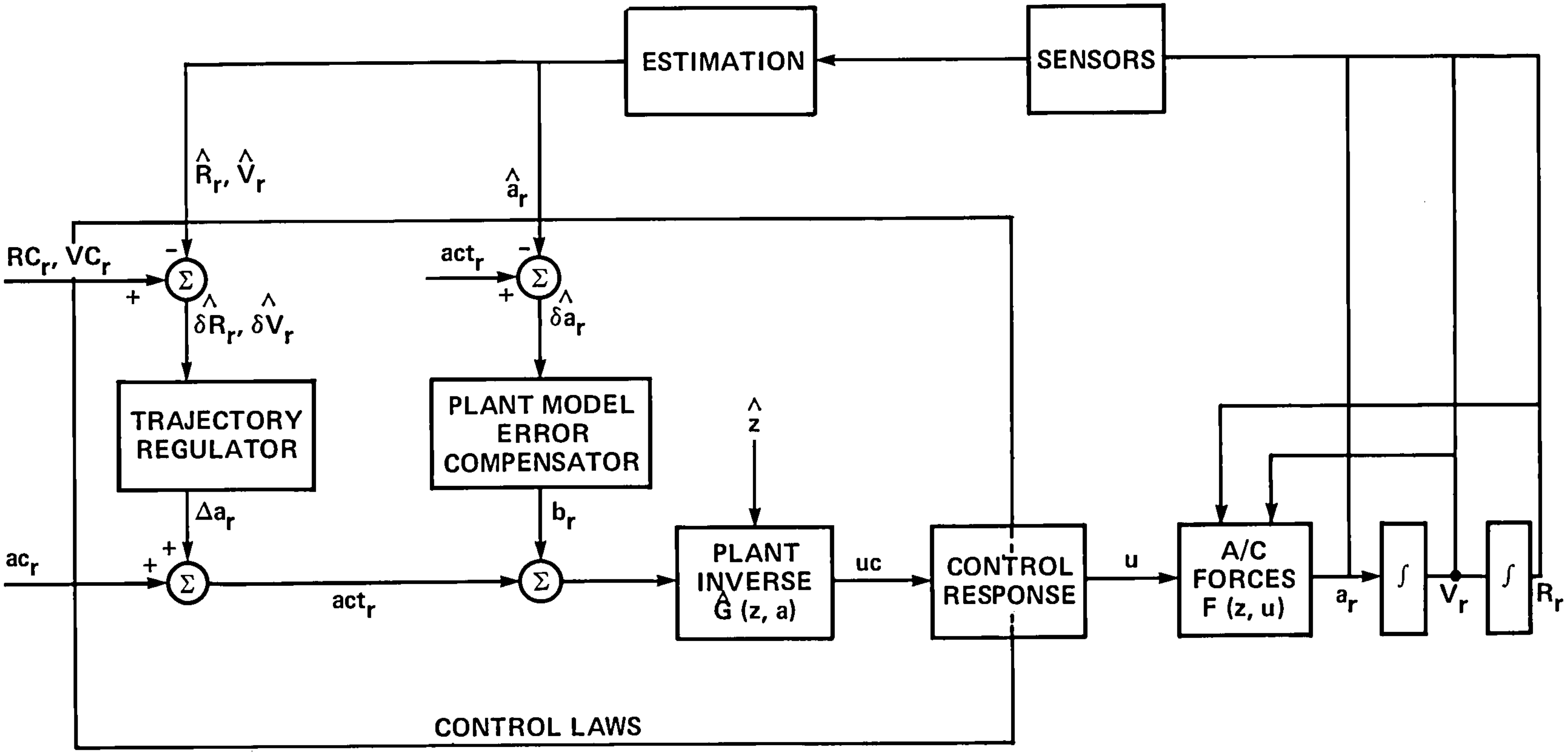

(a) Logical flow diagram.

Figure D1.- Automatic reference trajectory-tracking system: translational degrees of freedom.

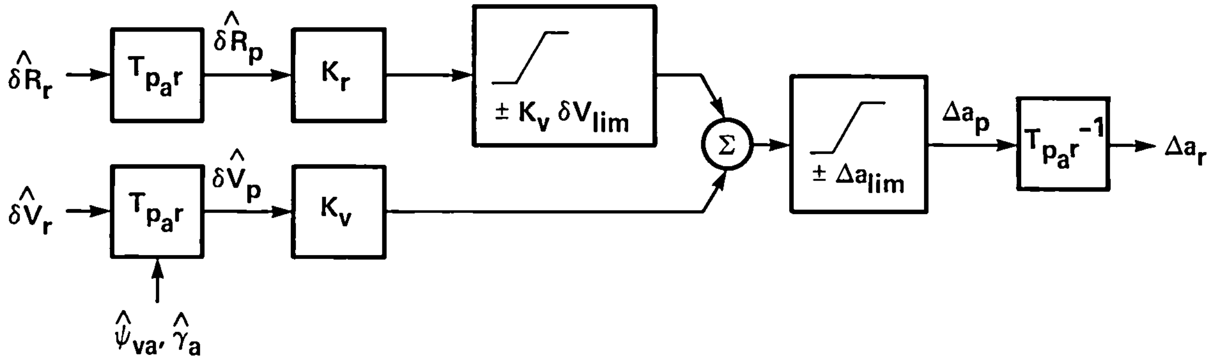

LINEAR DOMAIN CONTROL

$$\Delta a_p = K_r \, \delta\hat{R}_p + K_v \, \delta\hat{V}_p$$

$$K_r = \left[\diagdown \omega_{n_i}^2 \diagdown\right]$$

$$K_v = \left[\diagdown 2\zeta_i \omega_{n_i} \diagdown\right]$$

PARAMETER VALUES

$\zeta_i = 0.707, \; i = 1, 2, 3$

$\{\omega_{n_i}\} = \{0.125, 0.125, 0.3\}$ rps

$\{\delta V_{lim_i}\} = \{5, 5, 2.5\}$ mps

$\Delta a_{lim_i} = 0.1 \text{ g}, \; i = 1, 2, 3$

(b) Trajectory regulator.

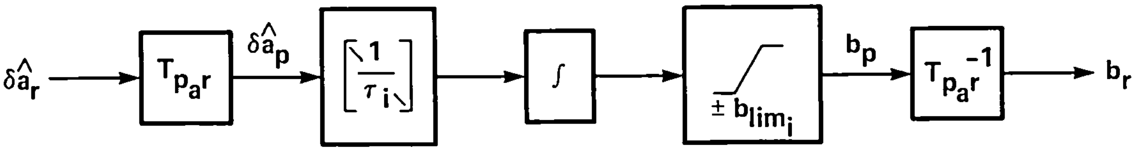

$$b_p \equiv \left[\diagdown \frac{1}{\tau_i s} \diagdown\right] \delta\hat{a}_p = -\left[\diagdown \frac{1}{\tau_i s + 1} \diagdown\right] (\tilde{G}_p + \tilde{a}_p)$$ LINEAR DOMAIN COMPENSATION

$$\left.\begin{aligned} \tau_i &= 5 \text{ sec} \\ b_{lim_i} &= 0.1 \text{ g} \end{aligned}\right\} \; i = 1, 2, 3$$ PARAMETER VALUES

(c) Acceleration response error compensation.

Figure D1.- Continued.

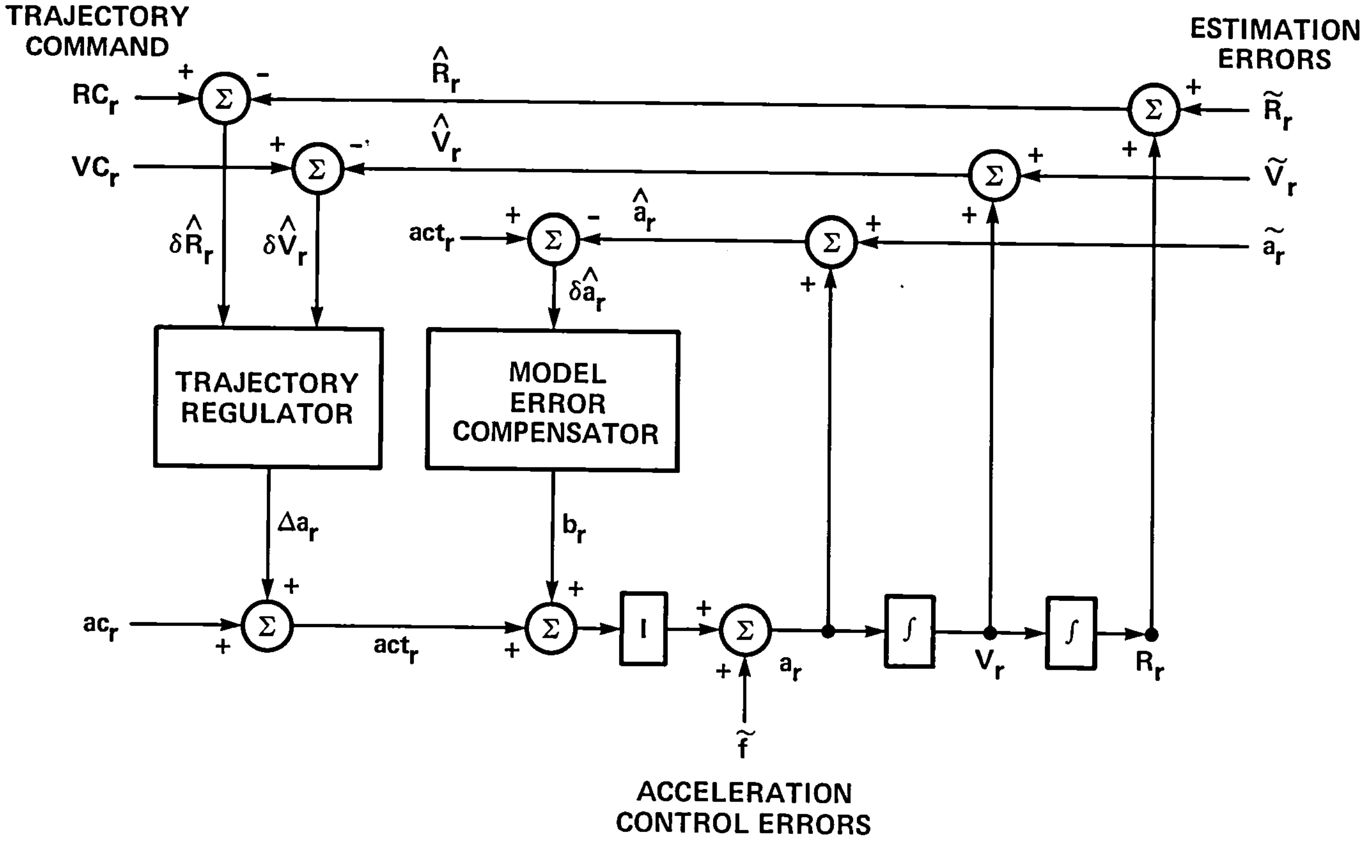

(d) Simplified estimation and control system model.

Figure D1.- Concluded.

angle, and angle of attack.[3] Suitable control law parameter values for passenger operations are listed in figure D1(b). The natural frequency ω_n determines system bandwidth and is a useful gain-adjusting parameter to modify system dispersions caused by disturbances or to maintain acceptable control activity. Its selected values for the present discussion are representative of passenger operations where ω_n ranges approximately from 0.05 to 0.5 rps, depending on trajectory segment, control axis, and disturbance levels.

The system described so far will reproduce the reference trajectory and achieve the specified transient response in the absence of estimation and trajectory synthesis errors, provided the total acceleration command $\underline{act}$ is reproduced exactly by the combined plant inverse, control response, and aircraft acceleration generation

---

[3] However, some coupling and alteration of the path axis transient dynamics is introduced by Coriolis accelerations in the kinematic relations:

$$\delta\dot{R}_p = \delta V_p - (\underline{\omega} \otimes \delta R)_p + \text{HOT's}$$

$$\delta\dot{V}_p = \Delta a_p - (\underline{\omega} \otimes \delta V)_p + \text{HOT's}$$

Nonnegligible effects occur principally during turns in combination with large horizontal plane tracking errors.

process; that is, provided this combination is unity. In general, this combination differs from unity because of identification and approximation errors in the plant inverse, $\hat{G}$, and the control response dynamics. However, the plant inverse errors are assumed to be slowly varying compared with the bandwidth of the acceleration commands and can be estimated and compensated automatically by feedback of the integrated acceleration error; this feedback and its control law are shown in figures D1(a) and D1(c). In addition, the control response dynamics in figure D1(a) refer to the remaining aircraft degrees of freedom (attitude, engine, and actuator dynamics) together with their appropriate control laws, sensors, and estimation logic; in passenger operations, it can be assumed that the dynamics for these subsystems are an order of magnitude faster than the bandwidth of the acceleration commands so that they can be neglected in modeling the translational motion and its control.

The model of the translational control system can now be simplified to that shown in figure D1(d). Errors in controlling acceleration that result from control response dynamics, plant inversion errors, errors in estimating the variables of the inner loop control, and external disturbances are collectively represented by the additive disturbance, $\tilde{f}$. However, $\tilde{f}$ can be ignored here since its effects on trajectory control are independent of those owing to translational state estimation errors, and then the simulation is easily expanded to include the control system of figures D1(b), D1(c), and D1(d) in order to study these latter effects.

The design structure of the automatic control, which is given in figure D1(a) and which leads to the simplified model in figure D1(d), has been proposed and flight tested at Ames in recent years (refs. 43 and 44). Conventional automatic control systems based on a linear perturbation model associated with a nominal operating point can be rearranged to give the structure shown in figure D1(d) for the neighborhood of its operating point so that the results given next for relations between estimation errors and system dispersions apply to conventional designs as well.

TRACKING ERRORS AND CONTROL ACTIVITY CAUSED BY ESTIMATION ERRORS

Transfer functions relating system output variables to estimation errors are readily derived from the model in figures D1(b)-D1(d) and are given in figure D2(a) for the path axis components of the apparent dispersions ($\hat{\delta}R_p,\hat{\delta}V_p,\hat{\delta}a_p$); for the true dispersions, ($\delta R_p,\delta V_p,\delta a_p$); and for the control activity, including the net activity, $c_p = \Delta a_p + b_p$ (Coriolis effects are neglected and results apply to the linear (unsaturated) control domain). The steady state step responses are included in the table and these responses show that constant estimation errors for any state, $\tilde{R},\tilde{V},\tilde{a}$, are converted by the control to a position offset, δR, with no steady state velocity error or net control offset. In effect, the control can detect and null out constant velocity and acceleration estimation errors at the cost of a position hang off and it leaves information on these biases in the steady state apparent dispersions and control offsets.

Frequency response magnitudes provide further information on excitation of the system by the estimation errors. Analytical expressions are given in figure D2(b) for the true dispersions and net control activity; as seen, all output variables depend on all input estimation errors (δR depends on $\tilde{R},\tilde{V},\tilde{a}$, and similarly for $\delta V,c$) and the asymptotic behavior ($\omega \to \infty$) indicates nonzero control activity in response to $\tilde{R},\tilde{V}$ over the entire frequency spectrum. Numerical amplitude ratio results are shown in figure D2(c) for several values of the control bandwidth. These results indicate the following trends. First, steady state position tracking error responds

$$
\begin{array}{ll}
\text{APPARENT DISPERSIONS} & \\
\text{TRUE DISPERSIONS} & \\
\text{CONTROLS} &
\end{array}
\begin{bmatrix} \hat{\delta R} \\ \hat{\delta V} \\ \hat{\delta a} \\ \delta R \\ \delta V \\ \delta a \\ \Delta a \\ b \\ c \end{bmatrix}
=
\underbrace{\begin{bmatrix}
\frac{K_r}{q} - 1 & \frac{K_v}{q} & \frac{1}{q(\tau s + 1)} \\
s\frac{K_r}{q} & s\frac{K_v}{q} - 1 & \frac{s}{q(\tau s + 1)} \\
0 & 0 & -\frac{\tau s}{\tau s + 1} \\
\frac{K_r}{q} & \frac{K_v}{q} & \frac{1}{q(\tau s + 1)} \\
s\frac{K_r}{q} & s\frac{K_v}{q} & \frac{s}{q(\tau s + 1)} \\
s^2\frac{K_r}{q} & s^2\frac{K_v}{q} & \frac{s^2}{q(\tau s + 1)} \\
-s^2\frac{K_r}{q} & -s^2\frac{K_v}{q} & \left(1 - \frac{s^2}{q}\right)\frac{1}{\tau s + 1} \\
0 & 0 & -\frac{1}{\tau s + 1} \\
-s^2\frac{K_r}{q} & -s^2\frac{K_v}{q} & -\frac{s^2}{q(\tau s + 1)}
\end{bmatrix}}_{\text{TRANSFER FUNCTIONS}}
\begin{bmatrix} \tilde{R} \\ \tilde{V} \\ \tilde{a} \end{bmatrix}
\underset{s \to o}{=}
\underbrace{\begin{bmatrix}
0 & \frac{K_v}{K_r} & \frac{1}{K_r} \\
0 & -1 & 0 \\
0 & 0 & 0 \\
1 & \frac{K_v}{K_r} & \frac{1}{K_r} \\
0 & 0 & 0 \\
0 & 0 & 0 \\
0 & 0 & 1 \\
0 & 0 & -1 \\
0 & 0 & 0
\end{bmatrix}}_{\text{STEADY STATE STEP RESPONSE}}
\begin{bmatrix} \tilde{R} \\ \tilde{V} \\ \tilde{a} \end{bmatrix}
$$

NOTES:

$q \equiv s^2 + sK_v + K_r$

$\delta R \equiv RC - R$

$\delta V \equiv VC - V$

$\delta a \equiv act - a$

$c \equiv \Delta a + b$

(a) Linear domain transfer functions.

$$
\begin{pmatrix} \delta R \\ \delta V \\ c \end{pmatrix}
= \frac{1}{|q_1|}
\begin{bmatrix}
1 & 2\rho/\omega_n & 1/\omega_n^2 q_2 \\
\omega & 2\rho\omega/\omega_n & \omega/\omega_n^2 q_2 \\
\omega^2 & 2\rho\omega^2/\omega_n & \omega^2/\omega_n^2 q_2
\end{bmatrix}
\begin{pmatrix} \tilde{R} \\ \tilde{V} \\ \tilde{a} \end{pmatrix}
\underset{\omega \to \infty}{=}
\begin{bmatrix}
0 & 0 & 0 \\
0 & 0 & 0 \\
\omega_n^2 & 2\rho\omega_n & 0
\end{bmatrix}
\begin{bmatrix} \tilde{R} \\ \tilde{V} \\ \tilde{a} \end{bmatrix}
$$

WHERE $|q_1| \equiv \sqrt{(1 - (\frac{\omega}{\omega_n})^2)^2 + (2\rho\frac{\omega}{\omega_n})^2}$

$|q_2| \equiv \sqrt{1 + \omega^2\tau^2}$

(b) Frequency-response amplitude ratios.

Figure D2.- Trajectory-tracking errors and control activity resulting from estimation errors.

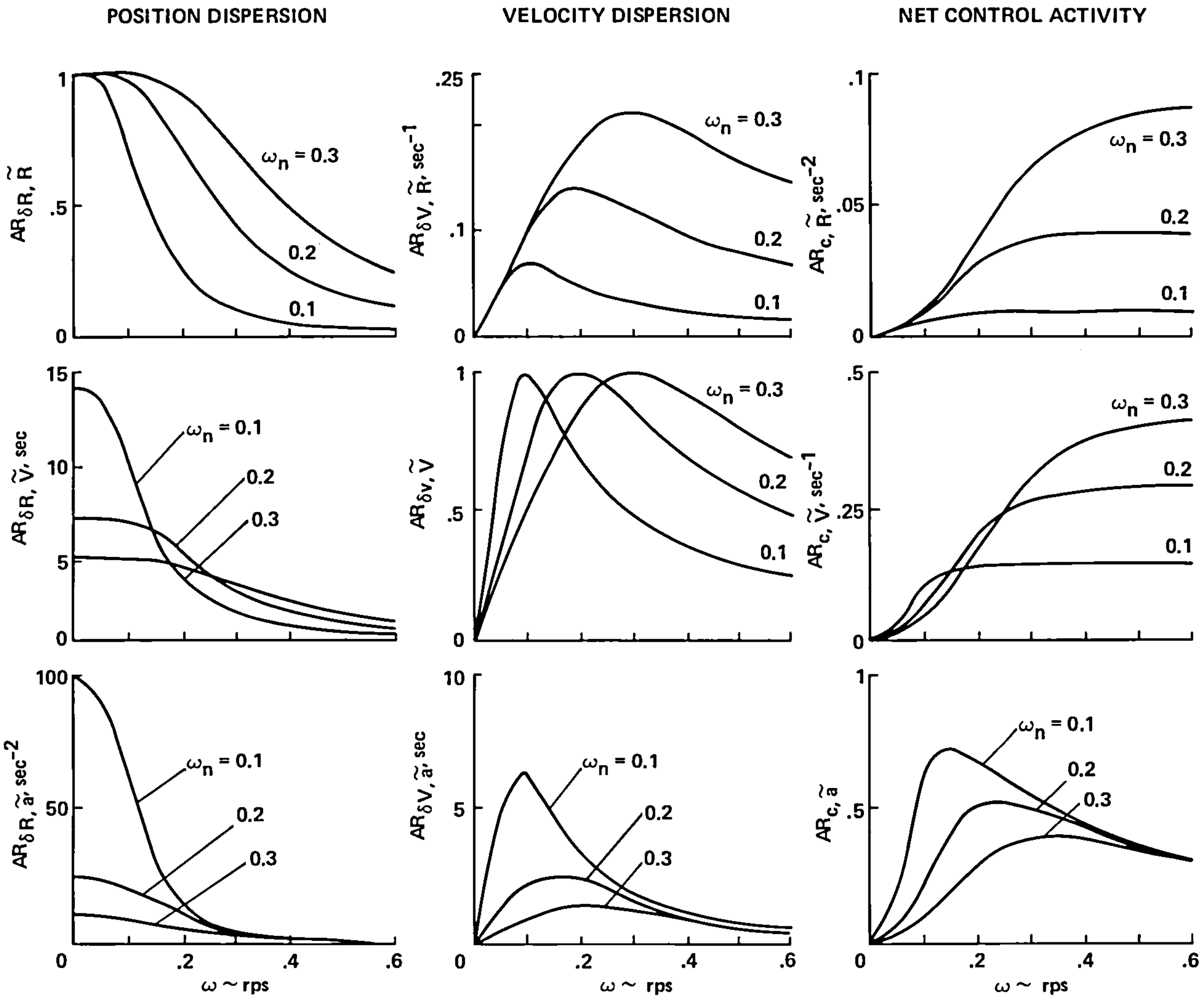

(c) Frequency-response amplitude ratios: ρ, τ = 0.707, 5 sec.

Figure D2.- Concluded.

principally to low-frequency estimation errors (below ω_n), with maximum sensitivity at $\omega_n = 0$. Bias errors in any state estimate are mapped by the control into position hangoff, and higher-frequency errors are attenuated so that position dispersions will be "smoother" than the estimation errors. Second, steady state velocity tracking errors are unaffected by estimation error biases and have maximum sensitivity to errors at the control bandwidth ($\omega = \omega_n$); sensitivity to $\tilde{V}$ is 1.0 at ω_n and otherwise velocity dispersions reproduce principally the estimation error content at frequencies near ω_n. And third, the net control activity is insensitive to low-frequency errors; it responds principally to frequencies at and above the control bandwidth and reflects the higher frequency content of $\tilde{R}$ and $\tilde{V}$.

Thus, it is the frequency of the estimation error relative to the control bandwidth that determines its effect on the system outputs. In this regard, we note that flight safety considerations depend principally on position tracking accuracy and, therefore, on the low-frequency estimation errors; on the other hand, velocity variations, control activity, and ride quality depend principally on the estimation error spectrum at and above ω_n.

SIMULATION RESULTS: TRACKING ERRORS

Ensemble rms and sample case trajectory tracking errors excited by the navigation errors are given in figures D3 and D4, along with a comparison with the corresponding state estimation errors. These results contain various effects not studied in the response analysis described above, including control system transient responses, control saturation, neglected Coriolis effects, and the collective effects of mutually correlated state estimation errors.

The position dispersions show several features. First, rms(δR) exceeds rms($\tilde{R}$) significantly and persistently in response to large changes in rms($\tilde{R}$), such as the lateral axis ramp reduction during leg 1 and the step changes on all axes at entry to

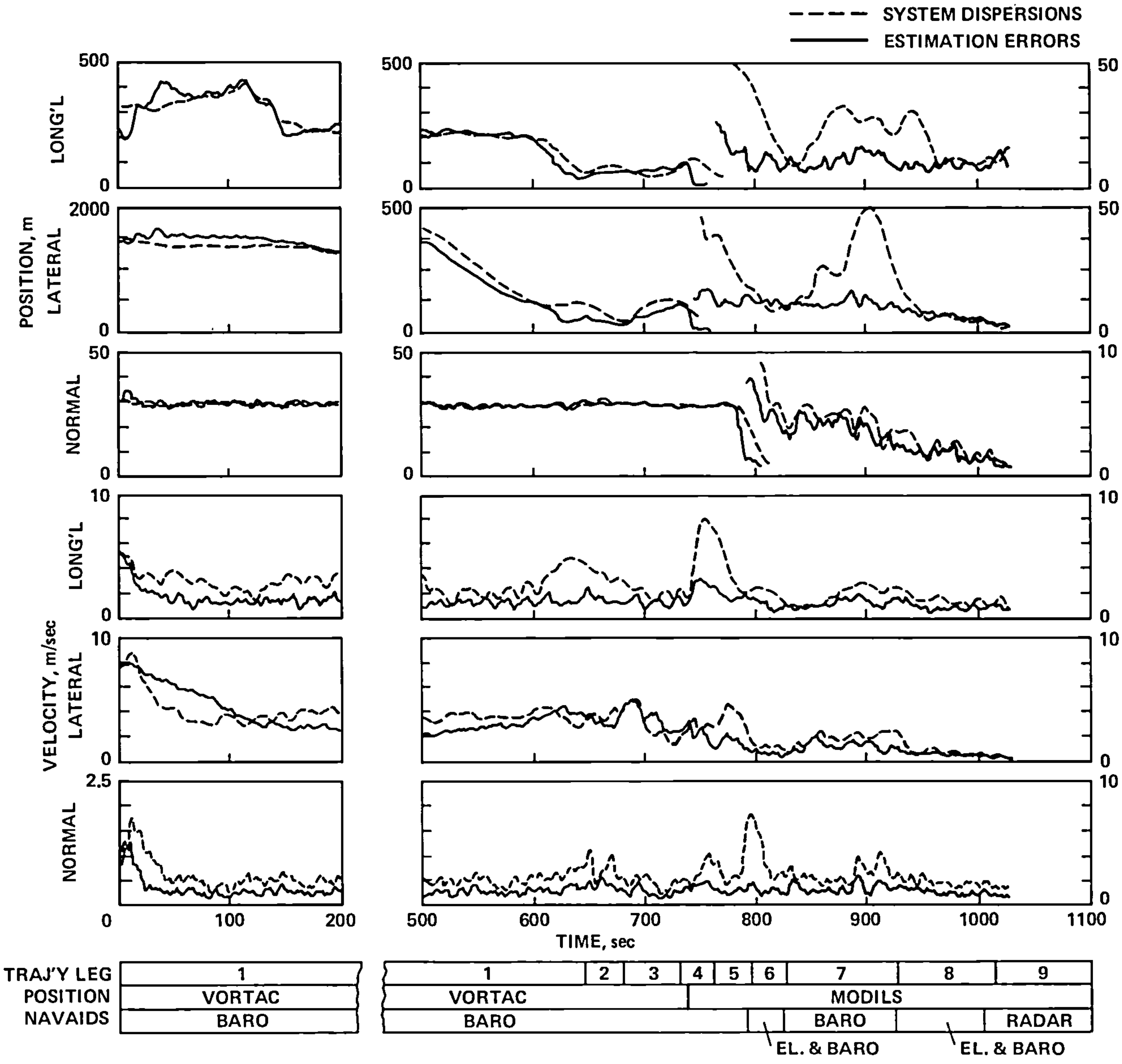

Figure D3.- System response to estimation errors: ensemble rms.

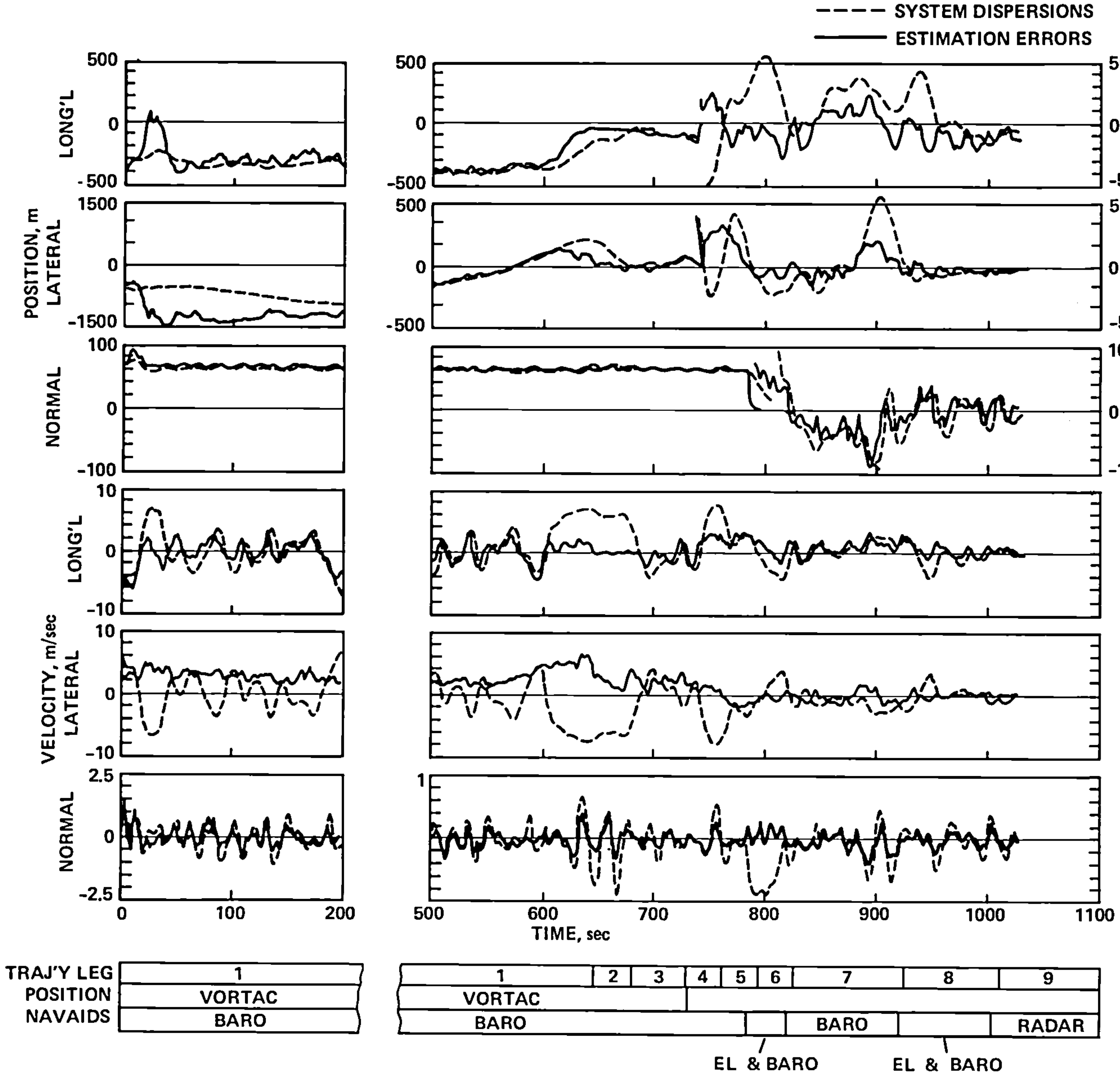

Figure D4.- System response to estimation errors: sample case.

MODILS or elevation coverage. During these periods, the control system maneuvers within the rate limit, δV_{LIM}, to null the apparent dispersions, $\delta\hat{R}$, so that δR necessarily lags $\tilde{R}$. Excursions in excess of rms($\tilde{R}$) are also excited on the longitudinal and lateral axes during turns because of (1) low-frequency changes in $\tilde{R}$ imposed by rotation of the path axes and (2) cross-coupling of the path axes dispersions by uncompensated Coriolis effects. Second, rms(δR) and rms($\tilde{R}$) are the same size where the estimation error is predominantly bias (examples are seen in both rms and sample case results for the normal and longitudinal axes before calibration of the baroaltimeter and VORTAC range biases, respectively). This result also occurs on the glide slope where $\tilde{R}$ variations are low in amplitude and δR reproduces the low-frequency content of $\tilde{R}$ with some lag and little amplification (e.g., the sample case normal axis errors). Third, the sample case history shows that $\delta R_p(t)$ is significantly smoother than $\tilde{R}_p(t)$, as expected.

The velocity dispersion satisfies the identity

$$\delta V_p = -\tilde{V}_p + \delta\hat{V}_p$$

and reproduces the estimation error frequency content near the control bandwidth (principally $\tilde{V}$ in the frequency range 0.5 ω_n to 3 ω_n) combined with the transient maneuvering velocity needed to null the apparent position dispersion. The control law limits the maneuvering dispersion to δV_{LIM}.

The rms velocity excursions show excursions well in excess of rms($\tilde{V}$) during large changes in rms($\tilde{R}$) (e.g., on the longitudinal axis when passing near the VORTAC and on all axes at entry to MODILS or elevation coverage). These excursions reflect the maneuvering needed to null the apparent position dispersion. The rms lateral velocity dispersion is initially smaller than rms($\tilde{V}$) as a result of the control law's ability to null the lateral velocity estimation bias owing to bearing bias. More generally, rms(δV) shows persistent excess over rms($\tilde{V}$) by a factor of 1.5 to 2.0, because the velocity estimate is generally unbiased, except as noted above, and because the control is continually excited by estimation errors. The sample case illustrates the underlying behavior in detail; the normal axis velocity dispersion is seen to reproduce $\tilde{V}$ with some amplification of most peaks during the extended periods of stationary errors, and a low-frequency excursion is superposed on this behavior at entry to MODILS coverage. The longitudinal and lateral axis results show additional examples of the behavior described above.

Ensemble extremes of position and velocity dispersions were reviewed and found generally to be twice the rms dispersions given in figure D3. These extreme dispersions are due to the estimation errors of the present system and are experienced on one or more approaches out of 10 if they depend principally on sample case constants, or several times during an approach if they depend on random measurement noise.

SIMULATION RESULTS: CONTROL ACTIVITY

The net control activity excited by estimation errors is illustrated by the rms and sample-case results shown in figure D5. In conventional aircraft, these histories map into corresponding engine, roll angle, and pitch angle activity. Control activity depends on sensor accuracy, on the control bandwidth, and on details of the estimation errors. The rms longitudinal control for the present 4D guidance law is roughly uniform at an average level of 0.04 g throughout the approach; the normal axis, with better position and acceleration estimation accuracy, shows less activity, at about 0.02 g (this difference would be greater if the control bandwidth were identical for the two axes). On the other hand, longitudinal control activity is about the same during both MODILS and VORTAC use, indicating an insensitivity to position accuracy in the test context. To clarify the dependence on sensor accuracy, results for a high-accuracy IMU are included in figure D5. When results for the two IMU's during MODILS use are compared, it is apparent that control activity depends strongly on IMU accuracy when position accuracy is good. Similarly, a comparison of results during VORTAC use with those during MODILS use for the inertial grade IMU indicates a strong dependence on position estimation accuracy when IMU accuracy is good. Thus, for the present system, position sensor accuracy dominates longitudinal and lateral control requirements during VORTAC use, and the IMU accuracy dominates it during MODILS use. Finally, it is apparent that both the VORTAC and IMU accuracy must be improved to obtain significant reduction in control activity because of estimation errors throughout the terminal area.

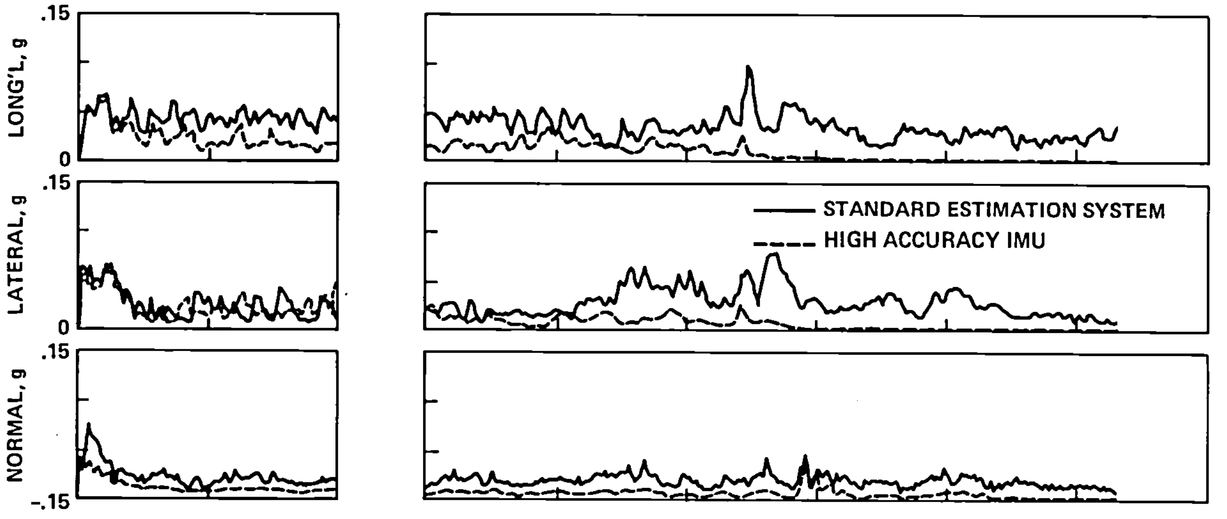

(a) ENSEMBLE AVERAGE

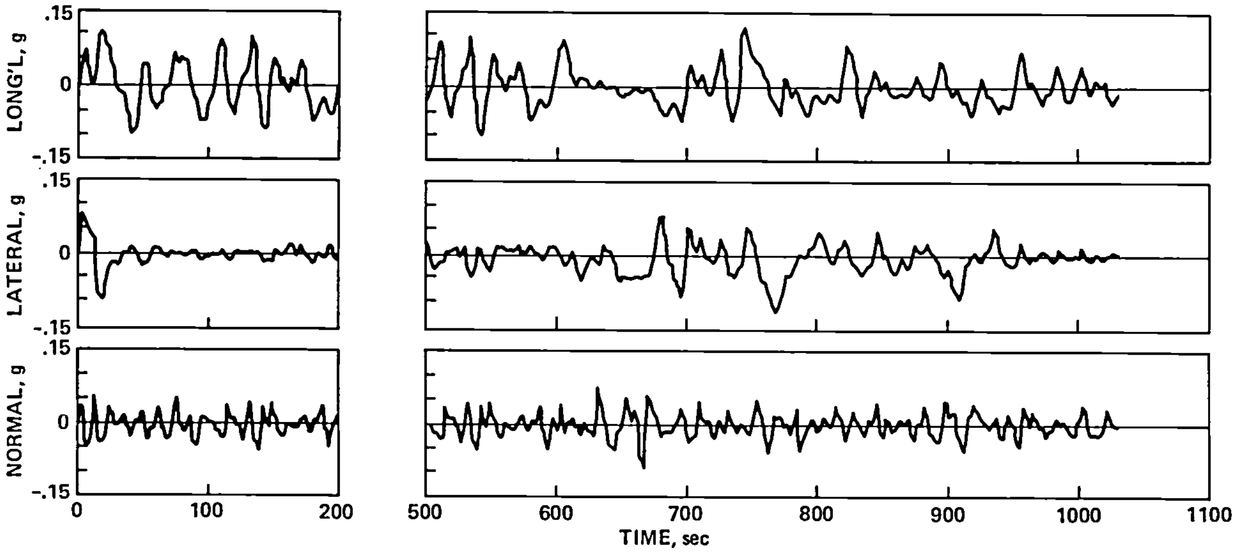

(b) SAMPLE CASE

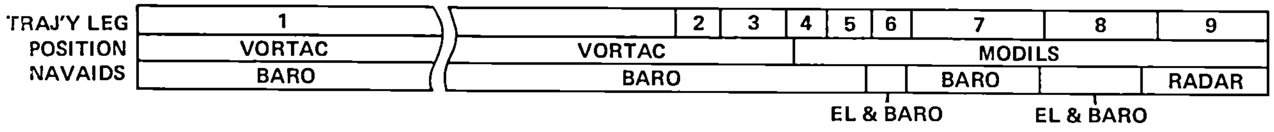

Figure D5.- System response to estimation errors: net control activity ($\{\omega_{n_i}\} = \{0.125, 0.125, 0.3\}_{\text{rps}}$).

The regulator control authority is typically 0.1 g; the rms control activity in figure D5 indicates that 20% to 40% of this authority, depending on control axis, is used up by the estimation errors for the present system but that this could be reduced to negligible levels compared to the authority with improved sensors. For aircraft, turbulence maps into acceleration disturbances oriented principally along the normal axis so that a sufficient reserve of control margin for external disturbances is more important for this axis. For the remaining axes, it is likely that estimation errors excite a larger average disturbance, $\Delta a(\tilde{R},\tilde{V},\tilde{a})$, than does the turbulence field. Control activity that results from estimation errors also depends on the control bandwidth ω_n and increases with ω_n, as does the frequency of saturation, while reserve margin and dispersion peaks decrease. Some results for the effect of bandwidth on rms control activity (averaged over the entire approach) are given in figure D6 for the present system; it illustrates this trend and also confirms the distinctly lower control activity for the normal axis at a given ω_n because of its distinctly better estimation error environment.

The sample case history (fig. D5) shows typical details: the dominant frequencies are seen to be higher than those of the dispersions $\delta R_p, \delta V_p$, as expected, and saturation of the control authority occurs infrequently on the longitudinal and lateral axes and not at all on the normal axis.

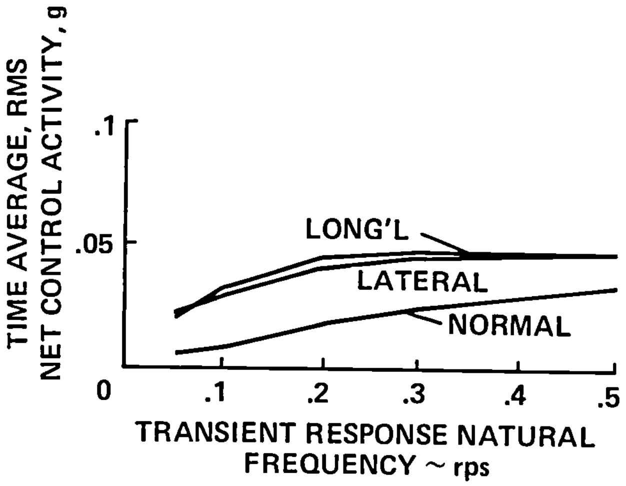

Figure D6.- Average control activity.

EFFECT OF ATTITUDE ESTIMATION ERRORS ON SYSTEM PERFORMANCE

A detailed study of the effects of inner loop sensor and estimation errors on system performance is beyond the scope of our simulation, but some general comments can be made.

Inner loop estimation errors result in acceleration control errors, $\tilde{f}$, which induce dispersions and compensation activity by the translational control in accordance with the model of figure D1(d). In particular, the attitude measurements provided by the gyroscopes of the present system have low-frequency errors that can be assumed to result in like attitude control errors and corresponding errors in controlling aerodynamic force. These latter errors induce dispersions and control activity, depending on frequency, but can be compensated by the plant model error compensator $\underline{b}$, up to the limit of its authority (0.1 to 0.2 g). An important effect of this compensation activity is the corresponding loss of margin to compensate for aircraft identification errors in the plant inverse portion of the control laws, $\hat{G}(z,a)$.

Roll angle determines lift force orientation about the longitudinal axis and is the primary control over lateral accelerations; roll errors of 0.5° result in acceleration errors of 0.01 g — an appropriate accuracy level for the roll control. In the present tests, the roll angle measurement shows poorer accuracy, with excursions to ±1.5° during turns.

Angle of attack, which is controlled through pitch attitude, determines the lift force magnitude and is the primary control over normal acceleration in conventional aircraft. Lift sensitivity to angle-of-attack control errors is C_{L_α}/C_L g/rad.

This ratio typically increases with airspeed and was found to be in the range 0.04 to 0.2 g/deg over the speed range of the test approach path for an example STOL aircraft. For this example, angle-of-attack estimation accuracies of 0.25° to 0.05° are needed, depending on airspeed, to obtain lift control accuracy at 0.01 g. Angle-of-attack error is a superposition of several errors (eq. (5.12)), with pitch measurement errors dominating the low-frequency content. In the present test, pitch measurement error showed excursions over ±1.5° during maneuvering; the excursions were independent of speed, and are, therefore, an important outer loop disturbance, particularly in higher speed maneuvering where the error is an order of magnitude larger than the desired accuracy.

Last, sideslip angle determines side force and is controlled through heading angle. However, sideslip is unobservable to the present estimation system and cannot be controlled. In this case, the automatic control relies on the aircraft's weathervane stability to null side force in steady state, and the control is insensitive to the large error in the directional gyroscope.

REFERENCES

1. Grgurich, J.; and Bradbury, P.: STOLAND Final Report. NASA CR-137072, 1976.

2. Schmidt, S. F.; Weinberg, J. D.; and Lukesh, J. S.: Application of Kalman Filtering to the C-5 Guidance and Control System. Theory and Application of Kalman Filtering, AGARDograph No. 139, 1970.

3. McGee, L.; Smith, G. L.; et al.: Flight Test Results from a Study of Aided Inertial Navigation Applied to Landing Operations. NASA TN D-7302, 1972.

4. Schmidt, S. F.: Presision Navigation for Approach and Landing Operations. Proceedings, Joint Automatic Control Conference, Stanford, California, American Automatic Control Council, Aug. 1972.

5. Schmidt, S. F.: Experiences in the Development of Aided INS for Aircraft. AGARD Lecture Series No. 82, 1976.

6. Berube, R. A.: RNAV Benefits Today: Current and Future Requirements. International Air Transportation Conference, Vol. I, American Society of Civil Engineers, 1979.

7. Blaydon, C. J.: The Introduction of STOL and RNAV to Large Commercial Operations. International Air Transportation Conference, Vol. I, American Society of Civil Engineers, 1979.

8. Cassell, R.: Evolution of Area Navigation in the Air Traffic Control System. Proceedings of the National Aerospace Symposium, Institute of Navigation, 815 15th Street, Suite 832, Washington, D.C., Apr. 1978.

9. Jazwinski, A. H.: Stochastic Processes and Filtering Theory. Academic Press, New York, 1970.

10. Kaminski, P. G.: Square Root Filtering and Smoothing for Discrete Processes. SUDAAR No. 427, Stanford U., Stanford, Calif., July 1971.

11. Kaminski, P. G.; Bryson, A. E.; and Schmidt, S. F.: Discrete Square Root Filtering: A Survey of Current Techniques. IEEE Transactions on Automatic Control, Dec. 1971.

12. Kayton, Fried: Avionics Navigation Systems. John Wiley and Sons, New York, 1969.

13. Shiesser, E. R.; Mayer, J. P.; et al.: Navigation Systems Characteristics, Revision I. Johnson Space Center Internal Note No. 72-FM-190, Houston, Tex., July 1973.

14. Neumann, F.; and Warner, N. D.: A STOL Terminal Area Navigation System. NASA TM X-62348, 1974.

15. Ludlam, A. G.: STOLAND Software Program Document: Augmentor Wing and Twin Otter Air Data Program. Report No. 5442-0222-P11, Sperry Flight Systems, Phoenix, Arizona, Nov. 1975.

16. Adams, G. P.: Evaluation of a STOL Modular Instrument Landing System (MODILS). FAA Report FAARD-72-4, NAFEC, New Jersey, May 1972.

17. Minimum Performance Standards — Airborne Low Range Radar Altimeters. RTCA SC-102 Paper 96-63/DO-123, Radio Technical Commission for Aeronautics, 1717 H Street, Washington, D.C., Aug. 1963.

18. Johansen, H.: A Survey of General Coverage Navaids for VSTOL Aircraft — A VOR/DME Error Model. NASA CR-1588, 1970.

19. Warner, N. D.; and Moran, J. F.: Flight Test Evaluation Errors in the MODILS and TACAN Navigation Aids at NALF, Crows Landing. NASA TM-78584, 1979.

20. Texas Instruments Basic Narrow Microwave Landing System, Crows Landing, California. U.S. Submission to the International Civil Aviation Organization All Weather Operations Panel, Feb. 1978.

21. Warner, N. D.; and Moran, F. J.: Flight Test of Navigation and Guidance Sensor Errors Measured on STOL Approaches. NASA TM-81154, 1979.

22. Athans, M.; Whiting, R. M.; and Gruber, M.: A Suboptimal Estimation Algorithm with Probabalistic Editing of False Measurements with Application to Target Tracking with Wake Phenomena. IEEE Transactions on Automatic Control, June 1977.

23. Beatie, E. C.; Laprad, R. F.; McGlone, M. E.; Rock, S. M.; and Akhter, M. M.: Sensor Failure Detection System. NASA CR-165515, Aug. 1981.

24. Cicolani, L. S.: Equivalent Measurements, Observability and Calibration Accuracy Limits in Linear Estimation. NASA TN D-6388, 1971.

25. Lear, W. M.: Onboard Navigation of the Space Shuttle. Proceedings, 11th International Symposium on Space Technology and Science, Tokyo, Japan, July, 1975. AGNE Publishing Co.

26. Schmidt, S. F.; Flanagan, P. F.; and Sorensen, J. A.: Development and Flight Test of a Kalman Filter for Navigation during Terminal Area and Landing Operations. NASA CR-3015, 1978.

27. Cicolani, L. S.; and Weissenberger, S.: A Nonlinear Trajectory Command Generator for a Digital Flight Control System. NASA TP-1221, 1978.

28. Teunissen, H. W.: Characteristics of Mean Wind and Turbulence in the Planetary Boundary Layer. UTIAS Review No. 32, Toronto U., Toronto, Ont., 1974.

29. Barr, N. M.; Gangsaas, D.; and Schaeffer, D. R.: Wind Models for Flight Simulator Certification of Landing and Approach Guidance and Control Systems. DOT Report No. FAA-RD-74-206, Dec. 1974.

30. Garg, S. C.; Morrow, L. N.; and Mamen, R.: Strapdown Inertial Technology: A Literature Survey. AIAA J. Guidance Control, May-June 1978.

31. Durbin, E.; and McGeer, T.: An Airspeed Vector Sensor for VSTOL Aircraft. AIAA Journal of Aircraft, June 1982.

32. Pruet, C. D.; Wolf, H.; Heck, M. L.; and Siemers, P. M.: An Innovative Air Data System for the Space Shuttle Orbiter: Data Analysis Techniques. AIAA Paper 81-2455, Las Vegas, Nev., 1981.

33. Automatic Landing Systems. FAA Advisory Circular No. 20-57A, Jan. 1971.

34. Price, C. R.; et al.: An Evaluation of the Microwave Landing System and Other Terminal Navaids for Use by the Space Shuttle. NASA Manned Spacecraft Center Internal Note MSC-EG-72-46, Houston, Tex., Nov. 1972.

35. Criteria for Approving Category I and Category II Landing Minimum for FAR 121 Operations. FAA Advisory Circular No. 120-29, Sept. 1970.

36. Approval of Area Navigation Systems for Use in the U.S. National Airspace System. FAA Advisory Circular No. 90-45A, Feb. 1975.

37. Hoffman, W. C.; Zvara, J.; and Hollister, W. M.: Analysis of Navigation and Guidance Requirements for Commercial VTOL Operations. Proceedings of the 31st Annual National Forum of the American Helicopter Society, 1975.

38. A New Guidance System for Approach and Landing, Vol. 2. SC-117 Committee Report, Document DO-148, Radio Technical Commission for Aeronautics, 1717 H Street, Washington, D.C., Dec. 1970.

39. Cicolani, L. S.: Position Determination Accuracy from the Microwave Landing System. NASA TN D-7116, 1973.

40. Leondes, T. C., ed.: Principals and Operational Aspects of Precision Position Determination Systems. AGARDograph AG-245, July 1979.

41. Global Positioning System; Navigation, ION 0-936406-00-3, Institute of Navigation, 815 15th Street, Suite 832, Washington, D.C., 1980.

42. Civil Application of Differential GPS Using a Single Channel Sequential Receiver. NASA CR-166168, 1981.

43. Meyer, G.; and Cicolani, L. S.: A Formal Structure for Automatic Flight Control Systems. NASA TN D-7940, 1975.

44. Meyer, G.; and Cicolani, L. S.: Application of Nonlinear Systems Inverses to Automatic Flight Control Design — System Concepts and Flight Evaluations. Theory and Applications of Optimal Control in Aerospace Systems, AGARDograph No. 251, July 1981.

1. Report No.
NASA TP-2035

2. Government Accession No.

3. Recipient's Catalog No.

4. Title and Subtitle
DEVELOPMENT AND EVALUATION OF A KALMAN-FILTER ALGORITHM FOR TERMINAL AREA NAVIGATION USING SENSORS OF MODERATE ACCURACY

5. Report Date
July 1983

6. Performing Organization Code

7. Author(s)
Gerd Kanning, Luigi S. Cicolani, and Stanley F. Schmidt

8. Performing Organization Report No.
A-8955

9. Performing Organization Name and Address
NASA Ames Research Center
Moffett Field, Calif. 94035

10. Work Unit No.
T-5281 Y

11. Contract or Grant No.

12. Sponsoring Agency Name and Address
National Aeronautics and Space Administration
Washington, D.C. 20546

13. Type of Report and Period Covered
Technical Paper

14. Sponsoring Agency Code
505-07-31-07

15. Supplementary Notes
Point of Contact: Luigi S. Cicolani, Ames Research Center, MS 210-3, Moffett Field, Calif. 94035. (415)965-5446 or FTS-5446.

Stanley F. Schmidt: Analytical Mechanics Associates, Inc., Mountain View, California.

16. Abstract

Translational state estimation in terminal area operations, using a set of commonly available position, air data, and acceleration sensors, is described. Kalman filtering is applied to obtain maximum estimation accuracy from the sensors but feasibility in real-time computations requires a variety of approximations and devices aimed at minimizing the required computation time with only negligible loss of accuracy. Accuracy behavior throughout the terminal area, its relation to sensor accuracy, its effect on trajectory tracking errors and control activity in an automatic flight control system, and its adequacy in terms of existing criteria for various terminal area operations are examined. The principal investigative tool is a simulation of the system.

17. Key Words (Suggested by Author(s))
Navigation
Flight control
Kalman filtering
Trajectory estimation

18. Distribution Statement
Unclassified - Unlimited

Subject category - 04

19. Security Classif. (of this report)
Unclassified

20. Security Classif. (of this page)
Unclassified

21. No. of Pages
147

22. Price*
A07

*For sale by the National Technical Information Service, Springfield, Virginia 22161

NASA-Langley, 1983

National Aeronautics and
Space Administration

Washington, D.C.
20546

NASA